Dissertation Nr. 26401

Determining Earth's mantle thermo-chemical structure from joint analysis of seismic and electromagnetic sounding data

A thesis submitted to attain the degree of

Doctor of Sciences of ETH Zürich

(Dr. sc. ETH Zürich)

presented by

Federico Daniel Munch

Geophysicist, National University of La Plata

born on September 26, 1991

citizen of Argentina

accepted on the recommendation of

Prof. Dr. Domenico Giardini	ETH Zürich
PD. Dr. Amir Khan	University of Zürich
	ETH Zürich
Prof. Dr. Alexey Kuvshinov	ETH Zürich
Dr. Alexander Grayver	ETH Zürich
Prof. Dr. Jakub Velimský	Charles University
Prof. Dr. Jeroen Ritsema	University of Michigan

2019

Abstract

Knowledge on the internal structure of planets is essential to our understanding of the origin and evolution of the solar system. As most of the Earth's interior remains geochemically un-sampled, geophysical techniques play a prominent role because of their ability to remotely sense structure with depth. Over the last decades, global seismic tomography has reached a certain level of maturity providing spectacular images of the Earth's interior that reveal mantle heterogeneities to exist at several length-scales (from continental to sub-regional) in the form of lateral variations in elastic properties. However, the nature and origin of these heterogeneities and its implications for mantle dynamics are still debated because separation of thermal and compositional contributions purely from seismic wave velocities is a challenging task. Furthermore, the role played by water in determining the evolution of Earth through its influence on chemical differentiation and mantle dynamics is essential to our understanding of the mantle dynamics. However, recent studies reported that seismic velocities are insensitive to the presence of water (hydrogen) at the temperature and pressure conditions in the mantle.

An alternative technique to image the Earth's interior is deep electromagnetic (EM) sounding, which maps variations in electrical conductivity. Deep EM sounding techniques rely on the analysis of EM fields generated by electric currents flowing in the conductive Earth, which are induced by a time-varying external magnetic field. While seismic velocities are sensitive to variations in temperature and composition, electrical conductivity is mainly sensitive to variations in temperature and the presence of water and melt. Therefore, joint analysis of seismic and EM sounding data can potentially provide complementary information to separate the effects of temperature and composition as well as bring new insights on the distribution of water (hydrogen) in the mantle.

The present study aims at investigating variations in mantle temperature, composition, and water (hydrogen) distribution from the analysis of seismic and EM sounding data. Our approach interfaces the geophysical inversion with self-consistent mineral phase equilibria calculations and laboratory-measured electrical conductivity of mantle minerals to predict profiles of bulk elastic properties and electrical conductivity as a function of pressure, temperature, bulk composition, and water content. The geophysical inversion is solved in a probabilistic approach to provide estimates on model uncertainty.

We first focus on the analysis of P–to–s conversions (in the form of receiver functions) occurring at the discontinuities bounding the mantle transition zone and surface wave dispersion data to investigate variations in mantle temperature and composition beneath a number of different tectonic settings. This required the development of a new methodology to directly invert P–to–s receiver functions waveforms for mantle temperature and composition. After assessing the robustness of the methodology, we built and inverted a global high-quality dataset of receiver function waveforms from an initial pool of 151 stations enhanced with the most recent available global dataset of Rayleigh wave phase velocity dispersion for the fundamental mode and up to fifth overtone. We find that a compositional boundary is not required to explain the seismic data underneath stable continental regions, whereas compositional layering can explain part of the complexity present in the data recorded near subduction zones and volcanically active regions. Furthermore, our findings suggest that: 1) cratonic regions are characterized by low mantle potential temperatures and significant lateral variability in mantle composition; and 2) chemical equilibration seems more difficult to achieve beneath stable cratonic regions suggesting that the lithologic integrity of the subducted basalt and harzburgite is better preserved for geologically significant times underneath these regions.

Moreover, we estimated and inverted long period (3–85 days) EM sounding data to infer the 1D conductivity structure beneath a set of worldwide distributed geomagnetic observatories. The retrieved conductivity profiles are best constrained between 400–1400 km depth. In order to improve the model resolution, we incorporated EM sounding data from ionospheric origin (period range 6–24 hours) into the inversion for a set of inland geomagnetic observatories. The incorporation of EM variations in the daily-band leads to a significant improvement in model resolution, particularly in the upper mantle and transition zone. The inverted conductivity profiles were subsequently interpreted in terms of variations in upper mantle and transition zone water content using constraints on mantle temperature and composition derived from the analysis of seismic data. Our results indicate a relatively dry upper mantle underneath all stations, whereas significat lateral variability in mantle transition zone water content is observed. Our findings suggest the existence of a relatively dry transition zone beneath Europe and a water-enriched transition zone underneath North America and Asia.

Zusammenfassung

Das Wissen über den Aufbau von Planeten, ist von wesentlicher Bedeutung für unser Verständnis des Ursprungs und der Entwicklung des Sonnensystems. Da große Teile des Erdinneren geochemisch nicht beprobt werden können, spielen geophysikalische Methoden dabei eine herausragende Rolle, da sie in der Lage sind die innere Struktur der Erde aus der Ferne zu erfassen. Seit den letzten Jahrzehnten ermöglich es die globale seismische Tomographie spektakuläre Bilder des Erdinneren anzufertigen. Diese zeigen Mantelheterogenitäten in Form von Variationen der elastischen Eigenschaften auf verschieden Längen-Skalen (von kontinental bis sub-regional). Allerdings ist die Art und Herkunft dieser Heterogenitäten immer noch Gegenstand von Debatten, da aus seismischen Geschwindigkeiten die thermischen und kompositorischen Beiträge nur schwer zu unterscheiden sind. Durch seinen Einfluss auf chemische Differenzierung und Manteldynamik, fällt Wasser eine wesentliche Rolle bei unserem Verständnis des Erdmantels zu. Aktuelle Studien zeigen, dass seismische Geschwindigkeiten, unter den relevanten Druck- und Temperaturbedingungen des Erdmantels, keine Empfindlichkeit bezüglich des Vorhandenseins von Wasser aufweisen.

Eine alternative Methode ist die elektromagnetische Tiefenforschung (EM), welche Variationen in der elektrischen Leitfähigkeit abbildet. EM-Methoden beruhen auf der Analyse der elektromagnetischen Felder, welche durch elektrische Ströme im leitfähigen Erdinneren erzeugt werden. Der Ursprung der elektrischen Ströme liegt in den Variationen des magnetischen Außenfeldes. Während seismische Geschwindigkeit empfindlich gegenüber Variationen in der Zusammensetzung und Temperatur sind, ist die elektrische Leitfähigkeit hauptsächlich für Temperatur und das Vorhandensein von Wasser und Schmelze empfindlich. Eine gemeinsam Analyse von seismischen Geschwindigkeiten und EM-Daten hat das Potential den jeweiligen Einfluss von Temperatur und Zusammensetzung abzuschätzen, oder neue Einsichten in die Verteilung von Wasser im Mantel zu gewähren.

Es ist das Ziel der vorliegenden Arbeit, durch die Analyse von seismischen und EM-Daten, Variationen in Temperatur, Zusammensetzung und Wassergehalt des Erdmantels zu untersuchen. Unser Ansatz bringt geophysikalische Inversion, selbstkonsistente Berechnung von Phasengleichgewichten, sowie Labormessungen der elektrischen Leitfähigkeit von Mantelmineralen zusammen. Dies ermöglicht uns Tiefenprofile der elastischen Eigenschaften und elektrischen Leitfähigkeit, in

Abhängigkeit von Druck, Temperatur, Zusammensetzung und Wassergehalt des Mantels, zu erhalten. Um eine Abschätzungen der Modellunsicherheit zu ermöglichen, wird die Inversion in einem probabilistischen Ansatz durchgeführt.

Zunächst konzentrieren wir uns auf die Analyse der P-zu-s Wellen Konvertierung (in Form von Empfängerfunktionen), die an den Diskontinuitäten der Mantelübergangszone auftritt, sowie auf Daten zu Dispersion von Oberflächenwellen, um Variationen der Temperatur und Zusammensetzung des Mantels unterhalb verschiedener tektonischer Regime zu untersuchen. Dies erforderte die Entwicklung einer neuartigen Methode zur direkten Inversion der Wellenform von P-zu-s Empfängerfunktionen nach Manteltemperatur und Zusammensetzung. Nach der Überprüfung der Robustheit unserer Methode, erstellten wir einen hochqualitativen, globalen Datensatz mit Empfängerfunktionen aus einem ursprünglichen Pool von 151 Stationen. Dieser wurde zudem um modernste globale Daten zur Dispersion in der Phasengeschwindigkeit von Rayleigh-Wellen ergänzt.

Wir stellen fest, dass keine kompositorische Grenze nötig ist, um die seismischen Daten unterhalb stabiler kontinentaler Region zu erklären, wohingegen kompositorische Schichtung Teile der Komplexität in den Daten nahe von Subduktionszonen und vulkanisch aktiven Regionen erklärt. Des weiteren legen unsere Ergebnisse nahe, dass: 1) kratonische Regionen durch eine niedrige potentielle Temperatur und signifikante laterale Variabilität charakterisiert werden; und 2) chemischer Ausgleich unter kratonischen Regionen schwerer erreichbar zu sein scheint. Dies deutet darauf hin, dass subduzierte Basalte und Harzburgite unterhalb dieser Regionen auch über geologische Zeiträume unversehrt bleiben.

Des weitern berechneten und invertierten wir langzeit-EM-Daten (3 bis 85 Tage), um die 1D Tiefenstruktur unterhalb ausgewählter, weltweit verteilter, geomagnetischer Observatorien zu erhalten. Die daraus erhaltenen Profile sind im Bereich von 400 bis 1400km tiefe am besten eingegrenzt. Um die Modellauflösung zu verbessern, integrierten wir EM-Daten ionosphärischen Ursprungs (Periodelänge zwischen 6 und 24 Stunden) in unseren Inversionsdatensatz für die Observatorien im Landesinneren. Dies führt zu einer signifikanten Verbesserung der Modellauflösung, insbesondere im oberen Mantel und in der Mantelübergangszone. Die invertierten Leitfähigkeitsprofile wurden anschliessend im Hinblick auf Variationen im Wassergehalt des oberen Mantels und der Mantelübergangszone interpretiert. Dabei wurden die, aus den seismischen Daten berechneten, Rahmenbedingungen bezüglich Wassergehalt und Zusammensetzung berücksichtigt. Unsere Ergebnisse deuten auf einen relativ trockenen oberen Mantel unterhalb aller Stationen hin, wohingegen wir eine signifikante laterale Variation im Wassergehalt der Mantelübergnangszone beobachten. Unsere Ergebnisse legen die Existenz einer relative trockenen Mantelübergangszone unterhalb von Europa und eine mit Wasser angereicherte Mantelübergangszone unterhalb von Nordamerika und Asien nahe.

The Earth is a very small stage in a vast cosmic arena.
– Carl Sagan

Contents

Chapter 1

Introduction

Since the acceptance of solid-state mantle convection as the driving mechanism of plate tectonics in the late 1960s, geoscientists have been debating about the mantle thermo-chemical structure and the detailed morphology of convection. Geophysical techniques have played a key role in this debate because of their ability to remotely sense structure with depth. In particular, seismic tomography (e.g., *Nettles and Dziewoński*, 2008; *Tape et al.*, 2009; *Fichtner et al.*, 2009; *Lekić and Romanowicz*, 2011; *Yuan et al.*, 2011; *Schaeffer and Lebedev*, 2013; *French and Romanowicz*, 2014; *Krischer et al.*, 2018) has provided important constraints on the global structure of the mantle such as: 1) the existence of a strong correlation between velocity patterns in the top 200 km and surface tectonics; 2) the presence of subducted slabs penetrating into lower mantle or stagnating at the bottom of the mantle transition zone (MTZ); 3) the existence of a low-velocity zone under ocean basins; and 4) the presence of two antipodal large low-shear-velocity provinces at the base of the mantle under central Pacific and Africa.

In addition, recent advances in mineral physics databases (e.g., *Stixrude and Lithgow-Bertelloni*, 2005a,b; *Xu et al.*, 2008; *Holland and Powell*, 2011; *Zunino et al.*, 2011) and knowledge on elastic properties of mantle phases (e.g., *Jackson et al.*, 2005; *Murakami et al.*, 2012; *Schulze et al.*, 2018) at high pressure and temperature triggered quantitative research on the nature of observed variations in seismic properties. Previous studies (e.g., *Forte and Perry*, 2000; *Goes et al.*, 2000, 2005; *Deschamps and Trampert*, 2004; *Trampert et al.*, 2004; *Cammarano and Romanowicz*, 2007; *Cobden et al.*, 2008; *Utada et al.*, 2009) have attempted to infer thermo-chemical variations in the mantle by using mineral physics databases to interpret 1D and 3D seismic velocity models finding significant deviations in temperature and composition from the standard pyrolite model of *Ringwood* (1975). However, due to the trade-off between temperature and composition on seismic velocities (see Figure 1.1), separation of thermal and chemical effects solely from seismic velocities is a challenging task (*Trampert et al.*, 2004; *Simmons et al.*, 2009; *Khan et al.*, 2011a). Consequently, the thermal and/or chemical origin of the observed velocity

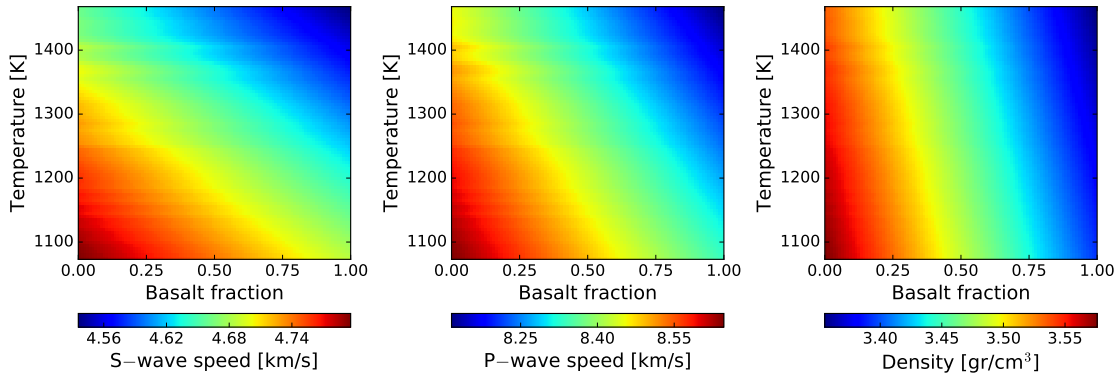

Figure 1.1: Elastic properties (S–wave and P–wave speeds) and density as a function of temperature and composition (basalt fraction) at constant pressure (4 GPa).

heterogeneities and their relation, if any, to the mode by which the mantle convects remain poorly understood.

Alternatively, efforts have recently focused on combining mineral physics databases directly with geophysical observations. For instance, *Khan et al.* (2007) developed a general formulation to constrain composition and thermal state from a priori unrelated geophysical data. The method is based on inverting for a set of parameters which describe the system of interest at a fundamental level, such as, chemical composition and temperature, rather than density and seismic-wave velocity. This provides a natural way of linking geophysical data that are not a priori related, such as seismic and gravity observations. Building on this concept, *Afonso et al.* (2013) developed a tool (LitMod3D; *Fullea et al.*, 2009) that integrates different geophysical observables (e.g., surface wave dispersion, body-wave tomography, magnetotelluric, geothermal, gravity, elevation, and geoid data) to map regional variations in lithospheric and sub-lithospheric upper mantle temperature and composition in a probabilistic framework. *Ritsema et al.* (2009a) employed a self-consistent thermodynamic method to analyze differences in observed and calculated differential traveltimes between P–waves converted into S–waves (P–to–s conversions) and S–wave reflections (*Ritsema et al.*, 2009b) occurring at the MTZ in terms of the mantle temperature. Furthermore, *Khan et al.* (2009) used global surface-wave phase-velocity dispersion data to directly image upper mantle Mg/Fe and Mg/Si variations and topography on the 410-km discontinuity concluding that compositional effects can not be excluded even at long wavelengths. Until now, short- (P–to–s conversions) and long- (Rayleigh wave dispersion) seismic data have not been combined to resolve mantle thermo-chemical structure down to the base of the MTZ.

Deep electromagnetic (EM) sounding techniques provide independent and complementary constraints on the Earth's interior by recovering the electrical conductivity distribution in the mantle (e.g., *Koyama et al.*, 2006; *Kelbert et al.*, 2009; *Shimizu et al.*, 2010; *Semenov and Kuvshinov*, 2012; *Sun et al.*, 2015). Deep EM

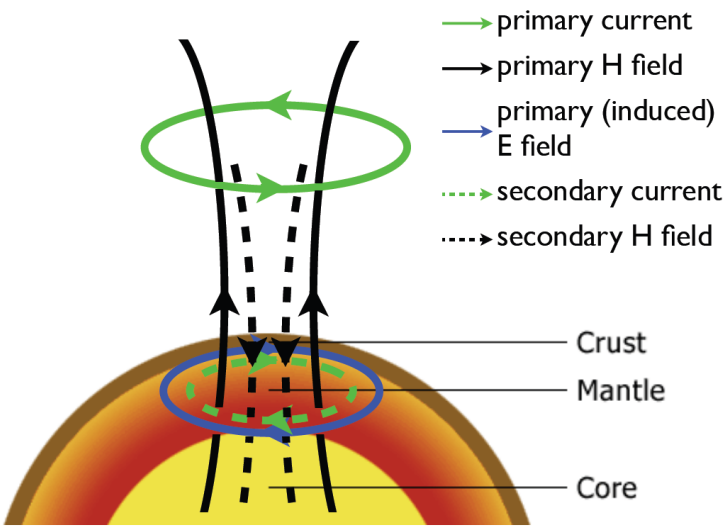

Figure 1.2: Cartoon illustrating the concept of electromagnetic induction. A primary time-varying current (green solid arrow) generates a primary time-varying magnetic field (black solid arrows); which induces an electric field in the conducting Earth (blue solid arrow). The latter subsequently drives a secondary current (green dashed arrow), generating a secondary magnetic field (black dashed arrows). As a result, measurements taken on the Earth's surface reflect contributions from both primary (external) and secondary (internal) fields. Figure extracted from *Püthe* (2015).

sounding techniques rely on the fact that primary magnetic fields (e.g., those that originate in the magnetosphere) penetrate into the deep Earth and induce secondary signals by virtue of electromagnetic induction (illustrated in Figure 1.2). Deep EM sounding techniques can be divided into the magnetotelluric (MT) method (*Simpson and Bahr*, 2005) and geomagnetic deep sounding (GDS) (e.g., *Banks*, 1973). The former relies on EM variations (up to a few hours) that originate from lightning activity and solar wind interaction with the magnetosphere, whereas the latter is based on EM variations ranging from 4 hours to several months. Variations in the daily band are produced by the ionospheric Sq current system (e.g., *Yamazaki and Maute*, 2017), while variations with periods longer than one day are generated by the magnetospheric ring current (e.g., *Daglis and Kozyra*, 2002) and are known as disturbed storm-time (Dst) variations. As the penetration depth depends on frequency, analyzing these signals in a wide range of periods allows sensing electrical conductivity variations as a function of depth (e.g., *Püthe et al.*, 2015a), which can be subsequently interpreted in terms of variations in mantle thermo-chemical structure (e.g., *Khan and Shankland*, 2012). Electrical conductivity is a transport property highly sensitive to water content (see Figure 1.3) and temperature, while being insensitive to other factors such as major element chemistry (e.g., *Karato and Wang*, 2013). Consequently, electrical conductivity represents a valuable tool to constrain the distribution of water in the mantle (e.g., *Khan*, 2016).

Hydrogen (water) affects the evolution of planets through its influence on rheological properties (e.g., *Mei and Kohlstedt*, 2000; *Karato and Jung*, 2003) and melting

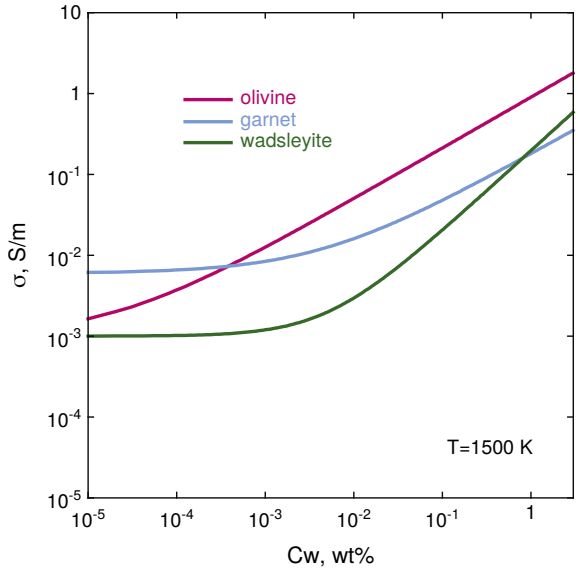

Figure 1.3: Influence of water content (Cw) on electrical conductivity (σ) at 1500 K in olivine (4 GPa), garnet (4 GPa), and wadsleyite (15 GPa). Figure modified from *Karato* (2010).

relationships (e.g., *Inoue*, 1994) and it has been found to be essential in sustaining plate tectonics (*Noack et al.*, 2012; *Gillmann and Tackley*, 2014). Therefore, insights on the processes by which water cycles between the different reservoirs (atmosphere, oceans, crust, and mantle) are essential to our understanding on the evolution and dynamics of the Earth. The deep water cycle operates by extracting water from the mantle via partial melting processes at several locations such as mantle wedges above subduction zones and up- and downwellings across the MTZ (*Williams and Hemley*, 2001; *Hirschmann*, 2006; *Karato*, 2010). Volcanically-outgassed water returns to the mantle via subduction of oceanic lithosphere (e.g., *Ohtani et al.*, 2004; *Ohira et al.*, 2014). As a slab descends into the mantle, part of the water stored in the crystal structure of minerals gets released inducing partial melting and resurfaces via volcanic eruptions (*Schmidt and Poli*, 1998). While the remaining part can be transported to the deep mantle along cold geotherms (e.g., *Ohtani et al.*, 2004) where it can reside either in solid mantle minerals or in the form of hydrous fluids or melts (e.g., *Keppler and Bolfan-Casanova*, 2006). High-pressure mineral-physics studies have reported that MTZ minerals can storage anomalously high amounts of water (∼1–3 wt%), whereas only lower amounts (∼0.1–0.2 wt%) can be stored in upper mantle minerals (e.g., *Bolfan-Casanova*, 2005; *Inoue et al.*, 2010). Supporting evidence for a relatively dry (∼0.02 wt%) upper mantle and a hydrous (∼1 wt%) MTZ has arisen from the analyses of mantle xenoliths (e.g., *Peslier and Bizimis*, 2015; *Peslier et al.*, 2010) and ringwoodite inclusions found in a natural diamond originated below the lithospheric mantle (*Pearson et al.*, 2014), respectively. These studies suggest that the mantle could potentially store the equivalent of several oceans of water (*Hirschmann et al.*, 2005) with the MTZ playing an important role in controlling the global water circulation (e.g., *Bercovici and Karato*,

2003). However, as the solubility limit represents an upper boundary on the water distribution (i.e., regions with high water solubility could have little water content), the present-day distribution of water in the Earth's interior and the mechanisms for water exchange between different reservoirs remains uncertain (e.g., *Ohtani et al.*, 2004; *Hirschmann*, 2006; *Bolfan-Casanova et al.*, 2006).

The main goal of this work is to map variations in mantle temperature, composition (major element), and water (hydrogen) content from the analysis of seismic (P–to–s converted waves and Rayleigh wave dispersion) and electromagnetic sounding (Sq and Dst variations) data. Building on previous experience (e.g., *Khan et al.*, 2007, 2009; *Khan*, 2016), our approach interfaces the geophysical inversion with self-consistent mineral phase equilibria calculations (*Connolly*, 2009; *Stixrude and Lithgow-Bertelloni*, 2005b, 2011) from which rock mineralogy and its elastic properties are computed as a function of pressure, temperature, and bulk composition. Furthermore, phase equilibrium computations are combined with laboratory-measured electrical conductivity of mantle minerals to self-consistently estimate bulk electrical conductivity profiles.

P-to-s converted waves are teleseismic P–waves that convert into S–waves when encountering a discontuinity in material properties. These waves contain a significant amount of information on the seismic structure beneath the receiver and are routinely used for qualitative detection of mineralogical phase changes at 410 and 660 km depth (e.g., *Helffrich*, 2000; *Lawrence and Shearer*, 2006a; *Tauzin et al.*, 2008). However, these waves are more rarely used in geophysical inversions to determine the thermo-chemical structure of the upper mantle and transition zone. In this context, we developed a novel methodology to directly invert P-to-s converted waves (in the form of receiver functions) for mantle temperature and composition. This new methodology is described in Chapter 2, which is based on one of the papers published during my PhD (*Munch et al.*, 2018b).

After assessing the robustness of the methodology by performing a set of synthetics tests, we applied the developed technique to a new global high-quality dataset of receiver function waveforms from an initial pool of 151 stations enhanced with the most recent available global dataset of Rayleigh wave phase velocity dispersion for the fundamental mode and up to fifth overtone (*Durand et al.*, 2015) to map global variations in mantle temperature and composition down to the base of the transition zone. Our main findings are presented and discussed in Chapter 3. The text in the chapter is based on a further publication (*Munch et al.*, 2019).

We independently investigated variations in mantle thermo-chemical structure from inversion of EM sounding data. Building on previous experience (*Semenov and Kuvshinov*, 2012), we estimated and inverted long period (3–85 days) EM sounding data to infer the 1D conductivity structure beneath a set of worldwide distributed geomagnetic observatories. A detailed description of the methodology applied and

main results are presented and discussed in Chapter 4, which closely follows one of the papers published during my PhD (*Munch et al.*, 2018a).

In Chapter 5, we present and discuss an strategy to infer variations in mantle temperature, composition, and water content from the inversion of multi-source seismic and electromagnetic data. The content of this chapter will be soon submitted for publication. First, we jointly inverted Sq (6–24 hours) and Dst (3-85 days) variations to constrain the electrical conductivity structure underneath a set of geomagnetic observatories, accounting for complex spatial structure in the ionospheric and magnetospheric sources (*Püthe et al.*, 2015b). The incorporation of ionospheric signals into the inversion leads to a significant improvement in model resolution, particularly in the upper mantle and MTZ. The inverted conductivity profiles were subsequently interpreted in terms of water content in the upper mantle and MTZ by combining phase equilibrium computations, laboratory-measured electrical conductivity of mantle minerals, and constrains on mantle temperature and composition derived from the analysis of short- and long-period seismic data.

Finally, the work presented in this thesis is summarized and its implications for future research are discussed in Chapter 6. The thesis also includes 4 appendices (A, B, C, and D) complementing the main text.

Chapter 2

Seismic investigation of the mantle transition zone: Methodology

The content of this chapter was published as: Munch, F. D., Khan, A., Tauzin, B., Zunino, A. & Giardini, D. (2018). *Stochastic inversion of P–to–s converted waves for mantle composition and thermal structure: methodology and application.* Journal of Geophysical Research: Solid Earth, vol 123, pp.10706-10726 (doi: 10.1029/2018JB016032).

Abstract

We present a new methodology for inverting P–to–s receiver function (RF) waveforms directly for mantle temperature and composition. This is achieved by interfacing the geophysical inversion with self-consistent mineral phase equilibria calculations from which rock mineralogy and its elastic properties are predicted as a function of pressure, temperature, and bulk composition. This approach anchors temperatures, composition, seismic properties, and discontinuities that are in mineral physics data, while permitting the simultaneous use of geophysical inverse methods to optimize models of seismic properties to match RF waveforms. Resultant estimates of transition zone (MTZ) topography and volumetric seismic velocities are independent of tomographic models usually required for correcting for upper mantle structure. We considered two end-member compositional models: the equilibrated Equilibrium Assemblage (EA) and the disequilibrated Mechanical Mixture (MM) models. Thermal variations were found to influence arrival times of computed RF waveforms, whereas compositional variations affected amplitudes of waves converted at the MTZ discontinuities. The robustness of the inversion strategy was tested by performing a set of synthetic inversions in which crustal structure was assumed both fixed and variable. These tests indicate that unaccounted-for crustal structure strongly affects the retrieval of mantle properties, calling for a two-step strategy presented herein to simultaneously recover both crustal and mantle parameters. As a proof of concept, the methodology is applied to data from two stations located in the Siberian and East

European continental platforms.

2.1 Introduction

P–to–s converted waves are teleseismic P–waves that convert a portion of their energy into S–waves when encountering a discontinuity in material properties. Such converted waves are recorded as part of the P–wave coda and contain a significant amount of information on the seismic structure beneath the receiver. However, they are strongly influenced by the seismic source signature and the structure encountered along their propagation path through the mantle. These influences can be eliminated by deconvolving the vertical component v(t) from the radial component r(t) (*Phinney*, 1964). The result is a time series called the receiver function (RF) (*Langston*, 1979) where time is a proxy for depth and positive (or negative) amplitudes roughly correspond to an increase (or decrease) in shear-wave velocities.

RF waveforms are mostly sensitivity to the shape of velocity gradients and contain little information on absolute velocities (*Rondenay*, 2009). Constraints on absolute velocities are typically gained by adding a priori information from a global/regional seismic model (e.g., *Ammon et al.*, 1990) or by combining RF waveforms with other geophysical observables such as surface wave group and phase velocities (e.g., *Moorkamp et al.*, 2010; *Shen et al.*, 2013; *Calò et al.*, 2016). More commonly, RF waveforms are used to identify discontinuities in seismic velocities such as the Moho (e.g., *Kind and Vinnik*, 1988; *Langston and Hammer*, 2001; *Lodge and Helffrich*, 2009; *Lombardi et al.*, 2009; *Calò et al.*, 2016), the lithosphere-asthenosphere boundary (*Sodoudi et al.*, 2006; *Heit et al.*, 2007; *Kumar et al.*, 2012; *Kind et al.*, 2012), and the 410– and 660–km discontinuities (*Lawrence and Shearer*, 2006a; *Tauzin et al.*, 2008; *Vinnik et al.*, 2009; *Cottaar and Deuss*, 2016). The latter discontinuities are the most seismically-visible features of the mantle transition zone (MTZ). The 410–km discontinuity reflects the exothermic olivine→wadsleyite phase transition, and the 660–km discontinuity is mainly produced by the endothermic ringwoodite→bridgmanite+ferropericlase transition (*Ringwood*, 1975). As these phase transitions are sensitive to variations in mantle thermo-chemical state, changes in temperature or composition affect location and sharpness of the discontinuities and MTZ velocity gradients (e.g., *Bina and Helffrich*, 1994; *Shearer*, 2000; *Khan et al.*, 2009).

As shown in Figure 2.1, P410s and P660s correspond P–to–s waves converted at the 410– and 660–km discontinuities, respectively. These converted waves can be used to map variations in the sharpness and depth range of velocity gradients in the mantle MTZ (e.g., *Helffrich*, 2000; *Lawrence and Shearer*, 2006b; *Schmandt*, 2012). In this context, previous studies have mapped both regional (e.g., *Farra and Vinnik*, 2000; *Owens et al.*, 2000; *Chen and Ai*, 2009; *Cao and Levander*, 2010) and

global (e.g., *Chevrot et al.*, 1999; *Lawrence and Shearer*, 2006a; *Tauzin et al.*, 2008) variations in MTZ thickness and velocity. Interpretation of the inferred variations in terms of mantle temperatures are typically reported as deviations from an arbitrarily chosen reference geotherm (e.g., *Deuss et al.*, 2006, 2013; *Tauzin and Ricard*, 2014; *Cottaar and Deuss*, 2016) and are often based on knowledge of the Clapeyron slope for pure $(Mg,Fe)_2SiO_4$-phases, but neglect the contribution from other phases (e.g., pyroxene and garnet) (e.g., *Owens et al.*, 2000; *Tauzin et al.*, 2013).

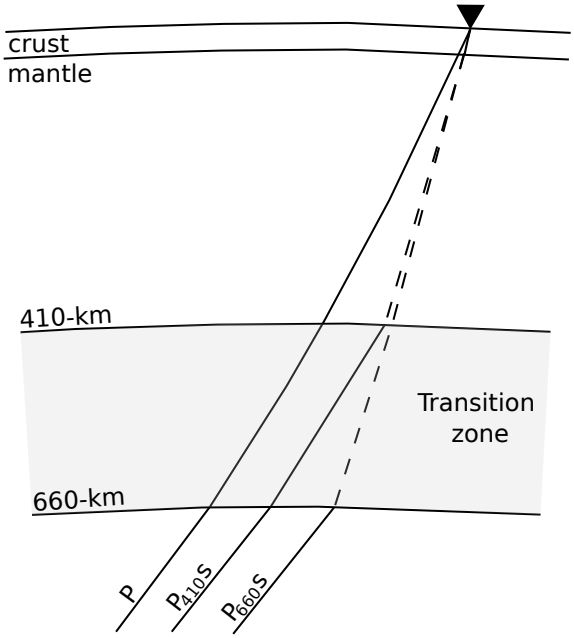

Figure 2.1: Schematic representation of teleseismic P–to–s waves scattered in the mantle transition zone and recorded at a seismic station (black triangle). Solid and dashed lines correspond to P and S ray path segments, respectively. Figure modified from *Schmandt* (2012).

Here, we describe a strategy to determine composition, thermal state, mineralogy, and seismic properties of Earth's mantle, directly from the inversion of P–to–s converted waves in the form of RF waveforms. The inversion scheme makes use of self-consistent mineral phase equilibria calculations from which rock mineralogy, and ultimately its elastic properties, can be predicted as a function of pressure, temperature, and bulk composition from thermodynamic data. The advantage of this approach is that it inserts plausible geophysical/petrological knowledge of seismic discontinuities, while permitting the simultaneous use of geophysical inverse methods to optimize profiles of physical properties (e.g., bulk and shear modulus and density) to match geophysical data (e.g., *Stixrude and Lithgow-Bertelloni*, 2005a; *Cammarano et al.*, 2005; *Khan et al.*, 2006, 2009; *Tirone et al.*, 2009; *Cobden et al.*, 2008; *Afonso et al.*, 2013; *Drilleau et al.*, 2013). As an illustration hereof, *Khan et al.* (2013) used surface-wave phase-velocity dispersion data to directly image upper mantle Mg/Fe and Mg/Si variations and topography on the 410–km discontinuity beneath the Australian continent. This study showed that (1) compositional effects could not be excluded even at long wavelengths and (2) the thermochemically-

induced phase transformations strongly contribute to lateral variations in structure and topography across the 410–km discontinuity (see also *Zunino et al.*, 2016). In contrast to estimation of MTZ topography and thickness derived from RF migration (e.g., *Tauzin et al.*, 2013; *Cottaar and Deuss*, 2016), the methodology proposed here does not require the use of a tomographic model to correct for crustal and upper mantle effects. While a previous study (e.g., *Ritsema et al.*, 2009b) only attempted to map effects related to temperature variations in the upper mantle from comparison of theoretical and observed differential travel times between P410s and P and between P660s and P410s, we perform a systematic study that considers variations in the entire RF waveform with respect to all relevant parameters.

In summary, in the present study we wish to extend the methodology employed by *Khan et al.* (2013) to invert RF waveforms directly for mantle thermo-chemical parameters with the ultimate goal of improving constraints on MTZ structure. Synthetic RF waveforms are computed from the thermodynamically-predicted velocity profiles as described in Sections 2.3 and 4.3.2. The inverse problem is solved by combining a Markov chain Monte Carlo method with a stochastic optimization technique (Section 2.5). We first performed a series of synthetic tests (Sections 4.5) in order to examine the effectiveness and robustness of the proposed approach. Finally, as a proof of concept, we apply the proposed strategy to retrieve crustal and mantle structure beneath two permanent stations located in two distinct stable continental regions.

2.2 Model parameterization

2.2.1 Computation of Mantle Mineral Phase Equilibria

Mineralogical models of the Earth typically view the mantle as either homogeneous and pyrolitic (*Ringwood*, 1975; *Francis*, 1987; *Bass*, 1995) or chemically stratified with homogeneous and equilibrated compositions in each layer (e.g., *Mattern et al.*, 2005). To first order, such models are capable of explaining the observed composition of mid-ocean ridge basalts (*McKenzie and Bickle*, 1988; *Frey et al.*, 1978; *Chen et al.*, 1991) and seismic velocities of the upper mantle and transition zone (*Weidner*, 1985; *Ita and Stixrude*, 1992; *Irifune*). However, experimental measurements of mantle mineral chemical diffusivity (e.g., *Hofmann and Hart*, 1978) suggest that equilibration may not be accomplished over the age of the Earth for the amount of stretching and folding predicted in mantle convection simulations (e.g., *Xie and Tackley*, 2004; *Nakagawa and Buffett*, 2005; *Davies*, 2006; *Brandenburg and Van Keken*, 2007). Moreover, trace element chemistry of basalts (e.g., *Hofmann and White*, 1982; *Sobolev et al.*, 2007) and analysis of scattered seismic waves (e.g., *Hedlin et al.*, 1997; *Helffrich*, 2006; *Bentham and Rost*, 2014; *Tauzin et al.*, 2017) also point to the mantle as consisting of a mechanical mixture.

Xu et al. (2008) explored the effect of major element disequilibrium on seismological properties of the mantle. The authors considered two types of mantle compositional models: mechanical mixture and equilibrium assemblage. The former represents the scenario in which pyrolitic mantle has undergone complete differentiation to basaltic and harzburgitic rocks. The bulk properties of this model are computed as the Voigt–Reuss–Hill (VRH) average (*Watt et al.*, 1976) of the properties of the minerals in the basaltic and harzburgitic end-members. In contrast, bulk properties of the equilibrium model are computed based on the mineralogy of the averaged bulk composition. *Xu et al.* (2008) demonstrated that even with identical bulk compositions, an equilibrium assemblage and a mechanical mixture result in different mineral modes and, as a consequence, different bulk S–, P–wave velocities (V_s and V_p, respectively), and densities (ρ). The authors also reported that mechanically mixed models are characterized by faster S–wave velocities as well as sharper velocity gradients.

In view of this and to test these models quantitatively against data, here we consider both the equilibrium assemblage (EA) and mechanical mixture (MM) model. The mineralogy for the EA model is defined as

$$\phi[\mathrm{f}\,\mathbf{X_B} + (1-\mathrm{f})\,\mathbf{X_H}], \tag{2.1}$$

and the phase assemblage for the MM model is given by

$$\mathrm{f}\,\phi[\mathbf{X_B}] + (1-\mathrm{f})\,\phi[\mathbf{X_H}], \tag{2.2}$$

where ϕ corresponds to the phase proportions given the bulk compositions of basalt $\mathbf{X_B}$, harzburgite $\mathbf{X_H}$, and the basalt fraction f. For the purpose of this work, we follow *Xu et al.* (2008) and consider the mantle to be compositionally homogeneous. The choice of basalt and harzburgite as end-members of mantle composition relies on crust formation processes at mid-ocean ridges. To first order, mid-ocean ridges represent the major source of chemical differentiation of the Earth's mantle. At ridges, partial melting generates a basaltic crust leaving behind its depleted complement, harzburgite (*McKenzie and Bickle*, 1988). The resulting physically and chemically stratified oceanic lithosphere is then cycled back into the mantle at subduction zones, becomes entrained in the mantle flow and remixes (e.g., *Tackley et al.*, 2005). In this work, basalt and harzburgite compositions are described using the CFMASNa model chemical system comprising the oxides CaO-MgO-FeO-Al_2O_3-SiO_2-Na_2O (Table 2.1); which account for $\sim 98\%$ of the mass of Earth's mantle (e.g., *Irifune*, 1994).

Mantle thermal structure is described by an adiabatic geotherm underneath a conductive lithosphere. The lithospheric temperature is estimated as a linear gradient defined by the temperature (T_0) at the surface and the temperature (T_{lit}) at

Component	$\mathbf{X_B}$	$\mathbf{X_H}$
CaO	13.05	0.50
FeO	7.68	7.83
MgO	10.49	46.36
Al_2O_3	16.08	0.65
SiO_2	50.39	43.64
Na_2O	1.87	0.01

Table 2.1: CFMASNa basalt $\mathbf{X_B}$ and harzburgite $\mathbf{X_H}$ end-member model compositions (in wt%) taken from *Khan et al.* (2009).

the bottom of the lithosphere (z_{lit}); where z_{lit} is defined as the depth at which the conductive lithospheric geotherm intersects the mantle adiabat defined by the entropy of the lithology at the temperature T_{lit} and pressure P_{lit}. The pressure profile is obtained by integrating the load from the surface.

We combine the free-energy minimization strategy described by *Connolly* (2009) with the self-consistent thermodynamic formulation of *Stixrude and Lithgow-Bertelloni* (2005b) and the parameters given by *Stixrude and Lithgow-Bertelloni* (2011) to estimate rock mineralogy, seismic velocities, and density as a function of pressure, temperature, and bulk composition. The free-energy minimization can be carried out in two ways: by dynamic or by static implementation. Dynamic implementation means minimizing the Gibbs free-energy of the system at a particular value of pressure, temperature, and composition during the inversion process (e.g., *Khan et al.*, 2006; *Duesterhoeft and Capitani*, 2013; *Afonso et al.*, 2013; *Duesterhoeft et al.*, 2014; *Chust et al.*, 2017). Alternatively in the static implementation, physical properties are calculated for a certain range of pressure-temperature conditions and stored in tables prior to the solution of the inverse problem (e.g., *Zunino et al.*, 2011). *Zunino et al.* (2011) developed the Python/Fortran package PHEMGP (`https://github.com/inverseproblem/Phemgp`) that allows fast recovery of bulk rock properties by assembling three-dimensional (pressure-temperature-composition) tables from two-dimensional (pressure-temperature) precomputed tables for single compositions.

Static implementation is very suitable for computing properties in a mechanically mixed mantle because only tables for basalt and harzburgite are needed to calculate properties as a continuous function of mantle composition. A resolution of 0.1 in f is necessary to reproduce velocities in the equilibrium model with the accuracy required for most geophysical applications (*Zunino et al.*, 2011). In the present study, we employ a static implementation (PHEMGP) for computing properties in MM models and a dynamic implementation based on the software Perple_X (`http://perplex.ethz.ch/`) for calculation of mantle properties in EA models.

The present thermodynamic model of *Stixrude and Lithgow-Bertelloni* (2005b, 2011) has limitations. First, the equilibrium assumption is dubious at low temper-

atures because equilibrium might not be achieved (e.g., *Wood and Holloway*, 1984). Consequently, mineralogy for temperature below 1073 K is computed at 1073 K. The resultant mineralogy is then used to calculate physical properties at the temperature of interest. Second, deviations from adiabatic temperature profiles due to radioactive heating and thermal boundary layers induced by phase transitions are neglected (*Stixrude and Lithgow-Bertelloni*, 2011). The thermodynamic model presented here precludes consideration of redox effects (e.g., *Cline II et al.*, 2018) as well as minor phases and components such as H_2O and melt due to lack of thermodynamic data. Density and elastic moduli are estimated to be accurate to within ∼0.5 and ∼1–2%, respectively (*Connolly and Khan*, 2016).

Although it is difficult to quantify the error produced by neglecting H_2O, experimental evidence suggests that the presence of H_2O would tend to thicken the transition zone by moving the olivine-wadsleyite transition up (e.g., *Frost and Dolejš*, 2007) while deepening the dissociation of ringwoodite (*Ghosh et al.*, 2013). Furthermore, the presence of H_2O is expected to reduce seismic velocities due to the weakened chemical bonding by hydrogen (*Karato*, 2010). However, experimental studies suggest that the influence of water on high-frequency elastic wave velocities is minor ($< 0.1\%$) for water content less than ∼0.1wt% at relevant mantle conditions (e.g., *Mao et al.*, 2008; *Chang et al.*, 2015; *Thio et al.*, 2015; *Schulze et al.*, 2018). In addition to changes in phase equilibria, the solidus decreases with increasing water content (e.g., *Hirschmann*, 2010; *Litasov*, 2011). Therefore, a hydrated transition zone could also result in dehydration-induced partial melting on top of the 410–km and underneath the 660–km discontinuity (e.g., *Bercovici and Karato*, 2003; *Schmandt et al.*, 2014). These effects could potentially be significant in regions around subduction zones.

2.2.2 Crustal structure

In the present study, crustal structure is not modeled in terms of the thermochemical parameterization because the thermodynamic database considered here comprises only mantle minerals (*Stixrude and Lithgow-Bertelloni*, 2011). Instead, crustal structure beneath each station is parameterized in terms of five layers with variable S–wave velocity V_s^i and thickness d_i. Crustal velocities are assumed to increase as a function of depth ($V_s^1 < V_s^2 < V_s^3 < V_s^4 < V_s^5 < V_s^{Moho}$) with S–wave velocity below the Moho V_s^{Moho} determined by the mantle compositional and thermal structure (see Section 2.2.1). As discussed by *Roy and Romanowicz* (2017), the choice of crustal V_p/V_s ratio does not significantly affect the recovery of crustal velocity models. Therefore, crustal P–wave velocities and densities are computed using V_p/V_s and ρ/V_s ratios taken from PREM (*Dziewonski and Anderson*, 1981).

2.3 Data processing

The data consist of three-component seismograms recorded at two broad-band permanent stations (see Figure 2.2a) between 1976 and 2016. To ensure a good signal-to-noise ratio, we selected teleseismic events occurring at epicentral distances (Δ) between 40° and 95° with magnitudes larger than 5.5.

The records are first band-pass filtered using a Butterworth filter in the period range 1–100 s. Afterwards, the incident and scattered wavefields are separated by rotation of the three orthogonal components of the seismogram (N–S, E–W, and vertical) into radial (R), transverse (T), and vertical (Z) components. After rotation, the ratio between the maximum amplitude of the signal (measured on the vertical component in the time window $t_p - 5\text{ s} < t < t_p + 25\text{ s}$, where t_p is the theoretical P–wave arrival) and the averaged root-mean-square of the vertical component is computed. All seismograms for which this ratio is lower than 5 are discarded. The selected traces are then trimmed to the time-window $[t_\text{p}-50\,\text{s},\ t_\text{p}+150\,\text{s}]$ and iterative time-domain deconvolution (*Ligorria and Ammon*, 1999) is applied to deconvolve the Z and R components. Time-domain deconvolution is performed by progressively constructing the Earth's impulse response through iterative cross-correlation between the observed radial component and source wavelet (vertical component), and extraction of the highest correlated signal at each iteration. This approach has the advantage of providing long-period stability and requiring causality in the recovered RF waveforms (*Ligorria and Ammon*, 1999; *Rondenay*, 2009).

As the amplitudes of P410s and P660s are considerably smaller compared to the P–wave amplitude, the signal-to-noise ratio must be increased to guarantee the detectability of the converted waves (*Rondenay*, 2009). This can be achieved by stacking a large number of RF waveforms. Prior to stacking, RF waveforms are low-pass filtered to remove frequencies higher than 0.2 Hz. Frequencies higher than 0.2 Hz are removed because the amplitude of transition zone conversions on stacked waveforms significantly decreases at higher frequencies due to environmental noise, signal processing effects, and the effect of 3D heterogeneities on travel-times. The stacking procedure averages hundreds of RF waveforms from different events recorded at a station and thus characterized by different epicentral distances, ray parameters (slownesses) of the P–wave, and therefore P–wave incidence angles. As the path of P– and S–waves between the interface of conversion and the surface have different lengths depending on the angle of incidence, a curvature (move-out) is observed in the differential travel-time between the conversion and the P-wave. In order to coherently stack the converted waves, a correction for this curvature (move-out correction) should be applied prior to stacking. The move-out correction is here computed for the IASP91 (*Kennett and Engdahl*, 1991) velocity model at a reference slowness of 6.5 s/deg, which corresponds to a reference epicentral distance

of ∼65°. Finally, errors on stacked amplitudes $\delta\mathrm{RF}^{\mathrm{obs}}(t)$ (2 standard deviations) are estimated using a bootstrap resampling approach (*Efron and Tibshirani*, 1991). In order to test the influence of the velocity model used for the move-out correction on the final stacks, we computed corrections for IASP91 and a best-fitting velocity model (to be described in the following). Differences in the resulting waveforms (see Figure A1) were found to be negligible in comparison to $\delta\mathrm{RF}^{\mathrm{obs}}(t)$.

Figure 2.2c depicts observed RF waveforms as a function of epicentral distance before move-out correction, and the corresponding final move-out corrected stack for the two stations located in Figure 2.2a. Both conversions of interest at the 410-km and 660-km discontinuities, P410s and P660s, appear on individual RF waveforms at roughly 40 and 70 s after the P-wave. The strong conversion at the Moho discontinuity (Pms) and the multiple reverberations within the crust are at the origin of the strong amplitudes in the early part of the RF waveform.

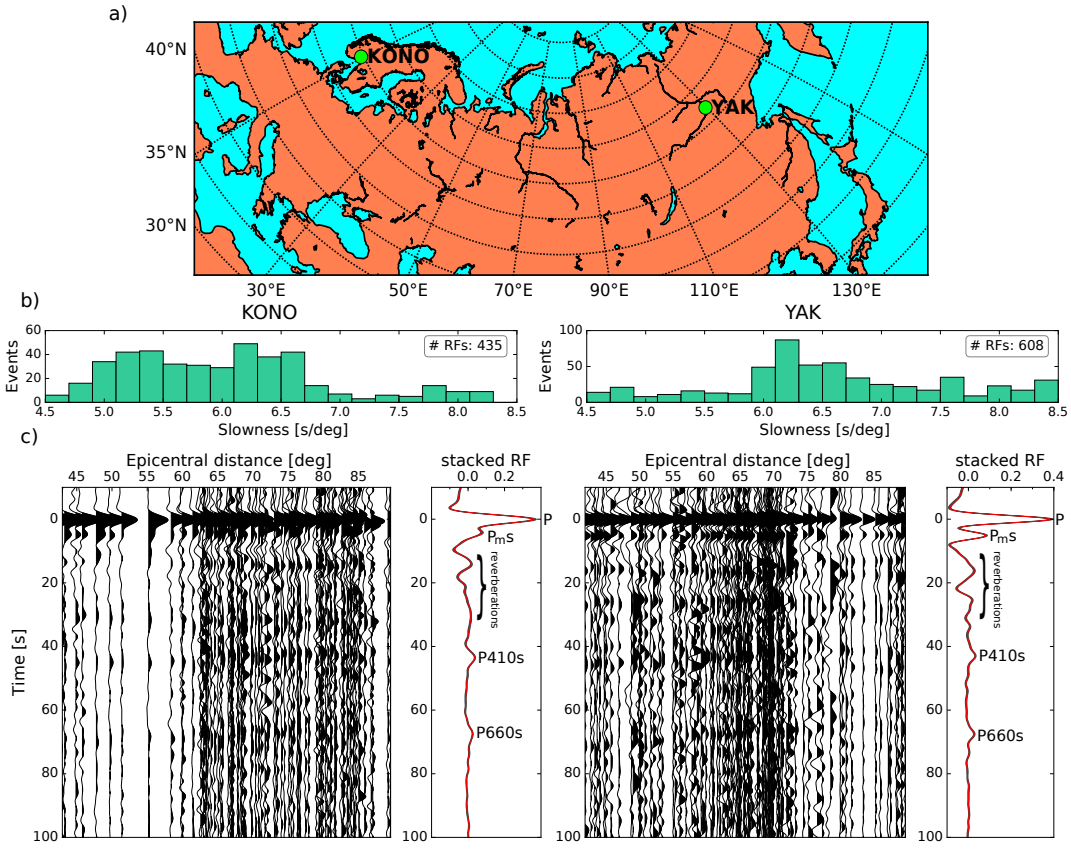

Figure 2.2: (a) Map showing geographical location of the two seismic stations considered in this study: Yakutsk (YAK) and Kongsberg (KONO). (b) Distribution of slownesses of the P–wave recorded at KONO (left) and YAK (right). (c) RF waveforms observed at KONO (left) and YAK (right) as a function of epicentral distance before move-out correction, resulting mean stacks (red), and uncertainties $\delta\mathrm{RF}^{\mathrm{obs}}(t)$ estimated using bootstrap resampling (black, almost indistinct from the mean).

2.4 Computation of synthetic receiver functions

2.4.1 Method

In the following, synthetic waveforms (frequency range: 0.01–0.3 Hz) for 25 slownesses (see Section 2.4.2) are computed using the reflectivity method (*Fuchs and Müller*, 1971; *Muller*, 1985) and subsequently filtered, deconvolved, and stacked using identical methods to those applied to the observed seismograms (Section 2.3). Applying identical methods to both observed and synthetic seismograms is essential for modeling RF waveforms as accurately as possible. The reflectivity method is based on numerical integration of the plane wave reflection coefficient (reflectivity) of a layered medium in the frequency-slowness domain and subsequent multiplication with the source spectrum to obtain synthetic seismograms. The method allows for modeling the full propagation from source to receiver and not only includes transmitted and converted waves, but also accounts for the interference of different phases (e.g., PP, PcP), surface multiples, and deviations of the wavefront from a plane wave at a moderate computational cost ($\sim$45 s per velocity model). As the source influence is removed by the deconvolution, the source characteristics do not have a significant effect on the synthetic RF waveforms. Hence, for simplicity, we model the source as a punctual explosion located at 25 km depth with time signature given by a Heaviside step function. The choice of source depth does not introduce artifacts in the stacked RF waveforms because the depth phases (pP, pS) have a completely different moveout curvature relative to direct conversions across the deconvolved time-slowness section and thus stack incoherently. The resulting RF waveforms have been benchmarked against RF waveforms computed using synthetic seismograms obtained by full waveform modeling methods (*Van Driel et al.*, 2015; *Krischer et al.*, 2017), see Figure A2 in Appendix A.

2.4.2 Slowness distribution

As the transmission coefficients and, consequently, amplitudes of P–to–s conversions depend on the angle of incidence (*Aki and Richards*, 2002), replication of the observed slowness distribution (SD) is essential for proper modeling of converted amplitudes. However, each stacked RF is typically composed of hundreds of single observations characterized by different incidence angles making the computation of synthetic RF waveforms for the entire range of observed slownesses computationally demanding. Here, we propose an alternative strategy to properly model converted amplitudes with relatively low computational cost. The proposed scheme consists of: 1) discretization of the SD into 25 evenly spaced slowness intervals; 2) estimation of the mean observed slowness p_i as well as the number of slownesses N_i in each interval; 3) computation of synthetic RF waveforms for all estimated p_i; and

4) move-out correction and stacking of synthetic RF waveforms weighting each RF according to N_i.

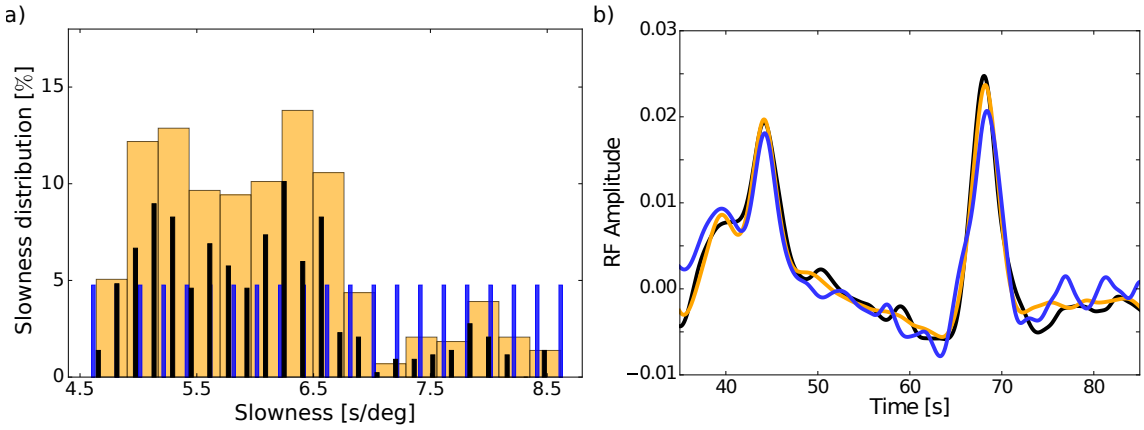

Figure 2.3: Influence of slowness distribution (SD) on the stacked receiver function (RF). a) SD recorded at KONO seismic station (orange), uniform SD (blue), and an approximation of KONO SD using 25 representative slowness values (black). b) stacked RF waveforms obtained for each of the aforementioned SD using the IASP91 velocity model (*Kennett and Engdahl*, 1991).

Figure 2.3 illustrates the importance of correctly accounting for the observed slowness distribution. Figure 2.3a shows the observed SD for KONO seismic station (orange), the discretized SD (black) obtained by the scheme presented above, and a uniform SD (blue). Additionally, Figure 2.3b depicts the stacked RF waveforms computed for the corresponding SD using the IASP91 velocity model (*Kennett and Engdahl*, 1991). No considerable time differences are observed between the computed stacks. However, the estimated P410s (∼44 s) and P660s (∼68 s) amplitudes significantly depend on the SD considered. In particular, computed amplitudes are underestimated when a uniform SD is assumed. That P660s is more affected than P410s can be attributed to the fact that the range of incidence angle is larger for the 660–km discontinuity making variations in conversion amplitude larger.

This example illustrates how inaccurate modeling of the observed slowness distribution can result in significant deviations of the mean slowness and, consequently, amplitudes of conversion. Therefore, the observational slowness distribution must be accurately replicated when inverting RF amplitudes. In this regard, the choice of reference slowness and velocity model used for computing the move-out correction is not significant while identical reference slownesses and velocity models are used on the observed and modeled RF waveforms. Alternatively, the dependency of stacked amplitudes on the heterogeneity of the observed slowness SD could be addressed during data processing. For instance, by partially stacking the observed RF waveforms into bins of slowness and subsequent stacking of the partial stacks. The resulting stack would be less dependent on the heterogeneity of the observed SD. However, such a strategy would potentially increase the weight of noisy data on the final stack. Alternative data processing schemes should be explored, but this is beyond the scope of this work.

2.4.3 Attenuation

As discussed by *Liu* (2003), the observed amplitudes and inferred depth of discontinuities can be significantly affected by anelastic effects (absorption and dispersion) (e.g., *Kanamori and Anderson*, 1977). This is illustrated in Figure 2.4, which shows synthetic RF waveforms computed assuming different shear attenuation (Q_μ) models: a fully-elastic medium (black), PREM reference model (blue), and two viscoelastic models (red and green) based on the extended Burgers model of *Jackson and Faul* (2010). Relatively small variations in shear attenuation model can result in non-negligible amplitude differences (e.g., blue and green models).

To account for anelastic effects, we rely on the extended Burgers viscoelastic model of *Jackson and Faul* (2010) and rheological parameters tabulated therein. This model is based on laboratory experiments of torsional forced-oscillation data on melt-free polycrystalline olivine. The main advantage of this model is that it can be directly linked with the thermodynamic computations as the latter provide the unrelaxed (infinite-frequency) shear modulus in addition to pressure and temperature (*Khan et al.*, 2018). More specifically, shear attenuation as a function of depth for a given thermo-chemical model is derived from the shear modulus, temperature, and pressure profiles obtained by mineral phase equilibria calculations. In case the resultant shear attenuation values are larger than 600 (PREM crustal values), Q_μ is set equal to 600. This model thus allows us to self-consistently account for the influence of temperature and pressure on the shear attenuation model.

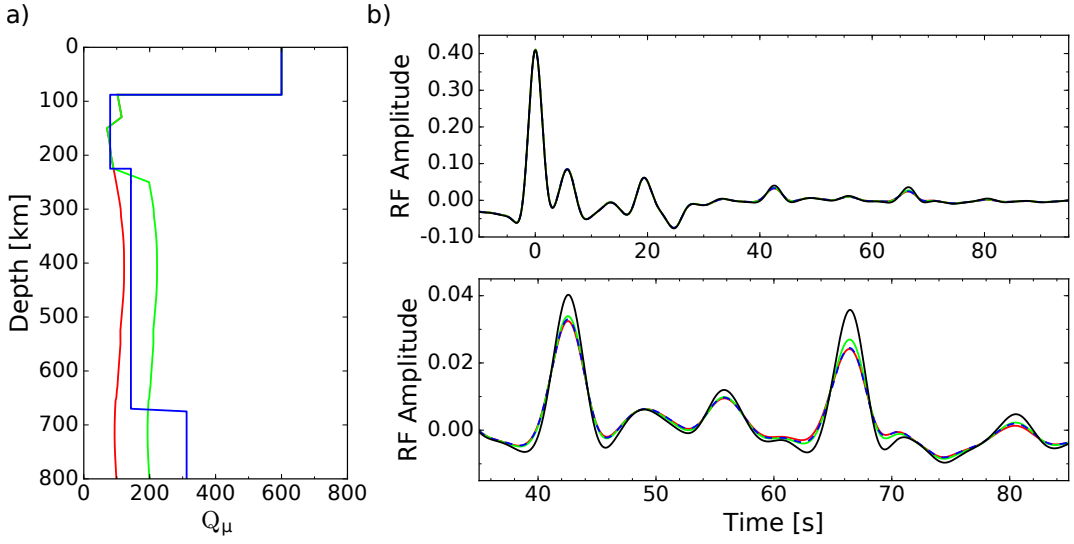

Figure 2.4: The effect of attenuation model on computed receiver functions (RF). (a) Shear attenuation models (Q_μ) correspond to: fully elastic medium (black), PREM reference model (blue), and two viscoelastic shear attenuation models (red and green) based on the rheological model of *Jackson and Faul* (2010). Note that the fully elastic model is not shown in panel a) since $Q_\mu = \infty$. (b) Corresponding RF waveforms.

2.4.4 Influence of temperature and composition on Receiver Functions

In this section, we analyze the dependency of RF waveforms on thermal and compositional variations. To this end, we computed seismic properties for a range of basalt fractions and geotherms following the methodology described in Section 2.2.1. The obtained properties were subsequently used to estimate synthetic RF waveforms as described in Section 2.4.1 using the PREM (*Dziewonski and Anderson*, 1981) shear attenuation model. Figure 2.5a-h summarize S–wave velocity profiles and RF waveforms obtained using EA and MM models, respectively. Variations in phase proportions (modal mineralogy) for each thermo-chemical model are shown in Appendix A (Figures A3–A4).

As reported in previous studies (e.g., *Bina and Helffrich*, 1994; *Xu et al.*, 2008; *Khan et al.*, 2009, among others), compositional and thermal variations affect the depth at which phase transitions occur as well as the amplitude and sharpness of the corresponding seismic discontinuity. For instance, Figure 2.5a shows that depth and amplitude of the 410–km seismic discontinuity decrease with increasing basalt fraction as the mode of $(Mg,Fe)_2SiO_4$-phases decreases (see Figure A3) and ultimately disappears for f>0.8. Moreover, depth, amplitude, and sharpness of the 660–km discontinuity decrease with increasing basalt fraction due to the occurrence of bridgmanite and its decreasing mode at greater depth (see Figure A3); which simultaneously triggers the appearance of a discontinuity at ∼800 km depth. Note that for f>0.5, sharpness and amplitude of this new discontinuity significantly increase relative to those associated with the 660–km discontinuity. Furthermore, differences in velocity profiles computed using the EA (Figure 2.5a) and MM (Figure 2.5e) models are observed; for instance, MM velocity profiles are characterized by sharper velocity gradients in comparison to the EA model (for a detailed discussion see *Xu et al.* (2008)).

Panels c and g in Figure 2.5 depict the influence of thermal structure on V_s for the EA and MM models, respectively. Thermal variations have a larger effect on bulk velocities relative to compositional variations. Furthermore, the depth of the 410–km discontinuity significantly increases (from ∼360 km to ∼440 km depth) with increasing temperature while the velocity jump remains almost constant. In contrast, the depth of the 660–km discontinuity decreases with increasing temperature while the sharpness of the discontinuity decreases due to an enrichment in majoritic garnet at higher temperatures (see Figure A4).

Figure 2.5 (b,d,f, and h) illustrates how the aforementioned velocity variations affect amplitudes and travel times of P–to–s conversions occurring at 410– and 660–km seismic discontinuities and Figure 2.5i-j depict differential traveltime ($t_{\mathrm{P660s}} - t_{\mathrm{P410s}}$) as a function of basalt fraction and temperature, respectively. The decrease in velocity jump and depth of the 410–km discontinuity associated with the increase in basalt fraction results in decreasing P410s amplitudes and earlier arrival times

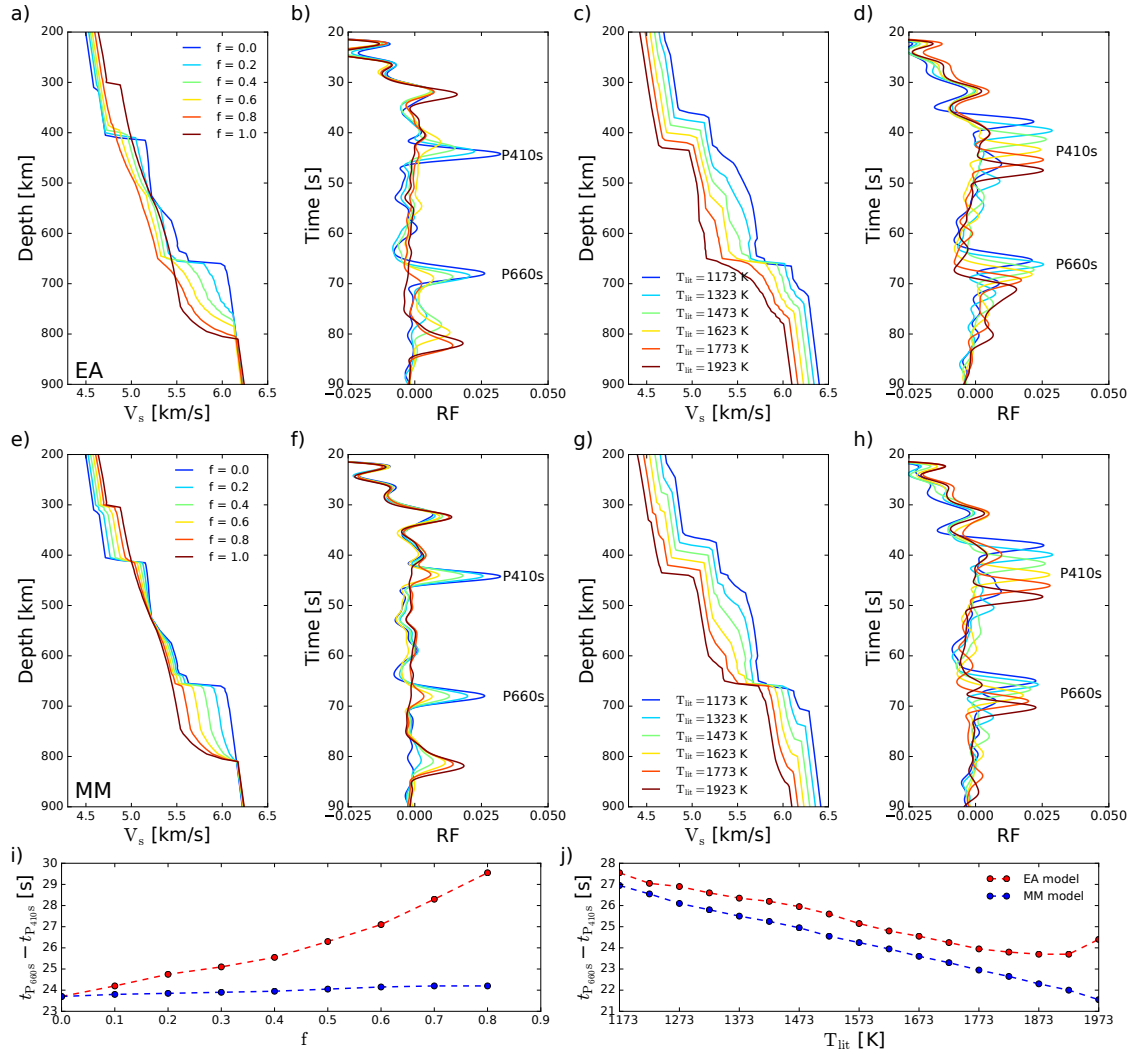

Figure 2.5: Shear-wave velocities (V_s) and receiver functions (RFs) as a function of mantle composition (f) and thermal structure (T_{lit}) for equilibrium assemblage (EA) and mechanical mixture (MM) mantle models. Velocity profiles as a function of basalt fraction f in a) and e) and the corresponding RF waveforms in b) and f) were computed assuming a sub-lithospheric adiabatic geotherm defined by the entropy of the lithology at a temperature T_{lit} of 1350 °C at the base of a 80 km thick lithosphere. V_s profiles as a function of temperature in c) and g) and the associated RF waveforms shown in d) and h) were computed for fully-equilibrated and mechanically-mixed homogeneous pyrolitic (f=0.2034) mantle models, respectively. Modal mineralogy associated with each thermo-chemical model is shown in Appendix A. Panels i) and j) depict differential travel times ($t_{P660s} - t_{P410s}$) as a function of basalt fraction and thermal structure, respectively. The differential travel times are tabulated in Appendix A (Tables A1 and A2)

with increasing f (Figure 2.5b). Furthermore, the appearance of a second seismic discontinuity at ∼800 km depth with increasing basalt fraction leads to changes in the P660s waveform from a single shallow peak (f=0) to a single deep peak (f=1) with a transition stage characterized by two distinct peaks.

Distinct 660 RF peaks have been reported in a number of regional and global studies (e.g., *Niu and Kawakatsu*, 1996; *Simmons and Gurrola*, 2000; *Andrews and Deuss*, 2008; *Ai et al.*, 2003; *Tauzin et al.*, 2018; *Maguire et al.*, 2018). Additionally, differences between EA and MM models are also reflected in P410s and P660s

waveforms. On the one hand, RF amplitudes for the MM model (Figure 2.5b) are slightly larger than the amplitudes estimated using the EA model (Figure 2.5f). Finally, the differential travel time increase with increasing basalt fraction for the EA model, whereas it is only weakly sensitive to compositional changes for the MM model (Figure 2.5i).

The influence of temperature on RF amplitude and travel time must be analyzed separately. Firstly, a linear increase in both P410s and P660s travel times is observed with increasing temperature (Figure 2.5d) due to a decrease in upper mantle velocities (Figure 2.5c). This typically results in the trade-off between the depth of an interface and upper mantle velocity seen in traditional approaches. Secondly, the decrease in MTZ thickness as a function of temperature (Figure 2.5c) results in decreasing differential travel times with increasing temperature (Figure 2.5j). This decrease is linear for the MM model, whereas, it is quasi-linear in the case of the EA model. Thirdly, P410s and P660s amplitudes depend non-linearly on temperature due to variations in the sharpness of the seismic discontinuities (Figure 2.5h). The occurrence of phase changes associated with majoritic garnet and ferropericlase (see Appendix A) adds additional complexity to the MTZ response. Hence, to avoid the pitfalls arising from the use of travel times of converted waves only, including the Clapeyron slope of $(Mg,Fe)_2SiO_4$-phases, all phase changes need to be considered to infer mantle temperatures properly. As a consequence, we use the entire RF waveform to map thermo-chemical variations in Earth's mantle. This allows for joint recovery of crust and mantle structure without the need for tomographic models to correct for crust and upper mantle effects.

Finally, bulk velocities are seen to affect the long-period content of RF waveforms. In particular, the long-period behavior seems relatively stable in the case of changes in basalt fraction (Figure 2.5a,b,e,f) leading to only small variations in bulk S–wave velocities within the mantle transition zone. In contrast, temperature variations trigger long-period changes in the RF waveform, especially for the EA model (Figure 2.5d, h). This behavior can be attributed to changes in the large-scale vertical velocity gradient, and suggests that very long-period waveforms may be suitable for constraining mantle velocity structure.

2.5 Inverse problem

To infer transition zone thermal and compositional structure, we invert the observed RF waveforms using the model parameterization and the forward operator described previously (Sections 2.2 and 4.3.2). Deterministic derivative-based methods, such as Gauss-Newton, can be applied, but these methods typically depend on the choice of initial model and converge to a local minimum. To overcome these limitations and the non-uniqueness of receiver function inversion (*Ammon et al.*, 1990; *Jacobsen and*

Svenningsen, 2008), we combine a Markov chain Monte Carlo (McMC) (*Tarantola*, 2005) method with a stochastic optimization technique known as Covariance Matrix Adaptation Evolution Strategy (*Hansen and Ostermeier*, 2001) (CMAES).

2.5.1 Covariance Matrix Adaptation Evolution Strategy

This technique aims to explore the model space globally showing remarkable robustness on ill-conditioned problems (*Hansen et al.*, 2011). The use of CMAES in geophysics is not common, but has recently been implemented as a global minimization method (*Alvers et al.*, 2013; *Diouane*, 2014; *Shen et al.*, 2015; *Grayver et al.*, 2016; *Munch et al.*, 2018a) outperforming other optimization techniques such as Genetic Algorithms and Particle Swarm Optimization (*Auger et al.*, 2009; *Arsenault et al.*, 2013; *Elshall et al.*, 2015).

We employ CMAES for finding the maximum a-posteriori model $\mathbf{m}_{\mathrm{MAP}}$ by solving the following optimization problem

$$\mathbf{m}_{\mathrm{MAP}} = \underset{\mathbf{m}}{\operatorname{argmin}} \left(\sum_{\mathrm{i}=1}^{\mathrm{N_w}} \phi_{\mathrm{i}}(\mathbf{m}) \right) \quad \text{with} \quad \phi_{\mathrm{i}}(\mathbf{m}) = \frac{1}{\mathrm{N_i}} \sum_{j=1}^{\mathrm{N_i}} \left[\frac{\mathrm{RF^{obs}}(t_j) - \mathrm{RF^{mod}}(\mathbf{m}, t_j)}{\delta \mathrm{RF^{obs}}(t_j)} \right]^2, \tag{2.3}$$

where $\mathrm{N_w}$ is the number of time windows of interest (see Section 2.6.2) and $\mathrm{N_i}$ is the number of samples in each time window; $\mathrm{RF^{mod}}$ indicates modeled RF waveform, whereas $\mathrm{RF^{obs}}$ denotes observed RF waveform with uncertainties $\delta\mathrm{RF^{obs}}$ (see Section 2.3). Vector $\mathbf{m} = (\mathrm{T_{lit}}, \mathrm{z_{lit}}, \mathrm{f}, \mathrm{V_s^1}, \ldots, \mathrm{V_s^5}, \mathrm{d_1}, \ldots, \mathrm{d_5})$ contains the various model parameters described previously (Sections 2.2.1 and 2.2.2). Table 2.2 summarizes model parameters and model parameters search ranges used in the inversions.

At every iteration the algorithm samples λ models from the current multivariate normal distribution and evaluates the misfit between observed and synthetic data. Then the best $\lambda/2$ candidates are selected and used to update the distribution mean, step size, and covariance matrix (*Grayver and Kuvshinov*, 2016). Following *Hansen and Ostermeier* (2001), a reasonable choice for the number of sampled models is given by $\lambda = 4 + 3\lfloor \ln M \rfloor$; where $\lfloor \cdot \rfloor$ is the floor function and M is the number of unknowns. This equation was used to choose the population size λ in all inversions. Finally, we considered different initial models and number of iterations N_{max} (25–400), but generally solutions were found to be equivalent for $N_{max} > 100$.

2.5.2 Markov chain Monte Carlo

We solve the non-linear inverse problem within a Bayesian framework using the probabilistic approach of *Tarantola and Valette* (1982). In this formulation, the solution to the inverse problem is described in terms of the posterior probability

distribution $\sigma(\mathbf{m})$ given by (*Mosegaard and Tarantola*, 1995)

$$\sigma(\mathbf{m}) = k\rho(\mathbf{m})\mathcal{L}(\mathbf{m}), \tag{2.4}$$

where k is a normalization constant, $\rho(\mathbf{m})$ is a probability distribution that describes the a priori information on model parameters (summarized in Table 2.2), and the likelihood function $\mathcal{L}(\mathbf{m})$ represents a measure of the similarity between the observed data and the predictions from model $\mathbf{m}$. Under the assumption that noise can be modeled using a Gaussian distribution, the likelihood function is given by (*Tarantola*, 2005)

$$\mathcal{L}(\mathbf{m}) \propto \exp\left(-\frac{1}{2}\sum_{\mathrm{i}=1}^{\mathrm{N_w}}\phi_{\mathrm{i}}(\mathbf{m})\right) \tag{2.5}$$

where $\mathrm{N_w}$ is the number of time windows of interest and $\phi_{\mathrm{i}}(\mathbf{m})$ is the misfit between observed and modeled data as defined by Equation (2.3).

We employ the Metropolis-Hastings (*Metropolis et al.*, 1953; *Hastings*, 1970) algorithm to sample the posterior distribution in the model space using the solution retrieved from the CMAES algorithm $\mathbf{m}_{\mathrm{MAP}}$ as initial model. This considerably improves the efficiency of the McMC method by significantly reducing the burn-in period (*Grayver and Kuvshinov*, 2016). To further improve the efficiency of the McMC stage, the sampling is performed using 10 independent chains (with a total length of 10,000 iterations) characterized by identical initial models but different randomly chosen initial perturbations. This strategy allows for sampling 100,000 models with moderate computational cost (∼5 days using 10 cores). Finally, the 50,000 best-fitting candidates are used to build histograms of the marginal probability distribution of each model parameter.

Description	Number of parameters	Notation	Range	Prior Distribution	Step length
Crustal nodes	5	$\mathrm{d_i}$	0–15 km	Uniform	4 km
Crustal velocities	1	$\mathrm{V_s^1}$	2.75–5 km/s	Uniform	0.10 km/s
	4	$\mathrm{V_s^i}$	$\mathrm{V_s^{i-1}}$–5 km/s	Uniform	0.10 km/s
Lithospheric thickness	1	$\mathrm{z_{lit}}$	60–250 km	Uniform	10 km
Temperature at $\mathrm{z_{lit}}$	1	$\mathrm{T_{lit}}$	1073–1937 K	Uniform	15 K
Basalt fraction	1	f	0–0.7	Uniform	0.05

Table 2.2: Prior information on model parameters and McMC step lengths.

2.6 Results

2.6.1 Synthetic inversion

In order to test the robustness of our inverse scheme, we performed different sets of synthetic inversions. To this end, a synthetic stack was computed for a homogeneous

pyrolitic mantle (f = 0.2034), a temperature T_{lit} of 1623 K at the base of a 150 km thick lithosphere, and crustal structure fixed to IASP91 (*Kennett and Engdahl*, 1991). The computed stack was then contaminated with 7% Gaussian noise filtered in the frequency band 0.01–0.2 Hz. Finally, the resulting synthetic RF waveform was inverted to retrieve: 1) the thermo-chemical parameters,i.e., T_{lit}, z_{lit}, f assuming a known crustal structure; and 2) both thermo-chemical and crustal parameters.

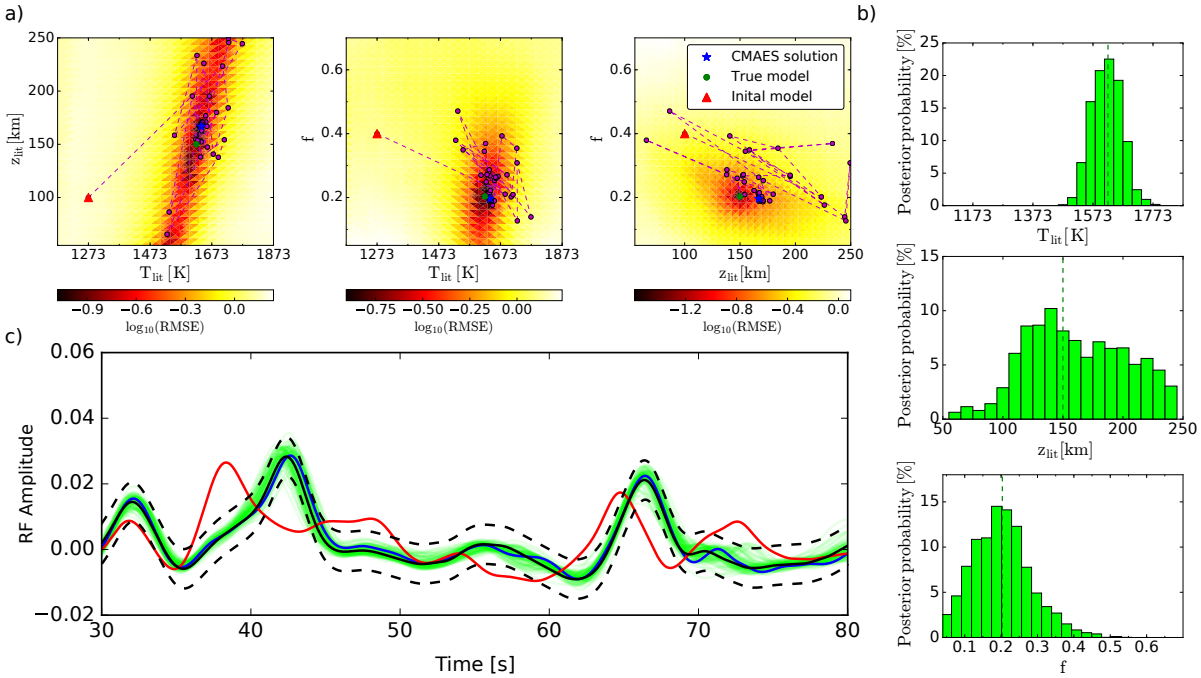

Figure 2.6: Inversion of synthetic receiver functions (RF) for thermo-chemical parameters with fixed crustal structure (IASP91). a) Root mean square error (RMSE) surfaces obtained by grid search exploration of the model space considering 30 points in each direction. Green dots, red triangles, and blue stars indicate the positions of true, initial, and final models, respectively. Magenta dots depict best-fitting solutions retrieved from the Covariance Matrix Adaptation Evolution Strategy (CMAES) at each iteration. b) Histograms showing thermo-chemical parameters sampled by Markov chain Monte Carlo (McMC) exploration of the model space around the CMAES final solution. Vertical dashed lines indicate true model parameters. c) Comparison between synthetic RF waveforms for the initial (red), CMAES (blue), and true (black) solutions. Green lines depict McMC sampled RF waveforms. Dashed lines indicate data uncertainties.

Figure 2.6 summarizes the main inversion results for mantle thermo-chemical parameters for the case where crustal structure is fixed to IASP91 (true solution) and an arbitrary choice of starting model. Figure 2.6a depicts root-mean-square error (RMSE) surfaces estimated by grid search exploration of the model space. Green dots represent the true solution and magenta dots indicate the best-fitting model candidate at each iteration of the CMAES evolution from starting model (red triangles) to the final model (blue star). Figure 2.6b shows histograms of marginal probability distributions for each model parameter built from the 50,000 best-fitting models sampled by the McMC method. As shown in Figure 2.6c, model parameters retrieved by CMAES algorithm (blue) and McMC sampled models (green) fit the

data (black) within uncertainties (dashed lines). Visual inspection of the RMSE surfaces reveals a positive correlation between z_{lit} and T_{lit} and the existence of a local minimum. Despite the non-linearity of the problem, CMAES succeeds in finding the global minimum. In the case of basalt fraction f, the CMAES solution is almost coincidental with the true model, whereas final values of T_{lit} and z_{lit} are slightly shifted with respect to the true solution. These small differences are attributed to the presence of noise in the data. Finally, sampled probability distributions provide uncertainties on the recovered model parameters ($\delta T_{lit} \sim 40$ K, $\delta z_{lit} \sim 25$ km , and $\delta f \sim 0.05$). Furthermore, the histogram for z_{lit} is broader suggesting a lack of sensitivity to this particular parameter. Sensitivity in the upper mantle can be increased by incorporating additional information from other geophysical techniques such as surface wave group and phase velocities (e.g., *Khan et al.*, 2009; *Bodin et al.*, 2012; *Shan et al.*, 2014; *Calò et al.*, 2016) or S–to–P conversions (e.g., *Yuan et al.*, 2006; *Oreshin et al.*, 2008).

In order to analyze the influence of unaccounted-for crustal structure on the retrieval of mantle thermo-chemical parameters, we performed a set of synthetic inversions using different crustal models. More specifically, we increased crustal velocities by 20% (*model A*) and Moho depth by 10 km (*model B*) from the true solution (IASP91). Fig 2.7a depicts best-fitting basalt fractions f, adiabatic geotherms (left panel), and the corresponding S–wave velocity profiles (right panel) retrieved for each crustal model. Figure 2.7b shows the fits between observed (black) and computed RF waveforms. Although P410s and P660s are explained within uncertainties, significant differences are observed in the time window $-5\,\mathrm{s} < t < 25\,\mathrm{s}$. The amplitude of the P-arrival as well as time and amplitude of the multiples significantly depend on the assumed crustal structure. As shown in Figure 2.7a, differences in the crustal model are seen to significantly affect the retrieval of mantle thermo-chemical parameters ($\Delta T_{lit} \sim 50$ K, $\Delta z_{lit} \sim 50$ km, and $\Delta f \sim 0.1$). This synthetic test illustrates the importance of accurately accounting for crustal structure when inverting for the transition zone structure.

2.6.2 Accounting for crustal structure

In light of the aforementioned results, an accurate characterization of the shallow structure beneath each station is essential. As a result, we propose an inverse strategy that allows simultaneous recovery of crust and mantle structure. Our strategy consists of two steps: in step 1, we invert the observed RF waveform in the time window $-5\,\mathrm{s} < t < 25\,\mathrm{s}$ for crustal structure (leaving mantle parameters variable), followed by a second inversion (step 2) of the entire observed RF waveform in the time windows $-5\,\mathrm{s} < t < 25\,\mathrm{s}$, $36\,\mathrm{s} < t < 50\,\mathrm{s}$, and $60\,\mathrm{s} < t < 80\,\mathrm{s}$ to recover both crustal and mantle thermo-chemical parameters with the model obtained from step 1 as input. We tested different time windows in which observations are fitted.

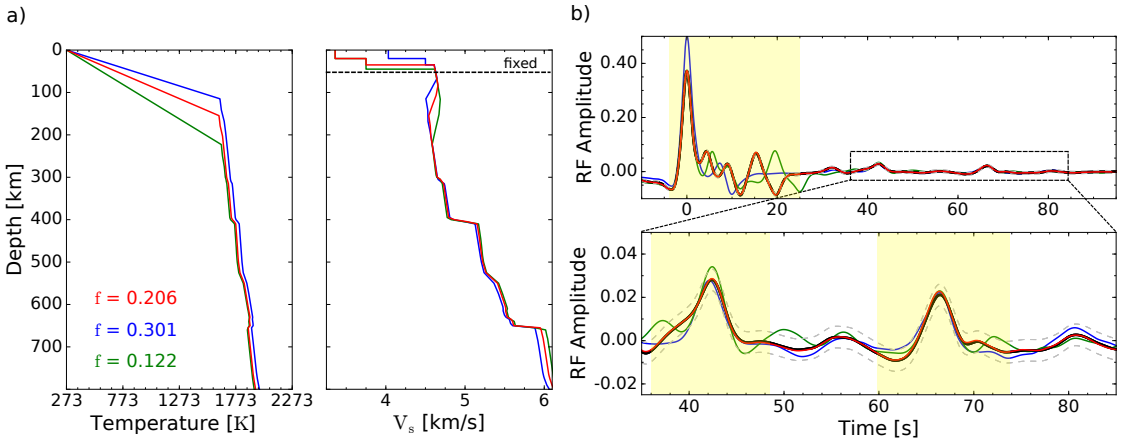

Figure 2.7: Single-step inversion of synthetic receiver functions (RF) for thermo-chemical parameters fixing crustal structure to three different crustal models (see detailed model description in Section 2.6.1): IASP91 (red), *model A* (blue), *model B* (green). Panel a) depicts best-fitting basalt fractions f and thermal structures (left) and corresponding S–wave velocity V_s as a function of depth (right). Panel b) shows datafit between observed (black) and computed RF waveforms, given the data uncertainties indicated by gray dashed lines. Yellow rectangles indicate the part of the RF waveform that is fitted in the inversion.

The final choice of specific time windows is somewhat arbitrary, but time windows containing considerably small or no signal can introduce undesirable noise into the misfit function and unnecessarily increase the complexity of the misfit surface.

Figure 2.8 illustrates the performance of the proposed two-step inversion strategy. The method succeeds in recovering the true thermal structure and basalt fraction, however, intra-crustal discontinuities are not well resolved. This can be explained by the fact that the proposed methodology mainly focuses on the recovery of mantle thermo-chemical structure and, thus, only an effective crustal structure that explains correctly the long-period waveforms (below 0.2 Hz) is retrieved. Higher frequency content (up to 1 Hz) should be included to increase the resolution in the crust. Future work will focus on incorporating the use of high frequency RF waveforms into our two-step procedure for better reconstructing crustal structure. Synthetic tests (not shown here) indicate that the use of the recovered model from step 1 as input model significantly improves the performance of the algorithm in finding the global minimum.

The synthetic tests presented above were performed using the same model parameterization to solve both forward and inverse problems. As an independent test, we computed a synthetic stacked RF waveform using the IASP91 velocity model (*Kennett and Engdahl*, 1991) and subsequently inverted it for crustal and mantle parameters. The main results are shown in Appendix A (Figure A5). Both EA and MM models explain the observed RF waveform with almost identical mantle thermo-chemical parameters. The recovered seismic profiles above the 410–km discontinuity are in reasonable agreement but show larger jumps at the 410–km discontinuity and

lower transition zone gradients. Finally, inferred Moho depth and absolute velocity in the first layer are in agreement with the true solution, although intra-crustal discontinuities are not well resolved.

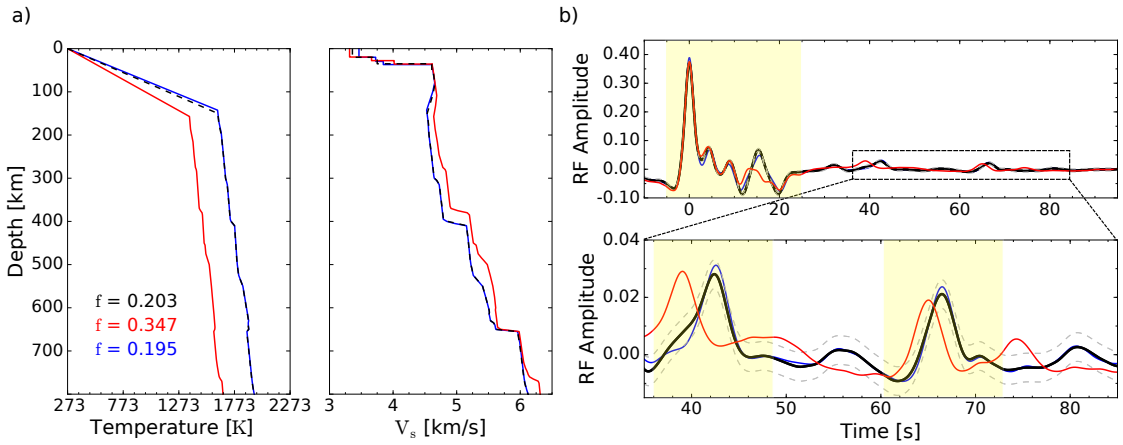

Figure 2.8: Two-step inversion of synthetic receiver functions (RF) for crustal and thermo-chemical parameters. Panel a) depicts best-fitting basalt fraction f and thermal structure (left panel) and corresponding S–wave velocity V_s (right panel). Panel b) shows fit between observed (black) and computed RF waveforms with yellow rectangles indicating time windows fitted in the inversion. Black curves correspond to the true model, red curves denote best-fitting model obtained by inverting the early part of the RF waveform (step 1, -5 s<t<25 s), and blue curves indicate best-fitting solution from inversion of the entire RF waveform (step 2).

2.6.3 Data examples

As a proof of concept, we apply the proposed methodology to infer mantle compositional and thermal structure beneath two permanent stations (see Figure 2.2a) located in two distinct stable continental regions: Kongsberg (KONO) in the East European craton and Yakutsk (YAK) in the Siberian craton. Observed stacks and uncertainty estimates (Figure 2.2c) were obtained by applying the data processing scheme detailed in Section 2.3.

Figures 2.9 and 2.10 summarize the main results obtained for KONO and YAK, respectively. Panels a) show sampled marginal probability distributions of mantle thermo-chemical parameters retrieved for the EA and MM mantle models; panels b) depict the fit between observed (black) and synthetic RF waveforms for the MM (red) and EA (green) mantle models; and panels c) show sampled S–wave velocity profiles. Mantle thermal profiles and the associated shear attenuation models are depicted in Appendix A (Figure A6).

All retrieved models succeed at explaining the observed P410s ($40\,\mathrm{s} < t < 50\,\mathrm{s}$) and P660s ($65\,\mathrm{s} < t < 71\,\mathrm{s}$) waveforms within uncertainties as well as the amplitude of the P-arrival ($-2\,\mathrm{s} < t < 2\,\mathrm{s}$) and main crustal reverberations ($5\,\mathrm{s} < t < 25\,\mathrm{s}$). The models also predict a positive pulse in the RF waveforms ($50\,\mathrm{s} < t < 60\,\mathrm{s}$) associated with the wadsleyite $\rightarrow$ ringwoodite transition. Such a feature is not

present in the observed RF waveforms for KONO, while it is partially observed for YAK. This difference can possibly be attributed to multiples originating from reflections atop sharp mid-lithospheric/cratonic discontinuities (e.g., *Rychert and Shearer*, 2009; *Calò et al.*, 2016) which can potentially mask weak P–to–s conversions occurring within the mantle MTZ. Alternatively, the wadsleyite→ringwoodite transition could be the result of the long-period behavior of RF waveforms, which depends on the large-scale velocity gradient across the mantle MTZ (see Section 2.4.4).

While the results generally tend to agree between the EA and MM models, subtle differences are palpable. For instance, marginally more harzburgite-enriched compositions are obtained for KONO (see Figure 2.9a) for the MM model relative to the EA model. Thermal parameters inferred for KONO (EA) are characterized by a broader distribution, whereas a relatively well-defined distribution is recovered for the MM model. Despite this difference, most probable T_{lit} and z_{lit} estimates are equivalent for both EA and MM. This contrasts with what was reported by *Ritsema et al.* (2009a) where the EA model was found to result in higher temperature estimates relative to MM. This discrepancy can be explained by the fact that *Ritsema et al.* (2009a) neglect compositional effects and only considers a pyrolitic mantle composition. To further distinguish between EA and MM models, additional sources of information should be considered such as temperature estimates from olivine thermometry (e.g., *Ritsema et al.*, 2009a).

Thermal parameters T_{lit} and z_{lit} inferred for YAK and KONO correspond to potential temperature estimates of 1500 ±30 K and 1550 ±35 K, respectively. These estimates are slightly lower than experimentally determined mantle potential temperature estimates (1600±40 K) by *Katsura et al.* (2010). This discrepancy can also be attributed to the fact that *Katsura et al.* (2010) focus on a pyrolitic mantle composition. Moho depths inferred beneath KONO (∼34 km) and YAK (∼40 km) are in agreement with estimates (∼35 km and ∼42 km, respectively) from the regional crustal models EUNAseis (*Artemieva and Thybo*, 2013) and SibCrust (*Cherepanova et al.*, 2013), respectively. These crustal models represent compilations of European and Siberian regional and local seismic models derived from controlled-source and receiver functions studies.

2.7 Discussion

First off, we performed waveform modeling in a homogeneous and radially stratified isotropically layered model. Consequently, this approach is unable to account for material anisotropy and diffraction effects related to three-dimensional mantle structure. In spite of stacking waveforms that sense the equivalent of a circular area exceeding 250 km in radius (at 660 km depth) beneath the station (see Figure 2 in *Tauzin et al.*, 2008), it is possible that these assumptions introduce errors into the

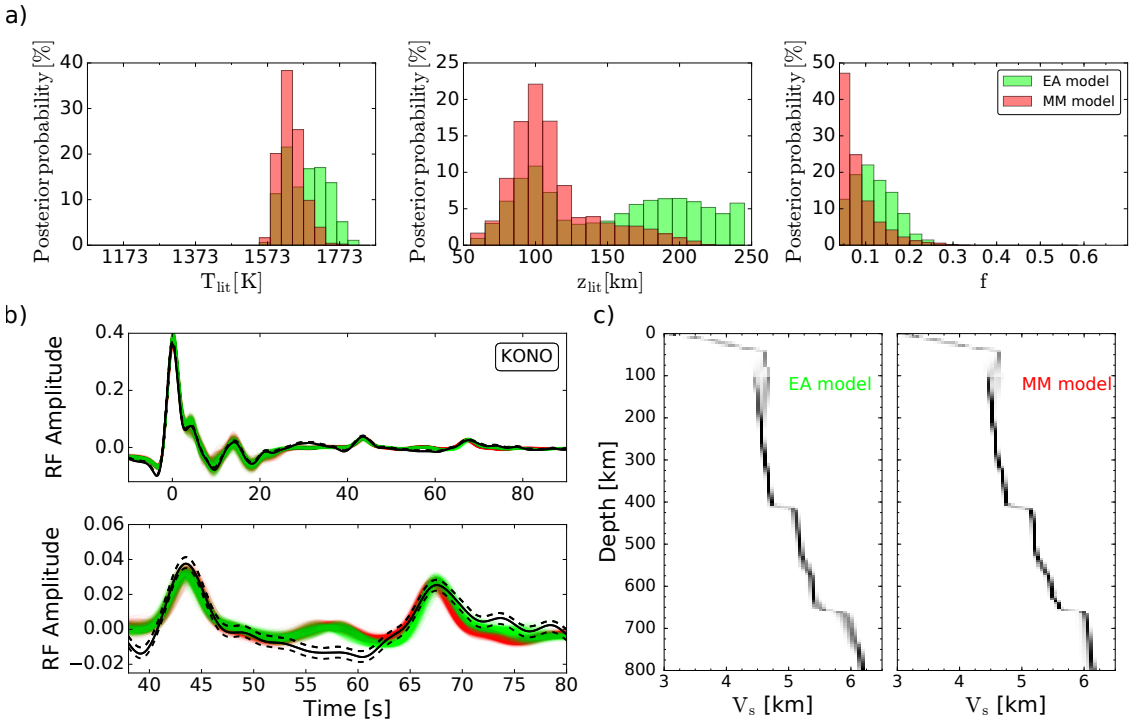

Figure 2.9: Inversion results for Kongsberg (KONO) station. Panel a) depicts sampled mantle thermo-chemical parameters for the equilibrium assemblage (EA) and mechanical mixture (MM) mantle models, respectively. Orange-colored binds indicate model parameters for which EA and MM overlap. Panel b) shows fit between observed (black) and synthetic receiver function (RF) waveforms for the MM (red) and EA (green) mantle models. Data uncertainties are indicated by black dashed lines. Panel c) depicts sampled S–wave velocity (V_s) profiles for the EA and MM models with black indicating most probable and white least probable.

recovered model. To obtain a better sense of the errors, wave propagation simulations based on more advanced waveform modeling schemes should be considered (e.g., *Monteiller et al.*, 2012; *Nissen-Meyer et al.*, 2014).

Secondly, the noise model considered in the synthetic examples (Section 2.6.1) does not account for noise due to incoherent stacking. As a quantitative description of this effect is challenging, we discuss the errors that could potentially be introduced hereby. Incoherent stacking could broaden and decrease the amplitude of converted waves. As a result, broader and smaller velocity gradients would be required to explain these waveforms. Given the influence of temperature and composition on RF waveforms (Section 2.4.4), the recovered thermo-chemical parameters would be biased in favour of more basalt-enriched compositions and higher temperature estimates.

Thirdly, the thermo-chemical parameterization (uniform adiabatic mantle) is technically limited to geotectonic settings representative of "normal" mantle conditions and will need to be modified to encompass subduction zones and other more complex geological settings. While reliance on basalt and harzburgite as end-members to model mantle composition presents a practical first-order approximation

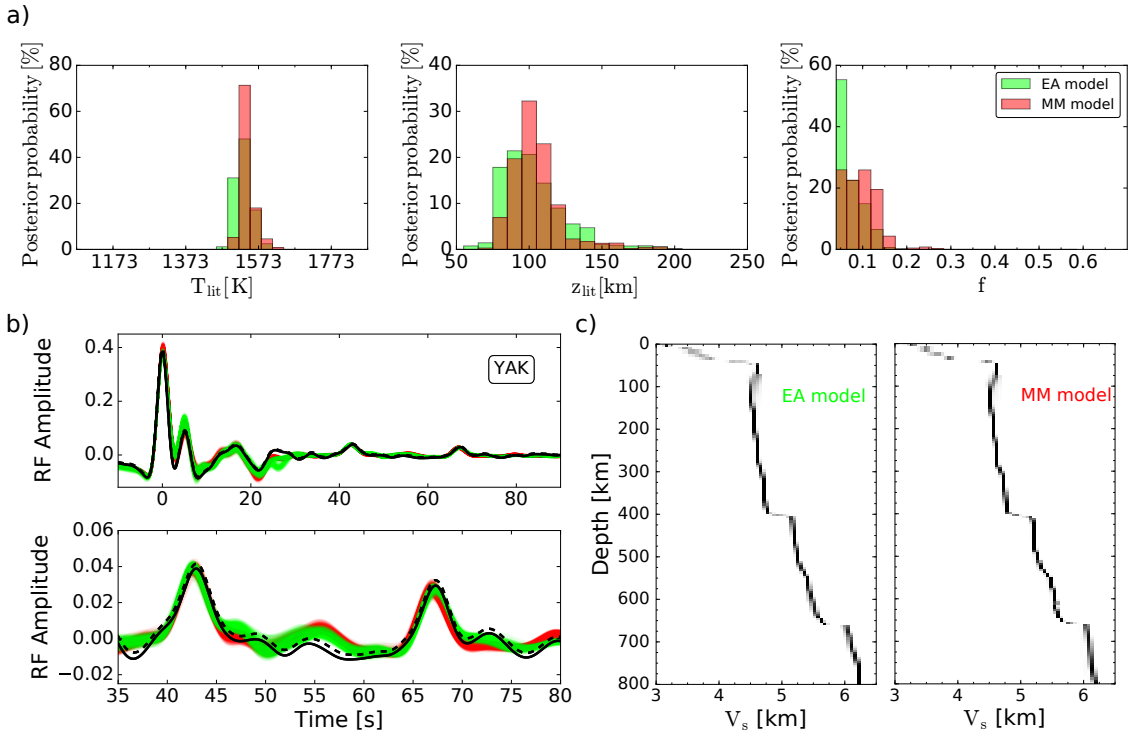

Figure 2.10: Inversion results for Yakutsk (YAK) station. Panel a) depicts sampled mantle thermo-chemical parameters for the equilibrium assemblage (EA) and mechanical mixture (MM) mantle models, respectively. Orange-colored binds indicate model parameters for which EA and MM overlap. Panel b) shows fit between observed (black) and synthetic receiver function (RF) waveforms for the MM (red) and EA (green) mantle models. Data uncertainties are indicated by black dashed lines. Panel c) depicts sampled S–wave velocity (V_s) profiles for the EA and MM models with black indicating most probable and white least probable.

from a geophysical point of view, more complicated models can be built by incorporating other plausible end-members such as lherzolitic and dunitic compositions. Although CFMASNa-equivalent basaltic and harzburgitic end-member compositions are non-unique (cf. *Brown and Mussett*, 1993; *Xu et al.*, 2008; *Khan et al.*, 2009; *Henderson and Henderson*, 2009), its influence on geodynamic models has been shown to be significant only for FeO and Al_2O_3 contents (*Nakagawa et al.*, 2010). Finally, the viscoelastic model of *Jackson and Faul* (2010) employed here only considers the viscoelastic behavior of olivine. Future studies, based on expanded experimental data, should consider the importance of other minerals in more detail.

In spite of these caveats, it is our contention that the methodology outlined here is capable of making significant quantitative predictions and presents several advantages with respect to classical inversion of RF waveforms: it anchors temperature, composition, and seismic discontinuities that are in laboratory-based data and models, while simultaneously permitting the use of geophysical inverse methods to optimize profiles of physical properties (e.g., bulk and shear modulus and density) to match RF waveforms. As a result, depth and sharpness of 410–km and 660–km discontinuities are determined self-consistently from composition, temper-

ature, and pressure. In contrast to studies relying on RF migration, estimates of transition zone topography and volumetric velocities derived here are independent of global/regional tomographic models and, finally, assumptions about Clayperon slopes for interpretation of transition zone thermal structure are obviated.

2.8 Concluding remarks and outlook

We presented a methodology for stochastic inversion of P–to–s converted waves to directly infer variations in mantle temperature and composition. To this end, we employ self-consistent mineral phase equilibria calculations to estimate mantle elastic properties as a function of pressure, temperature, and composition. Two end-member compositional models for mixing harzburgite and basalt were considered: the completely equilibrated Equilibrium Assemblage (EA) model and the disequilibrated Mechanical Mixture (MM) model.

We first analyzed the effect of thermal and compositional variations on receiver functions. The former was found to influence arrival times, whereas the latter affected the amplitude of waves converted at the discontinuities that bound the transition zone. Based on this, we proceeded to consider interpretation of RF waveforms as an inverse problem with the goal of determining mantle thermo-chemical and crustal structure by interfacing the geophysical analysis with phase equilibria computations. During the inversion, the slowness distribution recorded at each station must be accurately replicated and identical methods should be applied to both observed and synthetic seismograms. The robustness of our inverse strategy was tested by performing a set of synthetic inversions in which crustal structure was assumed both fixed and variable. This analysis indicated that unaccounted-for crustal structure strongly affects the retrieval of mantle structure. Therefore, an accurate characterization of crustal structure beneath a given station is needed. To properly account for the influence of the crust, we first inverted for crustal structure, then used this model as input, and finally inverted for both crust and mantle structure.

As a proof of concept, we applied the proposed methodology to data from two permanent stations located in two distinct stable continental regions: Yakutsk on the Siberian craton and Kongsberg on the East European craton. The retrieved models based on both EA and MM succeeded in explaining the main features of the observed RF waveforms within uncertainties with only minor differences in the retrieved candidates: the MM model leads to marginally more harzburgite-enriched compositions beneath Kongsberg. To further distinguish between the two models, petrological constraints (e.g., olivine thermometry) should be incorporated (e.g., *Ritsema et al.*, 2009a; *Afonso et al.*, 2016).

Future improvements will include: 1) inversion of RF waveforms in multiple frequency bands (e.g., *Schmandt*, 2012) and jointly with surface wave data (e.g., *Calò*

et al., 2016); 2) consideration of a depth-dependent composition; and 3) exploring deviations from an adiabatic profile. This will be needed to improve resolution in the upper mantle and the transition zone, address convection simulations that suggest the existence of local compositional gradients across the mantle (e.g., *Ballmer et al.*, 2015), and to enable us to consider regions or features that deviate from "normal" mantle conditions (e.g., stagnant slabs).

Chapter 3

Seismic investigation of the mantle transition zone: Application

The content of this chapter is currently under consideration for publication in Earth and Planetary Science Letters as: Munch, F. D., Khan, A., Tauzin, B., van Driel, M. & Giardini D. (2019). *Seismological evidence for the existence of thermo-chemical heterogeneity in Earth's continental mantle.*

Abstract

Earth's thermo-chemical structure governs mantle dynamics from microscale (e.g., rheology) to macroscale (e.g., modality of mantle convection and plate tectonics). While cosmochemical arguments (Palme and O'Neill, 2003) suggest the mantle to be compositionally and dynamically layered, geophysical observations (e.g., French and Romanowicz, 2014; Schaeffer and Lebedev, 2013) appear to support whole-mantle convection. In an attempt to overcome this controversy, mantle convection has been envisaged as an intermittent-stage process between layered and whole mantle convection with a globally-averaged compositional stratification at 660 km depth (Tackley, 2008; Ballmer et al., 2015). Here, we find that beneath stable continental regions, such a compositional boundary is not required to explain short- and long-period seismic data sensitive to the upper mantle and transition zone; yet, compositional layering can explain part of the complexity present in the data recorded near subduction zones and volcanically active regions. Our results further suggest that the mantle is neither completely chemically equilibrated nor fully mechanically mixed, but appears to be best described as an in-between amalgam. In particular, chemical equilibration seems less prevalent in regions of the mantle that are most isolated from convection processes such as beneath cratons. This, in combination with the evidence for the presence of locally-varying mid-mantle compositional layering, considerably strengthens the case for a mantle that convects, temporally as spatially, in an intermittent fashion.

Since the recognition that plate tectonics is driven by solid-state mantle convection in the late 1960s, geoscientists have been debating mantle thermo-chemical structure and the detailed morphology of convection. Geochemical analysis of volcanic rocks (*Pearson et al.*, 2003) support the existence of distinct reservoirs suggesting the mantle to be compositionally and dynamically layered, with the 660–km seismic discontinuity acting as compositional boundary. However, three-dimensional images of mantle structure from seismic tomography (e.g., *French and Romanowicz*, 2014; *Schaeffer and Lebedev*, 2013) indicate that subducted oceanic plates (known as slabs) can penetrate into the lower mantle as well as stagnate in the mantle transition zone (MTZ; region between 410 and 660 km depth) and around ∼1000 km depth, which rules out global layering at 660–km and appears to support whole-mantle convection instead. A range of hypotheses have been proposed to reconcile these observations (e.g., leaky layering at 660 km, layering deeper in the mantle, and ubiquitous compositional heterogeneity), yet the detailed morphology of convection patterns remains a matter of debate. The key question is whether the 660–km discontinuity is caused by a change in chemical composition (*Anderson*, 2007) or by a phase transition (*Ita and Stixrude*, 1992).

Numerical modeling of subduction suggests that a lower-mantle enrichment in basalt (∼8% with respect to the upper mantle) can explain slab stagnation at 660 and 1000 km depth, in the presence of whole-mantle convection (*Ballmer et al.*, 2015). This finding suggests that mantle convection occurs in an intermittent mode between layered- and whole-mantle convection, where slabs penetrate intermittently in space and time, while a globally-averaged compositional stratification at 660 km depth is maintained (*Tackley*, 2000). Supporting evidence arises from direct comparison of one-dimensional Earth reference velocity models and seismic observations sensitive to the bulk velocity structure of the mantle (P- and S-wave travel times and surface wave data) with estimates for a pyrolitic (*Ringwood*, 1975) and adabatic mantle based on insights obtained from theoretical and experimental mineral physics. These studies report that pyrolitic and adiabatic mantle models cannot explain global observations (*Cobden et al.*, 2008) and suggest that the lower mantle is either enriched or depleted in silicon relative to the upper mantle (e.g, *Khan et al.*, 2008; *Murakami et al.*, 2012). However, detailed analysis of short-period SS and PP precursors (*Deuss et al.*, 2006) that are sensitive to MTZ discontinuities, indicate that the observed amplitude variations (and even the absence of PP precursors in certain regions) are well-explained by lateral changes in mantle temperature or aluminium content for a pyrolite mantle.

Here, we investigate whether compositional mantle stratification is required to jointly explain seismic data sensitive to upper mantle and transition zone beneath a number of different tectonic settings by implementing a methodology that interfaces geophysical inversion of seismic data with self-consistent calculations of mineral

phase equilibria (*Munch et al.*, 2018b). The prediction of rock mineralogy and its elastic properties as a function of pressure, temperature, and bulk composition allows for self-consistent determination of depth and sharpness of the 410– and 660–km seismic discontinuities as well as upper mantle velocities. This enables the joint analysis of P-to-s receiver functions and Rayleigh surface wave dispersion data to directly infer global lateral variations of mantle temperature and composition. Until now, both data types have never been combined to resolve the structure down to the base of the MTZ.

P-to-s receiver functions (hereinafter RF) are the records of compressional waves that convert into shear waves when encountering a discontinuity in material properties and are sensitive to sharp seismic discontinuities within a ∼250 km-radius underneath seismic stations. Conversions occurring at the 410–km (P410s) and 660–km (P660s) discontinuities are routinely used for detection of mineralogical phase changes at 410 and 660 km depth (e.g., *Helffrich*, 2000; *Lawrence and Shearer*, 2006a; *Tauzin et al.*, 2008), but are rarely inverted to determine MTZ elastic structure. Building on previous experience (*Tauzin et al.*, 2008), we constructed a new global high-quality dataset of RF waveforms from an initial pool of 151 stations (see Methods section). We enhanced our dataset with the most recent available global dataset of Rayleigh wave phase velocity dispersion (*Durand et al.*, 2015) for the fundamental mode and up to fifth overtone. Rayleigh wave phase velocities are sensitive to the bulk velocity structure of the upper mantle and provide a better global coverage than the RFs, but with lower lateral resolution (∼650 km).

The inversion of RFs requires careful waveform inspection to ensure high quality data (see Methods section). We found 48 stations for which the signals corresponding to either the P410s or P660s conversions cannot be unambiguously isolated, due to the presence of interfering seismic phases or complex three-dimensional structure (see Type–B stations in Figure 3.1a and Figure B1). These stations are often located in regions where structure has previously been identified in seismic tomography models (*Schaeffer and Lebedev*, 2013) such as subducted slabs in northeast Asia and the Mediterranean Sea. Our analysis focuses on 99 stations (Type–A stations in Figure 3.1a) mainly located away from plate boundaries, where the RF waveforms can be accurately modeled with relatively low computational cost by methods that simulate full seismic wave propagation from source to receiver in spherical 1D Earth models (see Methods section).

The observed RFs and Rayleigh wave phase velocities are jointly inverted to map variations in mantle temperature and composition (see Methods section). Mantle composition is parameterized in terms of a single variable (f) that represents the amount of basalt in a basalt-harzburgite mixture, with the composition of basalt and harzburgite end-members described using the CFMASNa chemical model system comprising the oxides CaO-MgO-FeO-Al_2O_3-SiO_2-Na_2O. The choice of chemical

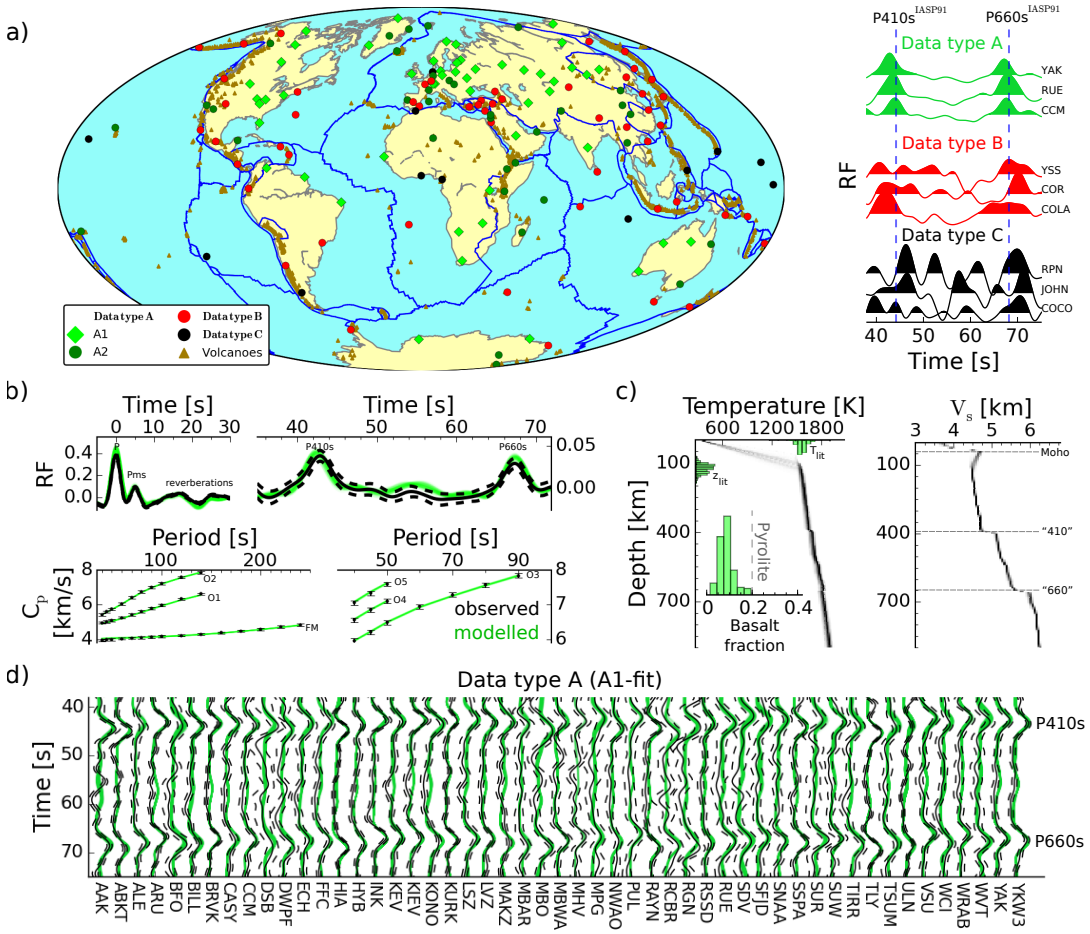

Figure 3.1: Geographic distribution of seismic stations, data, and fit to observations. a) In all 151 seismic stations were considered and classified by data quality (type A, B, and C). Type A stations are subdivided into two further categories based on the data fit, labelled "A1" and "A2". Waveforms to the right of the panel show examples of observed receiver functions (RF) for each data class. b) Example data fit (at station YAK) of RF waveforms and fundamental mode (FM) and overtone (O) Rayleigh wave phase velocities (C_p). Observed data are shown in black and predictions in green. c) Example inverted composition, thermal (temperature), and shear-wave velocity (V_s) structure, including marginal posterior distributions of the main thermo-chemical parameters basalt fraction, lithospheric thickness (z_{lit}) and temperature (T_{lit}). d) Observed (black) and computed (green) RF waveforms for A1-fit stations (RF waveforms for A2-fit stations are shown in Figure B1).

model parameterization relies on its proximity to mantle dynamical processes, i.e., partial melting of mantle material along mid-ocean ridges. This process produces a basaltic crust and its depleted residue (harzburgite), which are cycled back into the mantle at subduction zones and become entrained in the mantle flow and remixed. In spite of its simplicity, the concept of distinct chemical end-member compositions has been found to provide an adequate description of mantle chemistry, at least from a geophysical point of view (e.g., *Khan et al.*, 2009; *Ritsema et al.*, 2009a). Furthermore, the use of the CFMASNa model chemical system allows us to account for the effect of transitions in the olivine, garnet, and pyroxene components of the mantle. As a consequence, and in contrast to usual seismological practice (e.g., *Lawrence and Shearer*, 2006a; *Tauzin et al.*, 2008; *Schmandt*, 2012; *Cottaar and Deuss*, 2016), estimates of MTZ topography, volumetric velocities, and temperature derived here are independent of tomographic models or assumptions about the Clapeyron slope of $(Mg,Fe)_2SiO_4$-phases. The present mantle thermal structure is assumed to be adabatic with geotherms defined by the entropy of the lithology at a temperature T_{lit} at the bottom of a lithosphere of thickness z_{lit}. This simplification allow us to treat continents as conducting lids that float atop the convecting mantle. The seismic data are inverted using a Bayesian framework to provide estimates of model range and uncertainty. At each station, we recover the marginal probability distributions of parameters describing crustal and mantle thermo-chemical structure (Figure 3.1c). By-products are associated elastic profiles (Vp, Vs, and density) for the upper mantle down to 1000 km depth (Figure 3.1c). The sampled models must predict the observed Rayleigh wave phase velocities for the fundamental mode and overtones, as well as the main features of the observed RF waveforms (Figure 3.1b). Type-A stations are further separated into two categories based on the quality of the data fit (Figure 3.1a) determined by visual inspection of the RF waveforms (Figure 3.1d and Figure B1) and Rayleigh wave dispersion curves (Figures B2–B3).

Our results suggest significant regional deviations from a compositionally uniform and adiabatic mantle. The retrieved models succeed in explaining the observed data in the inner part of continents (A1 stations in Figure 3.1a), but not near active plate boundaries such as in the western US or northeast Eurasia, in oceanic regions (Hawaii, Iceland, Samoa), or regions of intra-plate volcanism such as the Afar (A2 stations in Figure 3.1a). Among 92 stations in the continents, we succeed to fit the seismic data at 58 stations: 13 stations in Phanerozoic provinces of age younger than 600 Myr, 19 stations in 600-2000 Myr old precambrian platforms, and 26 stations in cratonic regions older than 2.2 Byr (Figure 3.2a). The recovered crustal structure is in overall agreement with global crustal models (Figure B4).

We find mantle potential temperatures ranging between 1450–1700 K (Figure 3.2b,c), which are in good agreement with experimentally (*Katsura et al.*, 2010) determined mantle potential temperatures (1610±35 K) based on a pyrolitic composi-

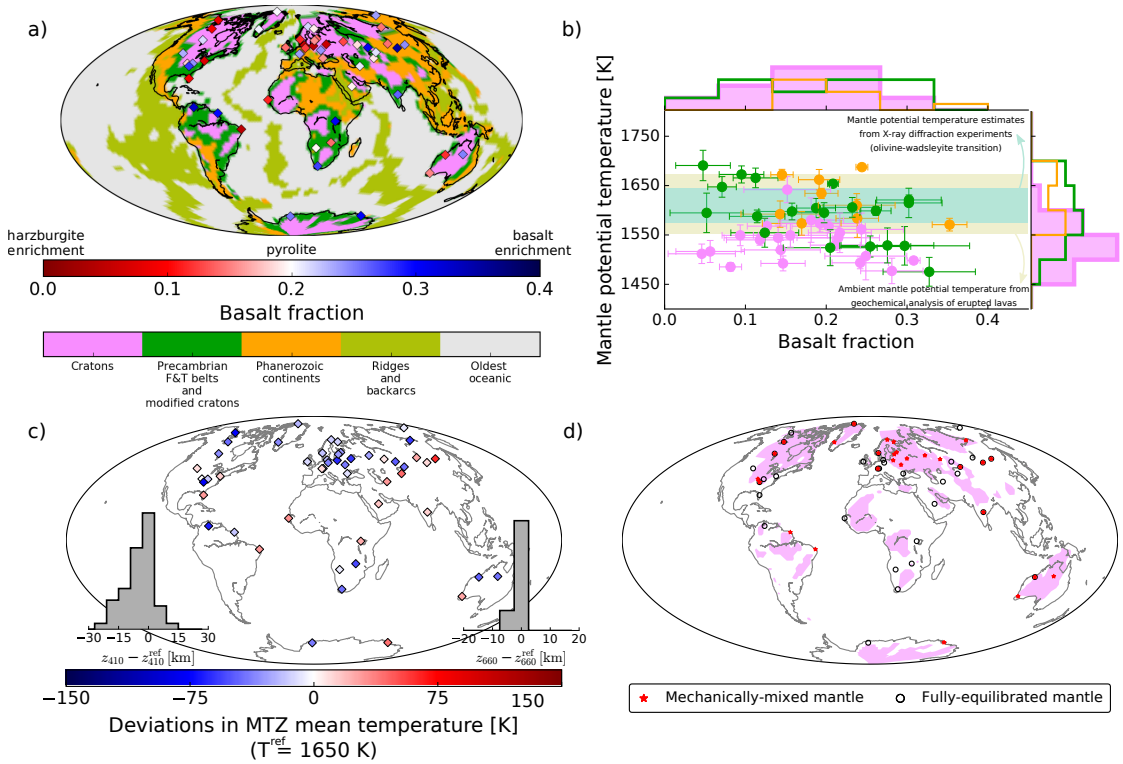

Figure 3.2: Global variations in mantle composition and thermal state. The results summarise the models that best fit (equivalent to the most probable model from the entire sampled model distribution) the observed receiver function and surface wave dispersion data at each station and include both fully equilibrated as mechanically mixed models (see panel d). a) Lateral variations in mantle composition (basalt fraction) for the well-fitted stations (indicated by diamonds in figure 1a). Coloured background shows a regionalised tectonic map derived from cluster analysis of tomographic models (*Schaeffer and Lebedev*, 2015). b) Most probable mantle potential temperature and basalt fraction estimates (taken from plot a) classified by tectonic setting and shown as dots including error bars and along the axes as distributions. Coloured areas depict experimentally-determined mantle potential temperatures (*Katsura et al.*, 2010) for a pyrolitic composition (light blue) and estimates derived from petrological and geochemical analysis of erupted lavas (*Herzberg et al.*, 2007) (yellow). c) Relative lateral variations in mean mantle transition zone (MTZ) temperature and discontinuity topography (histograms). The latter show changes in the "410-" and "660-km" seismic discontinuities that bound the transition zone. d) Global map of cratonic regions (pink areas) and distribution of stations for which the observed data are best explained by either a mechanically mixed or a fully equilibrated mantle compositional model. Results are summarized in `https://n.ethz.ch/~fmunch/RF/SI_Table_S3.pdf`.

tion and estimates derived from petrological and geochemical analysis of erupted lavas (*Herzberg et al.*, 2007) (1553–1673 K). Furthermore, we find that cratonic regions are characterized by low mantle potential temperatures (1450–1550 K) and significant lateral variability in mantle composition (f∼0.05–0.30), whereas higher mantle potential temperature estimates (1600–1675 K) and smaller deviations from a pyrolitic mantle composition (f∼0.15–0.25) are recovered underneath phanerozoic continents (Figure 3.2b). The variability in mantle composition is in overall agreement with geochemical observations that derive from analysis of mantle xenoliths (mantle fragments carried to the surface by explosive eruptions) in the form of Mg# (Mg/(Mg+Fe)) and Mg/Si estimates (see Figure B5), particularly for Precambrian fold-thrust belts (F&T belts) and Phanerozoic continents. Mantle xenoliths from Archean regions, in particular the Siberian and Kaapval cratons, are characterized by an excess in SiO_2. This Si-enrichment was first believed to be a general characteristic of Archean subcontinental mantle (*Boyd et al.*, 1997). However, lower SiO_2 concentrations were measured in xenoliths from the Slave (*Kopylova and Russell*, 2000) and North Atlantic (*Bernstein et al.*, 1998) cratons suggesting that Si-enrichment is a secondary (metasomatic) feature imposed upon the subcontinental mantle after its formation as a residue of melting (*Carlson et al.*, 2005). The compositional changes imposed by such metasomatic processes can be addressed by extending the chemical model to include other plausible end-members such as lherzolitic and dunitic components.

We determine an average MTZ thickness of ∼250 km with regional variations between 235 km and 270 km that mainly reflect changes in the topography of the 410–km discontinuity (Figure 3.2c), in agreement with previous global studies (*Deuss et al.*, 2013) . Furthermore, our results indicate that MTZ thickness is linearly correlated with MTZ temperatures, whereas no clear correlation with mantle composition can be identified (Figure B6).

In order to test the robustness of the thermo-chemical variations reported here, we performed an additional set of inversions in which we fixed mantle composition to pyrolite (f = 0.2). We find that data are better explained (∼2–15 % reduction in misfit values) when both thermal and compositional variations are considered (Figure B7). Furthermore, we find that it is not possible to explain the observed data solely by compositional variations (Figure B7c). This analysis confirms that although temperature plays a primary role in determining the seismic structure of the upper mantle and transition zone, the effect of composition cannot be neglected. We also investigated the correlation between the thermochemical parameters inverted for here (Figure B8). As reported in previous work (*Munch et al.*, 2018b), no significant trade-offs are found between thermal and compositional parameters signaling that temperature and composition are independently resolvable. In the context of erroneously mapping shallow into deeper structure, one could envisage

mapping fast lithospheric phase velocities into cold temperatures. As a result, lower mantle temperatures would ensue, which correspond to larger MTZ thicknesses, and thus increased differential RF travel times. To compensate, a systematic decrease in basalt fraction would be required (*Munch et al.*, 2018b), which would result in a strong correlation between potential temperature and basalt fraction in the sub-continental mantle. Such a correlation is, however, not observed (see Figure 3.2b) indicating that shallow cold continental structure is unlikely to be mapped into MTZ structure. As an added observation, we might note that while it has been proposed (*Lenardic et al.*, 2005) that continents can act as thermal insulators by inhibiting heat loss, thereby increasing mantle temperatures regionally, this effect is not supported here.

Mineralogical models of the Earth typically view the mantle as either homogeneous and pyrolitic (*Ringwood*, 1975) or chemically stratified with homogeneous and equilibrated compositions in each layer (*Mattern et al.*, 2005). To first order, such models are capable of explaining the observed composition of mid-ocean ridge basalts (*McKenzie and Bickle*, 1988) and seismic velocities of the upper mantle and transition zone (*Ita and Stixrude*, 1992). However, experimental measurements of mantle mineral chemical diffusivity (*Hofmann and Hart*, 1978) suggest that equilibration may not be accomplished over the age of the Earth for the amount of stretching and folding predicted in mantle convection simulations (*Nakagawa and Buffett*, 2005). Furthermore, trace element chemistry of basalts (*Sobolev et al.*, 2007) also point to the mantle as consisting of a non-equilibrated mechanical mixture. This led to the concept of two distinct mantle compositional models: mechanical mixture and equilibrium assemblage (*Xu et al.*, 2008). The former represents the scenario in which pyrolitic mantle has undergone complete differentiation to basaltic and harzburgitic rocks, whereas the latter assumes the mantle to be well-mixed and fully-equilibrated. These two types of mantle compositional models generate subtle differences that are rarely accounted for in the interpretation of seismic data (*Ritsema et al.*, 2009a).

Here, we investigate the extent to which the mantle is well-mixed or chemically equilibrated by quantitatively comparing the quality of the data fit obtained for each compositional model. We find 40 stations for which relative differences in the misfit values for the best-fitting models (calculated as described in the Methods section) are larger than 5% (Figure B9). Our results suggest that the mantle is neither completely equilibrated nor fully mechanically mixed, but appears to be best described by an amalgam between the two with cratonic regions best characterized by a mechanically mixed model and Precambrian fold-thrust belts best described by an equilibrium assemblage (see Figure 3.2d). This suggests that the lithologic integrity of the subducted basalt and harzburgite is better preserved for geologically significant times beneath stable cratonic regions, i.e., chemical equilibration is more difficult to achieve. Further to this, the presence of lower potential

mantle temperatures underneath cratonic regions support the existence of deep low-temperature continental roots whose signal extends into the MTZ (*Jordan*, 1978) and which might be isolated from the main mantle flow associated with ridges and trenches (ref). In contrast hereto, our results suggest that these regions are not systematically depleted in basalt component.

Despite subtle differences, we find that temperature and compositional estimates appear to be independent of compositional model (Figure B10). This contrasts with a previous study (*Ritsema et al.*, 2009a) where the equilibrium assemblage model was found to result in higher temperature estimates relative to the mechanical mixture model based on comparison of theoretical and observed differential travel times of waves reflected underneath the MTZ discontinuities. This discrepancy can be explained by the fact that Ritsema et al. (*Ritsema et al.*, 2009a) only considered a pyrolitic mantle composition and therefore mapped all variations of chemistry into temperature.

A recent analysis of short-scale (∼10 km) variations in 660–km discontinuity topography suggested the potential existence of chemical layering at the top of the lower mantle (*Wu et al.*, 2019). In this context, our results indicate that a compositional boundary at 660 km depth is not required beneath stable continental regions to explain the observed seismic signals. However, we find significant complexity in the RF waveforms (see Figure B1) recorded near active plate boundaries (e.g., western US or northeast Eurasia), in oceanic regions (e.g., Hawaii and Iceland), and regions of intra-plate volcanism (e.g., Afar) that cannot be explained by a compositionally uniform and adabatic mantle. Visual comparison of the observed seismic signals with synthetic RF waveforms computed for different depth-dependent compositional profiles based on predictions from mantle convection simulations (*Tackley*, 2008; *Ballmer et al.*, 2015) suggest that a significant part of the complexity present in the RF waveform data between 60 and 75 seconds (P660s) can be explained by local radial changes in mantle composition (Figure B11). Despite being a qualitative comparison, this result supports the existence of local lower-mantle enrichment in basalt (∼5–10% with respect to the upper mantle) and the local accumulation of basalt (∼15–30%) in the MTZ. Compositional layering has also been found necessary to explain regional SS precursors signals beneath Hawaii (*Yu et al.*, 2018) and narrow high-velocity anomalies beneath the MTZ in regions of mantle upwellings (*Maguire et al.*, 2017). Although the detailed morphology of mantle compositional gradients remains uncertain, all these observations support geodynamical simulations that describe mantle convection as a mixture of layered and whole-mantle convection (*Tackley*, 2000), where cold and/or basaltic material accumulates above 660 km depth until huge avalanches precipitate it into the lower mantle, "flushing" the local upper mantle through broad cylindrical downwellings to the core-mantle boundary in a globally asynchronous manner (*Tackley*, 2008).

Methods

P-to-s receiver function

The data consists of three-component seismograms recorded at 151 broad-band permanent stations between 1997 and 2018. In order to ensure a good signal-to-noise ratio, only teleseismic events for epicentral distances between 40° and 95° with magnitudes larger than 6 were selected. Receiver function (RF) waveforms at each station were obtained by: 1) filtering of the records in the period range 1–100 s; 2) rotation of the seismograms into radial, transverse, and vertical components; 3) calculation of signal-to-noise ratio between the maximum amplitude of the signal and the averaged root-mean-square of the vertical component; 4) construction of RF waveforms through iterative time domain deconvolution (*Ligorria and Ammon*, 1999) for traces with signal-to-noise ratio larger than 5 ; and 5) low-pass filtering of the RF waveforms to remove frequencies higher than 0.2 Hz. Finally, RF waveforms were corrected for move-out (using IASP91 velocity model and a reference slowness of 6.5 s/deg) and subsequently stacked. Error on the stacked amplitudes were estimated using a bootstrap resampling approach (*Efron and Tibshirani*, 1991).

Data selection

The stations were classified into three quality classes (see Table B1) by visual inspection of the stacked RF waveforms (Figure 3.1a). Type-A stations correspond to RF waveforms with high signal-to-noise ratio and clear P410s and P660s signals. Type-B stations are characterized by RF waveforms with high signal-to-noise ratio but the signals corresponding to either the P410s or P660s conversions cannot be clearly isolated due to the potential presence of interfering seismic phases or complex three-dimensional structure. Type-C stations correspond to locations where only a small number of data could be stacked resulting in highly noisy RF waveforms with no clear P410s and P660s signals.

Rayleigh wave dispersion curves

We extracted Rayleigh wave dispersion curves at each station from the global phase velocity dataset of Durand et. al (*Durand et al.*, 2015) consisting of 60 phase velocity maps and uncertainties the fundamental mode and up to the fifth overtone on a $2^\circ \times 2^\circ$ grid. We would like to note that this data set is the result of a global tomographic inversion and hence is affected by the chosen regularization. If overly damped, phase velocity maps will be smoothened as a result of which dispersion curves and RF waveforms might possibly sense slightly different structure.

Model parameterization and forward problem

The crustal structure underneath each station is described in terms of five layers with variable S–wave velocity V_s^i and thickness d^i (i = 1...5). Mantle velocities below the Moho are derived from a set of model parameters that describe mantle composition and thermal structure (*Munch et al.*, 2018b). The former is parameterized in terms of a single variable that represents the amount of basalt (f) in a basalt-harzburgite mixture. Mantle composition $\mathbf{X}$ is then estimated as $\mathbf{X} = f\mathbf{X_B} + (1-f)\mathbf{X_H}$, where $\mathbf{X_B}$ and $\mathbf{X_H}$ are the basalt and harzburgite end-members composition, respectively, in the CFMASNa chemical model system comprising the oxides CaO-MgO-FeO-Al_2O_3-SiO_2-Na_2O. Mantle thermal structure is delineated by a conductive lithosphere (linear gradient) on top of an adiabatic geotherm. The lithospheric temperature is defined by the temperature (T_0) at the surface and the temperature (T_{lit}) at the bottom of the lithosphere. The bottom of the lithosphere (z_{lit}) corresponds to the depth at which the conductive lithospheric geotherm intersects the mantle adiabat defined by the entropy of the lithology at the temperature T_{lit} and pressure P_{lit}. The pressure profile is obtained by integrating the load from the surface.

Mantle mineralogy and its elastic properties as a function of depth are computed by means of free-energy minimization (*Connolly*, 2009; *Stixrude and Lithgow-Bertelloni*, 2011). Furthermore, shear attenuation is self-consistently derived from the shear modulus, temperature, and pressure profiles using the extended Burgers viscoelastic model (*Bagheri et al.*, 2019). The resulting velocity and attenuation profiles are then used to compute synthetic RF waveforms and Rayleigh wave phase velocities. The former are computed with the reflectivity method (*Muller*, 1985) and iterative time domain deconvolution (*Ligorria and Ammon*, 1999). The latter are estimated using a spectral element-based python toolbox (J. Kemper et al., 2019; A spectral element normal mode code for the generation of synthetic seismograms; manuscript in preparation).

The thermodynamic model presented here precludes consideration of redox effects (*Cline II et al.*, 2018) as well as minor phases and components such as H_2O and melt due to lack of thermodynamic data. Density and elastic moduli are estimated to be accurate to within ∼0.5% and ∼1–2%, respectively (*Connolly and Khan*, 2016).

Inverse problem

The inverse problem is solved within a Bayesian framework where the solution is described in terms of the posterior probability distribution $\sigma(\mathbf{m}|\mathbf{d}) \propto \rho(\mathbf{m})\mathcal{L}(\mathbf{m}|\mathbf{d})$. The probability distribution $\rho(\mathbf{m})$ describes the a priori information on model parameters (summarized in Table 2.2) and the likelihood function $\mathcal{L}(\mathbf{m}|\mathbf{d})$ represents a measure of the similarity between the observed data $\mathbf{d}$ and the predictions from

model $\mathbf{m} = (\mathrm{T_{lit}}, \mathrm{z_{lit}}, \mathrm{f}, \mathrm{V_s^1}, \ldots, \mathrm{V_s^5}, \mathrm{d_1}, \ldots, \mathrm{d_5})$. As time windows containing considerably small or no signal can introduce undesirable noise into the misfit function and unnecessarily increase the complexity of the misfit surface (*Munch et al.*, 2018b), the modeled and observed RF waveforms are compared in three specific time windows: 1) $-5\,\mathrm{s} < t < 30\,\mathrm{s}$ (crustal signals); 2) $40\,\mathrm{s} < t < 50\,\mathrm{s}$ (P410s conversion); and 3) $60\,\mathrm{s} < t < 80\,\mathrm{s}$ (P660s conversion). Consequently, the likelihood function can be written as

$$\mathcal{L}(\mathbf{m}|\mathbf{d}) \propto \exp\left\{-\frac{1}{2}\sum_{\mathrm{i}=1}^{3}\phi_{\mathrm{i}}^{\mathrm{RF}}(\mathbf{m}|\mathbf{d}) - \frac{1}{2}\sum_{\mathrm{i}=0}^{5}\phi_{\mathrm{i}}^{\mathrm{SW}}(\mathbf{m}|\mathbf{d})\right\}, \tag{3.1}$$

with

$$\phi_{\mathrm{i}}^{\mathrm{RF}}(\mathbf{m}|\mathbf{d}) = \frac{1}{3\mathrm{N_i}}\sum_{j=1}^{\mathrm{N_i}}\left[\frac{\mathrm{RF}^{\mathrm{observed}}(t_j) - \mathrm{RF}^{\mathrm{modeled}}(\mathbf{m}, t_j)}{\delta\mathrm{RF}^{\mathrm{observed}}(t_j)}\right]^2 \tag{3.2}$$

and

$$\phi_{\mathrm{i}}^{\mathrm{SW}}(\mathbf{m}|\mathbf{d}) = \frac{1}{6\mathrm{M_i}}\sum_{j=1}^{\mathrm{M_i}}\left[\frac{\mathrm{C_p}^{\mathrm{i,observed}}(T_j) - \mathrm{C_p}^{\mathrm{i,modeled}}(T_j, \mathbf{m})}{\delta\mathrm{C_p}^{\mathrm{i,observed}}(T_j)}\right]^2, \tag{3.3}$$

where $\mathrm{C_p}^{\mathrm{i}}(T_j)$ denotes Rayleigh wave phase velocities for mode i and period T_j with $\mathrm{M_i}$ being the number of observed periods for each mode, δ observed uncertainties for each data type, and $\mathrm{N_i}$ the number of samples in each time window of interest.

We sample the posterior distribution in the model space by combining a Metropolis-Hastings Markov chain Monte Carlo (McMC) method (*Mosegaard and Tarantola*, 1995) with a stochastic optimization technique (*Hansen et al.*, 2011). The latter is used to obtain a good initial model for the McMC algorithm. This strategy improves the efficiency of the McMC method by significantly reducing the burn-in period. The McMC sampling is performed using 10 independent chains (with a total length of 10,000 iterations) characterized by identical initial models but different randomly chosen initial perturbations. This strategy allows for sampling 100,000 models with moderate computational cost (∼3 days using 10 cores). Finally, the 50,000 best-fitting candidates are used to build histograms of the marginal probability distribution of each model parameter.

Chapter 4

Electromagnetic sounding of the mantle

The content of this chapter was published as: Munch, F. D., Grayver, A. V., Kuvshinov, A. V & Khan, A. (2018). *Stochastic inversion of geomagnetic observatory data including rigorous treatment of the ocean induction effect with implications for transition zone water content and thermal structure.* Journal of Geophysical Research: Solid Earth, vol. 123, pp. 31-51, (doi: 10.1002/2017jb014691).

Abstract

In this chapter, we estimate and invert local electromagnetic (EM) sounding data for 1D conductivity profiles in the presence of non-uniform oceans and continents to most rigorously account for the ocean induction effect that is known to strongly influence coastal observatories. We consider a new set of high-quality time series of geomagnetic observatory data, including hitherto unused data from island observatories installed over the last decade. The EM sounding data are inverted in the period range 3–85 days using stochastic optimization and model exploration techniques to provide estimates of model range and uncertainty. The inverted conductivity profiles are best constrained in the depth range 400–1400 km and reveal significant lateral variations between 400 km and 1000 km depth. To interpret the inverted conductivity anomalies in terms of water content and temperature, we combine laboratory-measured electrical conductivity of mantle minerals with phase equilibrium computations. Based on this procedure, relatively low temperatures (1473–1623 K) are observed in the mantle transition zone (MTZ) underneath stations located in Southern Australia, Southern Europe, Northern Africa, and North America. In contrast, higher temperatures (1673–1773 K) are inferred beneath observatories on islands, Northeast Asia, and central Australia. MTZ water content beneath European and African stations is $\sim$0.05–0.1 wt%*, whereas higher water contents (*$\sim$0.5–1 wt%*) are inferred underneath North America, Asia, and Southern Australia. Comparison of the inverted water contents with laboratory-constrained water storage capacities suggests the presence of melt in or around the MTZ underneath four geomagnetic*

observatories in North America and Northeast Asia.

4.1 Introduction

Inferring the internal structure of the Earth is a key aspect for understanding its origin, evolution, and dynamics. In this regard, geophysical techniques such as seismic, geodetic, gravimetric, and electromagnetic (EM) studies play prominent roles because of their ability to sense structure at depth. In particular, EM studies aim at mapping electrical conductivity variations in the Earth. Electrical conductivity is sensitive to temperature, chemical composition, oxygen fugacity, water content, and the presence of melt (e.g. *Park and Ducea*, 2003; *Yoshino*, 2010; *Karato and Wang*, 2013). Hence, mapping electrical conductivity in turn enables constraining chemistry, mineralogy, and physical structure of the lithosphere and mantle (e.g. *Dobson and Brodholt*, 2000; *Xu et al.*, 2000; *Khan et al.*, 2006; *Toffelmier and Tyburczy*, 2007; *Fullea et al.*, 2011; *Pommier*, 2014; *Deschamps and Khan*, 2016, among others). For instance, global (*Kelbert et al.*, 2009; *Tarits and Mandéa*, 2010; *Semenov and Kuvshinov*, 2012; *Sun et al.*, 2015) and semi-global (e.g. *Koyama et al.*, 2006; *Shimizu et al.*, 2010; *Koyama et al.*, 2014) scale three-dimensional (3D) EM inversions of long-period geomagnetic data reveal the presence of large-scale lateral heterogeneities in the mantle.

Although significant improvements have been achieved in the last years with the emergence of the first set of 3D mantle conductivity models, 3D global and semi-global EM induction studies still face several challenges. First, because of the high computational cost of 3D forward operators only a coarse model parameterization is currently feasible resulting in limited radial resolution. Second, the deterministic approaches hitherto used in 3D EM inversion lack quantification of uncertainties in the recovered 3D conductivity models. Finally, the obtained 3D conductivity models have poor lateral resolution in many regions of the world, especially in the oceans, due to the extremely non-uniform distribution of geomagnetic observatories.

To improve the latter, considerable efforts have focused on improving global data coverage of ground-based geomagnetic observatories. In particular, several island geomagnetic observatories have been installed in the last decade (see next section). Availability of these new data provides an opportunity to study the deep electrical conductivity structure under hitherto unexplored regions of the Earth. *Kuvshinov et al.* (2002) showed that EM response functions in the form of local C-responses (*Banks*, 1969) are influenced by the presence of the conductive oceans at coastal and island observatories. However, due to the non-linearity of the problem, the most consistent way to account for the ocean induction effect (OIE) is to model it. In particular, for the period range considered here, oceans can be approximated by a thin surface shell of known conductance. *Semenov and Kuvshinov* (2012) com-

puted magnetic fields for conductance distributions with different lateral resolution concluding that a resolution of at least $1^\circ \times 1^\circ$ is necessary to accurately account for the OIE in the thin-shell approach. However, global 3D EM studies typically exploit a lower lateral resolution to preserve computational efficiency. In such cases, unaccounted-for OIE might be translated into spurious anomalies in the recovered conductivity images.

In the light of the aforementioned challenges, the main goal of this study is to map lateral variations of electrical conductivity in the Earth's mantle by relying on a quasi-1D approach. In short, we estimate local C-responses at a number of worldwide geomagnetic observatories and invert these individually for a local 1D conductivity profile in the presence of non-uniform oceans and continents. This quasi-1D inversion allows us to: a) improve radial resolution of local 1D conductivity models; b) properly account for the OIE; c) quantify uncertainties of the recovered conductivity profiles.

In the following, we describe estimation of local C-responses from a new dataset provided by the British Geological Survey (*Macmillan and Olsen*, 2013) that consists of cleaned-up time series of the Earth's magnetic field recorded at geomagnetic observatories distributed across the globe (Section 4.2). Section 4.3 introduces rigorous and accurate modeling of the OIE by implementation of a surface conductance map with lateral variable resolution. Section 4.4 presents the inverse problem formulation based on stochastic optimization and model exploration techniques. The inverted conductivity models and estimated uncertainties are discussed in Section 4.5, and interpreted in terms of variations in transition zone water content and temperature in Section 4.6.

4.2 Data analysis

4.2.1 Data selection

While satellite data are becoming increasingly important for constraining the electrical conductivity structure of the Earth (*Olsen et al.*, 2003; *Constable and Constable*, 2004; *Kuvshinov and Olsen*, 2006; *Velímskỳ*, 2010; *Püthe et al.*, 2015a; *Grayver et al.*, 2017, among others), ground-based observatory data remain a major input for global EM induction studies. However, as stated above, there are still major gaps in the geomagnetic observatory network, especially in oceanic areas and in the southern hemisphere. Over the last decade, a number of geomagnetic observatory projects have been initiated to improve the coverage by long-term measurements in oceanic regions. For instance, since 2007 GFZ (Helmholtz-Zentrum Potsdam) has been operating an observatory in the South Atlantic Ocean on St Helene Island (*Korte et al.*, 2009). In 2008, an observatory on Easter Island (South Pacific Ocean) was installed by the Institut de Physique du Globe de Paris (France) and Direccion Meteorologica

de Chile (*Chulliat et al.*, 2009). Since 2009 GFZ and the National Space Institute at the Technical University of Denmark have been operating an observatory on Tristan da Cunha Island in the South Atlantic Ocean (*Matzka et al.*, 2009). The Institute of Geophysics, ETH Zurich (Switzerland), installed two observatories in the Indian Ocean: on Gan island, Maldives (in cooperation with Maldives Meteorological Service and National Geophysical Research Institute, Hyderabad, India), and on Cocos Island (in cooperation with Geoscience Australia). The data from these stations have so far not been used for studying mantle conductivity structure.

To support the analysis of pre-SWARM and SWARM satellite data, the British Geological Survey (BGS) has recently provided a database of quality-controlled observatory hourly mean values for the years 1997-2016. This new dataset consists of definitive or close-to-definitive data derived from the World Data Center (WDC) for Geomagnetism (Edinburgh) for which any known discontinuity in the records (reported by the observatories in their annual mean values) have been corrected and poor-quality data removed (*Macmillan and Olsen*, 2013).

The BGS dataset contains data from 171 geomagnetic observatories distributed worldwide. In selecting data for this study, we excluded data from: 1) stations containing significant gaps or record lengths shorter than 3 years; 2) high-latitude stations which are known to be affected by the auroral current system (*Fujii and Schultz*, 2002; *Semenov and Kuvshinov*, 2012); and 3) on-land stations that have been frequently used in previous studies. Further, the selection procedure was applied so as to achieve as uniform global coverage as possible. To this end, we selected a subset of 39 high-quality stations from the BGS dataset, including six new island geomagnetic observatories (IPM, TDC, ASC, SHE, GAN, CKI) that are mainly located in the southern hemisphere. Additionally, we included definitive time series from the WDC dataset for two geomagnetic observatories (TKT and ODE) that have been inoperative for the last 20 years. Locations of the selected stations are shown in Figure 4.1.

4.2.2 Estimation of local C-responses

Time-series of the magnetic field, corrected for the main field and its secular variations, were used to determine local C-responses in the period range 3–85 days. Under the assumption that geomagnetic variations at the Earth's surface due to the magnetospheric ring current can be described via the first zonal harmonic in geomagnetic coordinates, C-responses are defined as (*Banks*, 1969)

$$C(\boldsymbol{r}_a, \omega) = -\frac{a \tan\theta}{2} \frac{Z(\boldsymbol{r}_a, \omega)}{H(\boldsymbol{r}_a, \omega)} \tag{4.1}$$

where $Z \equiv -B_r$ and $H \equiv -B_\theta$ correspond to the respective radial and co-latitudinal components of the geomagnetic field at location $\boldsymbol{r}_a = (r = a, \theta, \phi)$. The Earth's

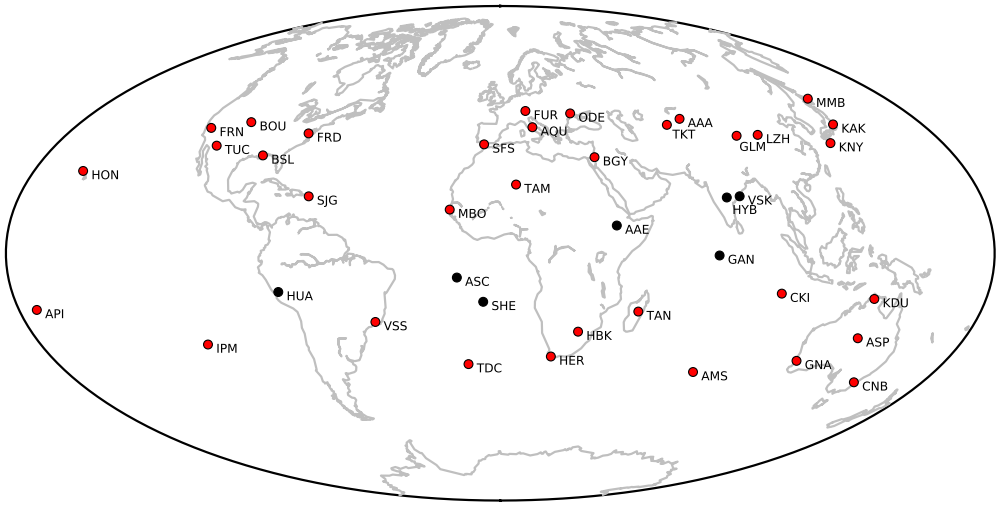

Figure 4.1: Distribution of geomagnetic observatories used in this study. Stations around dip equator (black) were not used in the inversion. Stations acronyms are defined in Table 1.

mean radius is denoted a, θ is the geomagnetic colatitude, and ϕ is the geomagnetic longitude. C-responses from observatory data were estimated using a section-averaging (e.g. *Olsen*, 1998) and iteratively re-weighted least squares approach (e.g. *Aster et al.*, 2005). Observational errors were determined using a jack-knife estimator (e.g. *Chave and Thomson*, 1989). This method provides unbiased estimations of C-response uncertainties without assumptions about the statistical distribution of experimental errors (*Efron*, 1982). The main field and secular variation have been removed following *Semenov and Kuvshinov* (2012).

As an example, Figure 4.2 shows C-responses and squared coherencies estimated for Alice Springs (ASP) and Honolulu (HON) geomagnetic observatories. For comparison, C-responses estimated using raw time series, provided by INTERMAGNET, for the time window 1957–2007 (*Semenov and Kuvshinov*, 2012) are also plotted. The new C-responses are characterized by an increase in smoothness and squared coherency, as well as a decrease in experimental uncertainties.

Further, visual inspection of the estimated C-responses and squared coherencies revealed a decrease in coherency for stations close to the dip equator and polar regions. The latter is likely explained by the fact that the radial component of the magnetic field goes trough zero at the dip equator. The former corresponds to violations of the source assumption because of the influence of polar currents that cannot be represented using the first zonal harmonic only. In what follows, we therefore considered data from 34 stations that provide C-responses with an average squared coherency >0.5. Detailed information of the selected geomagnetic observatories (red dots in Figure 4.1) is summarized in Table 4.1.

Code	Station	ϕ_{gg} [°]	λ_{gg} [°]	ϕ_{gm} [°]	λ_{gm} [°]	Data length
AAA	Alma Ata	43.20	76.90	34.31	153.05	2006-2012
AMS	Martin de Vivies	-37.80	77.57	-46.00	145.09	1999-2008
API	Apia	-13.80	188.22	-15.22	263.05	2012-2016
AQU	L'Aquila	42.38	13.32	42.17	94.62	1998-2009
ASP	Alice Springs	-23.77	133.88	-32.42	208.61	1998-2016
BGY	Bar Gyora	31.72	35.09	28.14	112.73	2004-2010
BOU	Boulder	40.14	254.76	47.99	321.47	1998-2016
BSL	Stennis Space Center	30.35	270.36	39.58	340.48	1998-2005
CKI	Cocos-Keeling Islands	-12.19	96.83	-21.90	168.54	2012-2016
CNB	Canberra	-35.32	149.36	-42.71	226.94	1998-2016
FRD	Fredericksburg	38.20	282.63	47.88	354.05	1998-2016
FRN	Fresno	37.09	240.28	43.19	306.13	1998-2013
FUR	Furstenfeldbruck	48.17	11.28	48.13	94.64	1998-2015
GLM	Golmud	36.40	94.90	26.54	168.47	2010-2015
GNA	Gnangara	-31.80	116.00	-41.93	188.84	1998-2016
HBK	Hartebeesthoek	-25.88	27.71	-27.04	95.12	1998-2013
HER	Hermanus	-34.43	19.23	-33.98	84.02	1998-2016
HON	Honolulu	21.32	202.00	21.60	270.41	1998-2016
IPM	Isla de Pascua	-27.20	250.58	-19.13	325.37	2010-2015
KAK	Kakioka	36.23	140.18	27.37	208.95	1998-2016
KDU	Kakadu	-12.69	132.47	-21.55	206.07	1998-2016
KNY	Kanoya	31.42	130.88	21.89	200.75	1998-2016
LZH	Lanzhou	36.10	103.84	26.02	176.52	1998-2015
ODE	Stepanovka	46.78	30.88	19.76	57.89	1957-1991
MBO	Mbour	14.38	343.03	35.52	211.87	1998-2016
MMB	Memambetsu	43.91	144.19	43.71	112.71	1998-2016
SFS	San Fernando	36.67	354.06	39.73	73.38	1998-2016
SJG	San Juan	18.11	293.85	27.83	6.62	1998-2016
TAM	Tamanrasset	22.79	5.53	24.39	82.09	1998-2016
TAN	Antananarivo	-18.92	47.55	-23.48	116.46	1998-2004
TDC	Tristan da Cunha	-37.07	347.69	-31.52	54.3	2009-2016
TKT	Tashkent	41.33	69.62	33.30	146.35	1957-1981
TUC	Tucson	32.18	249.27	39.50	316.9	1998-2013
VSS	Vassouras	-22.40	316.35	-13.51	27.15	2001-2010

Table 4.1: Summary of geomagnetic observatories acronyms, names, geodetic geographic latitude (ϕ_{gg}) and longitude (λ_{gg}), geomagnetic latitude (ϕ_{gm}) and longitude (λ_{gm}), and time interval of measured data. Time series for years 1997-2016 were provided by the British Geological Survey (*Macmillan and Olsen*, 2013). Additionally, data for Tashkent (TKT) and Stepanovka (ODE) geomagnetic observatories were taken from the World Data Centre for Geomagnetism (Edinburgh).

4.3 Forward problem and model parameterization

4.3.1 The ocean induction effect

Oceans are large conductive bodies that cause significant perturbations in C-responses at coastal and island observatories for periods <40 days (cf. *Kuvshinov et al.*, 2002).

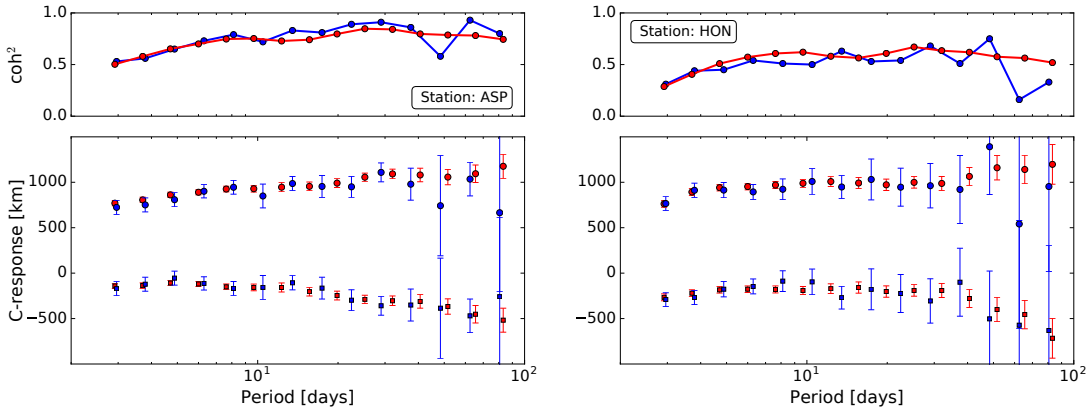

Figure 4.2: Real (positive) and imaginary (negative) parts of the experimental C-responses (bottom panel) and squared coherencies coh^2 (top panel) estimated in this study for Alice Springs (ASP) and Honolulu (HON) geomagnetic observatories using BGS data (red). Error bars indicate uncertainties of the experimental C-responses. For comparison, C-responses computed for the time window 1957–2007 (*Semenov and Kuvshinov*, 2012) are shown in blue.

In the following section, we stress the importance of accounting for the OIE when working with C-responses at observatories near the coast. As an illustration of this, Figure 4.3a-b show observed and synthetic C-responses for Hermanus and Kakioka geomagnetic observatories. Two types of synthetic C-responses were calculated: C^{1D} correspond to responses for a radially symmetric 1D conductivity structure derived from satellite and ground-based data (*Püthe et al.*, 2015a); $C^{\text{1D+shell}}$ denote responses estimated using the same 1D conductivity model overlain by a surface layer accounting for conductivities relevant to the oceans and continents. The vertical and horizontal components of the magnetic field were calculated by numerically solving Maxwell's equations in spherical geometry (*Kuvshinov*, 2008). As expected, for a radially symmetric geometry (*Weidelt*, 1972), the real part of C^{1D} monotonically increases with period, whereas the imaginary part is negative. However, the real part of the observed C-response at Hermanus observatory exhibits a non-monotonic behavior, while the imaginary part changes sign. At Kakioka observatory, the behavior of the C-response follows the monotonic variation expected for a radially symmetric geometry, but it nonetheless appears to be affected by the ocean. Accounting for the OIE clearly improves the fit to the observed C-responses.

Figure 4.3c-h show relative differences between 3D and 1D synthetic C-responses across Australia, Southern Africa, and Japan. These plots show that the OIE considerably distorts both real and imaginary parts of the C-responses. The largest distortions occur near the coasts where the imaginary part is influenced the most. This figure emphasizes that accounting for the OIE is essential when analyzing C-responses at coastal and island observatories.

Over the last decade, several approaches for correcting for the OIE have been proposed (*Everett et al.*, 2003; *Kuvshinov and Olsen*, 2006; *Semenov and Kuvshinov*, 2012; *Püthe et al.*, 2015a, among others). For example, *Utada et al.* (2003) proposed

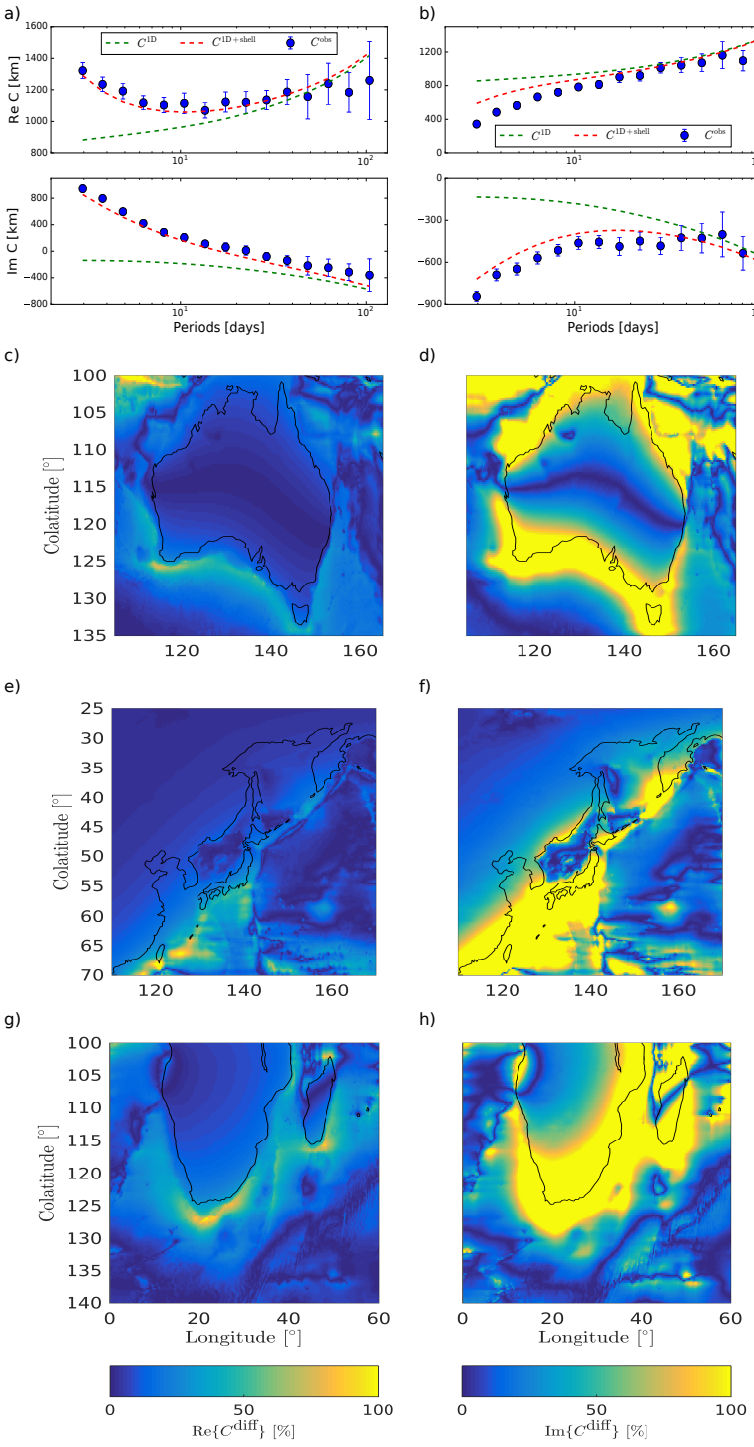

Figure 4.3: Real (left) and imaginary (right) parts of observed (C^{obs}) and synthetic C-responses for (a) Hermanus and (b) Kakioka geomagnetic observatories. Synthetic C-responses were calculated for a global average conductivity model (*Püthe et al.*, 2015a) with ($C^{\text{1D+shell}}$) and without (C^{1D}) ocean-induced fields. Plots (c)-(h) show real (left) and imaginary (right) parts of the relative differences C^{diff} between 3D and 1D synthetic C-responses for a period of 3 days across Australia (c,d), Japan (e,f) and Southern Africa (g,h).

the following (additive) correction

$$C^{\text{exp,corr}}(\omega) = C^{\text{exp}}(\omega) + C^{\text{1D}}(\omega) - C^{\text{1D+shell}}(\omega), \tag{4.2}$$

where C^{exp} corresponds to the observed experimental C-response, C^{1D} is the synthetic C-response of a radially symmetric conductive Earth (without oceans) and $C^{\text{1D+shell}}$ is the C-response of the same radially symmetric conductive Earth overlain by an inhomogeneous shell (which approximates the distribution of oceans). *Semenov and Kuvshinov* (2012) reported that the effectiveness of the correction depends on the lateral resolution of the conductance distribution and the 1D conductivity structure used for computing synthetic C-responses. The authors suggest that in order to accurately model the OIE using the thin-shell approximation, surface conductance should be described with a resolution of at least $1^\circ \times 1^\circ$ near the observation point. Furthermore, the conductivity structure must be representative of the region of interest. Although this correction succeeds in reducing the OIE in observed C-responses, it can not completely remove the influence of ocean-induced fields because of the non-linearity of the problem. Here, we propose to properly account for the OIE by modeling the ocean/continent conductivity distribution as a thin shell of laterally varying surface conductance.

4.3.2 Model parameterization

Our model parameterization consists of a thin spherical shell of known laterally varying surface conductance on top of a radially symmetric unknown conductivity profile (see Figure 4.4a). The thin-shell approximation is justified since for periods >3 days the penetration depth is much larger than the thickness of the oceanic layer. The surface conductance map was obtained by considering contributions from both sea water and sediments. The ocean conductance map was taken from *Manoj et al.* (2006) and incorporates bathymetry, salinity, temperature, and pressure variations. Conductance of the sediments was added for both continental and oceanic regions. The radially varying conductivity structure underneath consisted of 20 layers (50 km thick) between the surface and 1000 km depth, followed by 18 layers (100 km thick) down to the core-mantle boundary (∼2900 km depth). Vertical and horizontal components of the magnetic field for a 3D spherical geometry were computed using the frequency-domain 3D integral equation (IE) solver (X3DG) of *Kuvshinov* (2008). *Kelbert et al.* (2014) showed that for the model setup considered in this work, the methods based on IE formulation require significantly shorter CPU times than methods based on either finite elements, finite differences or spherical harmonic-finite elements.

Typically IE modeling is performed using a surface conductance of laterally uniform resolution. In this study, the ocean/continent conductivity distribution was modeled using a surface conductance with variable lateral resolution. The reason for this is twofold. First, at every location, fields are weakly influenced by the conductance distribution located far away from the observation point. And secondly, X3DG implementation works such that the computational time depends quadratically on

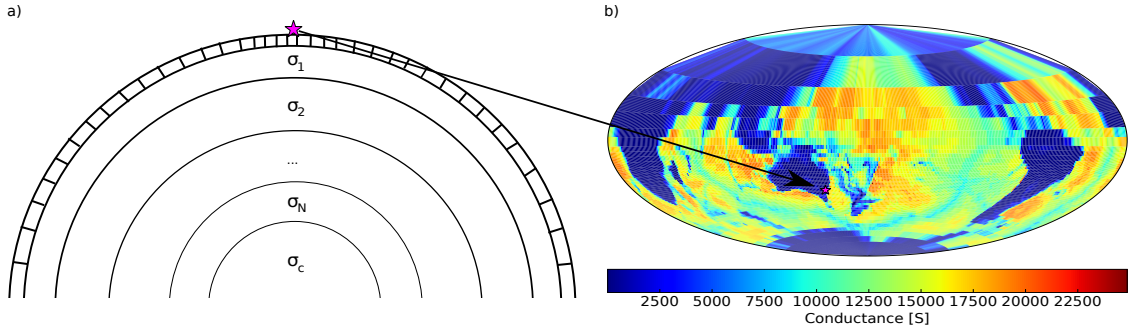

Figure 4.4: Model parameterization. (a) The Earth is parameterized as a thin spherical layer of laterally varying surface conductance (shown in plot b) on top of a radially symmetric conductivity profile. The radial conductivity structure consists of 20 layers (50 km thick) in the depth range 0–1000 km and 18 layers (100 km thick) in the depth range 1000–2900 km (b) Example of non-uniform conductance map built for Canberra geomagnetic observatory.

the number of cells in the latitudinal direction. Since in this study, C-responses were calculated at a single location, it was possible to use a non-uniform spacing without loss of accuracy. As a result, for every station a surface shell model was built. The conductance map had uniform (1°) resolution in longitude, and non-uniform resolution in latitude. Latitudinal resolution was 1° in a region of ±20° around the observation site and the grid-size was increased by a factor of 1.6 for every 10° beyond. As an example, Figure 4.4b depicts the non-uniform surface conductance map built for Canberra geomagnetic observatory. This non-uniform conductance map reduces computation time (without loss of accuracy) by a factor of 17 compared to a uniform 1° × 1° conductance distribution. Such a gain in performance allows us to ultimately apply a stochastic inverse technique.

The choice of model parameterization and strategy to solve the inverse problem (Section 4.4) was principally guided by our aim to overcome the aforementioned limitations existing in 3D global studies.

4.4 Stochastic inversion

Although significant improvements in the performance of X3DG have been achieved by introducing a non-uniform conductance distribution, the computational cost of the 3D forward operator makes purely probabilistic inversion algorithms based on Markov chain Monte Carlo (McMC) (*Tarantola*, 2005) infeasible. Alternatively, deterministic derivative-based methods, such as quasi-Newton or Gauss-Newton, can be applied. However, for non-linear inverse problems, these methods are highly dependent on the initial model, typically converge to a local minimum, require additional adjustments (e.g. *Borsic and Adler*, 2012) in the case of non-L_2 norms (*Grayver and Kuvshinov*, 2016), and do not provide uncertainty quantification. Therefore, our inverse problem formulation is based on a mixed scheme that combines a stochastic optimization technique known as Covariance Matrix Adaptation

Evolution Strategy (CMAES) (*Hansen and Ostermeier*, 2001) with McMC methods (e.g. *Mosegaard and Tarantola*, 1995).

CMAES explores the model space globally and exhibits a remarkable robustness on ill-conditioned problems (*Hansen et al.*, 2011). Although the use of CMAES in geophysics is not common, it has been implemented in recent studies as a global minimization method (*Alvers et al.*, 2013; *Diouane*, 2014; *Fonseca et al.*, 2014; *Shen et al.*, 2015; *Grayver et al.*, 2016, 2017) outperforming other techniques such as Genetic Algorithms and Particle Swarm Optimization (*Auger et al.*, 2009; *Arsenault et al.*, 2013; *Elshall et al.*, 2015). Additionally, *Grayver and Kuvshinov* (2016) showed that the use of CMAES for finding regions of low misfit can improve performance of conventional McMC methods.

In this section, we briefly present the algorithm; for details the reader is referred to *Grayver and Kuvshinov* (2016) and *Hansen and Ostermeier* (2001). Given M unknown parameters, at every iteration the algorithm samples $\lambda = 4+3\ln M$ models from the current multivariate normal distribution and evaluates the misfit function. Then, the best $\lambda/2$ candidates are selected and used to update the distribution mean, step size, and covariance matrix. We use the CMAES algorithm to find the maximum posterior probability model, $\mathbf{m}_{\mathrm{MAP}}$, by solving the following optimization problem

$$\mathbf{m}_{\mathrm{MAP}} = \underset{\mathbf{m}}{\operatorname{argmin}} \ \left[\phi_d(\mathbf{m}) + \beta\phi_m(\mathbf{m})\right], \tag{4.3}$$

where β is a regularization parameter. The data (ϕ_d) and model (ϕ_m) terms are given by

$$\phi_d(\mathbf{m}) = \frac{1}{2}\sum_{i=1}^{N}\left|\frac{C^{\mathrm{obs}}(\omega_i) - C^{\mathrm{mod}}(\mathbf{m},\omega_i)}{\delta C^{\mathrm{obs}}(\omega_i)}\right|^2, \tag{4.4}$$

and

$$\phi_m(\mathbf{m}) = \frac{1}{p}\sum_{i=1}^{M}|\nabla \mathrm{m}_i|^p, \tag{4.5}$$

where N is the number of measurements, C^{mod} indicate modeled C-responses, whereas C^{obs} denote observed C-responses with uncertainties δC^{obs}. Vector $\mathbf{m} = (\mathrm{m}_1, \mathrm{m}_2, ..., \mathrm{m}_M)^T$ denotes the radial part of the conductivity model. Note that different norms were used for data and regularization terms. For the former, a common L_2-norm is chosen, whereas the latter is computed using $\mathrm{L}_{1.5}$-norm ($p = 1.5$). This choice relies on studies performed by *Grayver and Kuvshinov* (2016) who showed that the $\mathrm{L}_{1.5}$-norm provides a good balance between sharp conductivity contrasts (L_1-norm) and smooth models.

4.5 Results

4.5.1 Datafit

The estimated C-responses were individually inverted to determine the most probable set of conductivities under each observatory. For each station, an L-curve analysis was performed to determine the optimal trade-off between data misfit and regularization term (see Figure C1). Figures 4.5-4.6 show observed and synthetic C-responses for the best-fit candidate model and final root mean square (RMS) error for each station. For most observatories considered in this work, both real and imaginary parts of the observed C-responses can be explained within experimental uncertainties using a 1D conductivity profile overlain by a high resolution thin shell. In particular, the non-monotonic behavior of observed C-responses at coastal observatories is successfully reproduced. Although a certain complexity is neglected when reducing the data into a finite set of complex-valued C-responses, the model parameterization considered in this work appears to be reasonable for mid-latitude data.

The final conductivity models, on average, have a RMS error <0.95. There are four stations (CKI, IPM, KDU, and MBO) for which RMS error ≈ 2. This increase is due to differences between the imaginary part of the observed and synthetic C-responses at short periods. As is shown in Figure 4.6 for Cocos Island (CKI) and Easter Island (IPM), synthetic C-responses explain the imaginary part of the observed C-responses at long periods (T>20 days), but disagree at shorter periods. One can speculate that differences in the imaginary part of C-responses for short periods reflect either the presence of anomalously shallow structures or are artifacts arising from un-modeled OIE. In order to address the latter, we additionally computed C-responses using a surface conductance map on a $0.25^\circ \times 0.25^\circ$ grid for the best-fit candidate models. No significant differences were observed between C-responses for $1^\circ \times 1^\circ$ and $0.25^\circ \times 0.25^\circ$ grids. One may therefore argue that differences between observed and computed C-responses are due to anomalous structure in the upper mantle, unless the conductance distributions considered in this work do not account for certain small-scale local features in bathymetry or sea water conductivity.

4.5.2 Uncertainty quantification

Uncertainty quantification of the final models is essential to evaluate the robustness and reliability of the retrieved conductivity structures. Studies based on deterministic approaches, typically perform sensitivity analysis based on applying small perturbations to the final conductivity model and comparing their effect on the computed responses (e.g. *Meqbel et al.*, 2014; *Baba et al.*, 2016). Although this

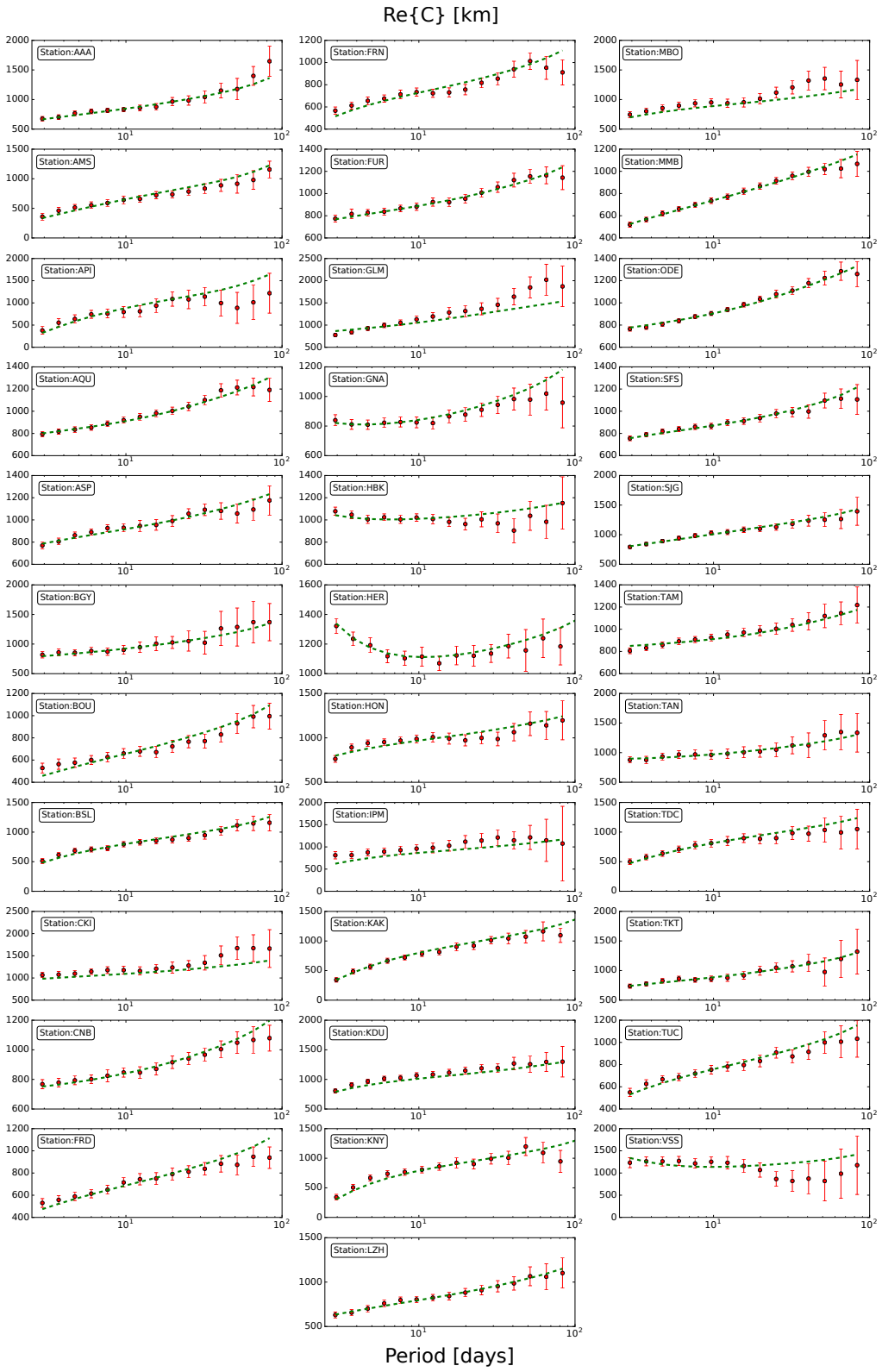

Figure 4.5: Real parts of observed (circles) and synthetic (dashed lines) C-responses for the best-fit conductivity models at the 34 geomagnetic observatories considered in the study (see Table 4.1). Uncertainties of observed C-responses are indicated by the error bars.

strategy provides some insight, one can argue that the region of the model space sampled in such a sensitivity analysis is strongly study-dependent (e.g. *Trampert*,

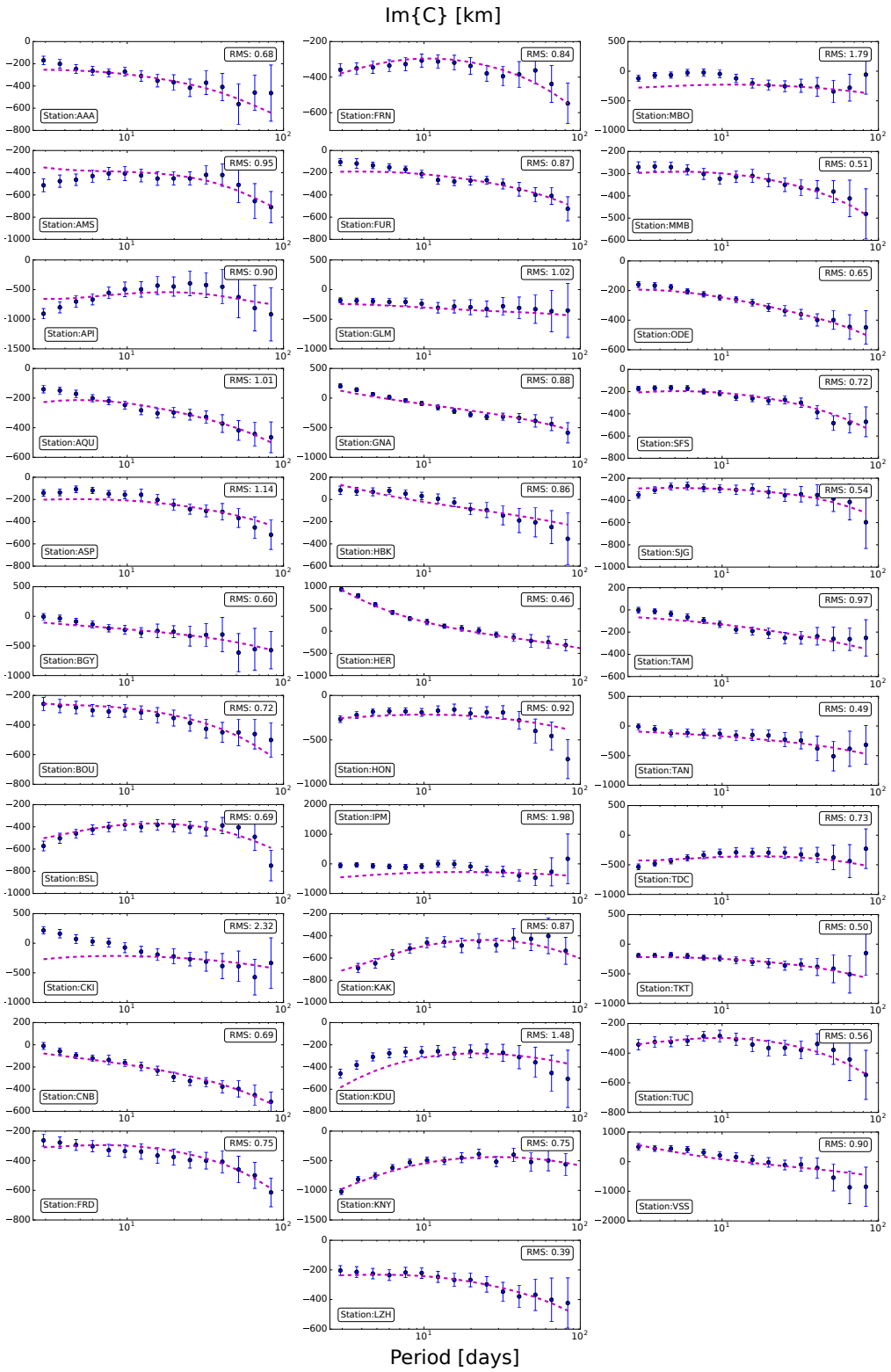

Figure 4.6: Imaginary parts of observed (circles) and synthetic (dashed lines) C-responses for the best-fit conductivity models at the 34 geomagnetic observatories considered in the study (see Table 4.1). Plots also include root-mean squared (RMS) error for real and imaginary parts of the responses. Uncertainties of observed C-responses are indicated by the error bars.

1998). Alternatively, a more consistent uncertainty quantification can be achieved by exploration of the model space around the best solution. Following this concept,

model uncertainties are estimated using a McMC (e.g. *Mosegaard and Tarantola*, 1995) method. However, inversions based on McMC require a substantial amount of forward computations. The computational cost of the 3D forward operator (even with the introduced laterally-varying grid) makes model space exploration based on purely McMC methods prohibitive. Here, we propose an alternative strategy where we explore the model space in the region around $\mathbf{m}_{\mathrm{MAP}}$. First, we computed 1D and 3D synthetic C-responses for $\mathbf{m}_{\mathrm{MAP}}$, followed by application of Eq. 4.2 to obtain experimental C-responses corrected for OIE. As mentioned in Section 4.3.1, if the conductivity model $\mathbf{m}_{\mathrm{MAP}}$ is a good estimation of the conductivity structure beneath the station, $C^{\mathrm{exp,corr}}$ is largely isolated from the influence of the oceans. Following this, we performed an exploration of the model space around the most probable candidate using the Metropolis-Hastings (*Metropolis et al.*, 1953; *Hastings*, 1970) algorithm considering $C^{\mathrm{exp,corr}}$ as observed data and employed a 1D forward operator to compute synthetic C-responses.

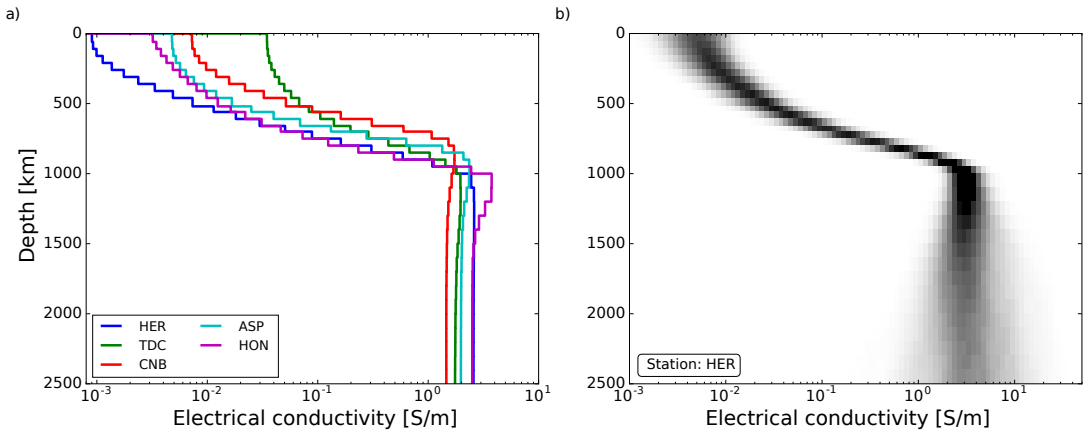

Figure 4.7: (a) Inverted conductivity models for Hermanus (HER), Tristan da Cunha (TDC), Honolulu (HON), Canberra (CNB), and Alice Springs (ASP) observatories. (b) Sampled posterior probability distribution for Hermanus geomagnetic observatory, with black most probable and white least probable. Final posterior probability distributions for all analysed stations are shown in Figures C2–C8.

For each geomagnetic observatory, we performed a total of 1.000.000 McMC iterations. The first 200.000 iterations were considered as burn-in period. Moreover, we analyzed the statistical independence of proposed models by estimating the cross-correlation between candidates from successive realizations. In order to ensure the independence of proposed models (cross-correlation<0.4), only one candidate per 1000 iterations was retained. The obtained models were used to estimate uncertainties of the electrical conductivity underneath each station assuming a log-normal distribution. Further, sampled conductivities were used to build a histogram of the marginal probability distribution for each layer. The sampled posterior probability distribution, shown in Figure 4.7b for a single station (HER), indicates increased uncertainty in the uppermost mantle (<400 km depth) and lowermost mantle (>1400 km depth). Therefore, and in agreement with previous studies (cf. *Khan et al.*,

2011b), the C-responses estimated in this work best constrain the conductivity structure in the depth range between 400 and 1400 km.

4.5.3 Conductivity models

In this section, we describe some of the most prominent features observed in the final conductivity models. To this end, Figure 4.7a shows the obtained conductivity structures for five geomagnetic observatories: Hermanus (HER), Tristan da Cunha (TDC), Honolulu (HON), Canberra (CNB), and Alice Springs (ASP). These five stations were chosen to highlight the significant variability of the final models. Additionally, a global average model derived from satellite and observatory data (*Püthe et al.*, 2015a) is shown for comparison. Firstly, there are considerable differences in the first 400 km. Although the sensitivity analysis described in Section 4.5.2 indicates low resolution in the uppermost mantle, the observed variability nonetheless suggests that our results are sensitive to the bulk conductivity of the uppermost mantle. Secondly, significant lateral variability is observed in the depth range 400–1100 km. And finally, variability is reduced in the lower mantle, reflecting more uniform structure in accordance with seismologic evidence (*Schaeffer and Lebedev*, 2015).

In order to visualize lateral variations in the inverted conductivity models, Figure 4.8 shows average conductivity values over four depth intervals: 410–520, 520–670, 670–900, and 900 –1100 km depth. Average conductivities for depths >1100 km are not shown because of the aforementioned reduced lateral variation. For comparison, Figure 4.8 also depicts conductivity values extracted from the global 3D conductivity model derived by *Semenov and Kuvshinov* (2012). The authors inverted local C-responses (period range 3–104 days) at 119 mid-latitude geomagnetic observatories to image the 3D global electrical conductivity distribution in the mantle. They parameterized the depth range 410–1600 km by five spherical layers of 110, 150, 230, 300, and 400 km thickness, respectively. All forward calculations were performed on a $3^\circ \times 3^\circ$ grid, whereas the lateral resolution of the inverse domain was chosen to be $9^\circ \times 9^\circ$. The observed C-responses were corrected for the ocean induction effect before inversion. Despite various differences in conductivity values, there is general similarity between both conductivity models. For instance, both models indicate small conductivity anomalies underneath Southern Europe and Northern Africa, whereas large conductivity anomalies are observed beneath North America and Northern Asia. The presence of a large conductivity anomaly underneath Northern Asia has also been reported by *Kelbert et al.* (2009) and more recently confirmed by *Sun et al.* (2015). Finally, both models suggest the presence of a large conductivity anomaly beneath Southern Australia. This feature is also consistent with the regional study performed by *Koyama et al.* (2014) and *Koch and Kuvshinov* (2015).

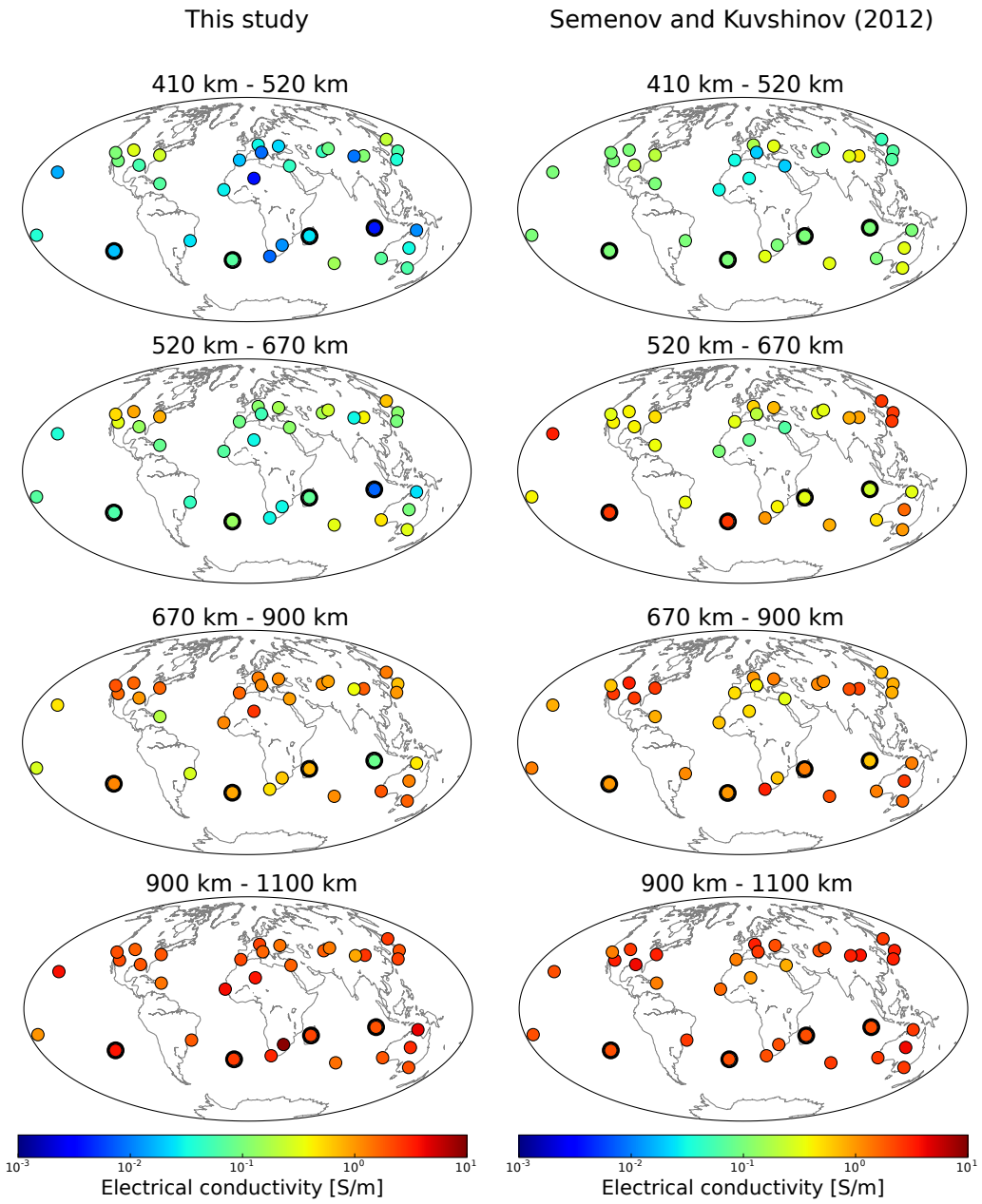

Figure 4.8: Conductivities recovered in this study (left) averaged over four depth intervals: 410–520, 520–670, 670–900, and 900–1100 km. For comparison, conductivities extracted from the 3D conductivity model derived by *Semenov and Kuvshinov* (2012) are shown in the right. Highlighted circles refer to island observatories that were not part of the *Semenov and Kuvshinov* (2012) data set.

The most significant difference between our results and the model derived by *Semenov and Kuvshinov* (2012) concerns geomagnetic observatories located on islands. In the model of *Semenov and Kuvshinov* (2012), more conductive anomalies are found beneath the island stations. This difference can be attributed to (a) lack of data from geomagnetic observatories located on Tamanrasset (TAM), Easter Island (IPM), Tristan da Cunha (TDC), and Cocos Island (CKI) (see Figure 4.8) and (b) the fact that the correction scheme applied by *Semenov and Kuvshinov* (2012) to account for the OIE is only approximate.

4.6 Thermo-chemical interpretation of conductivity anomalies

4.6.1 Laboratory-based conductivity profiles

In this section, we interpret the inverted conductivity anomalies in terms of transition zone thermal structure and water content. For this purpose, we compared the inverted conductivity models with laboratory-based conductivity profiles. We followed the approach described in detail in *Khan* (2016). Relative to *Khan* (2016), the conductivity database has been updated with recent measurements for clinopyroxene and Al-bearing bridgmanite. For brevity, only a summary is given here.

The laboratory-based conductivity profiles are computed from experimental measurements of mantle mineral conductivities in combination with mineral phase equilibrium computations. To compute phase equilibria, we employ the Gibbs free-energy minimization strategy described by *Connolly* (2009) and the self-consistent thermodynamic formulation of *Stixrude and Lithgow-Bertelloni* (2005b) with parameters given by *Stixrude and Lithgow-Bertelloni* (2011), which predicts stable mineralogy (mineral modes) for a given pressure, temperature, and composition. The obtained mineral phase proportions are combined with laboratory-measured mineral conductivities to compute electrical conductivity as a function of pressure, temperature, and composition. The contribution from individual minerals to bulk conductivity is obtained by averaging using effective medium theory (*Landauer*, 1952) to produce a self-consistent solution. *Khan* (2016) analyzed different averaging strategies and found the self-consistent solution to be the only estimator that consistently lies within the Hashin-Shtrikman bounds (*Hashin and Shtrikman*, 1963). The latter bounds correspond to the narrowest possible restrictions that exist on an arbitrary isotropic multi-phase system (*Mavko et al.*, 2009).

Electrical conductivity is known to be highly sensitive to temperature and presence of water (e.g. *Karato and Wang*, 2013). In order to account for the influence of temperature and water content on hydrous minerals, we employ the electrical conductivity data from *Yoshino and Katsura* (2009) and *Yoshino et al.* (2012) for olivine, from *Zhang et al.* (2012) for orthopyroxene, from *Zhao and Yoshino* (2016) for clinopyroxene, from *Yoshino and Katsura* (2012) for wadsleyite, and from *Yoshino et al.* (2008a, 2012) and *Yoshino and Katsura* (2009) for ringwoodite. Additionally, we consider electrical conductivity data from *Yoshino et al.* (2008b) for garnet, *Katsura et al.* (2007) for akimotoite, from *Yoshino et al.* (2011) for ferropericlase, from *Xu et al.* (2000) for calcium perovskite and from *Yoshino et al.* (2016) for Al-bearing bridgmanite. Figure 4.9a summarizes conductivities for all minerals as a function of temperature, pressure, and water content. Following *Khan* (2016), we parameterize the water content of the mantle in terms of the water contents of olivine and wadsleyite. Water contents of clinopyroxene, orthopyroxene, and ringwoodite are

estimated using the water partition coefficients based on measurements from *Inoue et al.* (2010) and *Ferot and Bolfan-Casanova* (2012). Although we presently only use the measurements of Yoshino, Katsura and coworkers because of their ready applicability, we have to acknowledge that experimental disagreements currently exists with regard to the electrical conductivity of wadsleyite and ringwoodite. *Dai and Karato* (2009) measured the influence of temperature and water content on wadsleyite and ringwoodite reporting results that differ from those of Yoshino and coworkers. Despite various efforts, the disagreement has not yet been resolved and the controversy still remains (*Karato*, 2010; *Yoshino and Katsura*, 2013).

To illustrate the approach, Figure 4.9d shows the modal mineralogy and associated laboratory-based bulk electrical conductivity profiles for a pyrolitic mantle (*Lyubetskaya and Korenaga*, 2007) with a moderate amount of water (0.01 wt%) in olivine (*Karato*, 2010; *Khan and Shankland*, 2012) and different amounts of water in wadsleyite (0.01 wt%, 0.1 wt%, and 1 wt%). The composition is described using the CMFASNa model system comprising the oxides CaO-MgO-FeO-Al_2O_3-SiO_2-Na_2O, which account for $\sim 98\%$ of the mass of Earth's mantle (*Anderson*, 2007). The lithospheric temperature is computed by a linear gradient, whereas the sub-lithospheric mantle adiabat is defined by the entropy of the lithology at the base of the lithosphere (corresponding to 1623 K at 100 km depth). The pressure profile is obtained by integrating the load from the surface.

4.6.2 Transition zone temperature and water content

From Figure 4.9d, we observe that laboratory-based conductivity profiles implicitly incorporate discontinuities across the major phase transitions (olivine $\rightarrow$ wadsleyite, wadsleyite $\rightarrow$ ringwoodite, and ringwoodite $\rightarrow$ bridgmanite+ferropericlase), whereas the conductivity profiles retrieved from the inversion of C-responses (Figure 4.7a) are characterized by a continuous conductivity increase down to depths of $\sim$1000 km. These differences represent a fundamental challenge when comparing laboratory-based conductivity profiles with models retrieved from inversion of C-responses across the entire depth range. To overcome this complication, we focus our comparison on the depth ranges 400–650 km and 900–1400 km.

We first performed several synthetic inversions (not shown here) to characterize compositional, thermal, and water content anomalies that can be successfully recovered given the conductivity uncertainties estimated in Section 4.5.2. This synthetic analysis indicated that the conductivity profiles obtained from inversion of C-responses are mostly sensitive to variations in the thermal structure and water content of wadsleyite (C_{wad}). Based on this result, we computed 900 laboratory-based conductivity profiles for a pyrolitic mantle, where we varied thermal structure and water content between $T_0 \in [1173\text{ K}, 1973\text{ K}]$ and $\log(C_{wad}/C_0) \in [-3, 1.5]$; where T_0 corresponds to the temperature at the base of a 100 km thick lithosphere and

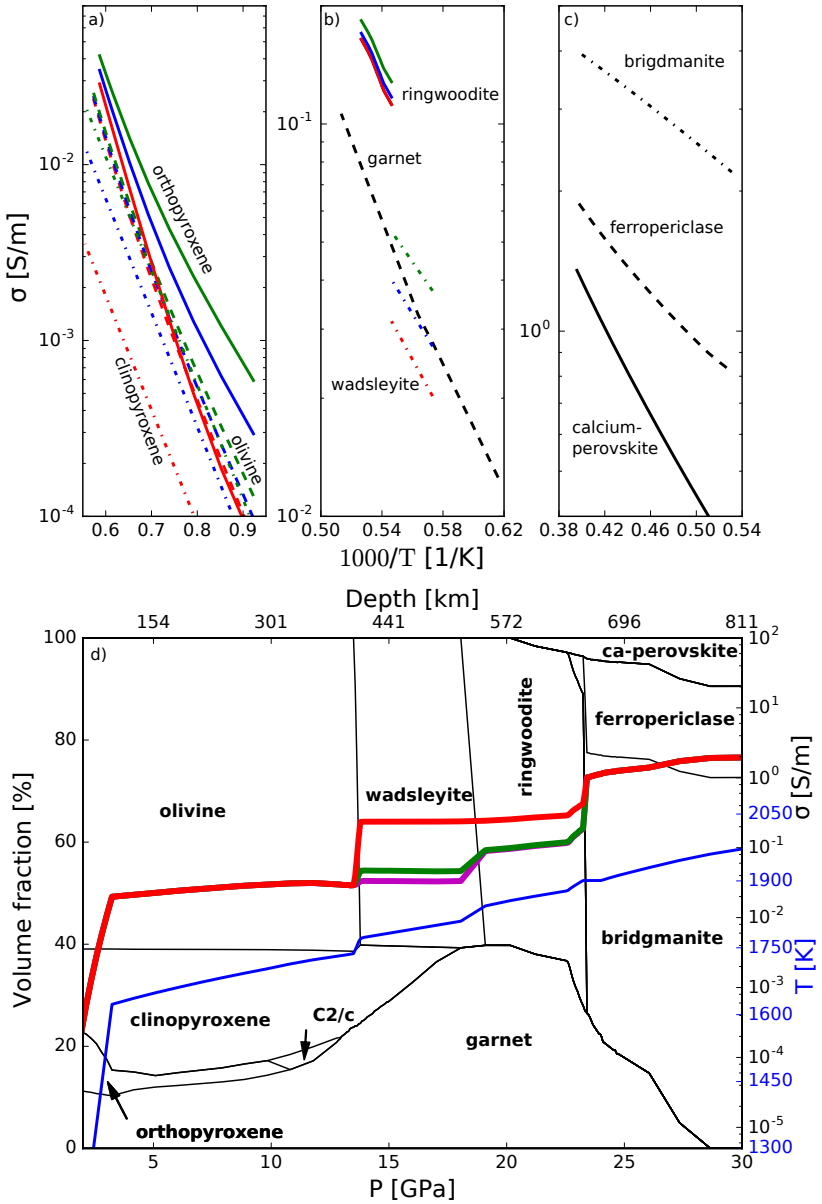

Figure 4.9: Summary of major upper mantle (a), transition zone (b), and lower mantle (c) single mineral electrical conductivities based on laboratory measurements as a function of inverse temperature, and water content. In Figure 4.9a colors scheme refers to differing water contents in nominally anhydrous upper mantle minerals: red, blue and green indicate 0.001 wt%, 0.005 wt%, and 0.01 wt% of water, respectively. In Figure 4.9b conductivity variations are computed for water contents of 0.01 wt% (red), 0.05 wt% (blue), and 0.1 wt% (green). Plot (d) shows modal mineralogy and bulk electrical conductivity for a pyrolitic mantle (composition from *Lyubetskaya and Korenaga* (2007)) with 0.01 wt% of water in olivine and different water contents in wadsleyite: 0.01 wt% (magenta), 0.1 wt% (green), and 1 wt% (red). The adiabatic geotherm (blue) is defined by the entropy of the lithology at a temperature of 1623 K at the base of a 100 km thick lithosphere.

C_0 is a normalizing constant equal to 1 wt%. Conductivities were compared using a L_2-norm misfit function. The uncertainties on the final temperatures (δT$\sim$30 K) and water contents ($\delta \log(C_{wad}/C_0) \sim 0.12$) were determined by visual inspection of the misfit surface. Figure 4.10 summarizes the water contents and temperatures

in the transition zone (at 500 km depth) that best explain the observed electrical conductivity profiles. All final models explain the observations within uncertainties.

Relatively low transition zone temperatures (1473–1623 K) are found underneath stations located in Southern Australia, Southern Europe, Northern Africa, and North America. In contrast, higher transition zone temperatures (1673–1773 K) are obtained underneath several island observatories (TDC, IPM, HON, TAN). These anomalies seem to be in agreement with higher potential temperatures beneath intraplate volcanic centers reported by *Courtier et al.* (2007). High temperature anomalies are also observed beneath Northeast Asia (MMB, KNY) and the central region of Australia (ASP). Temperature variations in the transition zone across the globe span ∼300–400 K and are in overall agreement with other regional studies (e.g. *Cammarano and Romanowicz*, 2007; *Ritsema et al.*, 2009a; *Khan et al.*, 2011a).

Regarding variations in transition zone water content, geomagnetic observatories in Europe and Africa are characterized by C_{wad}∼0.05−0.1 wt%; whereas higher water contents (C_{wad}∼0.5−1 wt%) are observed beneath stations located in North America, Asia, and Southern Australia. A dry transition zone below Europe has already been suggested by *Utada et al.* (2009) from joint analysis of electromagnetic and seismic tomographic models. Furthermore, temperatures and water contents obtained beneath ASP, FUR, HER, HON, LZH, and TUC are in general agreement with previous studies where a similar methodology was applied (*Khan and Shankland*, 2012; *Khan*, 2016). Based on experimental evidence of the water storage capacity (see below) of transition zone minerals (wadsleyite and ringwoodite), transition zone water content is higher than that of the upper mantle (olivine) ranging from ∼0.1–1 wt% (*Pearson et al.*, 2014; *Peslier et al.*, 2017).

Mantle water content has to be analyzed in terms of the water storage capacities of mantle minerals. The water storage capacity is the maximum amount of water that a mineral or rock is able to retain at a given temperature and pressure without producing a hydrous fluid (e.g. *Hirschmann et al.*, 2005). This implies that at locations where the water content exceeds the local storage capacity, hydrous melting ensues (e.g. *Kohlstedt et al.*, 1996). *Litasov et al.* (2011) reported that the temperature dependence of the water storage capacity of wadsleyite (C) can be described by the exponential equation $C = 637.07\,e^{-0.0048T}$, where T is in °C. This provides an upper limit on the amount of water that can be stored in nominally anhydrous minerals in the transition zone. In the present work, we compared the estimated water storage capacities with the inverted water contents beneath each station. As shown in Figure 4.10c, we found that water storage capacities are only exceeded underneath four locations (BOU, FRD, MMB, and LZH). This suggests that thin melt layers (∼10-20 km thick) could possibly exist in and around the transition zone underneath these locations.

Although the presence of melt can potentially increase conductivity by several

orders of magnitude (e.g. *Yoshino et al.*, 2010; *Pommier*, 2014), the resolution of the conductivity profiles obtained here is not good enough to resolve these layers, if present. The current observation of melt has to be viewed in the context of the physical parameterization of the behaviour of water-induced melting as observed experimentally by *Litasov et al.* (2011) and *Ferot and Bolfan-Casanova* (2012). Thus, although data might not be able to accurately resolve a thin melt-layer, physical conditions are such that melt is expected to appear.

It has been proposed that when material enriched in water is advected across the olivine→wadsleyite transition it will undergo, due to differences in storage capacities between the two reservoirs, partial melting, and leave behind a residue with a water content similar to that of the upper mantle (*Bercovici and Karato*, 2003). In the water filter hypothesis by *Bercovici and Karato* (2003), this process is expected to occur globally rather than being restricted to localized water-rich upwellings. Although an accurate characterization of the melt layer is beyond the scope of this work, our results nonetheless suggest that the water filter hypothesis is only likely to be operative on a local/regional scale. Experimental and seismic evidence in support of localized melt layers on top of the transition zone (around 410 km depth) has also accumulated in the form of observations of low shear-wave velocity anomalies at various locations of which many appear to be associated with areas where subduction has recently or is currently taking place (*Freitas et al.*, 2017). The locations include western, central, and eastern US (*Song et al.*, 2004; *Song and Helmberger*, 2006; *Courtier and Revenaugh*, 2006; *Jasbinsek and Dueker*, 2007), Siberian platform (*Vinnik and Farra*, 2007), Arabian plate (*Vinnik et al.*, 2003), off the coast of Japan (*Revenaugh and Sipkinf*, 1994; *Bagley et al.*, 2009), Southwest Pacific (*Courtier and Revenaugh*, 2007), and Afar Triple Junction in East Africa (*Thompson et al.*, 2015) among others.

The origin of water in the transition zone is likely due to water carried down with subducting plates along cold geotherms (e.g. *Schmidt and Poli*, 1998; *Ohtani et al.*, 2004; *Peslier et al.*, 2017) and due to upward percolation of hydrous melts from the lower mantle (e.g. *Hirschmann*, 2006), whose storage capacity is believed to be extremely low (e.g. *Bolfan-Casanova et al.*, 2002, 2003). The extent to which this actually results in a water-enriched region in the transition zone is unclear. The water contents inferred here for the transition zone show large variability and are relatively modest (∼0.1 wt%) beneath geomagnetic observatories located in Europe, Africa, and Northern Australia, but high (∼0.5–1 wt%) underneath stations in North America, Asia, and Southern Australia. These water contents are consistent with what has been experimentally determined (∼0.2wt%) by *Freitas et al.* (2017). Since there is no evidence from geodynamic models that the "410-km" discontinuity acts as a barrier to mantle flow (e.g., *Christensen*, 2001), material that is advected into the bottom of the upper mantle with passive upwellings, may provide an explanation

for how subducted water is being continuously drained from the transition zone and re-enters the upper mantle and becomes remixed there. The lateral variations in water content that we observe beneath the various regions may therefore be due to subduction of water and possibly upwelling of hydrous melts that produces local water-rich regions in the transition zone.

Finally, it should be mentioned that the thermal structure and water contents derived in this work are subject to several assumptions. Firstly, in the present thermodynamic model we preclude consideration of redox effects that might be expected to be important if native or ferric iron is present in Earth's mantle. Secondly, H_2O, TiO_2, Cr_2O_3, and partial melt are not considered in the phase equilibria calculations. Thirdly, although the pyrolitic model of *Ringwood* (1975) has become widely accepted as being representative of Earth's average upper mantle composition, compositional perturbations from the pyrolitic model should still be explored (*Khan et al.*, 2009). Finally, an inherent problem with the use of electrical conductivity for constraining transition zone water content and thermal structure is the trade-off between these different parameters. Here a slight negative correlation between T_0 and C_w is observed. Future studies will consider joint inversion of different geophysical observables in order to reduce this trade-off and help distinguishing thermal from compositional contributions (*Khan et al.*, 2009; *Verhoeven et al.*, 2009; *Utada et al.*, 2009; *Afonso et al.*, 2013, among others).

4.7 Concluding remarks and outlook

In this study, we estimated and inverted local C-responses (in the period range 3–85 days) at 34 mid-latitude geomagnetic observatories to map lateral variations in the mantle electrical conductivity in the depth range 400–1400 km. Novelties of this study include: a) usage of a new, high-quality, dataset including hitherto unused data from geomagnetic observatories installed on islands over the last 10 years; b) rigorous and accurate modeling of the ocean induction effect; and c) inversion of the data using a stochastic optimization technique. The ocean induction effect was rigorously accounted for by including a laterally varying surface conductance map in the computation of synthetic C-responses. Our inverse problem formulation was based on a mixed scheme that combines stochastic optimization (CMAES) with model space exploration (McMC) methods to estimate uncertainties of the retrieved models.

Uncertainty analysis demonstrates that the C-responses estimated in this work best constrain the conductivity structure in the depth range 400–1400 km. However, our results are also sensitive to the bulk conductivity of the uppermost mantle. The obtained conductivity models indicate strong lateral variability for depths <1100 km. The inverted conductivity structure was subsequently interpreted in terms

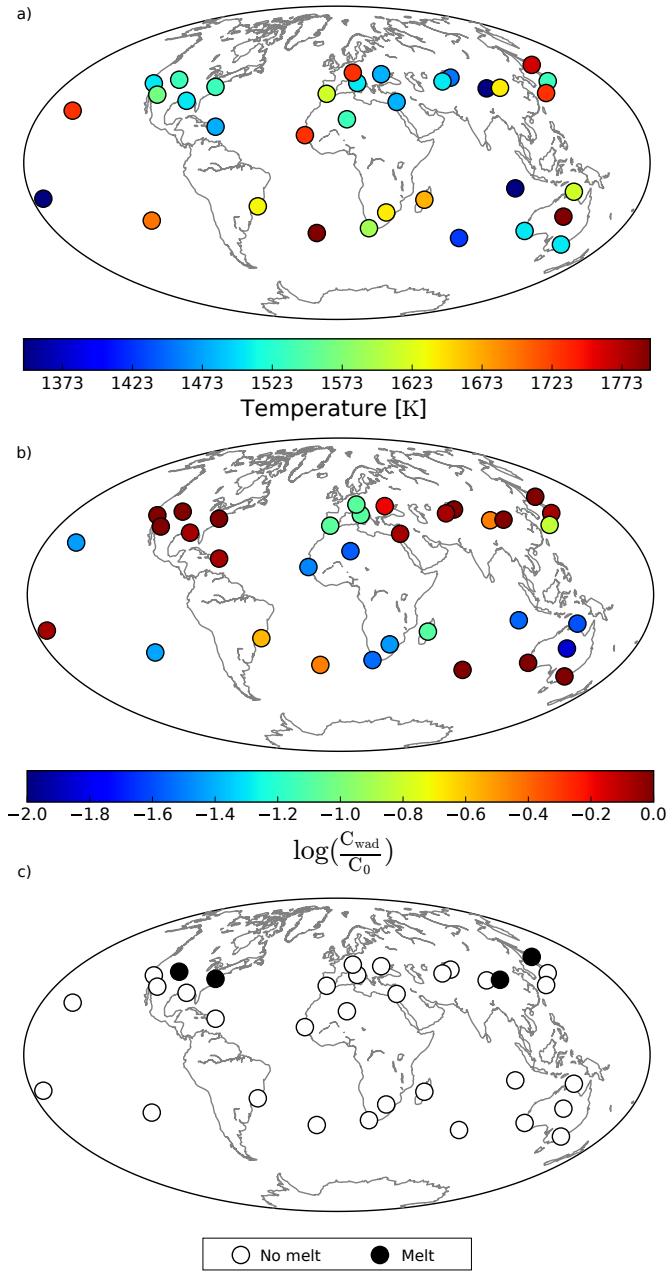

Figure 4.10: Spatial distribution of inverted transition zone temperatures (a) at 500 km depth and water content (b) in wadsleyite C_{wad} (C_0 is equal to 1 wt%). The maps were obtained by converting the conductivity maps (Figure 4.8) to temperature and water content using the approach described in Section 4.6. Comparison of inverted water content with experimentally-determined water storage capacities (*Litasov et al.*, 2011) show locations where melt could potentially be present (c).

of variations in thermal structure and water content in the transition zone. For this purpose, we compared the inverted conductivity models with laboratory-based conductivity profiles that were obtained by combining laboratory-measured electrical conductivity of mantle minerals with mantle mineralogy estimated using a self-consistent thermodynamic formulation. Transition zone temperature variations across the globe span ~350 K. The transition zone underneath stations located in Europe and Africa is characterized by water contents around ~0.05–0.1 wt%; while

higher water contents (∼0.5–1 wt%) are observed beneath geomagnetic observatories situated in North America, Asia, and Southern Australia. Finally, we compared the obtained water contents with the water storage capacities measured by *Litasov et al.* (2011) to inquire about the possible presence of melt. The comparison suggests the presence of melt underneath four geomagnetic observatories in North America and Northeast Asia.

Some limitations of this work should be noted. Firstly, high-latitude geomagnetic observatories were excluded from the analysis because of the influence of the auroral current system. Secondly, we described the field variations under consideration via the first zonal harmonic in geomagnetic coordinates. As a consequence, the potential complexity of the ring current system is not fully taken into account. Future work should focus on a) including observatories at higher latitudes; and b) increasing the complexity with which the source mechanism is described. Isolating high-latitude data from the influence of the auroral current system could be partially addressed by the application of principal component analysis (*Shore et al.*, 2016). A step toward handling more complex source models has been proposed by *Püthe et al.* (2015b). The authors introduced transfer functions that relate the local vertical magnetic field to the spherical harmonic coefficients describing the external part of the magnetic potential. However, this methodology implies that source and conductivity structure should be jointly determined. Deriving a suitable inversion scheme for this purpose is a challenge that will be considered in the future. Finally, resolution of lithospheric and uppermost mantle conductivity can be improved by jointly inverting multi-source data. For instance, *Grayver et al.* (2017) showed that 1D global conductivity models retrieved from joint inversion of tidal and magnetospheric signals better constrain the global conductivity structure of the upper mantle and transition zone.

Chapter 5

Coupling seismic and electromagnetic data

The content of this chapter will be submitted for publication to Geophysical Research Letters as: Munch, F. D., Grayver, A. V., Guzavina, M., Kuvshinov, A. V & Khan, A. *Coupling seismic and electromagnetic data to map lateral variations in upper mantle and transition zone water content.*

Abstract

We present a new way of investigating lateral variations of the water content and thermo-chemical structure in upper mantle and transition zone by a joint probabilistic analysis of electromagnetic (EM) and seismic data. Specifically, we inverted EM signals in a wide period band (from 6 hours to 85 days) to probe the electrical conductivity structure underneath 20 geomagnetic observatories. We accounted for complex spatial structure of the ionospheric and magnetospheric sources by means of transfer functions that relate local variations in the vertical magnetic field with global coefficients describing the source. We found that the joint inversion of EM data for the daily and long period bands led to a significantly improved model resolution in the upper mantle and transition zone. The inferred conductivity profiles reveal significant lateral variability, which we interpreted in terms of water content in the upper mantle and transition zone by a stochastic coupling of conductivity with constrains on the mantle thermo-chemical structure derived from the analysis of short- (P–to–S receiver functions) and long-period (Rayleigh wave dispersion) seismic data. To this end, we employed phase equilibrium computations and laboratory-based conductivity data for mantle minerals. Our results suggest the existence of a relatively dry transition zone beneath Europe and a water-enriched transition zone underneath North America and northen Asia.

5.1 Introduction

Constraining the water (hydrogen) distribution in the Earth's interior is a key to understanding the Earth's evolution and dynamics since water has a profound effect on rheological properties and melting relationships (e.g., *Peslier*, 2010; *Karato*, 2010). High-pressure mineral-physics studies have reported that mantle transition zone (MTZ) minerals can store high amounts of water (∼1–3 wt%), whereas much smaller amounts (∼0.1–0.2 wt%) can be stored in upper mantle minerals (e.g., *Bolfan-Casanova*, 2005). Supporting evidence for a relatively dry (∼0.02 wt%) upper mantle and a hydrous (∼1 wt%) MTZ has been provided by the analysis of mantle xenoliths (e.g., *Peslier et al.*, 2010; *Peslier and Bizimis*, 2015) and ringwoodite inclusions found in a natural diamond originated below the lithospheric mantle (*Pearson et al.*, 2014), respectively. However, the present distribution of water in the Earth's interior and the mechanisms for water exchange between different reservoirs remains uncertain (e.g., *Ohtani et al.*, 2004; *Hirschmann*, 2006; *Bolfan-Casanova et al.*, 2006).

Electrical conductivity is a transport property that is highly sensitive to temperature variations and the presence of water and melt (e.g., *Karato*, 2010; *Katsura and Yoshino*, 2015; *Khan*, 2016). In contrast, seismic wave velocities are rather insensitive to water (e.g., *Schulze et al.*, 2018), but highly sensitive to major element chemistry and temperature (e.g., *Karato*, 1995). Therefore, seismic and electromagnetic (EM) sounding methods sensitive to seismic wave velocities and electrical conductivity, respectively, provide complementary information to determine and isolate variations in mantle temperature, major element chemistry, and water content. The joint inversion of multiple data sets (e.g., surface wave dispersion and magnetotelluric data) has become increasingly popular to investigate crustal and lithospheric structure (e.g., *Gallardo and Meju*, 2007; *Fullea et al.*, 2009; *Moorkamp et al.*, 2010; *Afonso et al.*, 2013). However, studies focused on the asthenospheric mantle mainly rely on the analysis of either seismic (*Khan et al.*, 2009; *Ritsema et al.*, 2009a; *Vinnik et al.*, 2009; *Deuss et al.*, 2013) or EM sounding data (e.g., *Tarits et al.*, 2004; *Kelbert et al.*, 2009; *Velímskỳ*, 2010; *Semenov and Kuvshinov*, 2012; *Koyama et al.*, 2014; *Sun et al.*, 2015) alone. One of the main reasons for this is that EM sounding studies are often based on the analysis of either daily (4–24 hours) or long-period (3–100 days) data sensitive to electrical conductivity variations in the depth ranges 200–500 km or 500–1400 km, respectively, due to the complex morphology of the EM sources (cf., *Kuvshinov*, 2008).

A few EM sounding studies have attempted to combine EM responses due to different sources. For instance, *Egbert and Booker* (1992) and *Bahr et al.* (1993) combined signals from magnetospheric and ionospheric origin recorded at land geomagnetic observatories to obtain regional conductivity models of the mantle un-

derneath North America and Europe, respectively. However, these studies rely on simplistic source assumptions, which may result in model biases. Alternatively, *Olsen* (1998) accounted for a more complex source geometry (in the period range 3–720 h) by incorporating estimates of horizontal gradients of horizontal magnetic field. Given that direct measurement of these gradients on a single site is extremely challenging, the author estimated gradients from horizontal magnetic field components measured at an array of nearby observatories, which is only possible for regions with a dense network of geomagnetic observatories (e.g., Europe). More recently, *Grayver et al.* (2017) jointly inverted responses of magnetospheric origin and ocean tidal signals from satellite magnetic field measurements yielding a consistent global conductivity model of the oceanic upper mantle and transition zone.

Here, we perform inversions of daily (6–24 hours) and long period (3–85 days) responses recorded at a series of geomagnetic observatories to infer lateral variations in upper mantle and MTZ water content. We isolate the influence of water on the retrieved conductivity models from thermal effects by imposing prior constraints on mantle temperature and major element chemistry derived from the analysis of short- and long-period seismic data.

5.2 Methods

5.2.1 Multi-source EM global-to-local transfer functions

Signals due to the magnetospheric currents dominate natural geomagnetic variations at periods longer than one day (cf., *Finlay et al.*, 2017; *Olsen and Stolle*, 2017). The source of these signals is often described via a single – first zonal – spherical harmonic, leading to the widely-used local C-response (*Banks*, 1969). This transfer function (TF) relates vertical and horizontal components of the magnetic variations at an observational site. However, it is known that the magnetospheric source has a more complex structure, specially during the main phase of geomagnetic storms (e.g., *Daglis and Kozyra*, 2002; *Olsen and Kuvshinov*, 2004; *Balasis and Egbert*, 2006), thus potentially introducing errors in the estimated responses and subsequently biasing the retrieved conductivity structure (e.g., *Püthe et al.*, 2015b). Furthermore, geomagnetic field variations in the period range between a few hours and one day are dominated by the ionospheric current systems which are characterized by a complex morphology (e.g., *Yamazaki and Maute*, 2017). This complexity invalidates simplistic source models that would allow the use of a TF similar to the C-response. In order to account for complex ionospheric and magnetospheric sources, here we resort to an alternative set of global-to-local transfer functions $T_n^m(\mathbf{r}_a, \omega)$ that relate the vertical component of the time-varying magnetic field $Z(\mathbf{r}_a, \omega)$ at an observation site $\mathbf{r}_a$ to a set of global spherical harmonic (SH) expansion coefficients $\varepsilon_n^m(\omega)$ describing

the source structure (*Püthe et al.*, 2015b)

$$Z(\mathbf{r}_a, \omega) = \sum_{n=1}^{N_\varepsilon} \sum_{m=-n}^{n} \varepsilon_n^m(\omega)\, T_n^m(\mathbf{r}_a, \omega), \tag{5.1}$$

where N_ε is the maximum (cut-off) degree for the external SH coefficients and ω denotes the angular frequency.

The estimation of global-to-local transfer functions is a two step procedure: (i) external spherical harmonic coefficients describing the source are determined from horizontal components of the magnetic field measured at a global net of geomagnetic observatories assuming a priori one-dimensional conductivity model of the Earth and the distribution of oceans (see Appendix A); and (ii) TFs are estimated by relating the vertical component of the magnetic field measured at every site of interest with the source coefficients determined in the previous step. The data consists of hourly mean values of geomagnetic field variations measured at 132 mid-latitude (geomagnetic latitudes between $\pm 6°$ and $\pm 55°$) permanent geomagnetic observatories (see Figure D1) for the years 1998–2018 retrieved from British Geological Survey database (*Macmillan and Olsen*, 2013). After removal of the main field and its secular variations (*Olsen et al.*, 2006), source coefficients and global-to-local transfer functions for the daily and long period bands were determined following the procedures described in *Püthe et al.* (2015b) and *Guzavina et al.* (2019), respectively, using section-averaging (e.g., *Olsen*, 1998) and Huber-weighted robust least-squares methods (e.g., *Aster et al.*, 2005).

5.2.2 Probabilistic inversion

We employ the probabilistic approach of *Tarantola and Valette* (1982) and the Metropolis algorithm (e.g., *Metropolis et al.*, 1953; *Hastings*, 1970) to determine the conductivity structure underneath each station from the EM responses. Building on previous experience (*Munch et al.*, 2018a), we reduce the burn-in stage of the Metropolis algorithm by using a global optimization technique (Covariance Matrix Adaptation Evolution Strategy; *Hansen and Ostermeier*, 2001) to obtain a good initial model for every inversion. The solution of the non-linear inverse problem is then given in terms of the posterior probability distribution

$$\gamma(\mathbf{m}|\mathbf{d}) \propto \exp\left[-\frac{\phi(\mathbf{m}, \mathbf{d})}{2}\right] \exp\left[-\frac{\beta}{p_m} \sum_{i=1}^{M} |\nabla \mathrm{m}_i|^{p_m}\right], \tag{5.2}$$

where $\mathbf{d}$ denotes the observed data and $\mathbf{m} = [\lambda(\sigma_1) \cdots \lambda(\sigma_N)]$ represents the unknown conductivity structure, with $\lambda(\cdot)$ being a log-based transformation ensuring positivity of the argument. The regularization parameter β is determined by means of an L-curve analysis (*Hansen*, 1999) and the scalar p_m is set to 1.5 ($\mathrm{L}_{1.5}$ norm)

which provides a good balance between sharp conductivity contrasts (L_1 norm) and smooth models (L_2 norm) (*Grayver and Kuvshinov*, 2016). The data misfit term is given by

$$\phi(\mathbf{m}, \mathbf{d}) = \sum_{k \in \mathcal{M}} \left(\frac{1}{N_k} \sum_{i=1}^{N_k} \left| w_i^k \left(f_i^k(\mathbf{m}) - d_i^k \right) \right|^2 \right), \tag{5.3}$$

where $\mathcal{M}$ denote a set of methods and w^k, $f^k(\mathbf{m})$, and d^k are corresponding data weights (reciprocal of uncertainties), forward operator, and observed data, respectively. As discussed by *Grayver et al.* (2017), normalizing with the number of actual measurements (N_k) is an important aspect that helps balance contributions of different methods.

5.2.3 Inference of water content from retrieved conductivity profiles

We interpret the obtained conductivity profiles in terms of water content in the upper mantle and transition zone by comparing the retrieved models with laboratory-based conductivity profiles computed using the approach of *Khan* (2016). In order to reduce the trade-off between water content and temperature on the electrical conductivity, we constrain mantle temperature and major element chemistry underneath each geomagnetic observatory by incorporating into the inversion probability density functions independently derived from the inversion of short- (P-to-s receiver functions) and long-period (Rayleigh wave phase velocities) seismic data from a nearby seismic station (*Munch et al.*, 2019). Mantle composition is parameterized in terms of a single variable that represents the amount of basalt in a basalt-harzburgite mixture, with the composition of basalt and harzburgite end-members described using the CFMASNa chemical model system comprising the oxides CaO-MgO-FeO-Al_2O_3-SiO_2-Na_2O. Mantle temperature is described in terms of an adiabat defined by the mantle potential temperature T_p, which represents the temperature the mantle would have at the surface, if it ascended along an adiabat without undergoing melting (*McKenzie and Bickle*, 1988).

The laboratory-based conductivity profiles are computed from mineral phase equilibrium calculations and experimental measurements of mantle mineral conductivities. We employ the Gibbs free-energy minimization strategy of *Connolly* (2009) and a self-consistent thermodynamic formulation of *Stixrude and Lithgow-Bertelloni* (2005b) with parameters given by *Stixrude and Lithgow-Bertelloni* (2011) to predict stable mineralogy (mineral modes) as a function of pressure, temperature, and composition. Several independent measurements of the electrical conductivity for major upper mantle and MTZ minerals exist. To minimize subjectivity, we consider two databases built on the measurements of (i) Yoshino, Katsura, and coworkers (referred to as YK) and (ii) Karato, Dai, and coworkers (referred to as KD). Table 5.1 provides the list of data sources used to build YK and KD databases.

The laboratory-measured databases account for the effect of water content on the following hydrous minerals: olivine, orthopyroxene, clinopyroxene, wadsleyite, ringwoodite, and garnet (only KD database). Building on previous experience (e.g., *Khan*, 2016), we parameterize the water content of the mantle in terms of the water contents in olivine (upper mantle) and wadsleyite (transition zone). Water contents in orthopyroxene, clinopyroxene, and ringwoodite are estimated using the water partition coefficients based on measurements from *Inoue et al.* (2010) and *Ferot and Bolfan-Casanova* (2012). Water content in garnet (only relevant for KD database) is estimated using the water partition coefficients derived by *Mookherjee and Karato* (2010).

Mineral	YK database	KD database
Olivine	*Yoshino and Katsura* (2009)	*Wang et al.* (2006)
	Yoshino et al. (2012)	*Karato* (2010)
Orthopyroxene	*Zhang et al.* (2012)	*Dai and Karato* (2009)
Clinopyroxene	*Zhao and Yoshino* (2016)	*Xu et al.* (2000)
Akimotoite	*Katsura et al.* (2007)	*Xu et al.* (2000)
Garnet	*Yoshino et al.* (2008b)	*Karato* (2010)
Wadsleyite	*Yoshino and Katsura* (2012)	*Dai and Karato* (2009)
Ringwoodite	*Yoshino et al.* (2008a)	*Huang et al.* (2005)
	Yoshino et al. (2012)	
	Yoshino and Katsura (2009)	
Ferropericlase	*Yoshino et al.* (2011)	*Xu et al.* (2000)
Bridgmanite	*Yoshino et al.* (2016)	*Xu et al.* (2000)
Ca-perovskite	*Xu et al.* (2000)	*Xu et al.* (2000)

Table 5.1: List of studies by Yoshino, Katsura, and coworkers (YK database) and Karato, Dai, and coworkers (KD database) from which the laboratory-based conductivity databases were compiled.

5.3 Results

5.3.1 Observatory transfer functions

We estimated global-to-local magnetospheric transfer functions in the period range 3–85 days from 20 years (1998–2018) of ground-based observatory data. In order to better account for the complexity of the source, magnetospheric time series were parametrized in terms of 13 spherical harmonic coefficients (ε_1^0,ε_1^1,ε_1^{-1},ε_2^0, ε_2^1,ε_2^{-1},ε_2^2,ε_2^{-2},ε_3^2,ε_3^{-2},ε_4^0,ε_4^1, and ε_4^{-1}). The choice of source coefficients was done considering the trade-off between the coefficient of determination (i.e., measure of how well a proposed source geometry predicts the observed time series; see Figure D2) and the number of input source terms, which limits the maximum period for which multi-variate transfer functions can be estimated (*Püthe and Kuvshinov*, 2014). The estimation of source coefficients requires the assumption of a prior conductivity model to separate the external (inducing) from internal (induced) contributions in

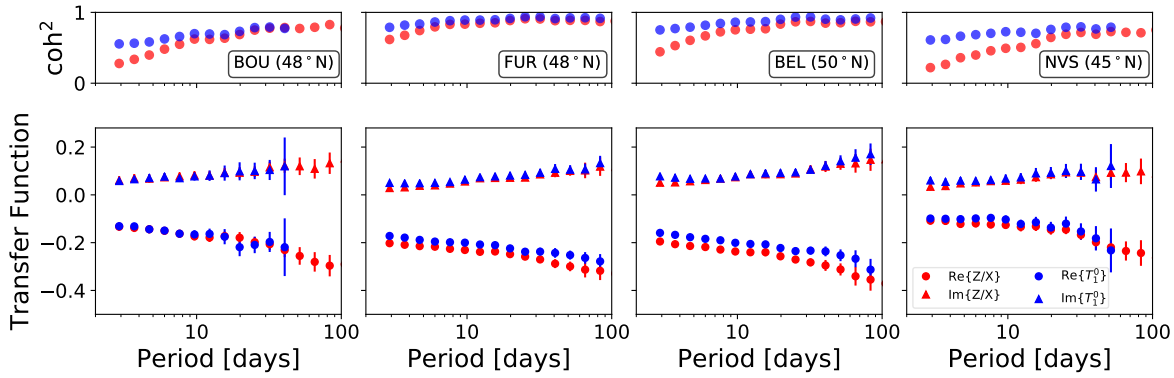

Figure 5.1: Real (negative) and imaginary (positive) parts of the experimental global-to-local (blue) transfer functions (bottom row) and squared coherencies coh^2 (top row) estimated in this study for Boulder (BOU), Fürstenfeldbruck (FUR), Belsk (BEL), and Novosibirsk (NVS) geomagnetic observatories. Error bars indicate uncertainties of the experimental transfer functions. For comparison, transfer functions obtained for a case when the source is described by single first zonal spherical harmonic (Z/H method; *Banks*, 1969) are shown in red.

the measured EM variations (see Appendix D). We find that differences on the long-period transfer functions introduced by the choice of a prior conductivity model are within observed uncertainties (see Figure D3). All source terms were used to estimate global-to-local transfer functions T_n^m in frequency domain, but only T_1^0 was considered in the inversion to retrieve the conductivity structure underneath each station because this transfer function is most sensitive to the radial structure of the Earth (*Kuvshinov*, 2008). The daily TFs were estimated at periods 6, 8, 12, and 24 hours following the procedure presented by *Guzavina et al.* (2019) using magnetically quiet equinoctial days.

Figure 5.1 shows estimated long-period responses, their uncertainties, and squared coherencies (coh^2) for four observatories: Boulder (BOU, USA), Fürstenfeldbruck (FUR, Germany), Belsk (BEL, Poland), and Novosibirsk (NVS, Russia). Compared to transfer functions estimated assuming that the source is described by a single first zonal spherical harmonic (Z/H method; *Banks*, 1969), we observe a substantial increase in coherency, especially at periods <10 days and geomagnetic latitudes >40°. The incorporation of additional source terms increases the coherency and hence, decreases the bias of the responses that could result from correlated noise and spatial aliasing (*Olsen*, 1998). Furthermore, we observe that simplistic source models introduce a systematic shift in the real part of the transfer functions which would bias the inversion towards more resistive models. Interestingly, a similar effect was also observed in transfer functions estimated from satellite data (e.g., *Grayver et al.*, 2017).

Code	**Acronym**	**Name**	**Lat.** [°]	**Lon.** [°]
G1	ASP	Alice Springs	-23.62	133.88
G2	BDV	Budkov	48.89	14.02
G3	BEL	Belsk	51.65	20.8
G4	BFO	Black Forest	48.14	8.32
G5	BMT	Beijing Ming Tombs	40.11	116.2
G6	BOU	Boulder	39.94	-105.23
G7	CLF	Chambon la Foret	47.83	2.27
G8	DOU	Dourbes	49.91	4.6
G9	IRT	Irkutsk	51.98	104.45
G10	KIV	Kiev	50.53	30.3
G11	LZH	Lanzhou	35.9	103.85
G12	MOS	Moscow	55.29	37.32
G13	NGK	Niemegk	51.88	12.68
G14	NVS	Novosibirsk	54.67	83.23
G15	PAG	Panagjurishte	42.33	24.18
G16	QIX	Qianling	34.37	108.2
G17	SPT	San Pablo-Toledo	39.36	-4.35
G18	SUA	Surlari	44.49	26.25
G19	TAM	Tamanrasset	22.66	5.53
G20	TUC	Tucson	31.99	-110.73
S1	BRVK	Borovoye	53.058	70.283
S2	KIEV	Kiev	50.701	29.224
S3	RSSD	Black Hills	44.121	-104.036
S4	RUE	Ruedersdorf	52.476	13.78
S5	TIRR	Tirgusor	44.458	28.413
S6	TLY	Talaya	51.681	103.644
S7	WRAB	Tennant Creek	-19.934	134.36

Table 5.2: Summary of geomagnetic observatories (G) and seismic stations (S) codes, acronyms, names, geographic latitudes and longitudes.

5.3.2 Recovered conductivity models

The subsurface was parametrized in terms of 25 layers ranging in thickness from 50 km in the upper mantle and MTZ to 400 km at the core-mantle boundary with a fixed core ($\sigma = 10^5$ S/m). The estimated transfer functions were individually inverted to determine the most probable set of conductivities underneath 20 inland geomagnetic observatories (see Figure 5.2a), where the transfer functions can be computed with low computation cost using analytical solutions for radial 1D Earth models. Coastal and island geomagnetic observatories have been excluded from this analysis because calculation of synthetic transfer functions for these location requires the use of 3D solvers to account for ocean induction effects (e.g., *Kuvshinov et al.*, 2002) making Markov chain Monte Carlo (e.g., *Mosegaard and Tarantola*, 1995) methods prohibitive.

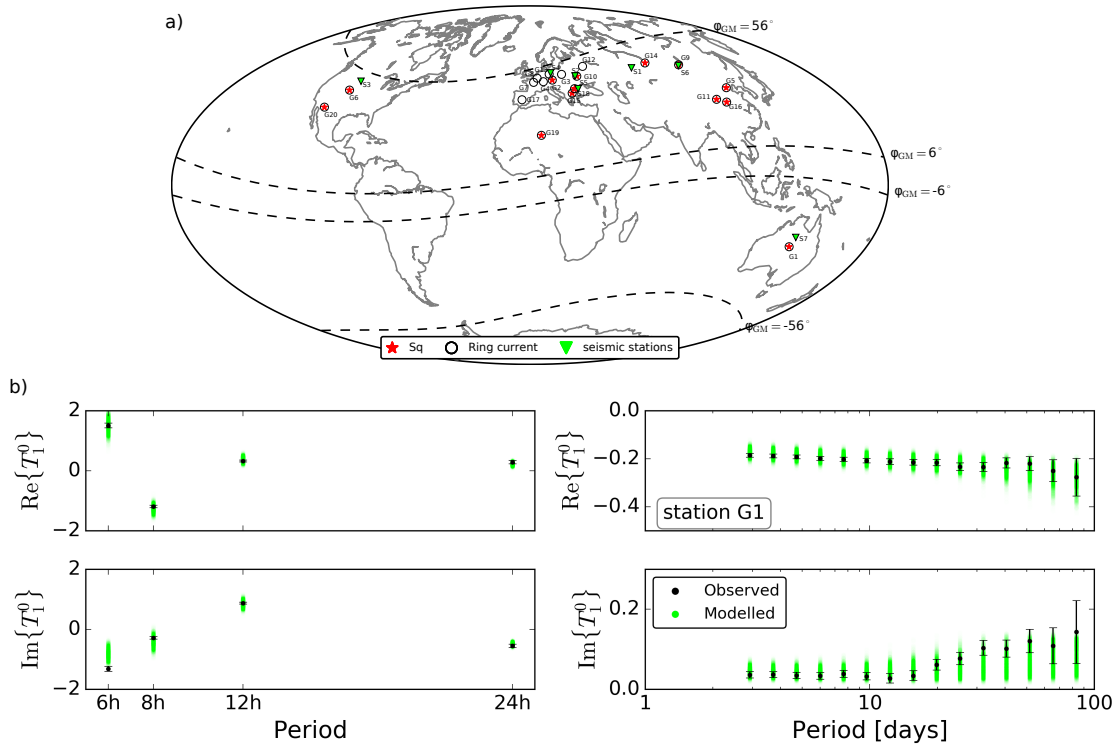

Figure 5.2: (a) Geographic location of mid-latitude observatories (geomagnetic latitudes between ±6° and ±55°) used in this study. Red stars and black circles denote stations at which the observed daily or/and long-period transfer functions, respectively, are successfully fit in the inversion. Green triangles indicate seismic stations for which constraints on mantle temperature and composition were derived by *Munch et al.* (2019) from analysis of short- and long-period seismic data. Station codes are defined in Table 5.2. (b) Real (top row) and imaginary (bottom row) parts of observed (black) and modelled (green) daily (left panel) and long-period (right panel) transfer functions for the most probably conductivity models retrieved from the joint inversion of daily and long-period TFs at Alice Springs geomagnetic observatory (G1). Uncertainties of the observed transfer functions are indicated by the error bars. Data fit for all stations are summarized in Figures D4–D6

We succeed at explaining the observed daily and long-period EM variations, shown in Figure 5.2b for a single station (Alice Spring in Australia), for 13 geomagnetic observatories (indicated in Figure 5.2a by red stars surrounded by black circles). However, we find a cluster of 7 stations located in Europe (black circles in Figure 5.2a) for which the fit of daily transfer functions is unsatisfactory under the 1-D assumption. One can speculate that this reflects: 1) the presence of anomalously shallow structure underneath central Europe and the Mediterranean linked to the subduction and ponding of slabs in the MTZ as suggested by seismic tomography (e.g., *Zhu et al.*, 2015; *Cottaar and Deuss*, 2016); or 2) artifacts due to the presence of noise (e.g., signals due to polar eletrojet currents) which is not accounted for in the presently used source parameterization.

Figures 5.3 illustrates the posterior probability distributions sampled when inverting daily and long-period signals separately and jointly at a single station (Alice Spring, Australia), with black indicating most probable and white least probable conductivity models. In agreement with previous studies, long-period signals best constrain the conductivity structure in the depth range between 400 and 1400 km (see Figure 5.3b) (e.g., *Khan et al.*, 2011b; *Munch et al.*, 2018a), while daily variations provide information on the conductivity structure between 200 and 500 km depth (see Figure 5.3a) (e.g., *Koch and Kuvshinov*, 2013). The models obtained from the joint inversion of daily and long-period signals (see Figure 5.3c) manage to resolve the conductivity structure in the upper mantle (300–400 km depth), MTZ (400–660 km depth), and the uppermost lower mantle (660–1300 km depth).

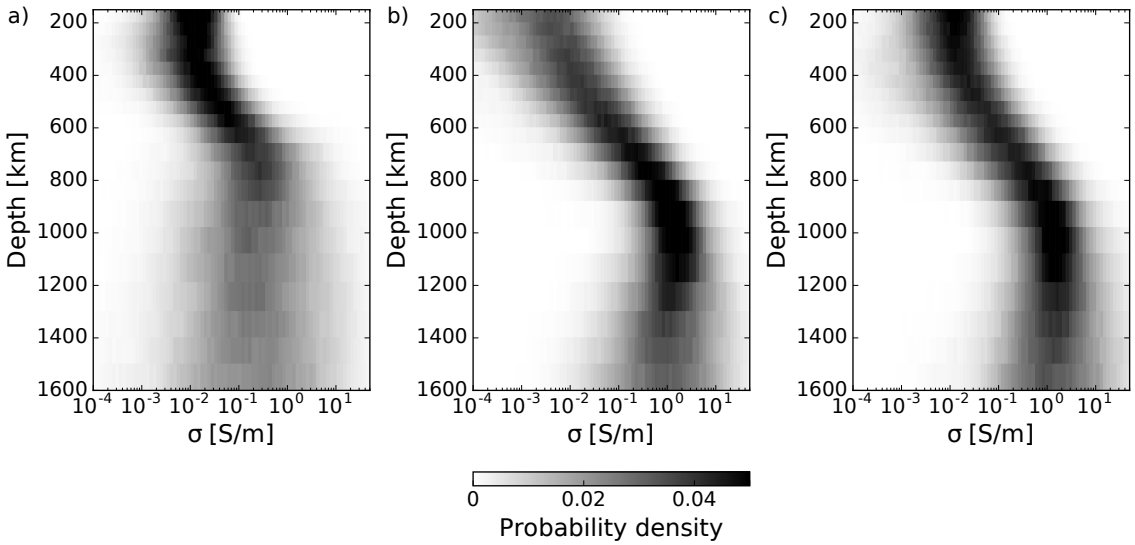

Figure 5.3: Sampled probability distributions for Alice Springs (G1) geomagnetic observatory obtained from the inversion of (a) daily transfer functions (TFs), (b) long-period TFs, and (c) daily and long-period TFs. The posterior probability distribution was determined by computing a histogram of inferred conductivities for each layer assuming a bin-size of 0.05 on the log scale. Dark regions indicate high probability.

5.3.3 Constraints on upper mantle and transition zone water content

We employed the Metropolis algorithm to determine the range of water contents in olivine and wadsleyite that best explain the inverted conductivity profiles between 300 and 1200 km depth. Conductivity models were compared using a L_2 norm misfit function. Figure 5.4 summarizes the conductivity models obtained from the joint inversion of long-period and daily signals (black) and best-fitting laboratory-based conductivity profiles (green) for 8 geomagnetic observatories. The choice of observatories relies on the fact that short- and long-period seismic data recorded at nearby stations (indicated by triangles in Figure 5.2) were found to be well explained by a compositionally uniform and adiabatic mantle (*Munch et al.*, 2019). We find an overall agreement between the inverted conductivity models and laboratory-based conductivity profiles particularly in the upper mantle and MTZ. Laboratory-based conductivity profiles implicitly incorporate discontinuities across the major phase transitions (olivine → wadsleyite, wadsleyite → ringwoodite, and ringwoodite → bridgmanite+ferropericlase), whereas the conductivity models retrieved from the inversion of observed EM responses are characterized by smooth conductivity profiles down to depths of ∼1000 km. Furthermore, we observe that laboratory-based conductivity profiles are systematically more conductive in the lower mantle (800–1200 km depth) than the conductivity models derived from the observed data. This difference might reflect that 1) inversion of seismic data tends to overestimate mantle temperatures; or 2) the laboratory-based conductivity databases here considered tend to overestimate the electrical conductivity of lower mantle minerals.

Sampled water contents in the upper mantle and MTZ minerals olivine (C_w^{ol}) and wadsleyite (C_w^{wad}) obtained using YK and KD databases are shown in Figure 5.5. As discussed by *Khan and Shankland* (2012), for a given water content, KD generally predicts higher conductivities compared to the YK database. As a result, YK database generally leads to significantly more hydrated upper mantle and MTZ estimates. In particular, the use of YK database results in anomalously high water contents (C_w^{ol}∼0.3 wt% and C_w^{wad}∼1.9 wt%) underneath stations located in northern Asia (NVS and IRT). These estimates significantly exceed the experimentally-determined water storage capacity of mantle minerals (e.g., *Hirschmann et al.*, 2005; *Litasov et al.*, 2011) which would result in the accumulation of partial melt atop the MTZ (*Bercovici and Karato*, 2003). However, no evidence for the existence of a melt layer (i.e., low shear-wave velocity anomaly) is observed in the seismic data and hence, further analysis are focused on estimates derived from KD database.

In agreement with previous studies (e.g., *Karato*, 2010; *Fullea et al.*, 2011; *Jones et al.*, 2012; *Khan and Shankland*, 2012), our results indicate a relatively dry upper mantle (C_w^{ol}<0.02 wt%) underneath all stations, whereas significat lateral variability in MTZ water content is observed. We find relatively low MTZ water contents (C_w^{wad} <0.05 wt%) in Australia (ASP) and Europe (BDV, PAG, SUA, and KIV),

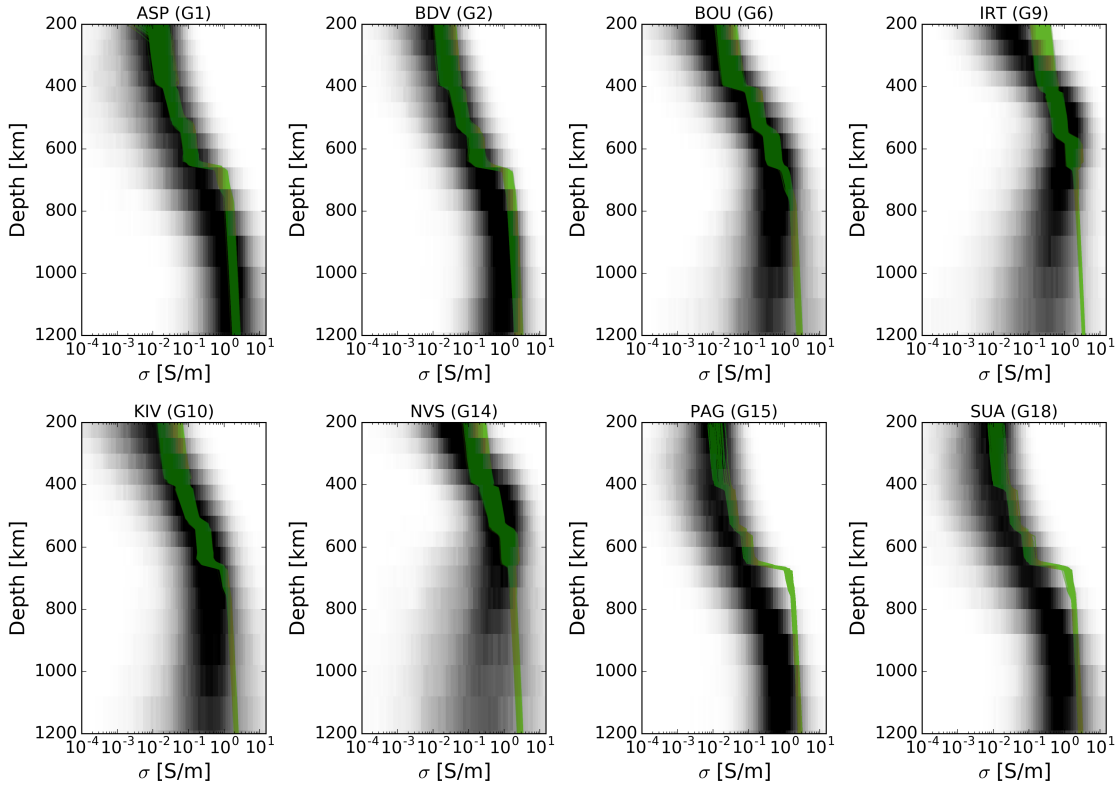

Figure 5.4: Sampled electrical conductivity profiles (σ) retrieved from the joint inversion of daily and long-period transfer functions (black) and best-fitting laboratory-based conductivity profiles (green) for KD database. Geographic location of each geomagnetic observatory are shown in Figure 5.2 and stations acronym are defined in Table 5.2. Best-fitting laboraty-based conductivity profiles obtained using YK database are shown in Figure D7.

whereas moderate (C_w^{wad}~0.15 wt%) and high water contents (C_w^{wad}~0.3 wt%) are required to explain the inverted conductivity profiles in Asia (IRT and NVS) and North America (BOU), respectively. A dry MTZ below Europe has already been suggested by *Utada et al.* (2009) from the joint analysis of seismic and electromagnetic models. In agreement with MTZ water contents experimentally determined by *Freitas et al.* (2017), our estimates suggest that the near-water saturated conditions implied by hydrous ringwoodite inclusions found in a natural diamond (*Pearson et al.*, 2014) are not representative of the whole MTZ.

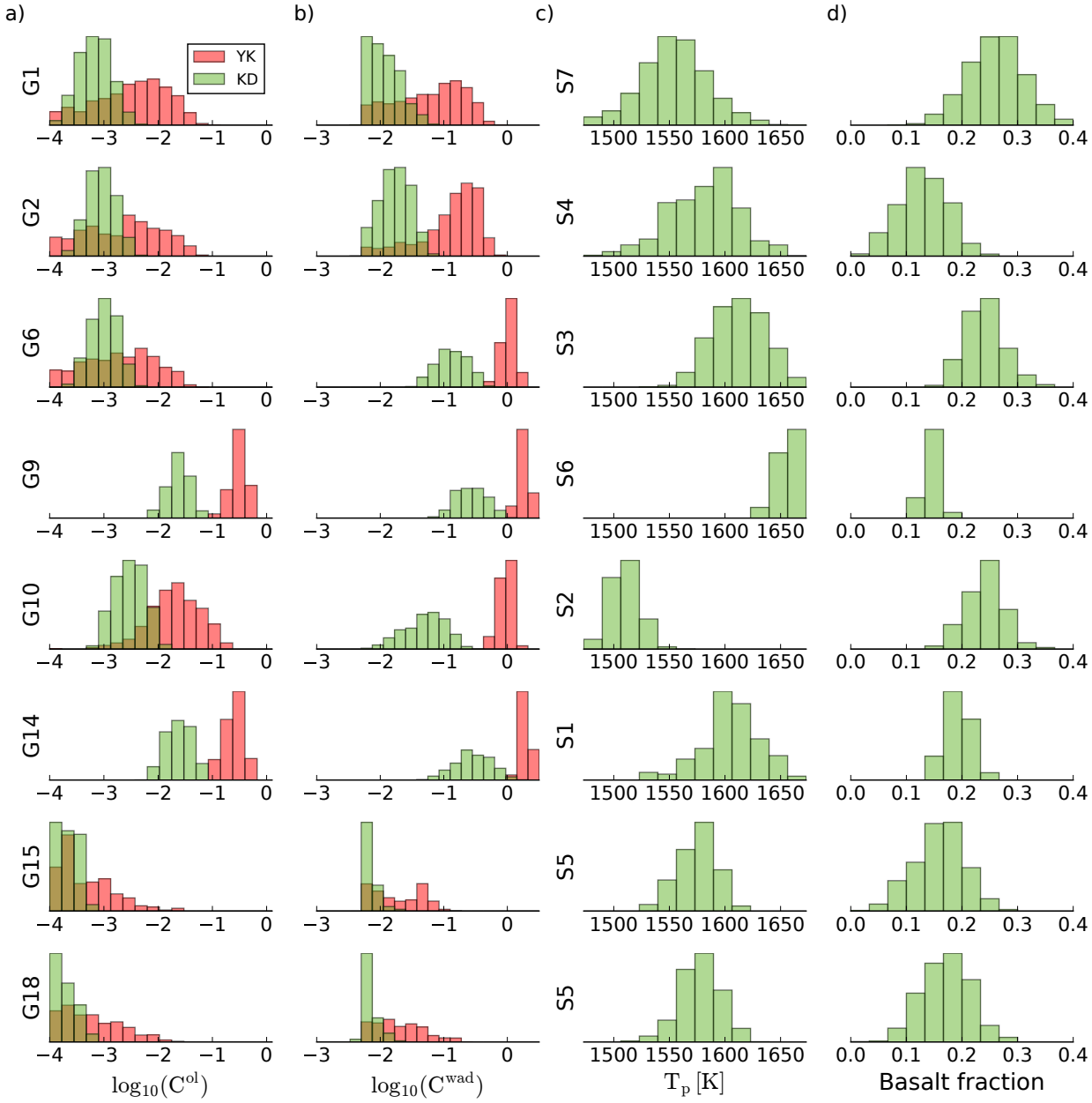

Figure 5.5: Sampled water content in (a) olivine and (b) wadsleyite retrieved using Yoshino-Katsura (YK) and Karato-Dai (KD) electrical conductivity databases. Water contents are given in terms of $C^x = C^x_w/C^x_w$, where x denotes either of the minerals, C^x_w is in wt%, and $C^0_w = 1\,\text{wt\%}$. Constraints on the probability distribution of (c) mantle potential temperature (T_p) and (d) composition (basalt fraction) were obtained from the inversion of P–to–s receiver functions and Rayleigh wave phase velocities (*Munch et al.*, 2019). Station codes are defined in Table 5.2.

5.4 Conclusions

In this study, we combined EM responses in a wide period band to infer the electrical conductivity structure underneath a set of inland geomagnetic observatories, accounting for complex spatial structure of the magnetospheric and ionospheric sources by means of a new method introduced by *Püthe et al.* (2015b). We found that simplistic source models can introduce significant errors on the estimated transfer

functions and bias the inferred conductivity models. Furthermore, the incorporation of daily-band responses (6–24 h) into the inversion leads to an improved model resolution, especially in the upper mantle and transition zone.

We coupled seismic and electromagnetic data to map lateral variations in upper mantle and transition zone water (hydrogen) content. This was achieved by introducing constraints on mantle temperature and composition derived from the inversion of short- and long-period seismic data for the interpretation of the inverted conductivity models through comparison with laboratory-based conductivity profiles. Our findings suggest the existence of a relatively dry transition zone beneath Europe (C_w^{wad} <0.05 wt%) and a water-enriched (C_w^{wad}∼0.3 wt%) transition zone underneath North America and northern Asia.

Chapter 6

Conclusions and outlook

Resolving the structure of the Earth's interior is one of the most challenging tasks in modern Geophysics. In these studies, we aimed at mapping lateral variations in mantle temperature, composition, and water (hydrogen) content mainly underneath continental regions. This was achieved by combining the geophysical inversion of seismic and electromagnetic (EM) sounding data with mineral phase equilibria calculations and laboratory-measured electrical conductivity of mantle minerals.

First, we focused on the analysis of P–to–s conversions in the form of receiver functions (RF) waveforms. This required the development a new methodology to stochastically invert RF waveforms to infer variations in mantle temperature and composition. During this process, we found that: 1) the slowness distribution recorded at each station must be precisely replicated in order to accurately model amplitudes; and 2) identical methods should be applied to both observed and synthetic seismograms during the inversion stage. As discussed in Section 2.7, our methodology relies on waveform modeling in radially stratified isotropically layered models. Hence, this approach is unable to account for material anisotropy and diffraction effects related to three-dimensional mantle structure. In order to account for these effects, wave propagation simulations based on more advanced waveform modeling schemes should be considered (e.g., *Monteiller et al.*, 2012; *Nissen-Meyer et al.*, 2014). Furthermore, future work should be focused on incorporating additional seismic observables such as 1) P–to–s RF waveforms in multiple frequency bands (*Schmandt et al.*, 2011); 2) variations in amplitude as a function of slowness (move-out); and 3) s–to–p RFs (e.g., *Yuan et al.*, 2006).

Second, we investigated whether compositional mantle stratification is required to jointly explain P-to-s receiver functions and Rayleigh surface wave dispersion data sensitive to upper mantle and transition zone beneath a number of different tectonic settings. To this end, we built a new global high-quality dataset of RF waveforms from an initial pool of 151 stations enhanced with the most recent available global dataset of Rayleigh wave phase velocity dispersion for the fundamental mode and up to fifth overtone. Our results can be summarized as:

1. a compositional boundary is not required to explain the seismic data underneath stable continental regions;

2. compositional layering can explain part of the complexity present in the data recorded near subduction zones and volcanically active regions;

3. cratonic regions are characterized by low mantle potential temperatures and significant lateral variability in mantle composition;

4. chemical equilibration seems more difficult to achieve beneath stable cratonic regions suggesting that the lithologic integrity of the subducted basalt and harzburgite is better preserved for geologically significant times underneath these regions;

5. the mantle is neither completely chemically equilibrated nor fully mechanically mixed, but appears to be best described as an admixture of the two.

These findings strengthen the case for a mantle that convects, temporally as spatially, in an intermittent fashion with cold and/or basaltic material accumulating above 660 km depth until huge avalanches precipitate it into the lower mantle, "flushing" the local upper mantle through broad cylindrical downwellings to the core-mantle boundary (e.g., *Tackley*, 2008; *Nakagawa et al.*, 2010). In this light, future work should be focused on extending the thermo-chemical parameterization (uniform adiabatic mantle) used in the inversion stage to encompass deviations in mantle temperature and composition as the ones predicted by mantle convection simulations near subduction zones and other more complex geological settings.

Additionally, we inverted EM sounding data in the period range 3–85 days to infer the 1D conductivity structure beneath a set of worldwide distributed geomagnetic observatories. The retrieved conductivity profiles are best constrained between 400–1400 km depth. To improve the model resolution in the upper mantle, we incorporated EM sounding data from ionospheric origin (period range 6–24 hours) into the inversion for a set of inland geomagnetic observatories. As expected, the incorporation of EM variations in the daily-band leads to a significant improvement in model resolution in the upper mantle and transition zone. Future work should be focused on improving model resolution in the crust and lithospheric mantle by introducing magnetotelluric data (e.g., *Simpson and Bahr*, 2005) into the inversion. We interpreted the inverted conductivity profiles in terms of variations in upper mantle and transition zone water content using constraints on mantle temperature and composition derived from the analysis of seismic data. Our results suggest the existence of a relatively dry transition zone beneath Europe and a water-enriched transition zone underneath North America and Asia, while the upper mantle underneath al stations is relatively dry. Despite being insightful, this analysis is merely

a proof of concept and hence, should be extended to coastal and island-based geomagnetic observatories to improve lateral resolution. As discussed by *Kuvshinov et al.* (2002), transfer functions in these regions are known to be strongly influenced by the presence of the conductive oceans, which can significantly bias the inversion results. As the approach used in Chapter 4 to correct observed transfer functions in the period range 3–85 days cannot be extended to transfer functions from ionospheric origin, the use of Markov chain Monte Carlo methods will become infeasible. Therefore, the use of new methodologies to estimate model uncertainties should be explored.

Finally, we would like to stress that the thermodynamic model and electrical conductivity databases here considered have limitations. In particular, the thermodynamic model of *Stixrude and Lithgow-Bertelloni* (2005b, 2011) precludes consideration of redox effects (e.g., *Cline II et al.*, 2018) as well as minor phases and components such as H_2O and melt due to lack of thermodynamic data. Future work should aim at 1) extending the thermodynamic database so as to model effects related to oxygen fugacity, water, and presence of melt; and 2) refining the laboratory-based mineral conductivity databases particularly for all major hydrous upper mantle, transition zone, and lower-mantle minerals. The largest remaining uncertainty is the degree to which hydrogen affects electrical conductivity in the lower mantle minerals. Determining the influence of hydrogen on electrical conductivity in lower mantle minerals is critical to make progress in understanding the global water circulation.

Appendix A

Introduction

As described in Section 2.3, we computed move-out corrections for the best-ftting and IASP91 velocity models and applied the corresponding corrections to the observed RF waveforms. Figure A1-a shows RF waveforms obtained at Kongsberg (KONO). No signifcant differences are observed in the stacked waveforms. These similarities can be understood by analysing the travel-time of conversions as a function of slowness. As an example, Figure A1-b depicts the travel-time of the P410S conversion computed using IASP91 (red solid line) and the best-ftting velocity models (blue solid line). In order to better compare differences in curvature, IASP91 predictions were shifted by ∼1.5 s (red dashed line) to make estimates from both models coincide at 4.5 s/deg. It is evident from Figure A1-b that the curvature of the travel-times predicted by both models is very similar, particularly for the slowness range 5-7 s/deg where most observations are recorded (see Figure 2.2b). This difference in move-out is not significant given the periods considered in this work (>5 s).

Figure A2 compares synthetic RF waveforms obtained using full waveform modeling technique Instaseis (*Van Driel et al.*, 2015; *Krischer et al.*, 2017) with RF waveforms computed using the reflectivity method (*Fuchs and Müller*, 1971). Overall, agreement between the stacked RF waveforms is good.

Figures A3 and A4 depict variations in phase proportions (modal mineralogy) obtained for each of the thermo-chemical models discussed in Section 4.4 (Figure 5). Figure A3 summarizes variations in phase proportions as a function of basalt fraction (f) for the equilibrium assemblage (EA) and mechanical mixture (MM) model, respectively. Figure A4 depicts changes in modal mineralogy as a function of temperature for both compositional models.

As discussed in Chapter 2, the robustness of the proposed methodology was tested by computing synthetic RF waveforms from an independent velocity model (IASP91 reference model) and subsequently invert it for crustal and mantle param-

eters. Main results are summarized in Figure A5. Panel a) shows sampled marginal probability distributions of mantle thermo-chemical parameters retrieved for the EA and MM mantle models, respectively; panel b) depicts fit between observed (black) and synthetic RF waveforms for the MM (red) and EA (green) models; and panel c) shows sampled S–wave velocity profiles.

Finally, Figure A6 depicts mantle temperature profiles and corresponding shear attenuation (Q_μ) models retrieved for Kongsberg (KONO) and Yakutsk (YAK) using the EA and MM models, respectively.

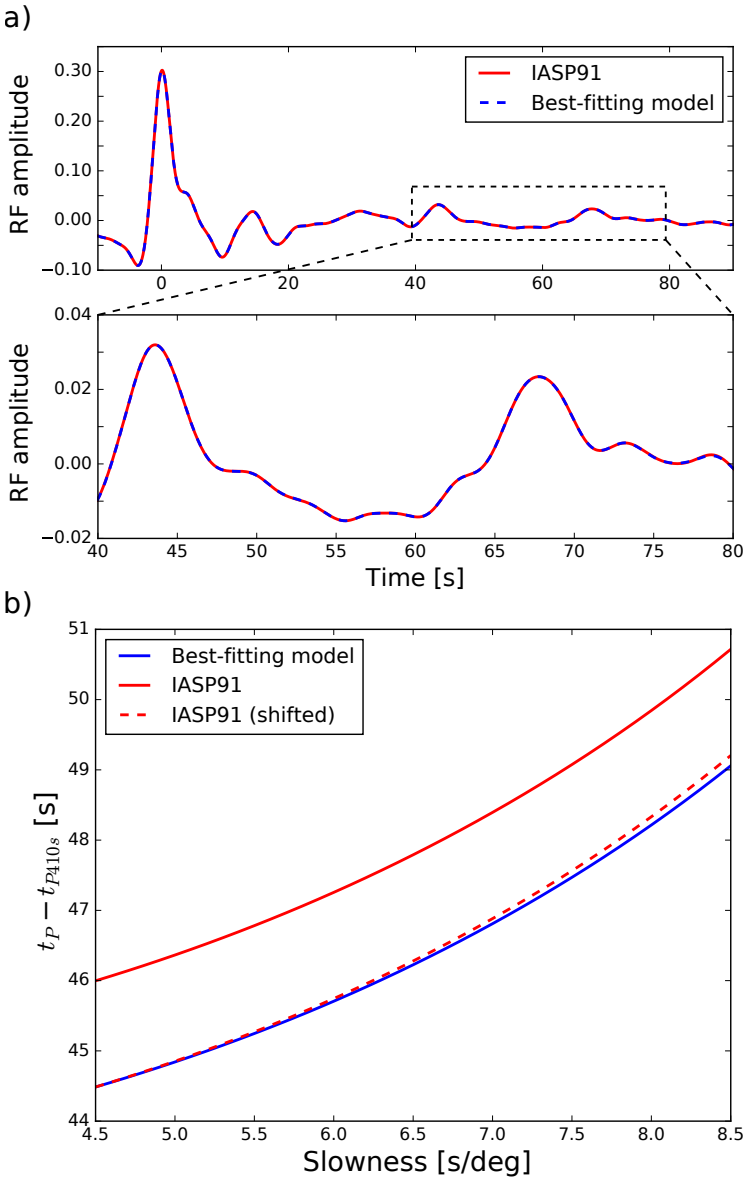

Figure A1: (a) Comparison between stacked receiver function waveforms obtained at KONO by applying move-out corrections computed using the best-fitting (blue) and IASP91 (red) velocity models. (b) Travel-time of P410s conversion at 440 km depth as a function of slowness for IASP91 (red solid line) and best-fitting (blue solid line) velocity models. To better compare differences in curvature, the IASP91 prediction was shifted (red dashed line) so that both models coincide at 4.5 s/deg.

f	$t_{\mathrm{P660s}} - t_{\mathrm{P410s}}$ [s]	
	EA	MM
0	23.70	23.70
0.1	24.20	23.80
0.2	24.75	23.85
0.3	25.10	23.90
0.4	25.55	23.95
0.5	26.30	24.05
0.6	27.10	24.15
0.7	28.30	24.20
0.8	29.55	24.20

Table A1: Differential traveltime between $P_{660}s$ and $P_{410}s$ ($t_{\mathrm{P660s}} - t_{\mathrm{P410s}}$) as a function of basalt fraction (f) for equilibrium assemblage (EA) and mechanical mixture (MM) mantle models. Thermal structure is fixed to a sub-lithospheric adiabatic geotherm defined by the entropy of the lithology at a temperature T_{lit} of 1623 K at the base of a 80 km thick lithosphere. Tabulated values correspond to Figure 2.5i.

T_{lit} [K]	$t_{\mathrm{P660s}} - t_{\mathrm{P410s}}$ [s]	
	EA	MM
1223	27.05	26.55
1273	26.90	26.10
1323	26.60	25.80
1373	26.35	25.50
1423	26.20	25.25
1473	25.95	24.95
1523	25.60	24.55
1573	25.15	24.25
1623	24.80	23.95
1673	24.55	23.60
1723	24.25	23.30
1773	23.95	22.95
1823	23.80	22.65
1873	23.70	22.30
1923	23.70	22.00
1973	24.40	21.55

Table A2: Differential traveltime between $P_{660}s$ and $P_{410}s$ ($t_{\mathrm{P660s}} - t_{\mathrm{P410s}}$) as a function of temperature (T_{lit}) for equilibrium assemblage (EA) and mechanical mixture (MM) mantle models. Composition corresponds to pyrolitic mantle (f=0.2034). Tabulated values correspond to Figure 2.5j.

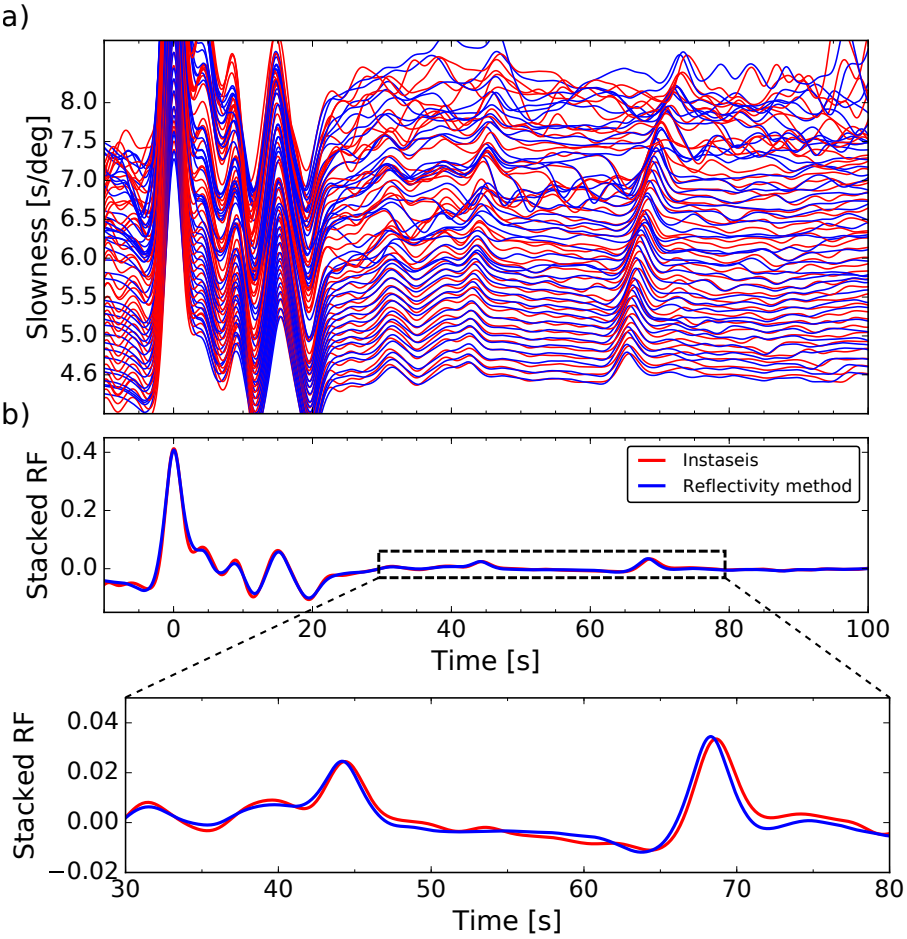

Figure A2: Comparison between synthetic RF waveforms computed using red the full waveform modeling technique Instaseis (red) (*Van Driel et al.*, 2015; *Krischer et al.*, 2017) and the reflectivity method (blue). a) RF waveforms as a function of slowness and b) corresponding stacked waveforms for the IASP91 velocity model.

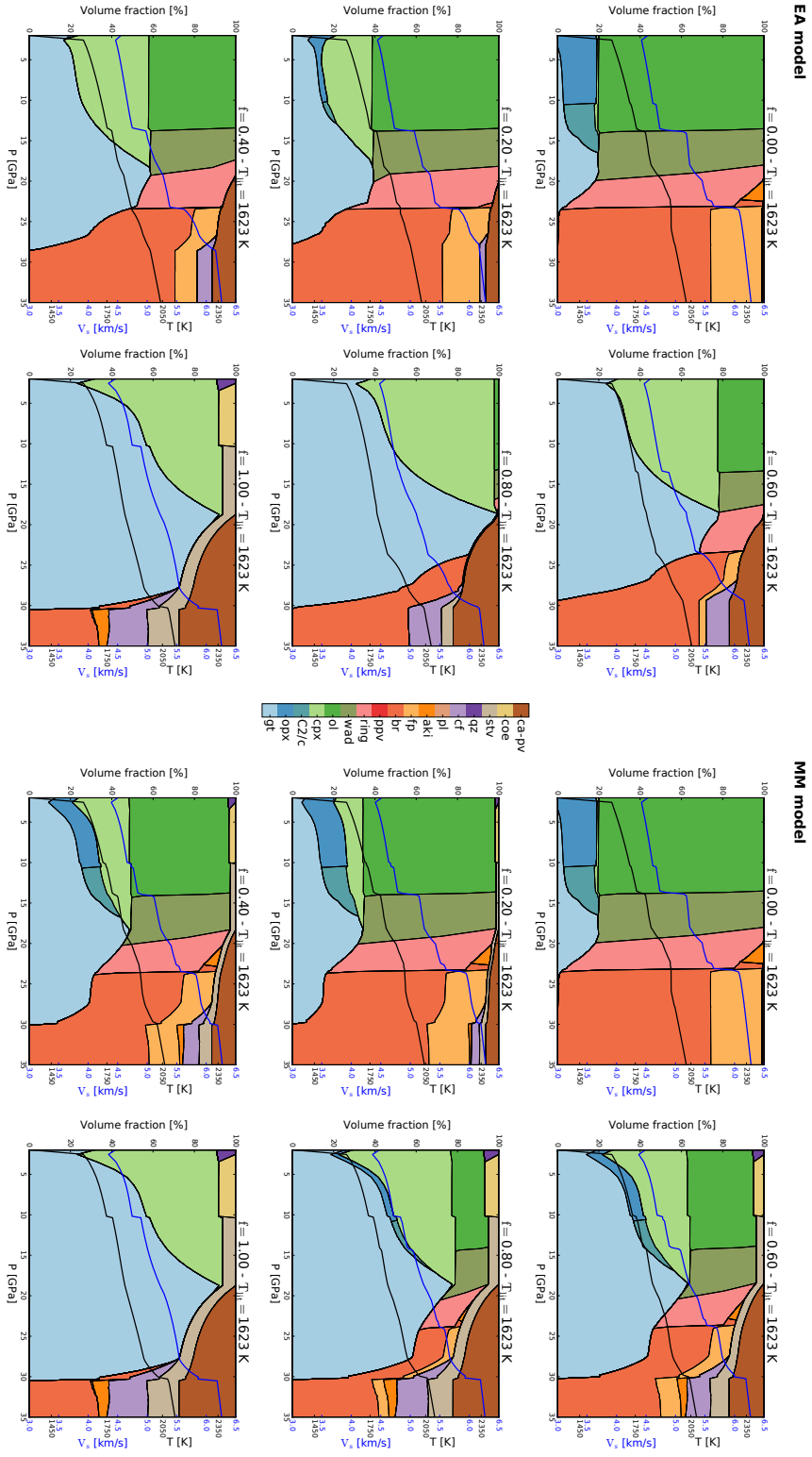

Figure A3: Variations in phase proportions (modal mineralogy) and S–wave velocity (V_s) as a function of basalt fraction f for equilibrium assemblage (EA) and mechanical mixture (MM) mantle models. The adiabatic geotherm (black) is defined by the entropy of the lithology at a temperature T_{lit} of 1623 K at the base of a 80 km thick lithosphere. Phases are: olivine (ol), orthopyroxene (opx), clinopyroxene (cpx), plagioclase (pl), coesite (coe), stishovite (stv), quartz (qz), high-pressure Mg-rich cpx (C2/c), garnet (gt), wadsleyite (wad), ringwoodite (ring), akimotoite (aki), calcium silicate perovskite (ca-pv), ferropericlase (fp), bridgemanite (br; formerly perovskite), post-perovskite (ppv), and calcium ferrite (cf).

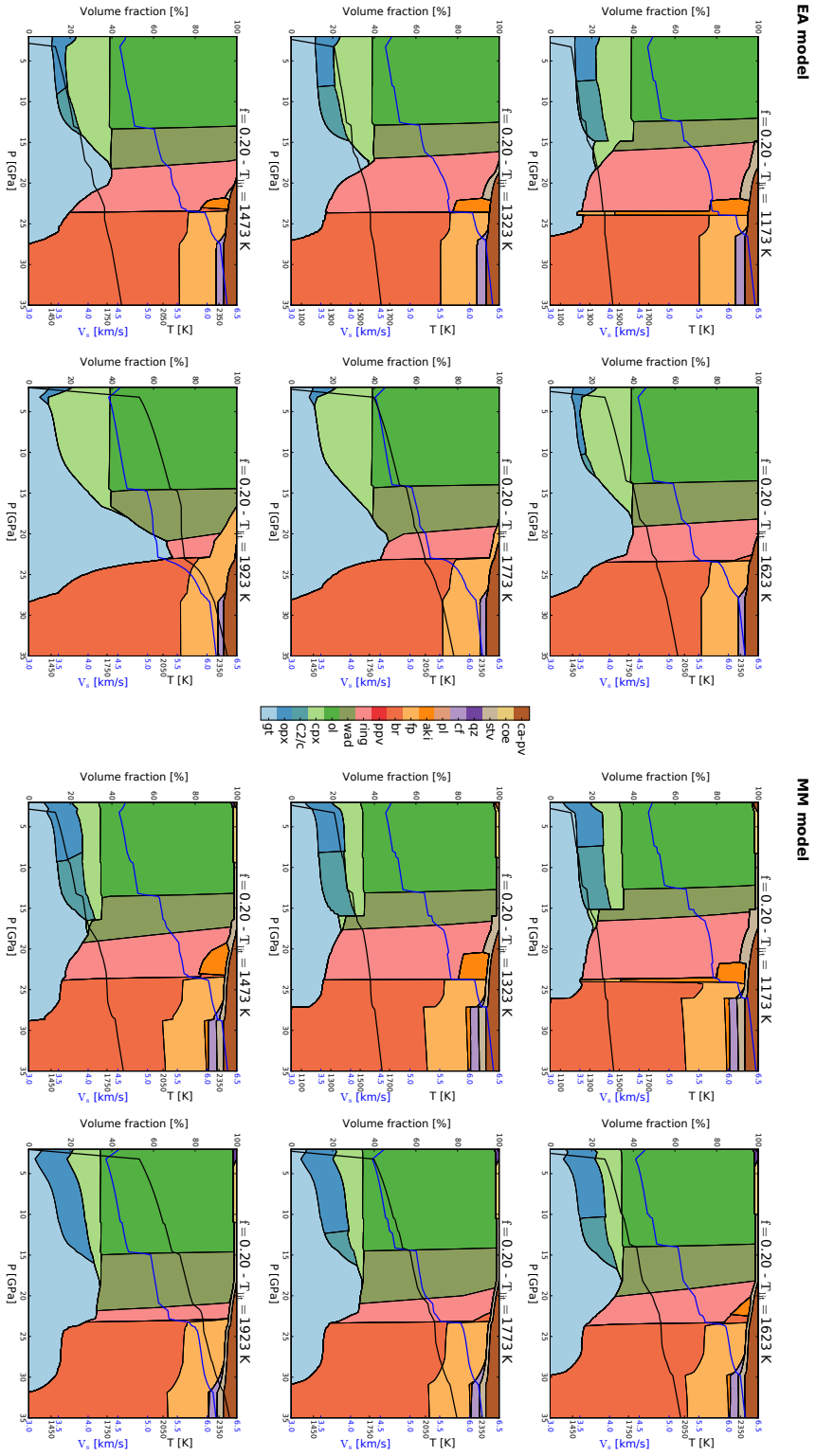

Figure A4: Variations in phase proportions (modal mineralogy) and S–wave velocity (V_s) as a function of temperature T_{lit} for fully-equilibrated (EA) and mechanically- mixed (MM) homogeneous pyrolitic (f=0.2034) mantle models. Phases are: olivine (ol), orthopyroxene (opx), clinopyroxene (cpx), plagioclase (pl), coesite (coe), stishovite (stv), quartz (qz), high-pressure Mg-rich cpx (C2/c), garnet (gt), wadsleyite (wad), ringwoodite (ring), akimotoite (aki), calcium silicate perovskite (ca-pv), ferropericlase (fp), bridgemanite (br; formerly perovskite), post-perovskite (ppv), and calcium ferrite (cf).

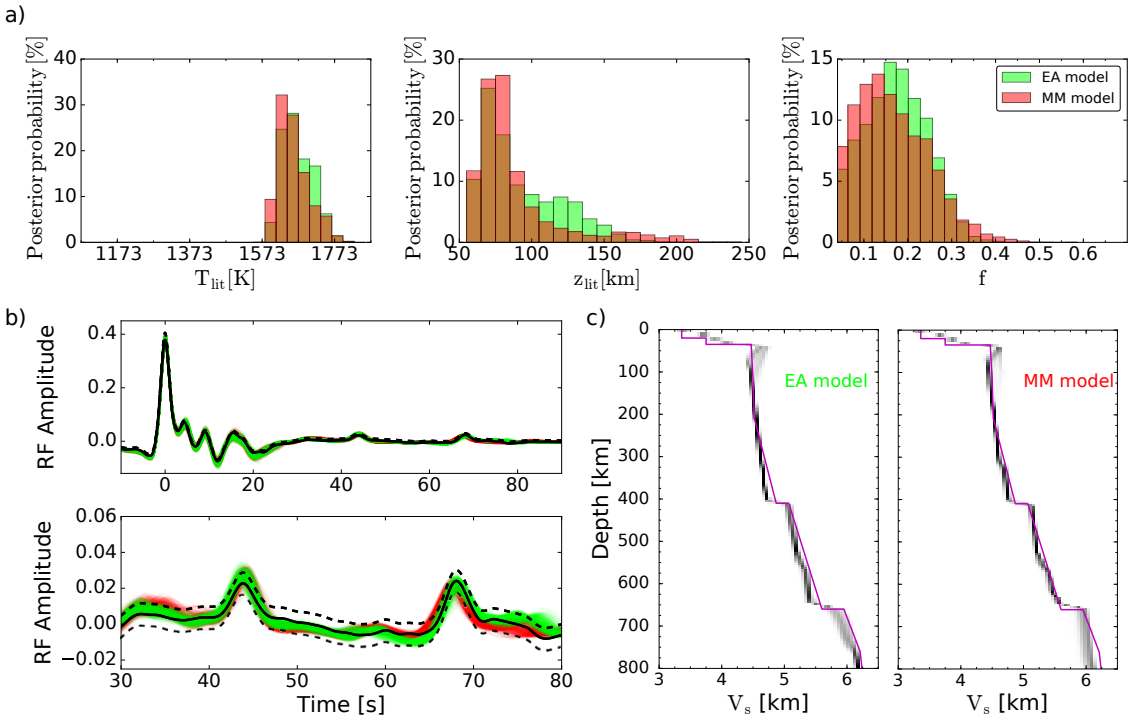

Figure A5: Inversion of synthetic RF waveform for crust and mantle structure. Synthetic RF waveforms were computed using the IASP91 velocity model. Panel a) depicts sampled mantle thermo-chemical parameters for the equilibrium assemblage (EA) and mechanical mixture (MM) mantle models, respectively. Brown-colored binds indicate model parameters for which EA and MM overlap. Panel b) shows fit between observed (black) and synthetic RF waveforms for the MM (red) and EA (green) mantle models. Data uncertainties are indicated by black dashed lines. Panel c) depicts sampled S–wave velocity (V_s) profiles for the EA and MM models with black indicating most probable and white least probable. Magenta curve depicts the IASP91 reference model (true solution).

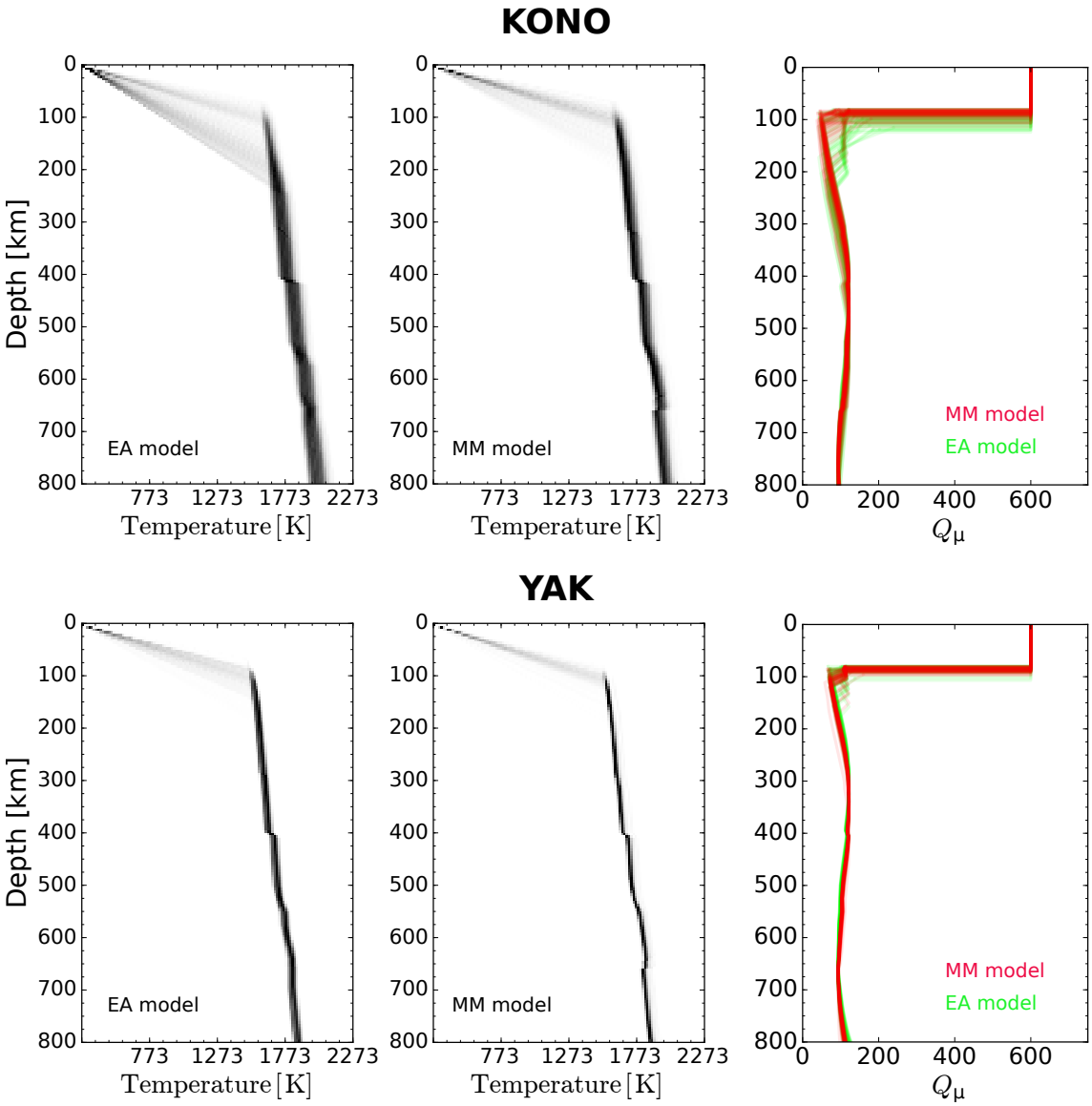

Figure A6: Sampled mantle thermal profiles and corresponding shear attenuation (Q_μ) models retrieved for Kongsberg (KONO) and Yakutsk (YAK) using the equilibrium assemblage (EA) and mechanical mixture (MM) mantle models, respectively. Color coding goes light (least probable) to dark (most probable).

Appendix B

Acronym	Network	Lat. [°]	Lon. [°]	# stacked RF	Data type	Fit quality
AAK	II	42.638	74.494	756	A	A1
ABKT	II	37.93	58.119	575	A	A1
ABPO	II	-19.018	47.229	120	A	A2
ADK	IU	51.882	-176.684	213	B	–
AFI	IU	-13.909	-171.777	92	A	A2
ALE	II	82.503	-62.35	257	A	A1
ANMO	IU	34.946	-106.457	524	B	–
ANTO	IU	39.868	32.793	527	B	–
APE	GE	37.069	25.531	75	B	–
ARU	II	56.43	58.563	716	A	A1
ATD	G	11.531	42.847	347	A	A2
BBSR	IU	32.371	-64.696	84	B	–
BFO	II	48.33	8.33	286	A	A1
BILL	IU	68.065	166.453	823	A	A1
BJT	IC	40.018	116.168	836	A	A2
BORG	II	64.747	-21.327	69	A	A2
BRVK	II	53.058	70.283	837	A	A1
CAN	G	-35.319	148.996	171	A	A2
CART	GE	37.587	-1.001	111	B	–
CASY	IU	-66.279	110.535	449	A	A1
CCD	G	-75.107	123.305	243	A	A2
CCM	IU	38.056	-91.245	270	A	A1
CHTO	IU	18.814	98.944	797	A	A2
CLF	G	48.026	2.26	174	B	–
COCO	II	-12.19	96.835	17	C	–
COLA	IU	64.874	-147.862	800	B	–
COR	IU	44.586	-123.305	173	B	–
COYC	G	-45.573	-72.081	8	C	–
CRZF	G	-46.431	51.855	82	B	–
CSS	GE	34.961	33.331	235	B	–
CTAO	IU	-20.088	146.255	248	A	A2
DAG	GE	76.771	-18.655	275	A	A2
DAV	IU	7.07	125.579	47	C	–
DGAR	II	-7.412	72.453	64	B	–
DRV	G	-66.665	140.002	488	B	–
DSB	GE	53.245	-6.376	59	A	A1
DWPF	IU	28.11	-81.433	119	A	A1

Acronym	Network	Lat. [°]	Lon. [°]	# stacked RF	Data type	Fit quality
ECH	G	48.216	7.159	401	A	A1
EIL	GE	29.67	34.951	705	B	–
EKNA	AF	4.234	9.328	40	C	–
ENH	IC	30.276	109.494	755	A	A2
ERM	II	42.015	143.157	249	B	–
FDF	G	14.735	-61.146	107	B	–
FFC	II	54.725	-101.978	325	A	A1
FURI	IU	8.895	38.68	464	A	A2
GNI	IU	40.148	44.741	723	B	–
GUMO	IU	13.589	144.868	27	C	–
HIA	IC	49.27	119.741	918	A	A1
HLG	GE	54.185	7.884	44	C	–
HNR	IU	-9.439	159.948	141	B	–
HRV	IU	42.506	-71.558	174	B	–
HYB	G	17.41867	78.552	439	A	A1
IBBN	GE	52.306	7.759	95	A	A2
INCN	IU	37.478	126.624	337	B	–
INK	CN	68.307	-133.525	682	A	A1
INU	G	35.35	137.029	93	B	–
ISP	GE	37.843	30.509	270	B	–
JER	GE	31.772	35.197	116	A	A2
JOHN	IU	16.733	-169.529	3	C	–
JTS	II	10.291	-84.953	104	B	–
KAPI	II	-5.014	119.752	404	B	–
KBS	IU	78.915	11.939	311	A	A2
KDAK	II	57.783	-152.584	449	B	–
KEV	IU	69.757	27.004	283	A	A1
KIEV	IU	50.701	29.224	427	A	A1
KIP	IU	21.42	-158.011	86	A	A2
KIV	II	43.955	42.686	910	B	–
KMBO	IU	-1.127	37.253	429	A	A2
KMI	IC	25.123	102.74	828	B	–
KONO	IU	59.649	9.598	290	A	A1
KSDI	GE	33.192	35.659	157	A	A2
KURK	II	50.715	78.62	772	A	A1
KWAJ	II	8.802	167.613	11	C	–
LSA	IC	29.703	91.127	625	B	–
LSZ	IU	-15.278	28.188	291	A	A1
LVZ	II	67.898	34.651	248	A	A1
MA2	IU	59.576	150.77	626	B	–
MAHO	GE	39.896	4.267	66	A	A2
MAKZ	IU	46.808	81.977	507	A	A1
MALT	GE	38.313	38.427	246	B	–
MBAR	II	-0.602	30.738	229	A	A1
MBO	G	14.392	-16.955	153	A	A1
MBWA	IU	-21.159	119.731	163	A	A1
MDJ	IC	44.617	129.591	828	B	–
MELI	GE	35.29	-2.939	29	C	–
MHV	GE	54.96	37.766	133	A	A1
MORC	GE	49.777	17.543	243	A	A2
MPG	G	5.11	-52.644	93	A	A1
MSEY	II	-4.674	55.479	166	A	A2
MSVF	II	-17.745	178.053	69	B	–
MTE	GE	40.4	-7.544	109	A	A2
NIL	II	33.651	73.269	242	A	A2
NWAO	IU	-32.928	117.239	168	A	A1
OTAV	IU	0.238	-78.451	136	B	–
PAB	IU	39.545	-4.35	387	B	–
PALK	II	7.273	80.702	327	B	–

Acronym	Network	Lat. [°]	Lon. [°]	# stacked RF	Data type	Fit quality
PEL	G	-33.144	-70.675	60	B	–
PET	IU	53.023	158.65	554	B	–
PFO	II	33.609	-116.455	505	A	A2
PMG	IU	-9.405	147.16	281	B	–
PMSA	IU	-64.774	-64.049	92	B	–
PSZ	GE	47.918	19.893	222	A	A2
PUL	GE	59.767	30.317	90	A	A1
QIZ	IC	19.029	109.845	323	B	–
RAYN	II	23.523	45.503	380	A	A1
RCBR	IU	-5.827	-35.901	95	A	A1
RGN	GE	54.548	13.321	117	A	A1
RPN	II	-27.127	-109.334	16	C	–
RSSD	IU	44.121	-104.036	408	A	A1
RUE	GE	52.476	13.78	149	A	A1
SBA	IU	-77.849	166.757	500	A	A2
SDV	IU	8.884	-70.634	192	A	A1
SFJD	IU	66.996	-50.621	169	A	A1
SHAI	AF	5.881	0.044	30	C	–
SHEL	II	-15.959	-5.746	62	B	–
SJG	IU	18.109	-66.15	145	B	–
SLBS	IU	23.686	-109.944	113	B	–
SNAA	GE	-71.671	-2.838	366	A	A1
SNZO	IU	-41.309	174.704	125	B	–
SPB	G	-23.593	-47.427	61	B	–
SSB	G	45.279	4.542	411	A	2
SSE	IC	31.095	121.191	382	B	–
SSPA	IU	40.636	-77.888	266	A	A1
SUMG	GE	72.576	-38.454	306	A	A2
SUR	II	-32.38	20.812	81	A	A1
SUW	GE	54.013	23.181	286	A	A1
TAM	G	22.791	5.528	387	A	A2
TARA	IU	1.355	172.923	43	C	–
TATO	IU	24.974	121.497	164	B	–
TAU	II	-42.91	147.32	66	B	–
TEIG	IU	20.226	-88.276	149	A	A2
TIRR	GE	44.458	28.413	268	A	A1
TIXI	IU	71.634	128.867	791	A	A2
TLY	II	51.681	103.644	698	A	A1
TSUM	IU	-19.202	17.584	285	A	A1
TUC	IU	32.31	-110.785	591	A	A2
UGM	GE	-7.913	110.523	80	B	–
ULN	IU	47.865	107.053	767	A	A1
UNM	G	19.33	-99.178	132	B	–
UOSS	II	24.945	56.204	363	A	A2
VSU	GE	58.462	26.735	320	A	A1
WCI	IU	38.229	-86.294	237	A	A1
WHY	CN	60.66	-134.883	570	A	A2
WLF	GE	49.665	6.153	187	B	–
WMQ	IC	43.814	87.705	749	B	–
WRAB	II	-19.934	134.36	196	A	A1
WVT	IU	36.13	-87.83	268	A	A1
XAN	IC	34.031	108.924	722	A	A2
YAK	IU	62.031	129.681	904	A	A1
YKW3	CN	62.562	-114.61	358	A	A1
YSS	IU	46.959	142.76	438	B	–

Table B1: Summary of seismic stations acronyms, network, latitude and longitude, number of stacked receiver function waveforms, data type quality, and fit quality type.

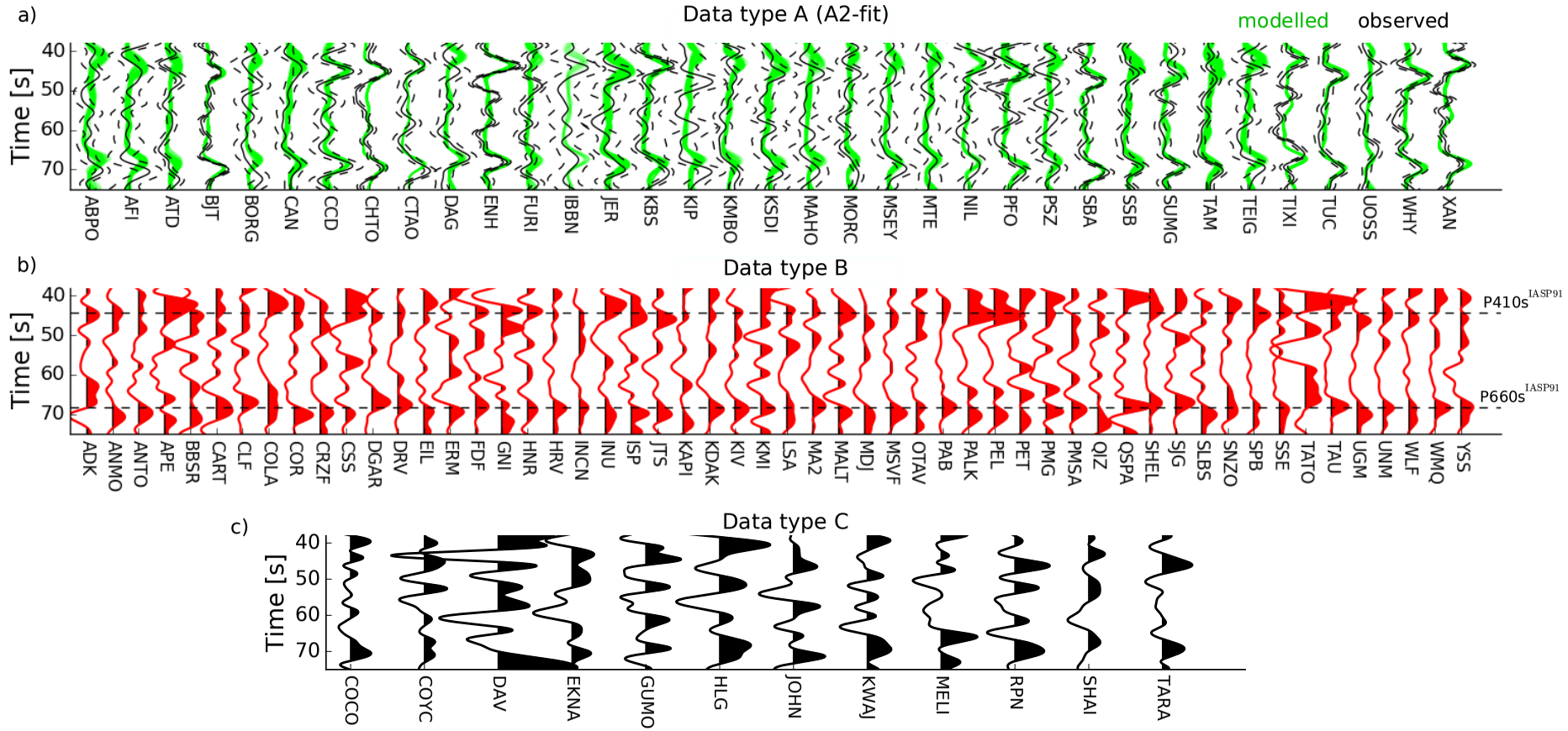

Figure B1: Receiver function (RF) waveforms classified by data quality type (see Table B1). a) Observed (black) and modelled (green) RF waveforms for "A2-fit" (dark green circles in Figure 3.1). b) Observed type B RF waveforms (red circles in Figure 3.1) and theoretical arrival times of P-to-s conversions occuring at the 410–km (P410s) and 660–km (P660s) discontinuities for IASP91 reference model (dashed lines). The signals corresponding to either the P410s or P660s conversions cannot be clearly isolated due to the potential presence of interfering seismic phases or complex three-dimensional structure. c) Observed RF waveforms for type C stations (black circles in Figure 3.1), where only a small number of data could be stacked resulting in highly noisy RF waveforms with no clear P410s and P660s signals.

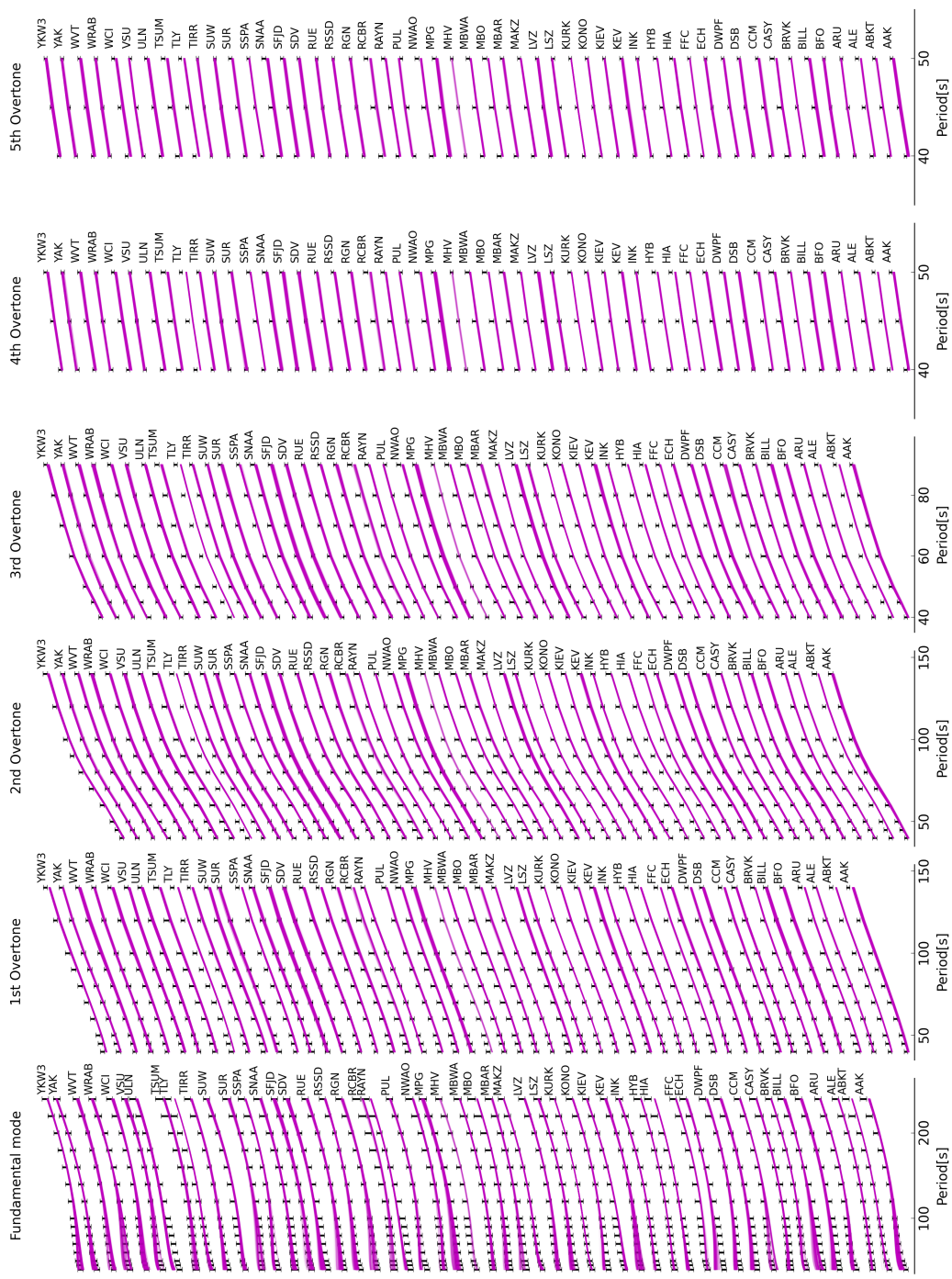

Figure B2: Observed (black) and modelled (magenta) Rayleigh wave fundamental mode and overtones phase velocities for "A1-fit" stations (light green diamonds in Figure 3.1). Despite subtle differences, the proposed models succeed at explaining the observed data within uncertainties (black error bars).

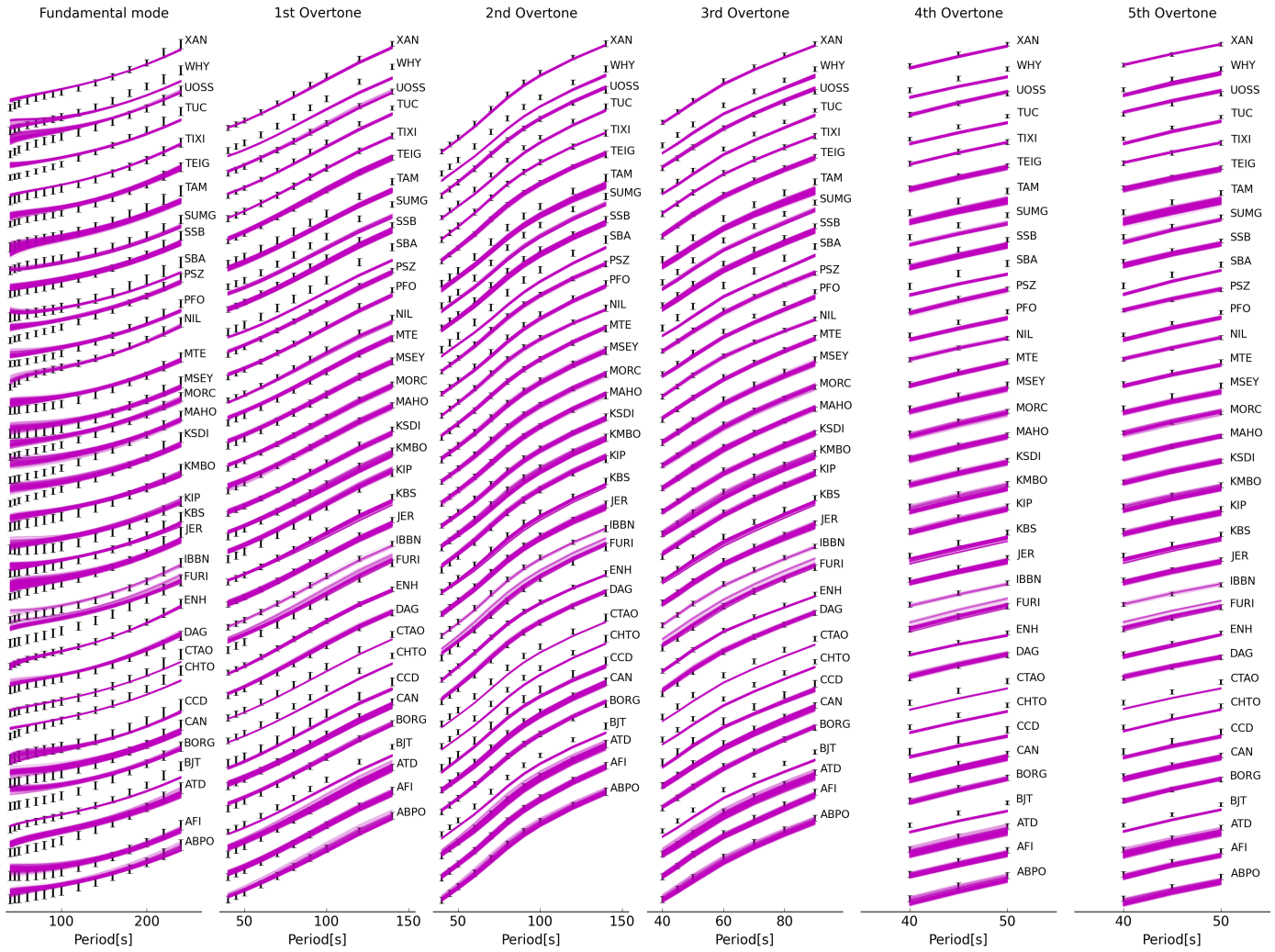

Figure B3: Observed (black) and modelled (magenta) Rayleigh wave fundamental mode and overtones phase velocities for "A2-fit" stations (dark green cirlces in Figure 3.1). The observed data cannot be explained by a compositionally uniform and adiabatic mantle model.

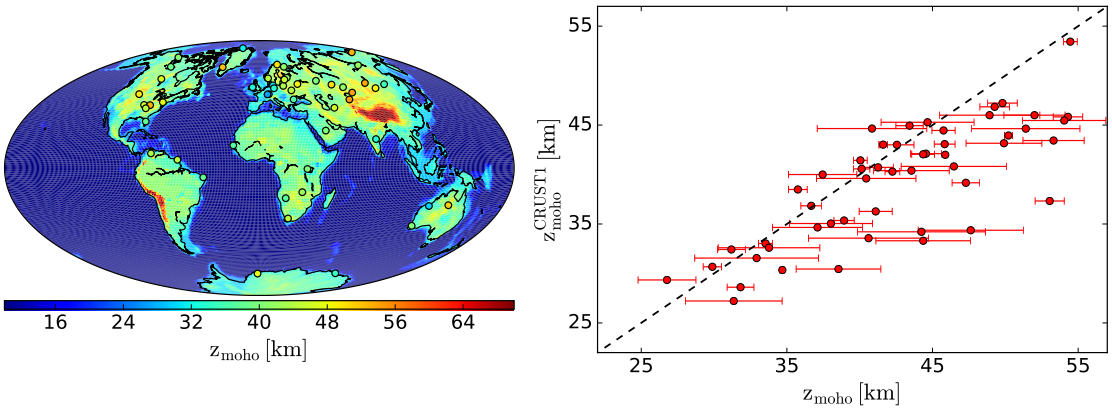

Figure B4: Most probable crustal thickness (z_{moho}) estimates inferred at each "A1-fit" station (circles) are in overall agreement with estimates from CRUST 1.0 reference model (background color).

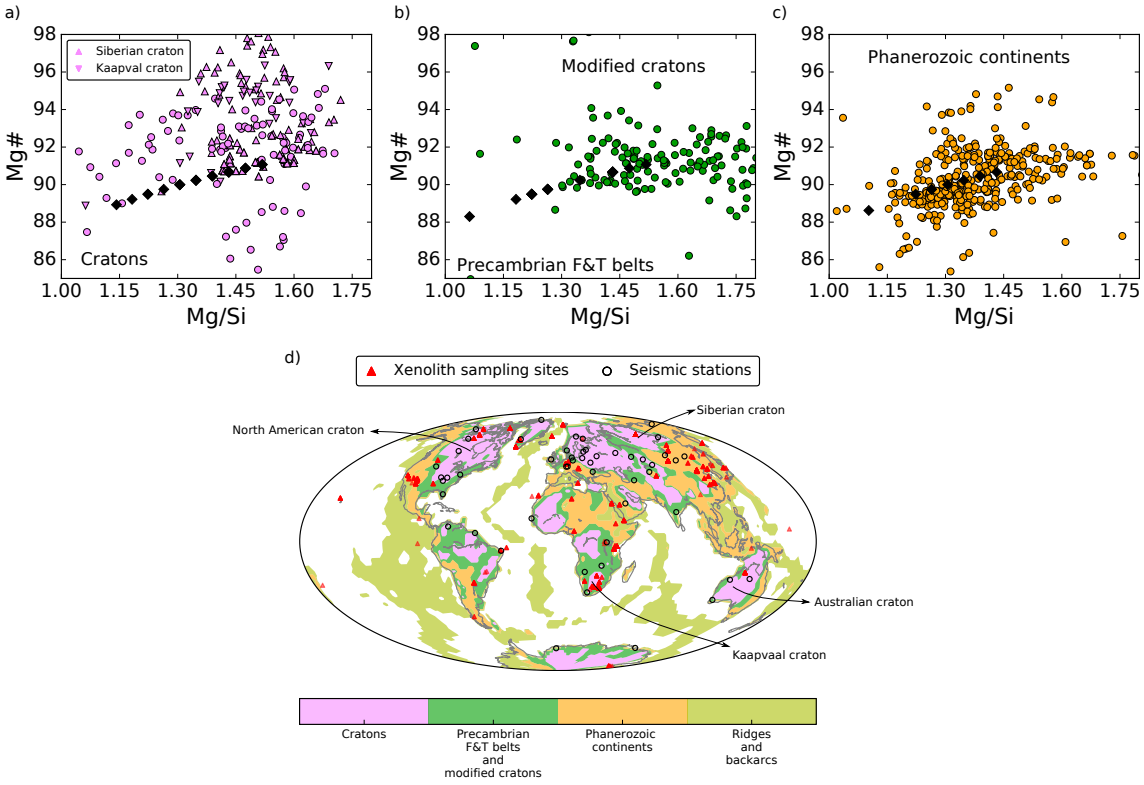

Figure B5: Variability in Mg# (Mg/(Mg+Fe)) and Mg/Si inferred in this study (black diamonds) and estimates derived from analysis of mantle xenoliths (coloured circles) extracted from the GEOROC database (`http://georoc.mpch-mainz.gwdg.de`) for different tectonic settings: a) cratonic regions; b) Precambrian fold-thrust belts; c) phanerozoic continents. Panel d) depicts geographic location of xenolith sampling sites (triangles) and seismic stations (circles). We find an overall agreement between the Mg# (Mg/(Mg+Fe)) and Mg/Si inferred in this study and estimates from mantle xenoliths, in particular for Precambrian fold-thrust belts (F&T belts) and Phanerozoic continents. Samples from Archean regions, in particular the Siberian and Kaapval cratons, are characterized by an excess in SiO_2 which reflect secondary metasomatic processes imposed on the samples after subcontinental mantle formation as a residue of melting (*Carlson et al.*, 2005).

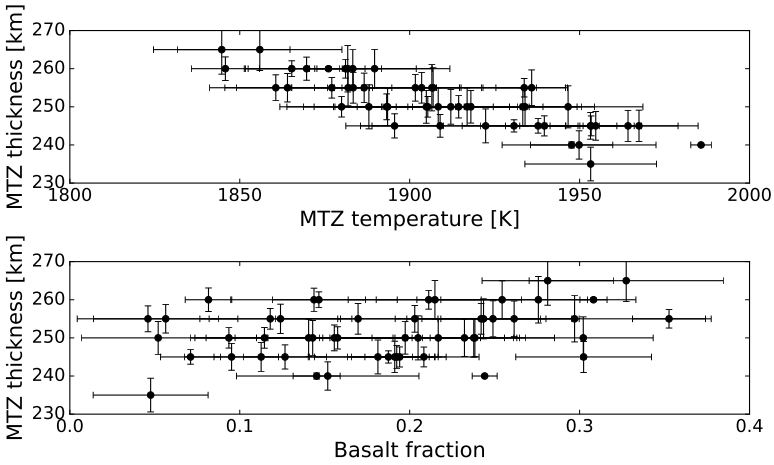

Figure B6: Comparison between most probable mantle transition zone (MTZ) thickness, mean temperature and basalt fraction for "A1-fit" stations. MTZ thickness is linearly correlated with MTZ temperatures, whereas no clear correlation with mantle composition can be identified

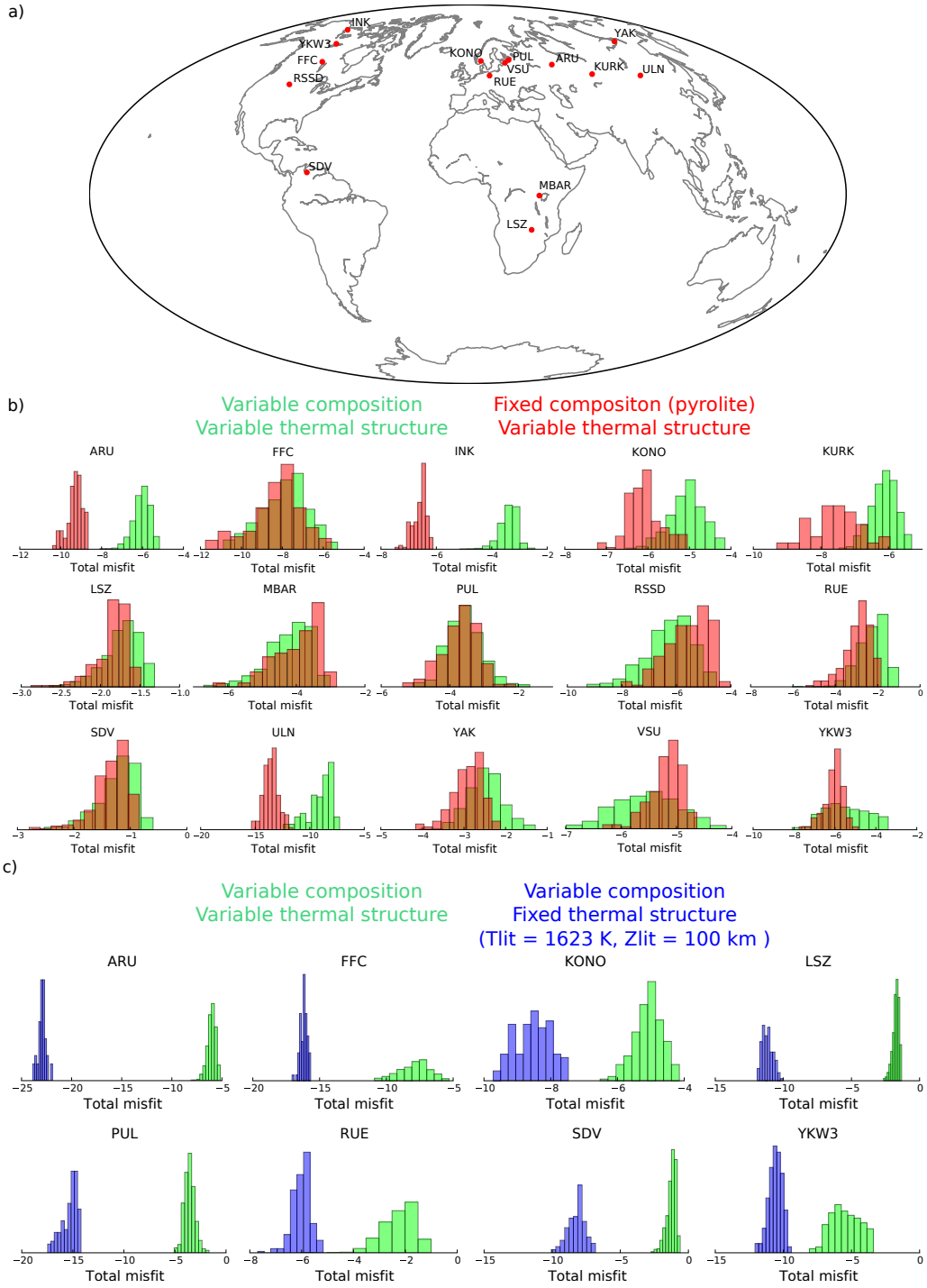

Figure B7: Histograms illustrating misfit values (computed as indicated in Methods section) obtained when fixing (b) mantle composition and (c) thermal structure for a set of "A1-fit" stations (summarized in panel a). Misfit values are generally reduced (∼2–15 % reduction) when compositional and thermal variations are considered. Smallest differences in the obtained misfits correspond to stations where the most probable basalt fraction estimates are close to pyrolite. We also find that it is not possible to explain the observed data solely by compositional variations. This analysis suggests that although temperature plays a primary role in determining the seismic structure of the upper mantle and transition zone, the effect of composition cannot be neglected.

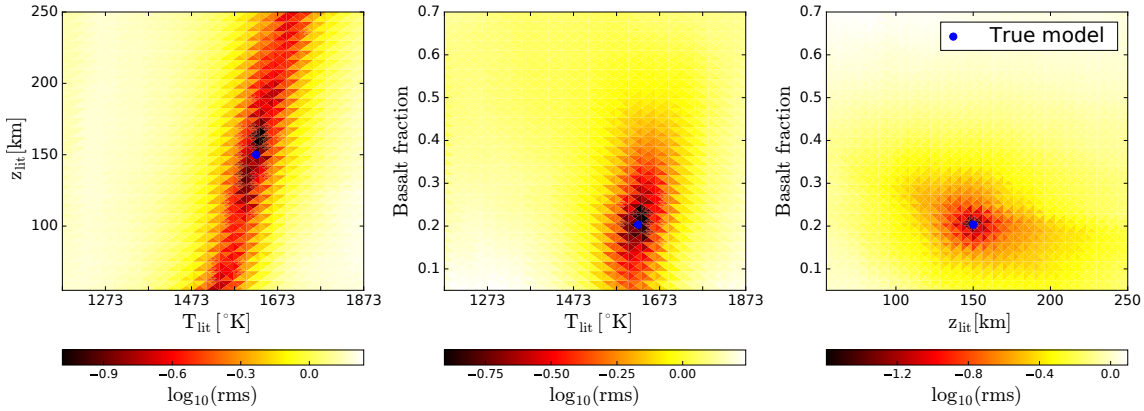

Figure B8: In order to test the robustness of our inverse scheme, we performed different sets of synthetic inversions. Here we show root-mean-square error (rms) surfaces estimated by grid search exploration of the model space for different combination of mantle thermo-chemical parameters (with fixed crustal structure). Blue dots indicate the model parameters used to create the synthetic data set used in the inversion. Small differences between the true solution and lowest misfit areas are attributed to the presence of noise in the synthetic data (7% Gaussian coloured noise). Visual inspection of the rms surfaces reveals a positive correlation between z_{lit} and T_{lit} which is the reason why we discuss our results in terms of mantle potential temperature estimates instead of z_{lit} and T_{lit} parameters. Furthermore, we find no significant trade-offs between thermal (T_{lit},z_{lit}) parameters and basalt fraction signaling that temperature and composition are independently resolvable.

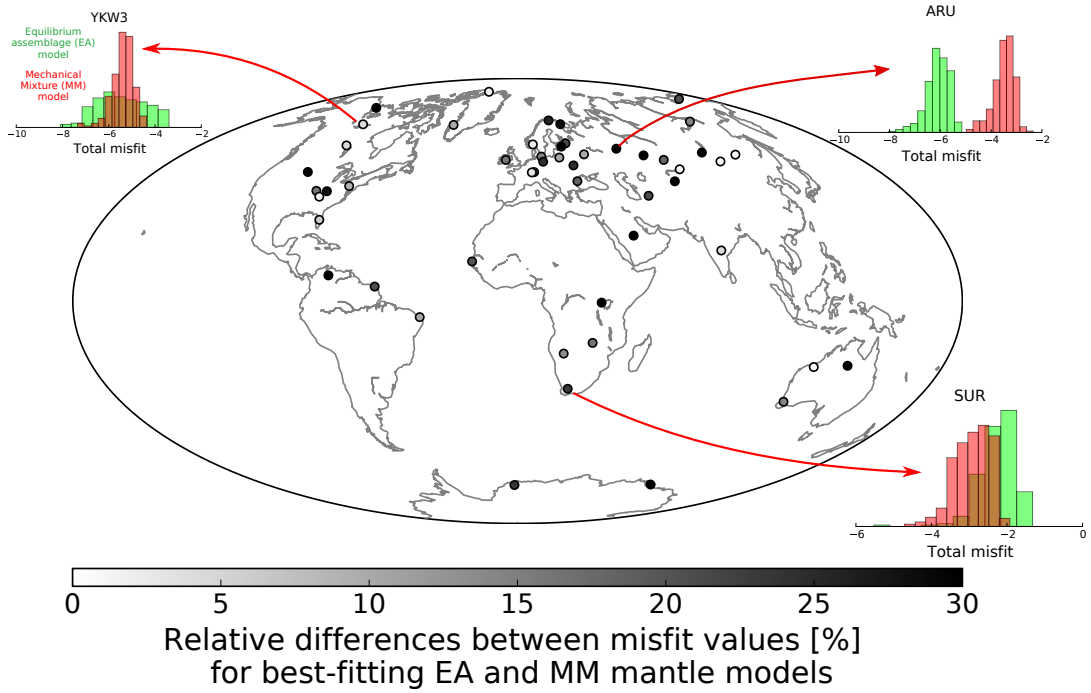

Figure B9: Map and histograms depicting relative differences between misfit values for models obtained assuming fully-equlibrated (EA) and mechanically-mixed (MM) mantle compositional models. We find 40 stations for which relative differences in the misfit values for the best-fitting models are larger than 5%. Our results suggest that the mantle is neither completely equilibrated nor fully mechanically mixed, but appears to be best described by an amalgam between the two

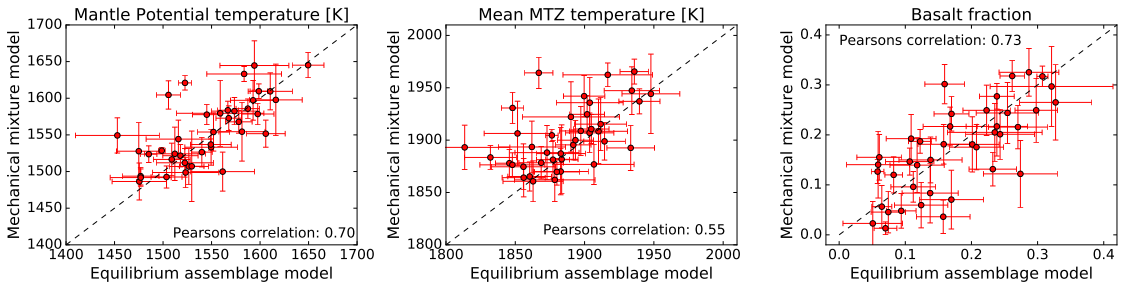

Figure B10: Mantle potential temperature, transition zone (MTZ) mean temperature, and basalt fraction estimates retrieved for equilibrium assemblage (EA) and mechanical mixture (MM) mantle models. Despite subtle differences, we find that temperature and composition estimates appear to be independent of mantle compositional model considered.

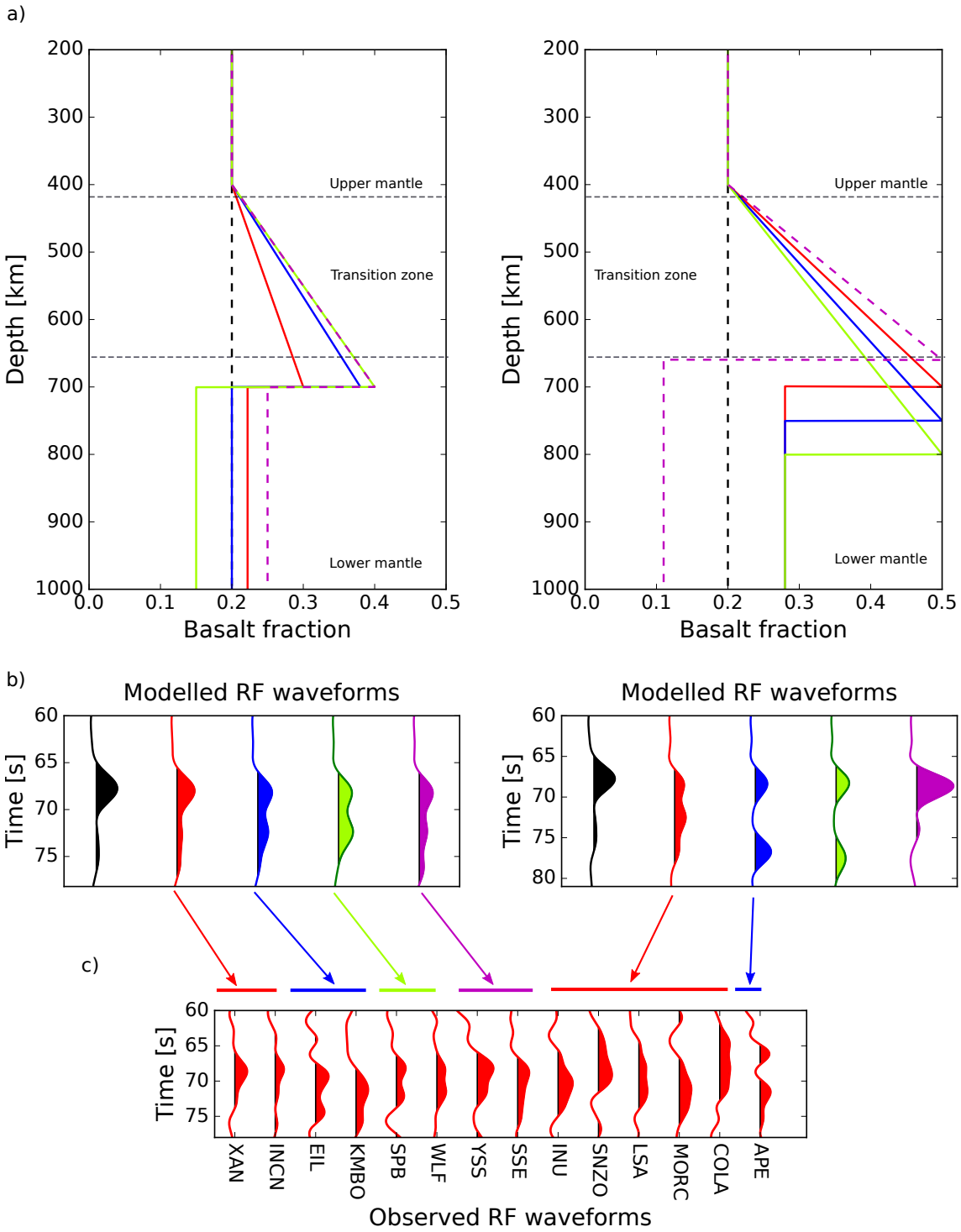

Figure B11: Comparison between observed and synthetic receiver function (RF) waveforms computed for different compositional gradients as predicted by mantle convection simulations (*Ballmer et al.*, 2015). a) Compositional profiles. b) Synthetic RF waveforms for each proposed model. c) Observed RF waveforms. We find an overall agreement between the observed and synthetic waveforms between 60 and 75 seconds (P660s) suggesting that the complexity observed in the data could be explained by radial changes in mantle composition. Variations in P660s travel time present in the observed RF waveforms (panel c) most likely reflect local changes in upper mantle velocities due to thermal and compositional variations.

Appendix C

Introduction

The conductivity models shown in Figure 4.7 were obtained from inversion of the local C-responses. For each geomagnetic observatory, an L-curve analysis was performed to determine the optimal trade-off between data misfit and regularization terms (Eq. 4.3). As an example, Figure C1 shows the L-curve and corresponding conductivity profiles computed for Canberra geomagnetic observatory. If the imposed regularization is too strong (black model), the solution does not fit the responses. In contrast, when the regularization parameter is too small (magenta model), data is well explained but the model is more likely to be contaminated by the data errors.

Additionally, Figures C2–C8 depict sampled posterior probability distributions and comparison between corrected experimental C-responses (Section 4.6) and synthetic responses computed for the sampled conductivity models for each geomagnetic observatory used in this study. The posterior probability at each station was determined by computing histograms of the marginal probability distribution of sampled conductivities for each layer.

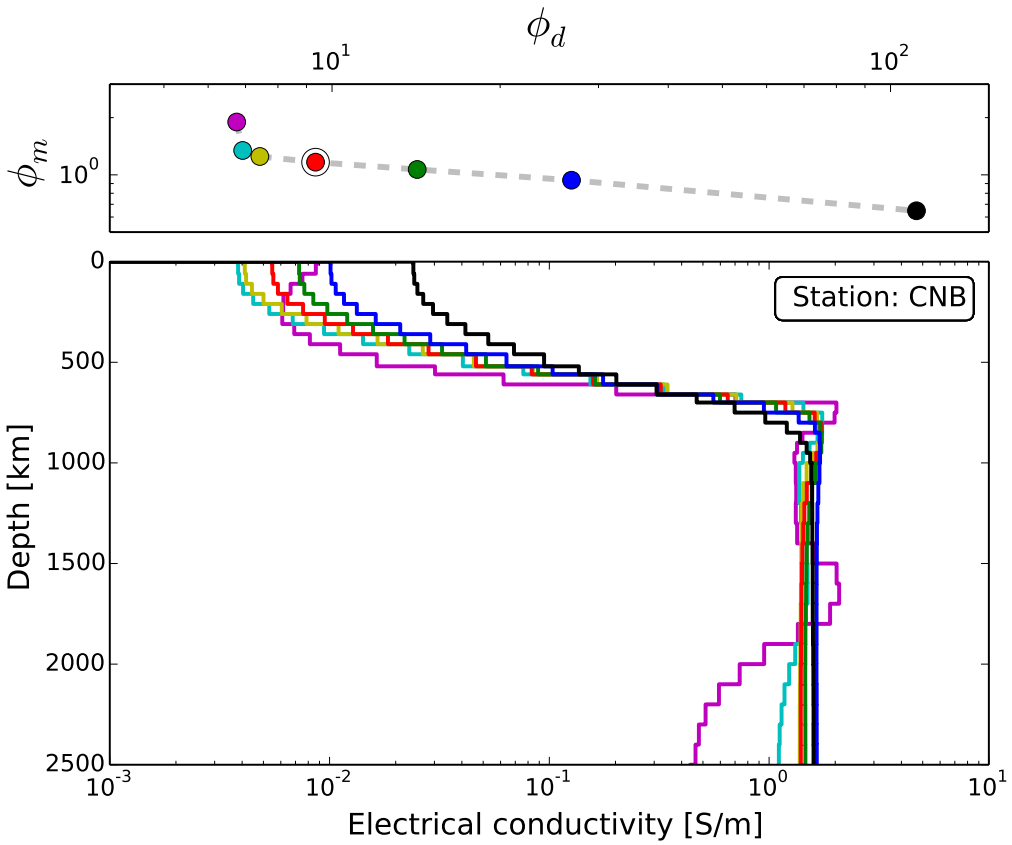

Figure C1: L-curve (top) and corresponding conductivity profiles (bottom) obtained for Canberra (CNB) observatory. Preferred regularized solution is indicated by the black unfilled circle.

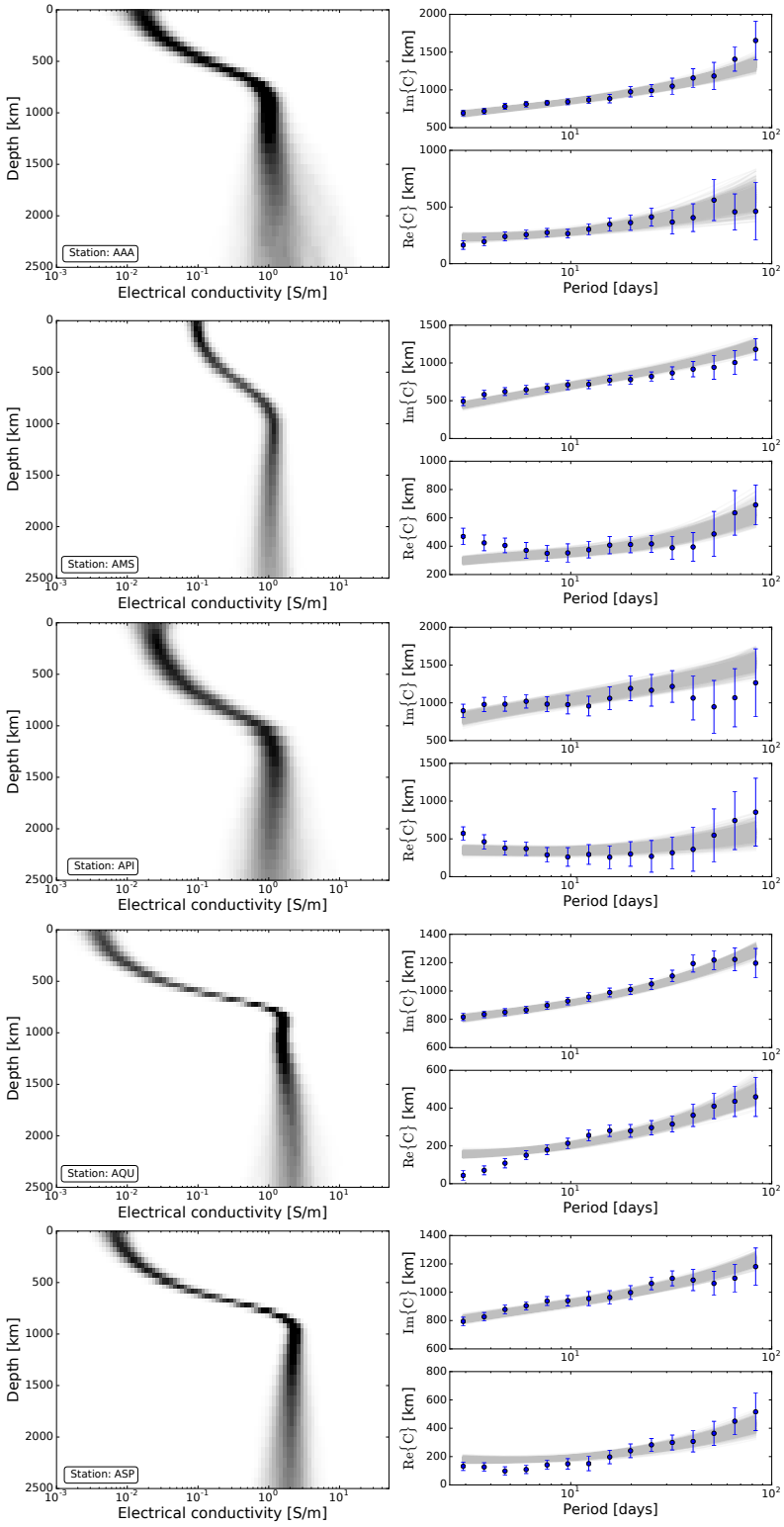

Figure C2: Sampled posterior probability distribution (left) and corresponding datafit (right) for Alma Ata (AAA), Martin de Vivies (AMS), Apia (API), L'Aquila (AQU), and Alice Springs (ASP) geomagnetic observatories. The posterior probability distribution was determined by computing a histogram of sampled conductivities for each layer assuming a bin-size of 0.05 on the log scale. Dark regions indicate high probability. Right panel shows datafit between the real (top) and imaginary (bottom) parts of experimental C-responses (blue) corrected for OIE using Eq. 4.2 (Section 4.3.1) and C-responses (gray) calculated for the sampled conductivity profiles; color intensity is proportional to the overlap of the responses.

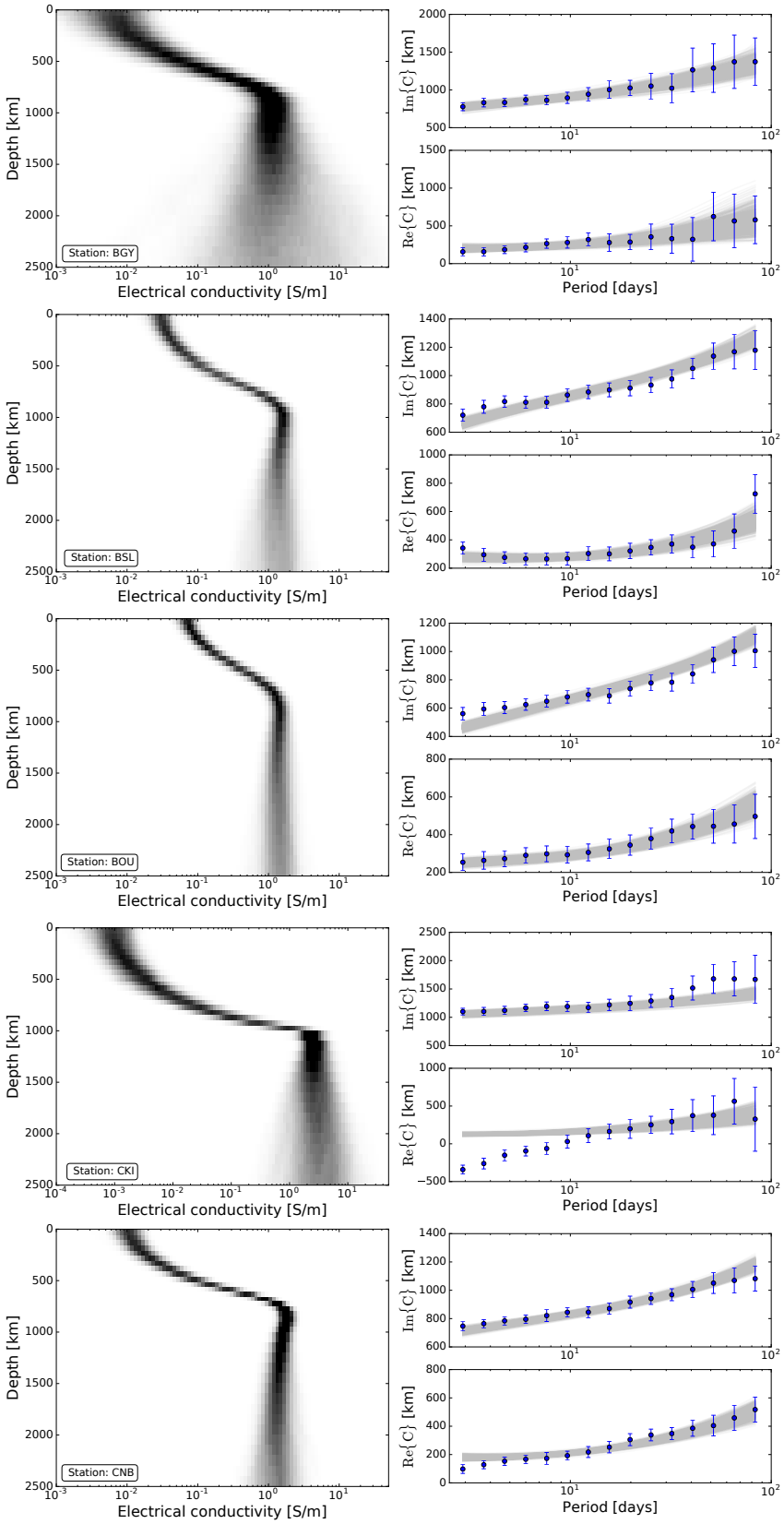

Figure C3: Sampled posterior probability distribution (left) and corresponding datafit (right) for Bar Gyora (BGY), Stennis Space Center (BSL), Boulder (BOU), Cocos-Keeling Islands (CKI), and Canberra (CNB) geomagnetic observatories. For more details, see Figure C2 caption.

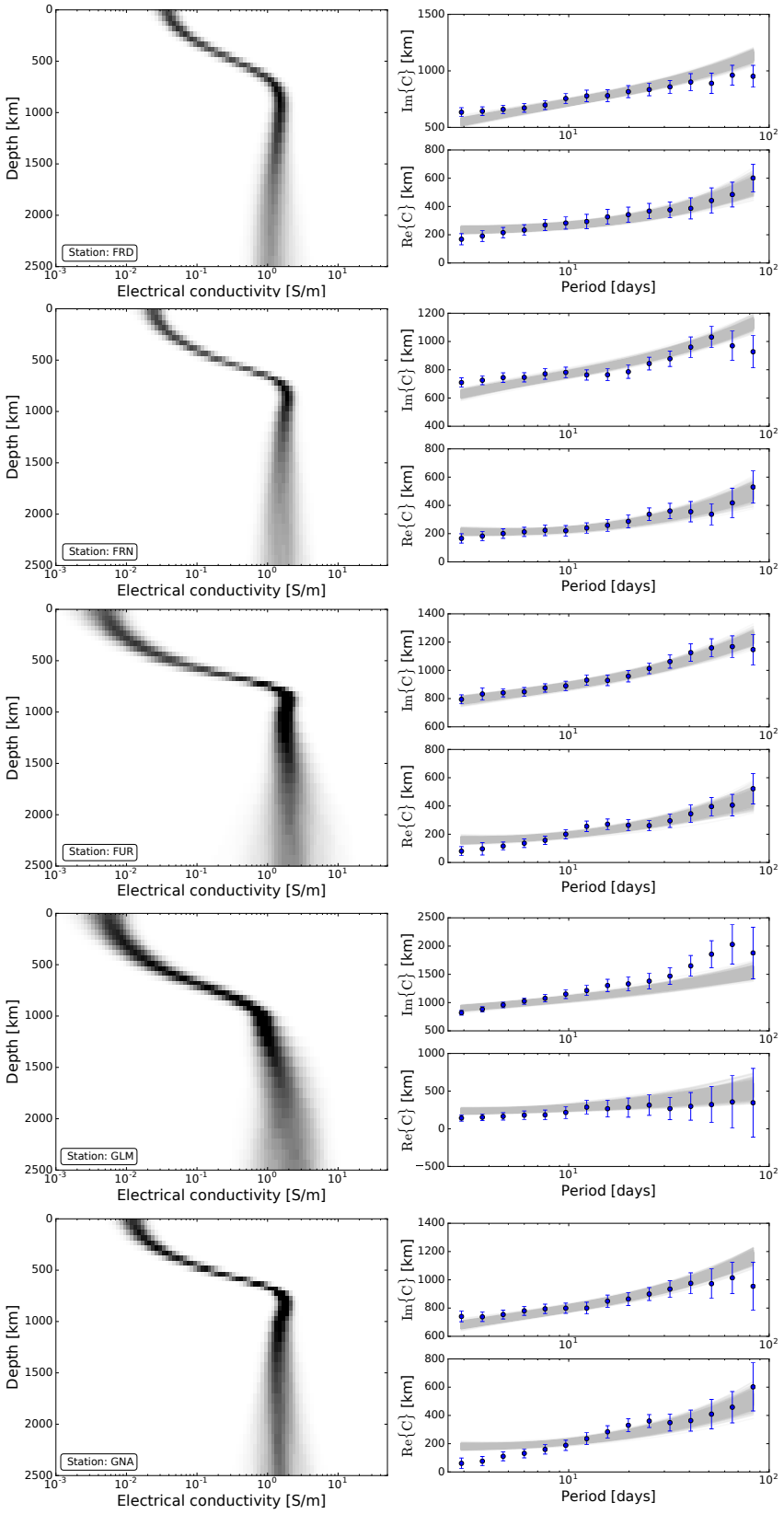

Figure C4: Sampled posterior probability distribution (left) and corresponding datafit (right) for Fredericksburg (FRD), Fresno (FRN), Furstenfeldbruck (FUR), Golmud (GLM), and Gnangara (GNA) geomagnetic observatories. For more details, see Figure C2 caption.

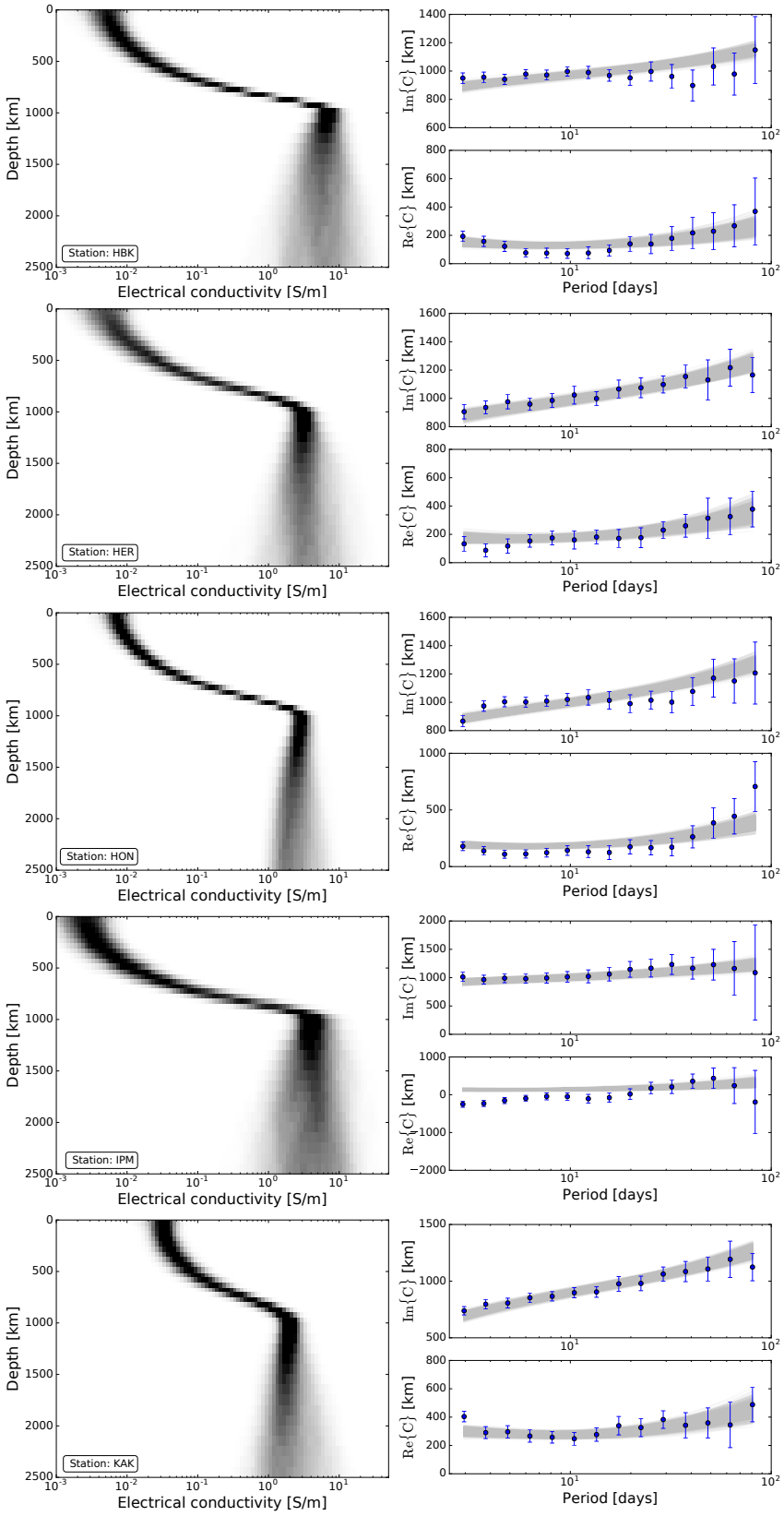

Figure C5: Sampled posterior probability distribution (left) and corresponding datafit (right) for Hartebeesthoek (HBK), Hermanus (HER), Honolulu (HON), Isla de Pascua (IPM), and Kakioka (KAK) geomagnetic observatories. For more details, see Figure C2 caption.

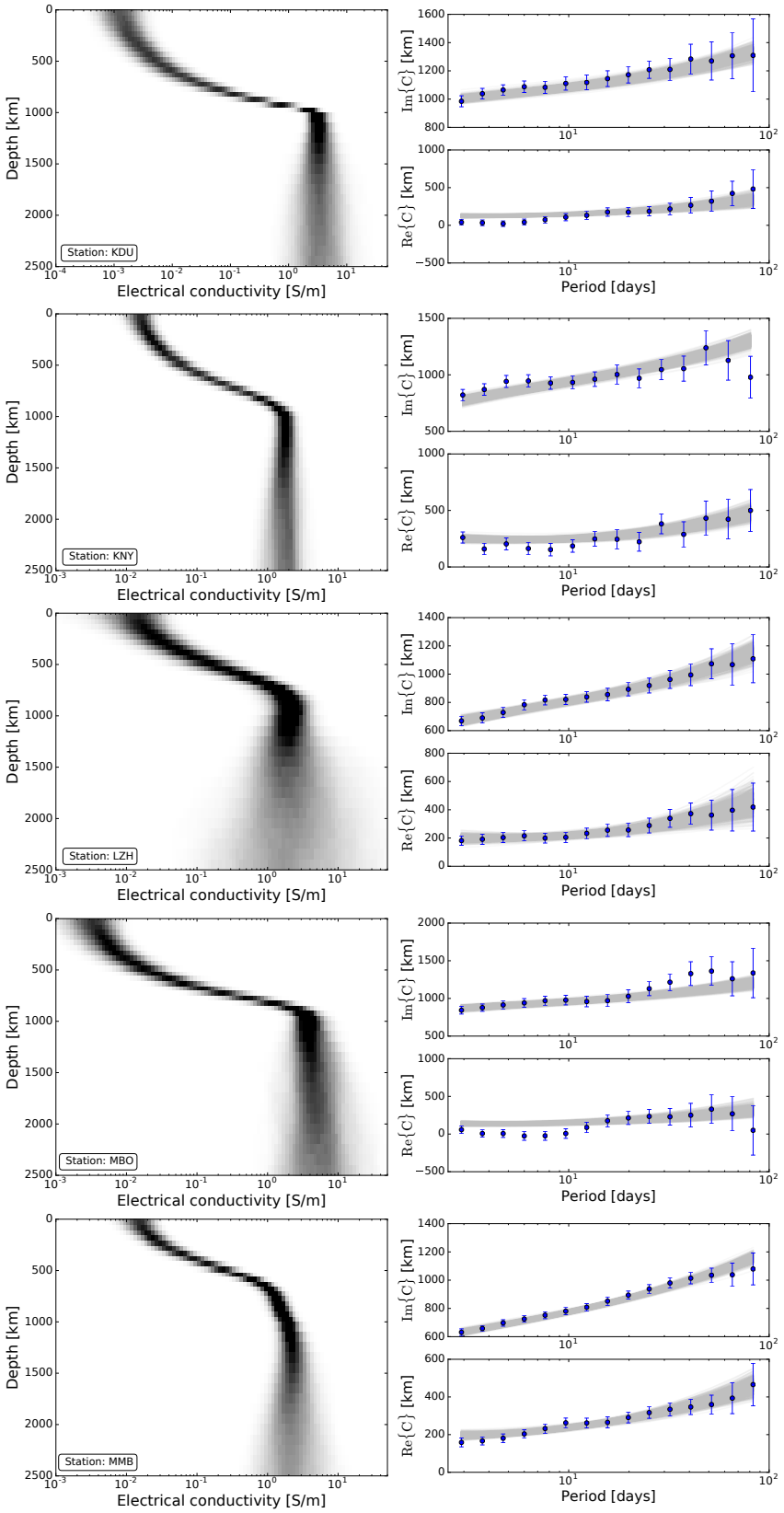

Figure C6: Sampled posterior probability distribution (left) and corresponding datafit (right) for Kakadu (KDU), Lanzhou (LZH), Stepanovka (ODE), Mbour (MBO), and Memambetsu (MMB) geomagnetic observatories. For more details, see Figure C2 caption.

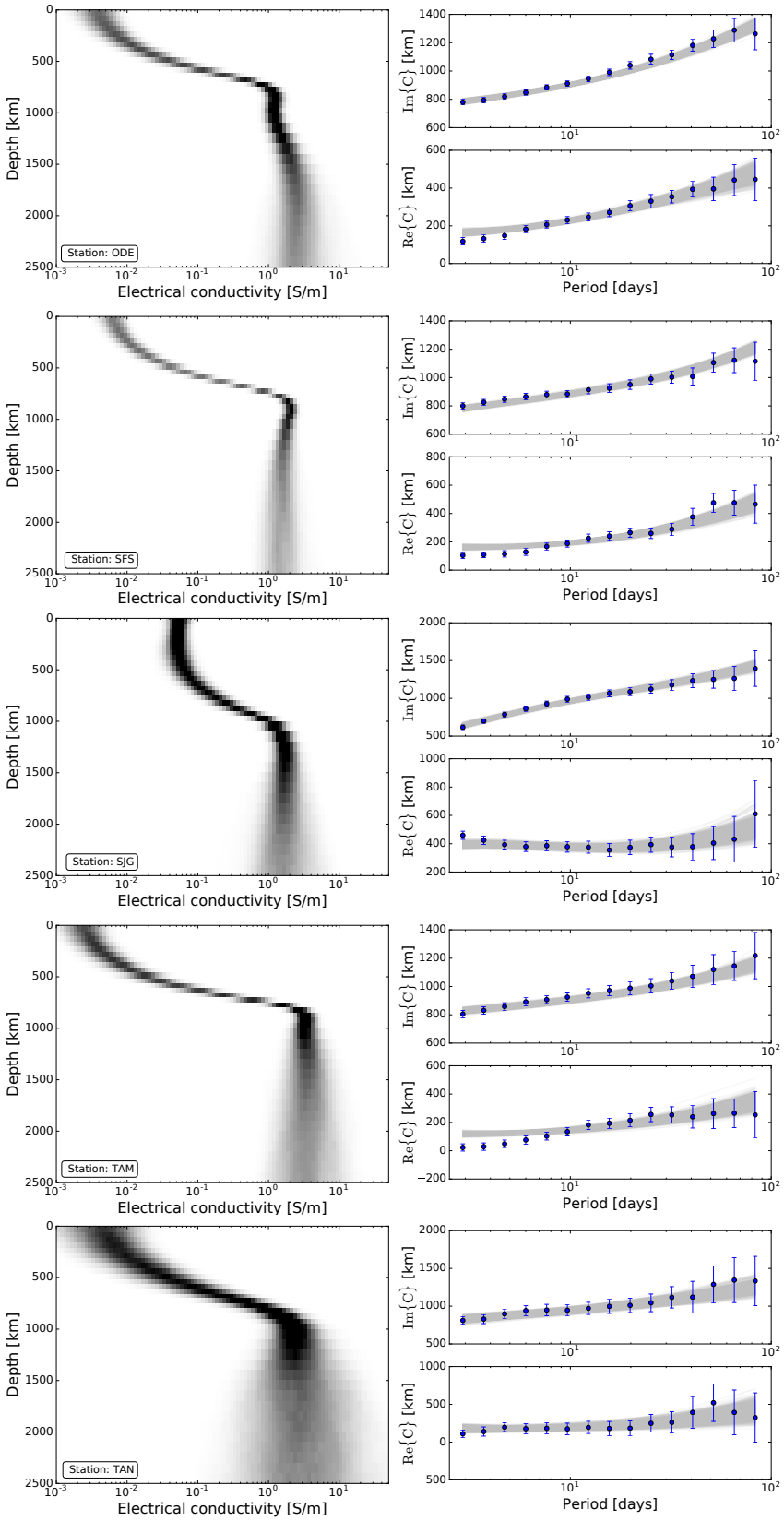

Figure C7: Sampled posterior probability distribution (left) and corresponding datafit (right) for San Fernando (SFS), San Juan (SJG), Tamanrasset (TAM), and Antananarivo (TAN) geomagnetic observatories. For more details, see Figure C2 caption.

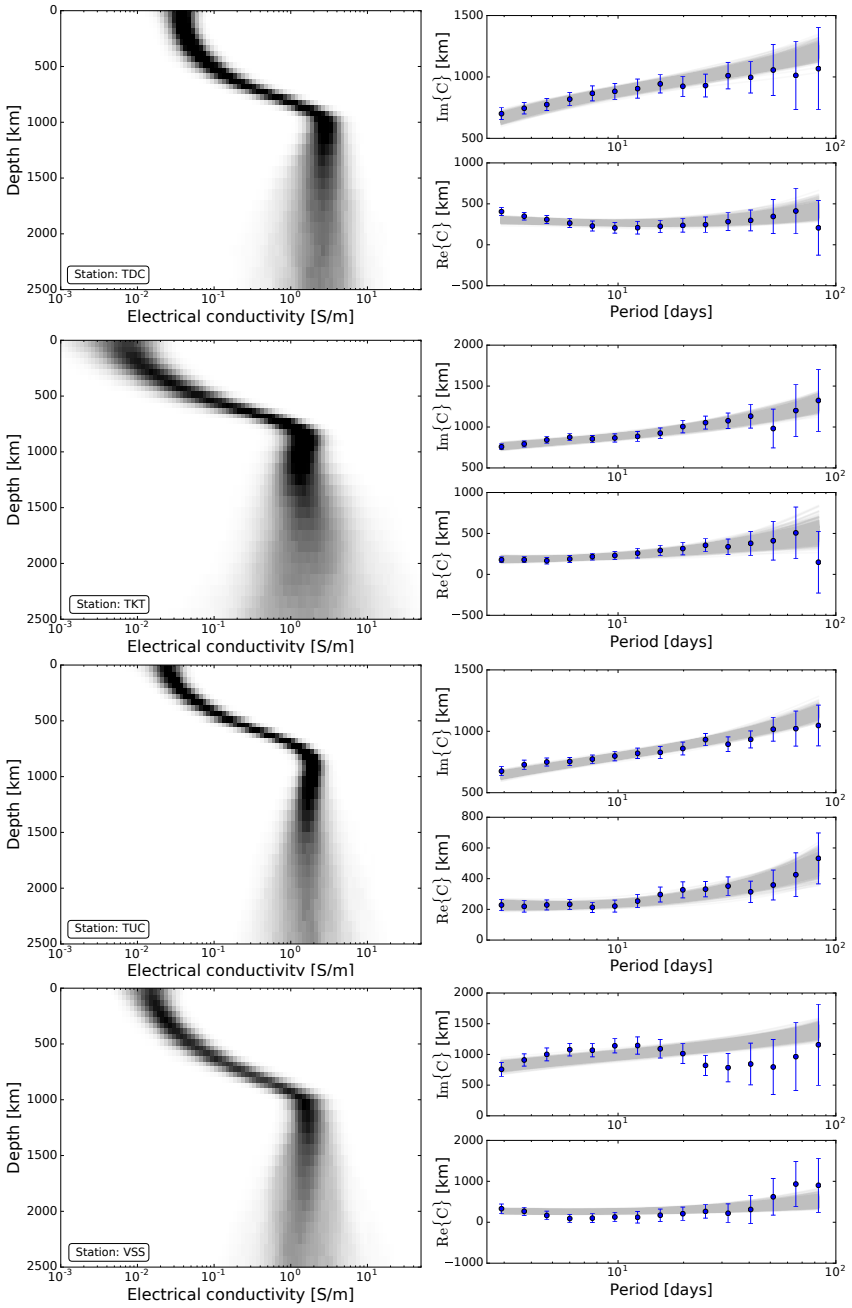

Figure C8: Sampled posterior probability distribution (left) and corresponding datafit (right) for Tristan da Cunha (TDC), Tashkent (TKT), Tucson (TUC), and Vassouras (VSS) geomagnetic observatories. For more details, see Figure C2 caption.

Appendix D

Introduction

Figure D1 summarizes the distribution of permanent geomagnetic observatories used for source coefficient estimation described in Section D.1. Figure D1 depicts times series of coefficient of determination obtained assuming different set of spherical harmonics coefficients to describe the magnetospheric ring current. We find significant differences in the estimated coefficients of determination for 8, 10, and 13 source coefficients, while no significant changes are observed when 15 SH coefficients are used.

The estimation of source coefficients requires the assumption of a 1D conductivity model of the Earth's interior and the conductance distribution of oceans and continents to separate the external (inducing) from internal (induced) contributions from the measured EM variations. Figure D3 depicts examples of transfer functions obtained when two different conductivity models are assumed during the source coefficient separation procedure. We find that differences in the estimated transfer functions are within experimental uncertainties.

Finally, Figures D4–D6 summarize the quality of the data fit for each geomagnetic observatory considered in this study. Figure D7 shows sampled electrical conductivity profiles retrieved from the joint inversion of magnetospheric and ionospheric transfer functions and best-fitting laboratory-based conductivity profiles for Yoshino-Katsura (YK) database.

D.1 Estimation of magnetospheric source coefficients

Maxwell's equations describe the spatio-temporal behavior of electromagnetic fields and can be formulated in frequency domain as

$$\frac{1}{\mu_0}\nabla \times \mathbf{B}(\mathbf{r},\omega) = \sigma(\mathbf{r})\mathbf{E}(\mathbf{r},\omega) + \mathbf{j}^{\text{ext}}(\mathbf{r},\omega), \tag{D.1}$$

$$\nabla \times \mathbf{E}(\mathbf{r},\omega) = i\omega\mathbf{B}(\mathbf{r},\omega), \tag{D.2}$$

where $\mathbf{B}$ and $\mathbf{E}$ represent the complex Fourier transforms of magnetic flux density and electric field at a location $\mathbf{r} = (r, \theta, \varphi)$. The distance from the Earth's center is denoted by r, θ is the colatitude, and φ is the longitude. Furthermore, $\mathbf{j}^{\text{ext}}(\mathbf{r},\omega)$ is the complex Fourier transform of an impressed source current density, $\sigma(\mathbf{r})$ represents the electrical conductivity distribution in the Earth, ω is the angular frequency, and μ_0 is the magnetic permeability of free space. Given that deep electromagnetic studies consider induction due to natural current systems which vary on time scales between 10^{-3} s and a few months, displacement currents are here neglected.

In a source-free region (above the conducting Earth and below the region enclosed by the current $\mathbf{j}^{\text{ext}}$), Eq. (D.1) reduces to $\nabla \times \mathbf{B} = 0$, thus $\mathbf{B}$ is a potential field that can described as a gradient of a scalar potential V ($\mathbf{B} = -\nabla V$). Since $\nabla \cdot \mathbf{B} = 0$, then V satisfies Laplace's equation ($\nabla^2 V = 0$) and hence, can decomposed into external and internal contributions such that $V = V^{\text{ext}} + V^{\text{int}}$, where

$$V^{\text{ext}} = a\sum_{n=1}^{N_\varepsilon}\sum_{m=-n}^{n}\varepsilon_n^m(\omega)\left(\frac{r}{a}\right)^n Y_n^m(\theta,\varphi), \tag{D.3}$$

$$V^{\text{int}} = a\sum_{k=1}^{N_\iota}\sum_{l=-k}^{k}\iota_k^l(\omega)\left(\frac{r}{a}\right)^{-(k+1)} Y_k^l(\theta,\varphi). \tag{D.4}$$

Here, a indicates the Earth's mean radius, $\varepsilon_n^m(\omega)$ and $\iota_k^l(\omega)$ are the spherical harmonic expansion (SHE) coefficients of the external (inducing) and internal (induced) parts of the potential, N_ε and N_ι are the maximum (cut-off) degrees for external and internal coefficients, respectively, and Y_n^m is the spherical harmonic of degree n and order m

$$Y_n^m(\theta,\varphi) = P_n^{|m|}(\cos\theta)e^{im\varphi}, \tag{D.5}$$

where $P_n^{|m|}(\cos\theta)$ corresponds to the Schmidt quasi-normalized associated Legendre function of degree n and order $|m|$. The magnetic field can then be written as

$$B_r(\mathbf{r},\omega) = -\left[\sum_{n=1}^{N_\varepsilon}\sum_{m=-n}^{n} n\varepsilon_n^m(\omega)\left(\frac{r}{a}\right)^{n-1} Y_n^m - \sum_{k=1}^{N_\iota}\sum_{l=-k}^{k}(k+1)\iota_k^l(\omega)\left(\frac{a}{r}\right)^{k+2} Y_k^l\right] \tag{D.6}$$

$$B_\theta(\mathbf{r},\omega) = -\left[\sum_{n=1}^{N_\varepsilon}\sum_{m=-n}^{n} \varepsilon_n^m(\omega)\left(\frac{r}{a}\right)^{n-1} \frac{\partial Y_n^m}{\partial\theta} - \sum_{k=1}^{N_\iota}\sum_{l=-k}^{k}\iota_k^l(\omega)\left(\frac{a}{r}\right)^{k+2} \frac{\partial Y_k^l}{\partial\theta}\right] \tag{D.7}$$

$$B_\varphi(\mathbf{r},\omega) = -\frac{1}{\sin\theta}\left[\sum_{n=1}^{N_\varepsilon}\sum_{m=-n}^{n} \varepsilon_n^m(\omega)\left(\frac{r}{a}\right)^{n-1} \frac{\partial Y_n^m}{\partial\varphi} - \sum_{k=1}^{N_\iota}\sum_{l=-k}^{k}\iota_k^l(\omega)\left(\frac{a}{r}\right)^{k+2} \frac{\partial Y_k^l}{\partial\varphi}\right] \tag{D.8}$$

If the same indices for external and internal parts are used, the components of the magnetic field at the Earth's surface ($\mathbf{r} = \mathbf{r_a}$) reduces to

$$B_r(\mathbf{r}_a,\omega) = -\sum_{n,m} z_n^m(\omega) Y_n^m(\theta,\varphi), \tag{D.9}$$

$$B_\theta(\mathbf{r}_a,\omega) = -\sum_{n,m} v_n^m(\omega)\frac{Y_n^m(\partial\theta,\varphi)}{\partial\theta}, \tag{D.10}$$

$$B_\varphi(\mathbf{r}_a,\omega) = -\sum_{n,m} v_n^m(\omega)\frac{1}{\sin\theta}\frac{Y_n^m(\partial\theta,\varphi)}{\partial\varphi}, \tag{D.11}$$

with $v_n^m = \epsilon_n^m + \iota_n^m$ and $z_n^m = n\epsilon_n^m - (n+1)\iota_n^m$. The approach here considered for source coefficient estimation (*Püthe et al.*, 2015b) consists of the following steps:

(1) Calculation of EM fields $\mathbf{B_n^m}(\mathbf{r}_a,\omega)$ induced by unit amplitude spherical harmonic sources ($\epsilon_n^m = 1$) in frequency domain at a set of logarithmically distributed frequencies ω_j using a numerical solver based on integral equation approach (*Kuvshinov*, 2008). This step requires the assumption of a 1D conductivity model of the Earth's interior and the conductance distribution of oceans and continents.

(2) Calculation of scalar Q-responses $Q_n(\omega_j)$ from the estimated $\mathbf{B_n^m}(\mathbf{r}_a,\omega_j)$ fields by using eq. (31) of *Püthe and Kuvshinov* (2014).

(3) Collection of hourly-mean time series of geomagnetic field components from mid-latitude permanent observatories (see Figure S1) and removal of the main field and its secular variations using the CHAOS model (*Olsen et al.*, 2006).

(4) Estimation of v_n^m coefficients using the horizontal components of the collected data and eqs.(D.10) and (D.11) for each time instant.

(5) Transformation of the unseparated coefficients from time domain to frequency domain.

(6) Interpolation of $Q_n(\omega_j)$ to the full set of frequencies contained in the data.

(7) Separation of internal and external contributions by means of the formula $\epsilon_n^m(\omega) = v_n^m(\omega)/[1 + Q_n(\omega)]$.

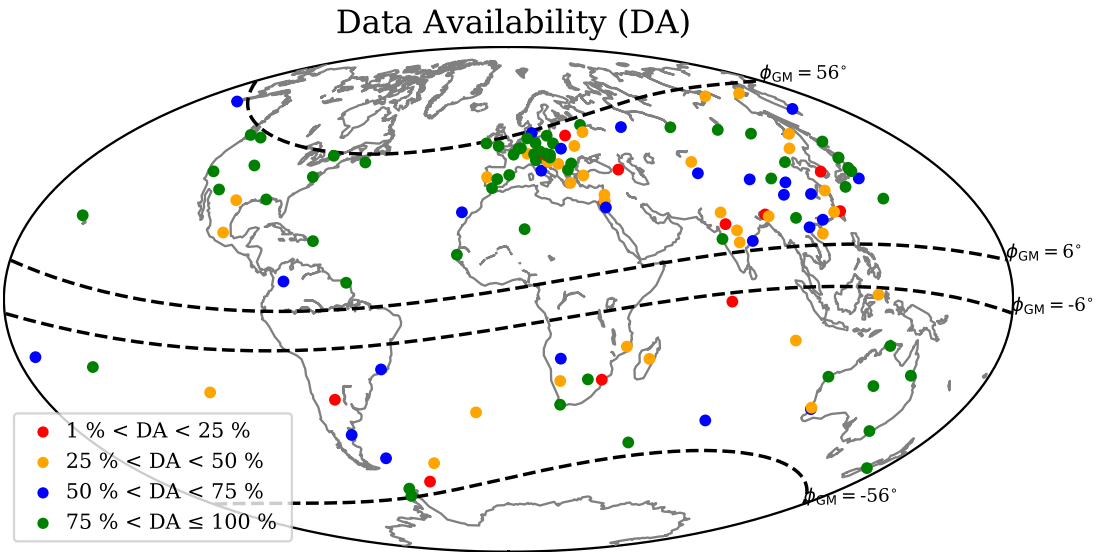

Figure D1: Distribution of permanent observatories (geomagnetic latitudes between ±6° and ±55°) used for source coefficient estimation (Section 5.2.1) color-coded by data availability (DA). DA equal to 100% corresponds to 20 years of data.

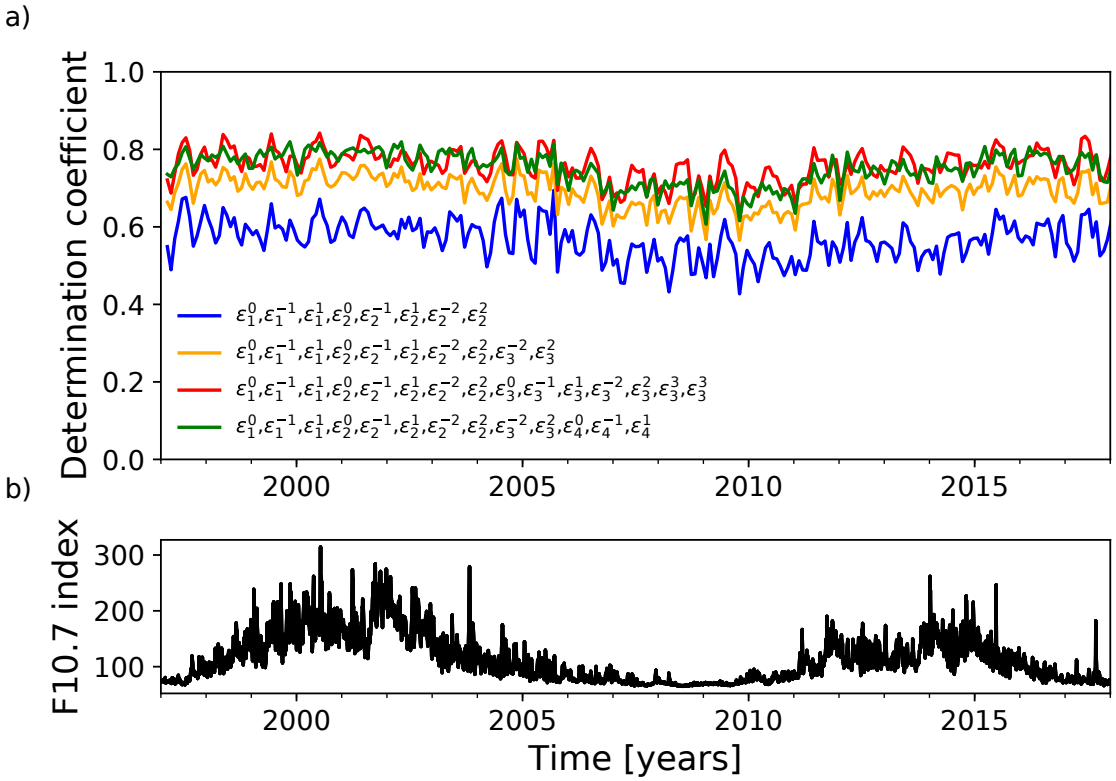

Figure D2: (a) Coefficients of determination obtained using different sets of spherical harmonic (SH) coefficients to describe the magnetospheric ring current. (b) Time series of F10.7 index (extracted from `http://lasp.colorado.edu/lisird/data/noaa_radio_flux/`), which is a good proxy for solar activity. We find a good correlation between the coefficients of determination and F10.7 index reflecting that magnetospheric sources are stronger during magnetically-active years.

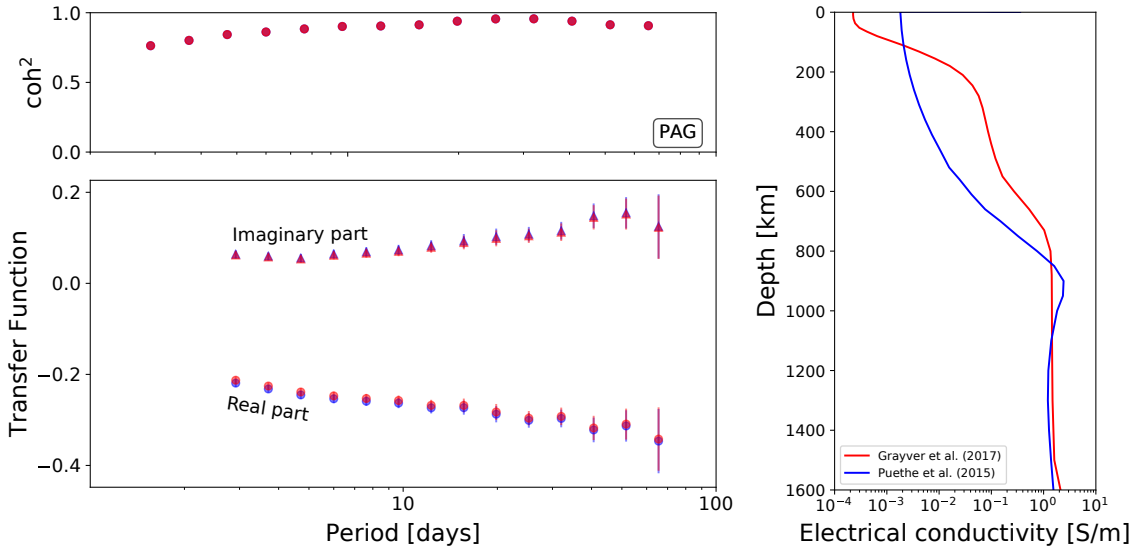

Figure D3: Example of the real (circles) and imaginary (triangles) parts of the transfer functions obtained when assuming two different conductivity models for source coefficient estimation. Differences in the estimated transfer functions are within observed uncertainties.

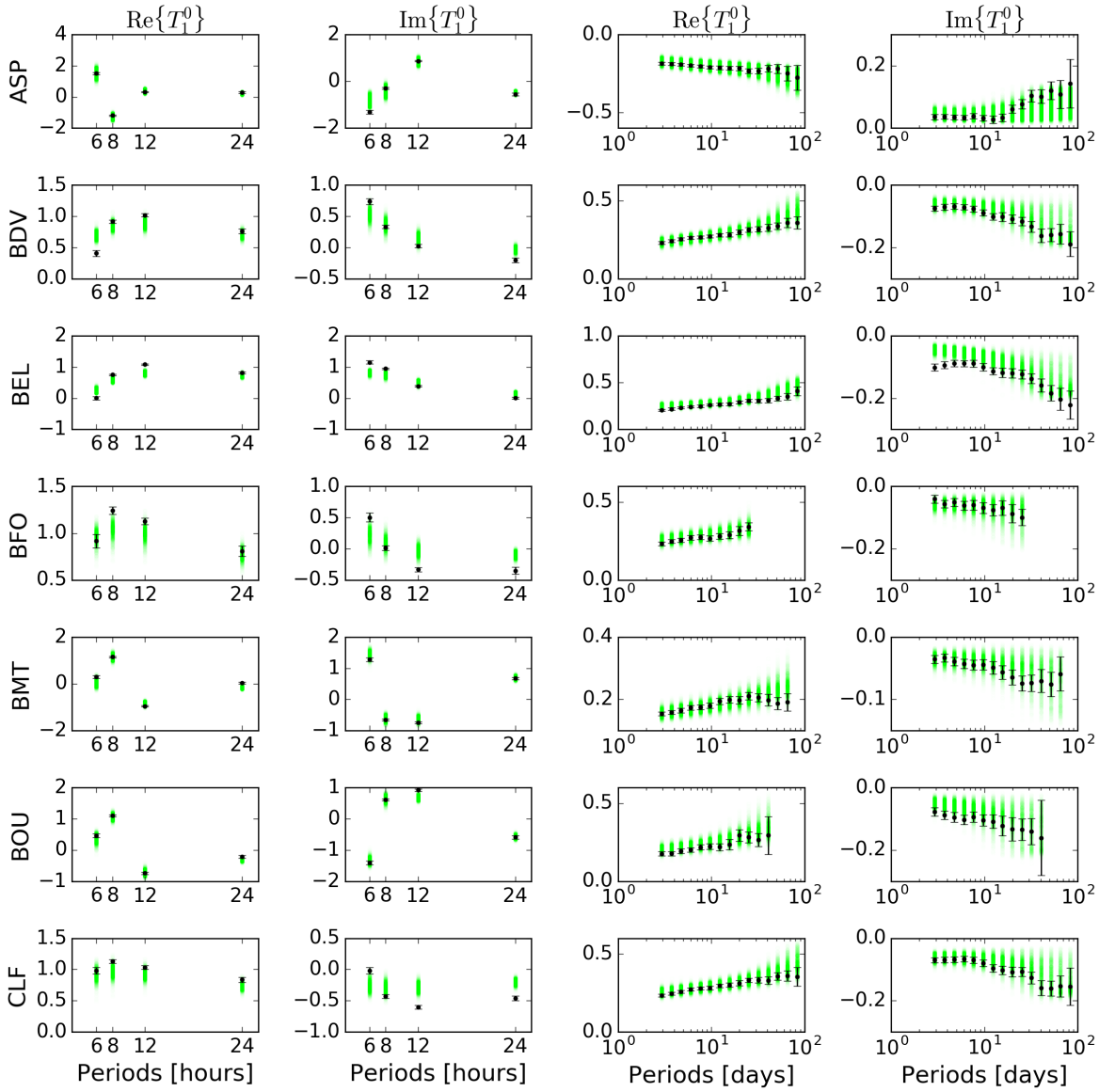

Figure D4: Real (Re) and Imaginary (Im) parts of the observed (black) and modelled (green) ionospheric (6–24 hours) and magnetospheric (3–85 days) transfer functions (T_1^0) for Alice Springs (ASP), Budkov (BDV), Belsk (BEL), Black Forest (BFO), Beijing Ming Tombs (BMT), Boulder (BOU), and Chambon la Foret (CLF) geomagnetic observatories. Uncertainties of the observed transfer functions are indicated by the error bars.

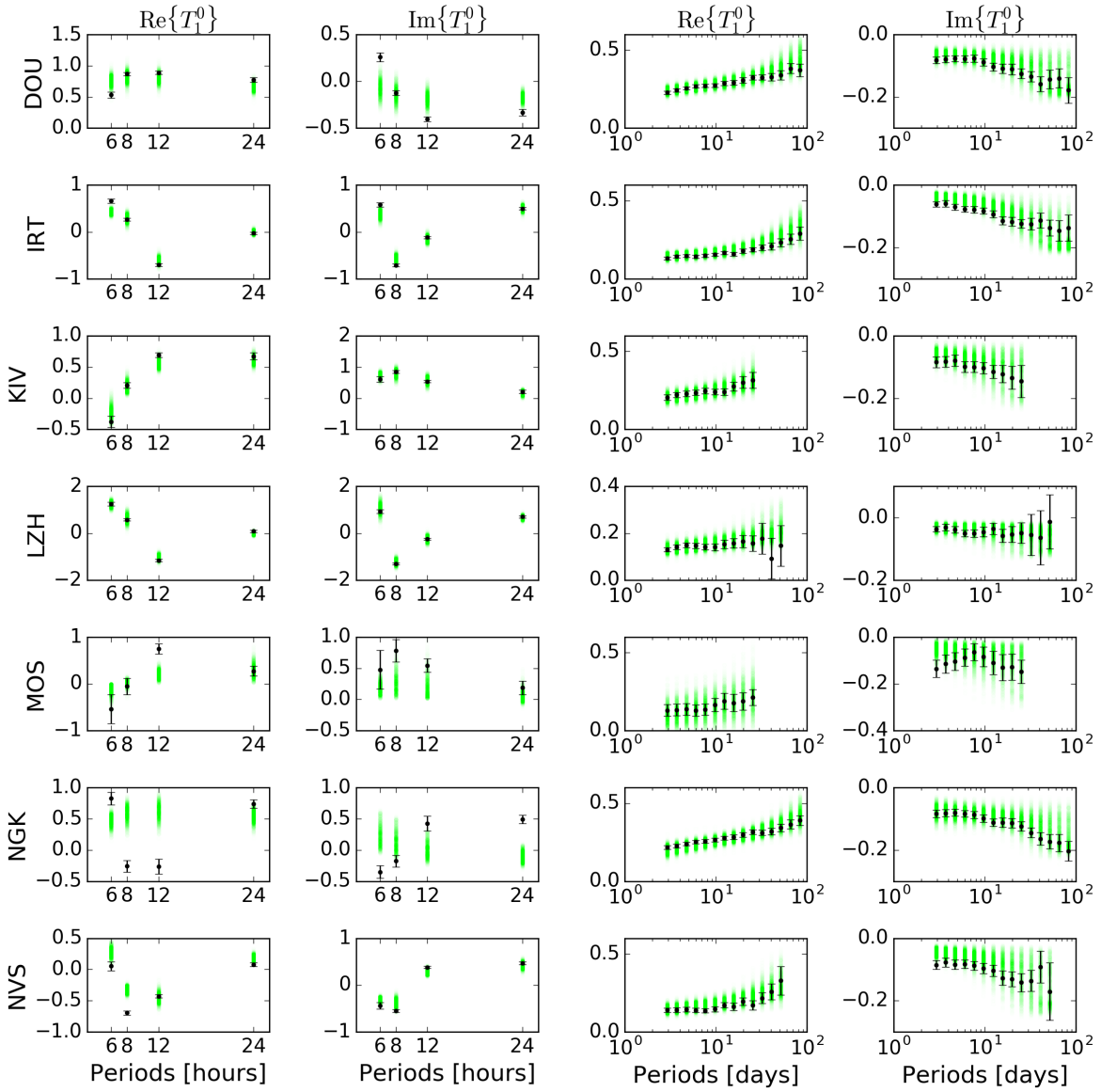

Figure D5: Real (Re) and Imaginary (Im) parts of the observed (black) and modelled (green) ionospheric (6–24 hours) and magnetospheric (3–85 days) transfer functions (T_1^0) for Dourbes (DOU), Irkutsk (IRT), Kiev (KIV), Lanzhou (LZH), Moscow (MOS), Niemegk (NGK), and Novosibirsk (NVS) geomagnetic observatories. Uncertainties of the observed transfer functions are indicated by the error bars.

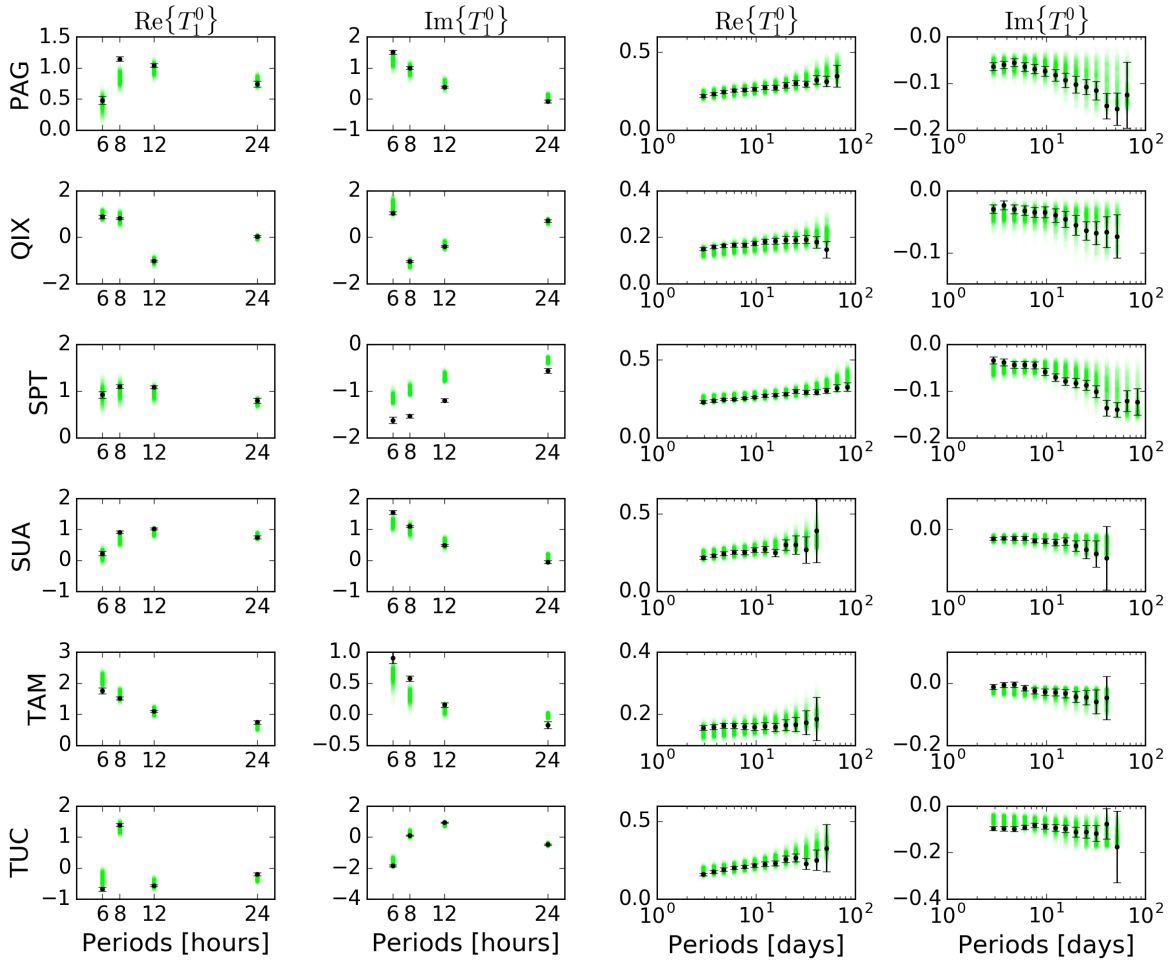

Figure D6: Real (Re) and Imaginary (Im) parts of the observed (black) and modelled (green) ionospheric (6–24 hours) and magnetospheric (3–85 days) transfer functions (T_1^0) for Panagjurishte (PAG), Qianling (QIX), San Pablo-Toledo (SPT), Surlari (SUA), Tamanrasset (TAM), and Tucson (TUC) geomagnetic observatories. Uncertainties of the observed transfer functions are indicated by the error bars.

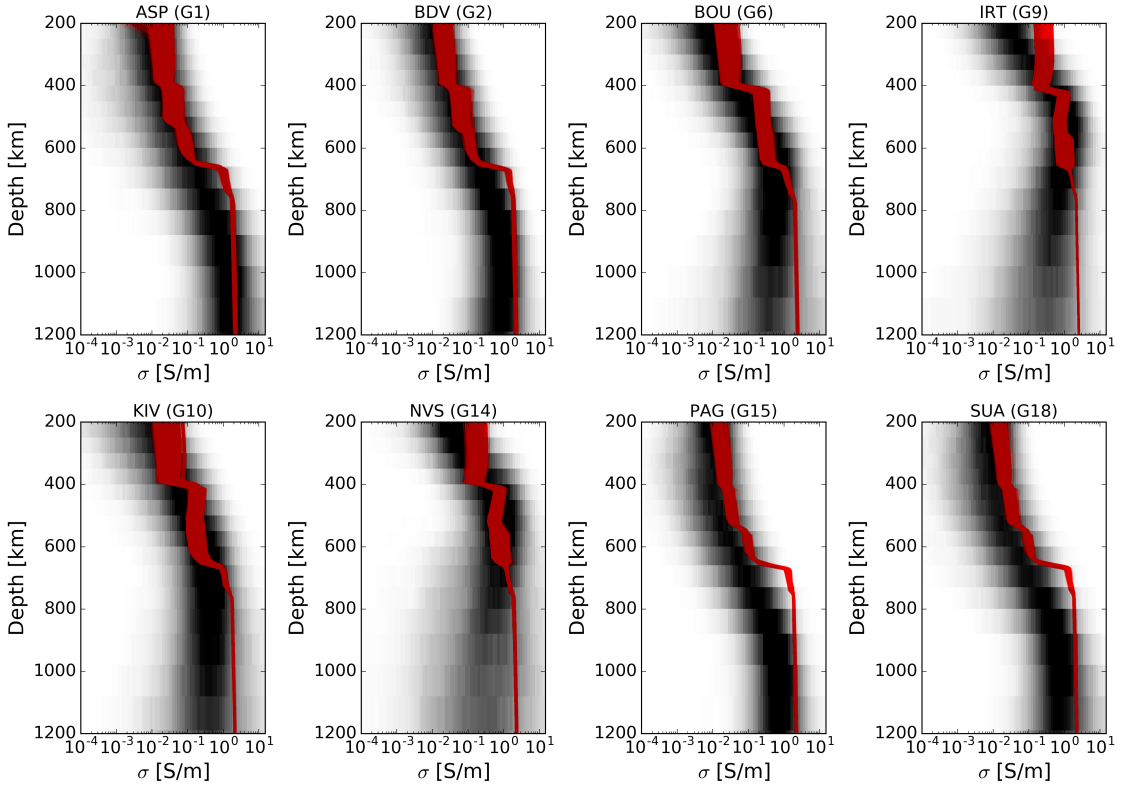

Figure D7: Sampled electrical conductivity profiles (σ) retrieved from the joint inversion of magnetospheric and ionospheric transfer functions (black) and best-fitting laboratory-based conductivity profiles (red) for YK database. Geographic location of each geomagnetic observatory are shown in Figure 5.2 and stations acronym are defined in Table 5.2.

Bibliography

Afonso, J., J. Fullea, Y. Yang, J. Connolly, and A. Jones (2013), 3-D multi-observable probabilistic inversion for the compositional and thermal structure of the lithosphere and upper mantle. II: General methodology and resolution analysis, *Journal of Geophysical Research: Solid Earth*, *118*(4), 1650–1676.

Afonso, J. C., N. Rawlinson, Y. Yang, D. L. Schutt, A. G. Jones, J. Fullea, and W. L. Griffin (2016), 3-D multiobservable probabilistic inversion for the compositional and thermal structure of the lithosphere and upper mantle: III. Thermochemical tomography in the Western-Central US, *Journal of Geophysical Research: Solid Earth*, *121*(10), 7337–7370.

Ai, Y., T. Zheng, W. Xu, Y. He, and D. Dong (2003), A complex 660 km discontinuity beneath northeast China, *Earth and Planetary Science Letters*, *212*(1-2), 63–71.

Aki, K., and P. G. Richards (2002), *Quantitative seismology*.

Alvers, M., H. Götze, B. Lahmeyer, C. Plonka, and S. Schmidt (2013), Advances in 3D potential field modeling, in *75th EAGE Conference & Exhibition incorporating SPE EUROPEC 2013*.

Ammon, C. J., G. E. Randall, and G. Zandt (1990), On the nonuniqueness of receiver function inversions, *Journal of Geophysical Research: Solid Earth*, *95*(B10), 15,303–15,318.

Anderson, D. L. (2007), *New theory of the Earth*, Cambridge University Press.

Andrews, J., and A. Deuss (2008), Detailed nature of the 660 km region of the mantle from global receiver function data, *Journal of Geophysical Research: Solid Earth*, *113*(B6).

Arsenault, R., A. Poulin, P. Côté, and F. Brissette (2013), Comparison of stochastic optimization algorithms in hydrological model calibration, *Journal of Hydrologic Engineering*, *19*(7), 1374–1384.

Artemieva, I. M., and H. Thybo (2013), EUNAseis: a seismic model for Moho and crustal structure in Europe, Greenland, and the North Atlantic region, *Tectonophysics*, *609*, 97–153.

Aster, R., B. Borchers, and C. Thurber (2005), Parameter estimation and inverse problems: Elsevier academic.

Auger, A., N. Hansen, J. M. P. Zerpa, R. Ros, and M. Schoenauer (2009), Experimental comparisons of derivative free optimization algorithms., *SEA*, *5526*, 3–15.

Baba, K., J. Chen, M. Sommer, H. Utada, W. H. Geissler, W. Jokat, and M. Jegen (2016), Marine magnetotellurics imaged no distinct plume beneath the Tristan da Cunha hotspot in the southern Atlantic Ocean, *Tectonophysics*.

Bagheri, A., A. Khan, D. Al-Attar, O. Crawford, and D. Giardini (2019), Tidal response of Mars constrained from laboratory-based viscoelastic dissipation models and geophysical data, *Journal of Geophysical Research: Planets*, doi:10.1029/2019JE006015.

Bagley, B., A. M. Courtier, and J. Revenaugh (2009), Melting in the deep upper mantle oceanward of the Honshu slab, *Physics of the Earth and Planetary Interiors*, *175*(3), 137–144.

Bahr, K., N. Olsen, and T. J. Shankland (1993), On the combination of the magnetotelluric and the geomagnetic depthsounding method for resolving an electrical conductivity increase at 400 km depth, *Geophysical research letters*, *20*(24), 2937–2940.

Balasis, G., and G. D. Egbert (2006), Empirical orthogonal function analysis of magnetic observatory data: Further evidence for non-axisymmetric magnetospheric sources for satellite induction studies, *Geophysical research letters*, *33*(11).

Ballmer, M. D., N. C. Schmerr, T. Nakagawa, and J. Ritsema (2015), Compositional mantle layering revealed by slab stagnation at ∼1000–km depth, *Science advances*, *1*(11), e1500,815.

Banks, R. (1969), Geomagnetic variations and the electrical conductivity of the upper mantle, *Geophysical Journal International*, *17*(5), 457–487.

Banks, R. (1973), Data processing and interpretation in geomagnetic deep sounding, *Physics of the earth and planetary interiors*, *7*(3), 339–348.

Bass, J. D. (1995), Elasticity of minerals, glasses, and melts, *Mineral physics & crystallography: a handbook of physical constants*, pp. 45–63.

Bentham, H., and S. Rost (2014), Scattering beneath Western Pacific subduction zones: evidence for oceanic crust in the mid-mantle, *Geophysical Journal International*, *197*(3), 1627–1641.

Bercovici, D., and S.-i. Karato (2003), Whole-mantle convection and the transition-zone water filter, *Nature*, *425*(6953), 39–44.

Bernstein, S., P. B. Kelemen, and C. K. Brooks (1998), Depleted spinel harzburgite xenoliths in Tertiary dykes from East Greenland: restites from high degree melting, *Earth and Planetary Science Letters*, *154*(1-4), 221–235.

Bina, C. R., and G. Helffrich (1994), Phase transition Clapeyron slopes and transition zone seismic discontinuity topography, *Journal of Geophysical Research: Solid Earth*, *99*(B8), 15,853–15,860.

Bodin, T., M. Sambridge, H. Tkalčić, P. Arroucau, K. Gallagher, and N. Rawlinson (2012), Transdimensional inversion of receiver functions and surface wave dispersion, *Journal of Geophysical Research: Solid Earth*, *117*(B2).

Bolfan-Casanova, N. (2005), Water in the Earth's mantle, *Mineralogical Magazine*, *69*(3), 229–257.

Bolfan-Casanova, N., S. Mackwell, H. Keppler, C. McCammon, and D. Rubie (2002), Pressure dependence of H solubility in magnesiowüstite up to 25 GPa: Implications for the storage of water in the Earth's lower mantle, *Geophysical Research Letters*, *29*(10).

Bolfan-Casanova, N., H. Keppler, and D. C. Rubie (2003), Water partitioning at 660 km depth and evidence for very low water solubility in magnesium silicate perovskite, *Geophysical Research Letters*, *30*(17).

Bolfan-Casanova, N., C. A. Mccammon, and S. J. Mackwell (2006), Water in transition zone and lower mantle minerals, *GEOPHYSICAL MONOGRAPH-AMERICAN GEOPHYSICAL UNION*, *168*, 57.

Borsic, A., and A. Adler (2012), A primal–dual interior-point framework for using the L1 or L2 norm on the data and regularization terms of inverse problems, *Inverse Problems*, *28*(9), 095,011.

Boyd, F., N. Pokhilenko, D. Pearson, S. Mertzman, N. Sobolev, and L. Finger (1997), Composition of the Siberian cratonic mantle: evidence from Udachnaya peridotite xenoliths, *Contributions to Mineralogy and Petrology*, *128*(2-3), 228–246.

Brandenburg, J., and P. Van Keken (2007), Deep storage of oceanic crust in a vigorously convecting mantle, *Journal of Geophysical Research: Solid Earth*, *112*(B6).

Brown, G. C., and A. E. Mussett (1993), The Inaccessible Earth: an Integrated View to its Structure and Composition.

Calò, M., T. Bodin, and B. Romanowicz (2016), Layered structure in the upper mantle across North America from joint inversion of long and short period seismic data, *Earth and Planetary Science Letters*, *449*, 164–175.

Cammarano, F., and B. Romanowicz (2007), Insights into the nature of the transition zone from physically constrained inversion of long-period seismic data, *Proceedings of the National Academy of Sciences*, *104*(22), 9139–9144.

Cammarano, F., A. Deuss, S. Goes, and D. Giardini (2005), One-dimensional physical reference models for the upper mantle and transition zone: Combining seismic and mineral physics constraints, *Journal of Geophysical Research: Solid Earth*, *110*(B1).

Cao, A., and A. Levander (2010), High-resolution transition zone structures of the Gorda Slab beneath the western United States: Implication for deep water subduction, *Journal of Geophysical Research: Solid Earth*, *115*(B7).

Carlson, R. W., D. G. Pearson, and D. E. James (2005), Physical, chemical, and chronological characteristics of continental mantle, *Reviews of Geophysics*, *43*(1).

Chang, Y.-Y., S. D. Jacobsen, C. R. Bina, S.-M. Thomas, J. R. Smyth, D. J. Frost, T. Boffa Ballaran, C. A. McCammon, E. H. Hauri, T. Inoue, et al. (2015), Comparative compressibility of hydrous wadsleyite and ringwoodite: Effect of H2O and implications for detecting water in the transition zone, *Journal of Geophysical Research: Solid Earth*, *120*(12), 8259–8280.

Chave, A. D., and D. J. Thomson (1989), Some comments on magnetotelluric response function estimation, *J. geophys. Res*, *94*(14), 215–14.

Chen, C.-Y., F. Frey, M. Garcia, G. Dalrymple, and S. Hart (1991), The tholeiite to alkalic basalt transition at Haleakala Volcano, Maui, Hawaii, *Contributions to Mineralogy and Petrology*, *106*(2), 183–200.

Chen, L., and Y. Ai (2009), Discontinuity structure of the mantle transition zone beneath the North China Craton from receiver function migration, *Journal of Geophysical Research: Solid Earth*, *114*(B6).

Cherepanova, Y., I. M. Artemieva, H. Thybo, and Z. Chemia (2013), Crustal structure of the Siberian craton and the West Siberian basin: An appraisal of existing seismic data, *Tectonophysics*, *609*, 154–183.

Chevrot, S., L. Vinnik, and J.-P. Montagner (1999), Global-scale analysis of the mantle Pds phases, *Journal of Geophysical Research: Solid Earth*, *104*(B9), 20,203–20,219.

Christensen, U. (2001), Geodynamic models of deep subduction, *Physics of the Earth and Planetary Interiors*, *127*(1), 25–34.

Chulliat, A., X. Lalanne, L. R. Gaya-Piqué, F. Truong, and J. Savary (2009), The new Easter island magnetic observatory, in *Proceedings of the XIIIth IAGA workshop on geomagnetic observatory instruments, data acquisition and processing*, pp. 2009–1226.

Chust, T., G. Steinle-Neumann, D. Dolejš, B. Schuberth, and H.-P. Bunge (2017), MMA-EoS: A Computational Framework for Mineralogical Thermodynamics, *Journal of Geophysical Research: Solid Earth*, *122*(12), 9881–9920.

Cline II, C., U. Faul, E. David, A. Berry, and I. Jackson (2018), Redox-influenced seismic properties of upper-mantle olivine, *Nature*, *555*(7696), 355.

Cobden, L., S. Goes, F. Cammarano, and J. A. Connolly (2008), Thermochemical interpretation of one-dimensional seismic reference models for the upper mantle: evidence for bias due to heterogeneity, *Geophysical Journal International*, *175*(2), 627–648.

Connolly, J. (2009), The geodynamic equation of state: what and how, *Geochemistry, Geophysics, Geosystems*, *10*(10).

Connolly, J., and A. Khan (2016), Uncertainty of mantle geophysical properties computed from phase equilibrium models, *Geophysical Research Letters*, *43*(10), 5026–5034.

Constable, S., and C. Constable (2004), Observing geomagnetic induction in magnetic satellite measurements and associated implications for mantle conductivity, *Geochemistry, Geophysics, Geosystems*, *5*(1).

Cottaar, S., and A. Deuss (2016), Large-scale mantle discontinuity topography beneath Europe: Signature of akimotoite in subducting slabs, *Journal of Geophysical Research: Solid Earth*, *121*(1), 279–292.

Courtier, A. M., and J. Revenaugh (2006), A water-rich transition zone beneath the eastern United States and Gulf of Mexico from multiple ScS reverberations, *Earth's Deep Water Cycle*, pp. 181–193.

Courtier, A. M., and J. Revenaugh (2007), Deep upper-mantle melting beneath the Tasman and Coral Seas detected with multiple ScS reverberations, *Earth and Planetary Science Letters*, *259*(1), 66–76.

Courtier, A. M., M. G. Jackson, J. F. Lawrence, Z. Wang, C.-T. A. Lee, R. Halama, J. M. Warren, R. Workman, W. Xu, M. M. Hirschmann, et al. (2007), Correlation of seismic and petrologic thermometers suggests deep thermal anomalies beneath hotspots, *Earth and Planetary Science Letters*, *264*(1), 308–316.

Daglis, I., and J. Kozyra (2002), Outstanding issues of ring current dynamics, *Journal of atmospheric and solar-terrestrial physics*, *64*(2), 253–264.

Dai, L., and S.-i. Karato (2009), Electrical conductivity of orthopyroxene: Implications for the water content of the asthenosphere, *Proceedings of the Japan Academy, Series B*, *85*(10), 466–475.

Davies, G. F. (2006), Gravitational depletion of the early Earth's upper mantle and the viability of early plate tectonics, *Earth and Planetary Science Letters*, *243*(3), 376–382.

Deschamps, F., and A. Khan (2016), Electrical conductivity as a constraint on lower mantle thermo-chemical structure, *Earth and Planetary Science Letters*, *450*, 108–119.

Deschamps, F., and J. Trampert (2004), Towards a lower mantle reference temperature and composition, *Earth and Planetary Science Letters*, *222*(1), 161–175.

Deuss, A., S. A. Redfern, K. Chambers, and J. H. Woodhouse (2006), The nature of the 660-kilometer discontinuity in Earth's mantle from global seismic observations of PP precursors, *Science*, *311*(5758), 198–201.

Deuss, A., J. Andrews, and E. Day (2013), Seismic observations of mantle discontinuities and their mineralogical and dynamical interpretation, *Physics and Chemistry of the Deep Earth*, pp. 297–323.

Diouane, Y. (2014), Globally convergent evolution strategies with application to Earth imaging problem in geophysics, Ph.D. thesis.

Dobson, D. P., and J. P. Brodholt (2000), The electrical conductivity and thermal profile of the Earth's mid-mantle, *Geophysical research letters*, *27*(15), 2325–2328.

Drilleau, M., E. Beucler, A. Mocquet, O. Verhoeven, G. Moebs, G. Burgos, J.-P. Montagner, and P. Vacher (2013), A Bayesian approach to infer radial models of temperature and anisotropy in the transition zone from surface wave dispersion curves, *Geophysical Journal International*, *195*(2), 1165–1183.

Duesterhoeft, E., and C. Capitani (2013), THERIAK_D: An add-on to implement equilibrium computations in geodynamic models, *Geochemistry, Geophysics, Geosystems*, *14*(11), 4962–4967.

Duesterhoeft, E., J. Quinteros, R. Oberhaensli, R. Bousquet, and C. de Capitani (2014), Relative impact of mantle densification and eclogitization of slabs on subduction dynamics: A numerical thermodynamic/thermokinematic investigation of metamorphic density evolution, *Tectonophysics*, *637*, 20–29.

Durand, S., E. Debayle, and Y. Ricard (2015), Rayleigh wave phase velocity and error maps up to the fifth overtone, *Geophysical Research Letters*, *42*(9), 3266–3272.

Dziewonski, A. M., and D. L. Anderson (1981), Preliminary reference Earth model, *Physics of the earth and planetary interiors*, *25*(4), 297–356.

Efron, B. (1982), *The jackknife, the bootstrap and other resampling plans*, vol. 38, SIAM.

Efron, B., and R. Tibshirani (1991), Statistical data analysis in the computer age, *Science*, pp. 390–395.

Egbert, G. D., and J. R. Booker (1992), Very long period magnetotellurics at Tucson observatory: implications for mantle conductivity, *Journal of Geophysical Research: Solid Earth*, *97*(B11), 15,099–15,112.

Elshall, A. S., H. V. Pham, F. T.-C. Tsai, L. Yan, and M. Ye (2015), Parallel inverse modeling and uncertainty quantification for computationally demanding groundwater-flow models using covariance matrix adaptation, *Journal of Hydrologic Engineering*, *20*(8), 04014,087.

Everett, M. E., S. Constable, and C. G. Constable (2003), Effects of near-surface conductance on global satellite induction responses, *Geophysical Journal International*, *153*(1), 277–286.

Farra, V., and L. Vinnik (2000), Upper mantle stratification by P and S receiver functions, *Geophysical Journal International*, *141*(3), 699–712.

Ferot, A., and N. Bolfan-Casanova (2012), Water storage capacity in olivine and pyroxene to 14GPa: Implications for the water content of the Earth's upper mantle and nature of seismic discontinuities, *Earth and Planetary Science Letters*, *349*, 218–230.

Fichtner, A., B. L. Kennett, H. Igel, and H.-P. Bunge (2009), Full seismic waveform tomography for upper-mantle structure in the Australasian region using adjoint methods, *Geophysical Journal International*, *179*(3), 1703–1725.

Finlay, C., V. Lesur, E. Thébault, F. Vervelidou, A. Morschhauser, and R. Shore (2017), Challenges handling magnetospheric and ionospheric signals in internal geomagnetic field modelling.

Fonseca, R., O. Leeuwenburgh, P. Van den Hof, J.-D. Jansen, et al. (2014), Improving the ensemble-optimization method through covariance-matrix adaptation, *SPE Journal*, *20*(01), 155–168.

Forte, A. M., and H. C. Perry (2000), Geodynamic evidence for a chemically depleted continental tectosphere, *Science*, *290*(5498), 1940–1944.

Francis, D. (1987), Mantle-melt interaction recorded in spinel lherzolite xenoliths from the Alligator Lake volcanic complex, Yukon, Canada, *Journal of Petrology*, *28*(3), 569–597.

Freitas, D., G. Manthilake, F. Schiavi, J. Chantel, N. Bolfan-Casanova, M. Bouhifd, and D. Andrault (2017), Experimental evidence supporting a global melt layer at the base of the Earth's upper mantle, *Nature communications*, *8*(1), 2186.

French, S., and B. Romanowicz (2014), Whole-mantle radially anisotropic shear velocity structure from spectral-element waveform tomography, *Geophysical Journal International*, *199*(3), 1303–1327.

Frey, F., D. Green, and S. Roy (1978), Integrated models of basalt petrogenesis: a study of quartz tholeiites to olivine melilitites from south eastern Australia utilizing geochemical and experimental petrological data, *Journal of petrology*, *19*(3), 463–513.

Frost, D. J., and D. Dolejš (2007), Experimental determination of the effect of H_2O on the 410–km seismic discontinuity, *Earth and Planetary Science Letters*, *256*(1-2), 182–195.

Fuchs, K., and G. Müller (1971), Computation of synthetic seismograms with the reflectivity method and comparison with observations, *Geophysical Journal International*, *23*(4), 417–433.

Fujii, I., and A. Schultz (2002), The 3D electromagnetic response of the Earth to ring current and auroral oval excitation, *Geophysical Journal International*, *151*(3), 689–709.

Fullea, J., J. C. Afonso, J. Connolly, M. Fernandez, D. García-Castellanos, and H. Zeyen (2009), LitMod3D: An interactive 3-D software to model the thermal, compositional, density, seismological, and rheological structure of the lithosphere and sublithospheric upper mantle, *Geochemistry, Geophysics, Geosystems*, *10*(8).

Fullea, J., M. Muller, and A. Jones (2011), Electrical conductivity of continental lithospheric mantle from integrated geophysical and petrological modeling: Application to the Kaapvaal Craton and Rehoboth Terrane, southern Africa, *Journal of Geophysical Research: Solid Earth*, *116*(B10).

Gallardo, L. A., and M. A. Meju (2007), Joint two-dimensional cross-gradient imaging of magnetotelluric and seismic traveltime data for structural and lithological classification, *Geophysical Journal International*, *169*(3), 1261–1272.

Ghosh, S., E. Ohtani, K. D. Litasov, A. Suzuki, D. Dobson, and K. Funakoshi (2013), Effect of water in depleted mantle on post-spinel transition and implication for 660 km seismic discontinuity, *Earth and Planetary Science Letters*, *371*, 103–111.

Gillmann, C., and P. Tackley (2014), Atmosphere/mantle coupling and feedbacks on venus, *Journal of Geophysical Research: Planets*, *119*(6), 1189–1217.

Goes, S., R. Govers, and P. Vacher (2000), Shallow mantle temperatures under Europe from P and S wave tomography, *Journal of Geophysical Research: Solid Earth*, *105*(B5), 11,153–11,169.

Goes, S., F. J. Simons, and K. Yoshizawa (2005), Seismic constraints on temperature of the Australian uppermost mantle, *Earth and Planetary Science Letters*, *236*(1-2), 227–237.

Grayver, A., F. Munch, A. Kuvshinov, A. Khan, T. Sabaka, and L. Tøffner-Clausen (2017), Joint inversion of satellite-detected tidal and magnetospheric signals constrains electrical conductivity and water content of the upper mantle and transition zone, *Geophysical Research Letters*.

Grayver, A. V., and A. V. Kuvshinov (2016), Exploring equivalence domain in nonlinear inverse problems using Covariance Matrix Adaption Evolution Strategy (CMAES) and random sampling, *Geophysical Journal International*, *205*(2), 971–987.

Grayver, A. V., N. R. Schnepf, A. V. Kuvshinov, T. J. Sabaka, C. Manoj, and N. Olsen (2016), Satellite tidal magnetic signals constrain oceanic lithosphere-asthenosphere boundary, *Science Advances*, *2*(9), e1600,798.

Guzavina, M., A. Grayver, and A. Kuvshinov (2019), Probing upper mantle electrical conductivity with daily magnetic variations using global-to-local transfer functions, *Geophysical Journal International (manuscript in review)*.

Hansen, N., and A. Ostermeier (2001), Completely derandomized self-adaptation in evolution strategies, *Evolutionary computation*, *9*(2), 159–195.

Hansen, N., R. Ros, N. Mauny, M. Schoenauer, and A. Auger (2011), Impacts of invariance in search: When CMA-ES and PSO face ill-conditioned and non-separable problems, *Applied Soft Computing*, *11*(8), 5755–5769.

Hansen, P. C. (1999), The L-curve and its use in the numerical treatment of inverse problems.

Hashin, Z., and S. Shtrikman (1963), A variational approach to the theory of the elastic behaviour of multiphase materials, *Journal of the Mechanics and Physics of Solids*, *11*(2), 127–140.

Hastings, W. K. (1970), Monte Carlo sampling methods using Markov chains and their applications, *Biometrika*, *57*(1), 97–109.

Hedlin, M. A., P. M. Shearer, P. S. Earle, et al. (1997), Seismic evidence for small-scale heterogeneity throughout the Earth's mantle, *Nature*, *387*(6629), 145–150.

Heit, B., F. Sodoudi, X. Yuan, M. Bianchi, and R. Kind (2007), An S receiver function analysis of the lithospheric structure in South America, *Geophysical Research Letters*, *34*(14).

Helffrich, G. (2000), Topography of the transition zone seismic discontinuities, *Reviews of Geophysics*, *38*(1), 141–158.

Helffrich, G. (2006), Heterogeneity in the mantle–its creation, evolution and destruction, *Tectonophysics*, *416*(1), 23–31.

Henderson, P., and G. M. Henderson (2009), The Cambridge handbook of Earth Science data.

Herzberg, C., P. D. Asimow, N. Arndt, Y. Niu, C. Lesher, J. Fitton, M. Cheadle, and A. Saunders (2007), Temperatures in ambient mantle and plumes: Constraints from basalts, picrites, and komatiites, *Geochemistry, Geophysics, Geosystems*, *8*(2).

Hirschmann, M. M. (2006), Water, melting, and the deep Earth H2O cycle, *Annu. Rev. Earth Planet. Sci.*, *34*, 629–653.

Hirschmann, M. M. (2010), Partial melt in the oceanic low velocity zone, *Physics of the Earth and Planetary Interiors*, *179*(1-2), 60–71.

Hirschmann, M. M., C. Aubaud, and A. C. Withers (2005), Storage capacity of H_2O in nominally anhydrous minerals in the upper mantle, *Earth and Planetary Science Letters*, *236*(1), 167–181.

Hofmann, A., and S. Hart (1978), An assessment of local and regional isotopic equilibrium in the mantle, *Earth and Planetary Science Letters*, *38*(1), 44–62.

Hofmann, A. W., and W. M. White (1982), Mantle plumes from ancient oceanic crust, *Earth and Planetary Science Letters*, *57*(2), 421–436.

Holland, T., and R. Powell (2011), An improved and extended internally consistent thermodynamic dataset for phases of petrological interest, involving a new equation of state for solids, *Journal of Metamorphic Geology*, *29*(3), 333–383.

Huang, X., Y. Xu, and S.-i. Karato (2005), Water content in the transition zone from electrical conductivity of wadsleyite and ringwoodite, *Nature*, *434*(7034), 746.

Inoue, T. (1994), Effect of water on melting phase relations and melt composition in the system Mg_2SiO_4–$MgSiO_3$–H_2O up to 15 GPa, *Physics of the Earth and Planetary Interiors*, *85*(3-4), 237–263.

Inoue, T., T. Wada, R. Sasaki, and H. Yurimoto (2010), Water partitioning in the Earth's mantle, *Physics of the Earth and Planetary Interiors*, *183*(1), 245–251.

Irifune, T. (), Phase transformations in the Earth's mantle and subducting slabs: Implications for their compositions, seismic velocity and density structures and dynamics, *Island Arc*, *2*(2), 55–71.

Irifune, T. (1994), Absence of an aluminous phase in the upper part of the Earth's lower mantle, *Nature*, *370*(6485), 131–133.

Ita, J., and L. Stixrude (1992), Petrology, elasticity, and composition of the mantle transition zone, *Journal of Geophysical Research: Solid Earth*, *97*(B5), 6849–6866.

Jackson, I., and U. H. Faul (2010), Grainsize-sensitive viscoelastic relaxation in olivine: Towards a robust laboratory-based model for seismological application, *Physics of the Earth and Planetary Interiors*, *183*(1-2), 151–163.

Jackson, J. M., J. Zhang, J. Shu, S. V. Sinogeikin, and J. D. Bass (2005), High-pressure sound velocities and elasticity of aluminous MgSiO3 perovskite to 45 GPa: Implications for lateral heterogeneity in Earth's lower mantle, *Geophysical Research Letters*, *32*(21).

Jacobsen, B. H., and L. Svenningsen (2008), Enhanced uniqueness and linearity of receiver function inversion, *Bulletin of the Seismological Society of America*, *98*(4), 1756–1767.

Jasbinsek, J., and K. Dueker (2007), Ubiquitous low-velocity layer atop the 410-km discontinuity in the northern Rocky Mountains, *Geochemistry, Geophysics, Geosystems*, *8*(10).

Jones, A. G., J. Fullea, R. L. Evans, and M. R. Muller (2012), Water in cratonic lithosphere: Calibrating laboratory-determined models of electrical conductivity of mantle minerals using geophysical and petrological observations, *Geochemistry, Geophysics, Geosystems*, *13*(6).

Jordan, T. H. (1978), Composition and development of the continental tectosphere, *Nature*, *274*(5671), 544.

Kanamori, H., and D. L. Anderson (1977), Importance of physical dispersion in surface wave and free oscillation problems, *Reviews of Geophysics*, *15*(1), 105–112.

Karato, S.-i. (1995), Effects of water on seismic wave velocities in the upper mantle, *Proceedings of the Japan Academy, Series B*, *71*(2), 61–66.

Karato, S.-i. (2010), Water distribution across the mantle transition zone and its implications for global material circulation, *Earth and Planetary Science Letters*, *301*(3), 413–423.

Karato, S.-I., and H. Jung (2003), Effects of pressure on high-temperature dislocation creep in olivine, *Philosophical Magazine*, *83*(3), 401–414.

Karato, S.-i., and D. Wang (2013), Electrical conductivity of minerals and rocks, *Physics and Chemistry of the Deep Earth*, pp. 145–182.

Katsura, T., and T. Yoshino (2015), Heterogeneity of electrical conductivity in the oceanic upper mantle, in *The Earth's Heterogeneous Mantle*, pp. 173–204, Springer.

Katsura, T., S. Yokoshi, K. Kawabe, A. Shatskiy, M. Okube, H. Fukui, E. Ito, A. Nozawa, and K.-i. Funakoshi (2007), Pressure dependence of electrical conductivity of (Mg, Fe) SiO3 ilmenite, *Physics and Chemistry of Minerals*, *34*(4), 249–255.

Katsura, T., A. Yoneda, D. Yamazaki, T. Yoshino, and E. Ito (2010), Adiabatic temperature profile in the mantle, *Physics of the Earth and Planetary Interiors*, *183*(1-2), 212–218.

Kelbert, A., A. Schultz, and G. Egbert (2009), Global electromagnetic induction constraints on transition-zone water content variations, *Nature*, *460*(7258), 1003–1006.

Kelbert, A., A. Kuvshinov, J. Velímskỳ, T. Koyama, J. Ribaudo, J. Sun, Z. Martinec, and C. J. Weiss (2014), Global 3-D electromagnetic forward modelling: a benchmark study, *Geophysical Journal International*, *197*(2), 785–814.

Kennett, B., and E. Engdahl (1991), Traveltimes for global earthquake location and phase identification, *Geophysical Journal International*, *105*(2), 429–465.

Keppler, H., and N. Bolfan-Casanova (2006), Thermodynamics of water solubility and partitioning, *Reviews in Mineralogy and Geochemistry*, *62*(1), 193–230.

Khan, A. (2016), On Earth's mantle constitution and structure from joint analysis of geophysical and laboratory-based data: An example, *Surveys in Geophysics*, *37*(1), 149–189.

Khan, A., and T. Shankland (2012), A geophysical perspective on mantle water content and melting: Inverting electromagnetic sounding data using laboratory-based electrical conductivity profiles, *Earth and Planetary Science Letters*, *317*, 27–43.

Khan, A., J. Connolly, and N. Olsen (2006), Constraining the composition and thermal state of the mantle beneath Europe from inversion of long-period electromagnetic sounding data, *Journal of Geophysical Research: Solid Earth*, *111*(B10).

Khan, A., J. Connolly, J. Maclennan, and K. Mosegaard (2007), Joint inversion of seismic and gravity data for lunar composition and thermal state, *Geophysical Journal International*, *168*(1), 243–258.

Khan, A., J. Connolly, and S. Taylor (2008), Inversion of seismic and geodetic data for the major element chemistry and temperature of the Earth's mantle, *Journal of Geophysical Research: Solid Earth*, *113*(B9).

Khan, A., L. Boschi, and J. Connolly (2009), On mantle chemical and thermal heterogeneities and anisotropy as mapped by inversion of global surface wave data, *Journal of Geophysical Research: Solid Earth*, *114*(B9).

Khan, A., A. Zunino, and F. Deschamps (2011a), The thermo-chemical and physical structure beneath the North American continent from Bayesian inversion of surface-wave phase velocities, *Journal of Geophysical Research: Solid Earth*, *116*(B9).

Khan, A., A. Kuvshinov, and A. Semenov (2011b), On the heterogeneous electrical conductivity structure of the Earth's mantle with implications for transition zone water content, *Journal of Geophysical Research: Solid Earth*, *116*(B1).

Khan, A., A. Zunino, and F. Deschamps (2013), Upper mantle compositional variations and discontinuity topography imaged beneath Australia from bayesian inversion of surface-wave phase velocities and thermochemical modeling, *Journal of Geophysical Research: Solid Earth*, *118*(10), 5285–5306.

Khan, A., C. Liebske, A. Rozel, A. Rivoldini, F. Nimmo, J. Connolly, A.-C. Plesa, and D. Giardini (2018), A geophysical perspective on the bulk composition of Mars, *Journal of Geophysical Research: Planets*.

Kind, R., and L. Vinnik (1988), The upper mantle discontinuities underneath the GRF array from P-to-S converted phases, *J. geophys*, *62*(13), 147.

Kind, R., X. Yuan, and P. Kumar (2012), Seismic receiver functions and the lithosphere–asthenosphere boundary, *Tectonophysics*, *536*, 25–43.

Koch, S., and A. Kuvshinov (2013), Global 3-D EM inversion of Sq variations based on simultaneous source and conductivity determination: concept validation and resolution studies, *Geophysical Journal International*, *195*(1), 98–116.

Koch, S., and A. Kuvshinov (2015), 3–D EM inversion of ground based geomagnetic Sq data. Results from the analysis of Australian array (AWAGS) data, *Geophysical Journal International*, *200*(3), 1284–1296.

Kohlstedt, D., H. Keppler, and D. Rubie (1996), Solubility of water in the α, β and γ phases of (Mg, Fe)$_2$SiO$_4$, *Contributions to Mineralogy and Petrology*, *123*(4), 345–357.

Kopylova, M. G., and J. K. Russell (2000), Chemical stratification of cratonic lithosphere: constraints from the Northern Slave craton, Canada, *Earth and Planetary Science Letters*, *181*(1-2), 71–87.

Korte, M., M. Mandea, H.-J. Linthe, A. Hemshorn, P. Kotzé, and E. Ricaldi (2009), New geomagnetic field observations in the South Atlantic Anomaly region, *Annals of Geophysics*, *52*(1), 65–81.

Koyama, T., H. Shimizu, H. Utada, M. Ichiki, E. Ohtani, and R. Hae (2006), Water content in the mantle transition zone beneath the north pacific derived from the electrical conductivity anomaly, *Earth's Deep Water Cycle*, pp. 171–179.

Koyama, T., A. Khan, and A. Kuvshinov (2014), Three-dimensional electrical conductivity structure beneath Australia from inversion of geomagnetic observatory data: evidence for lateral variations in transition-zone temperature, water content and melt, *Geophysical Journal International*, *196*(3), 1330.

Krischer, L., A. R. Hutko, M. Van Driel, S. Stähler, M. Bahavar, C. Trabant, and T. Nissen-Meyer (2017), On-demand custom broadband synthetic seismograms, *Seismological Research Letters*, *88*(4), 1127–1140.

Krischer, L., A. Fichtner, C. Boehm, and H. Igel (2018), Automated large-scale full seismic waveform inversion for North America and the North Atlantic, *Journal of Geophysical Research: Solid Earth*, *123*(7), 5902–5928.

Kumar, P., R. Kind, X. Yuan, and J. Mechie (2012), USarray receiver function images of the lithosphere-asthenosphere boundary, *Seismological Research Letters*, *83*(3), 486–491.

Kuvshinov, A. (2008), 3-D global induction in the oceans and solid Earth: recent progress in modeling magnetic and electric fields from sources of magnetospheric, ionospheric and oceanic origin, *Surveys in geophysics*, *29*(2), 139–186.

Kuvshinov, A., and N. Olsen (2006), A global model of mantle conductivity derived from 5 years of CHAMP, ørsted, and SAC-C magnetic data, *Geophysical research letters*, *33*(18).

Kuvshinov, A. V., N. Olsen, D. B. Avdeev, and O. V. Pankratov (2002), Electromagnetic induction in the oceans and the anomalous behaviour of coastal C-responses for periods up to 20 days, *Geophysical research letters*, *29*(12).

Landauer, R. (1952), The electrical resistance of binary metallic mixtures, *Journal of Applied Physics*, *23*(7), 779–784.

Langston, C. A. (1979), Structure under Mount Rainier, Washington, inferred from teleseismic body waves, *Journal of Geophysical Research: Solid Earth*, *84*(B9), 4749–4762.

Langston, C. A., and J. K. Hammer (2001), The vertical component P-wave receiver function, *Bulletin of the Seismological Society of America*, *91*(6), 1805–1819.

Lawrence, J. F., and P. M. Shearer (2006a), A global study of transition zone thickness using receiver functions, *Journal of Geophysical Research: Solid Earth*, *111*(B6).

Lawrence, J. F., and P. M. Shearer (2006b), Constraining seismic velocity and density for the mantle transition zone with reflected and transmitted waveforms, *Geochemistry, Geophysics, Geosystems*, *7*(10).

Lekić, V., and B. Romanowicz (2011), Inferring upper-mantle structure by full waveform tomography with the spectral element method, *Geophysical Journal International*, *185*(2), 799–831.

Lenardic, A., L.-N. Moresi, A. Jellinek, and M. Manga (2005), Continental insulation, mantle cooling, and the surface area of oceans and continents, *Earth and Planetary Science Letters*, *234*(3-4), 317–333.

Ligorria, J. P., and C. J. Ammon (1999), Iterative deconvolution and receiver-function estimation, *Bulletin of the seismological Society of America*, *89*(5), 1395–1400.

Litasov, K. (2011), Physicochemical conditions for melting in the Earth's mantle containing a C–O–H fluid (from experimental data), *Russian Geology and Geophysics*, *52*(5), 475–492.

Litasov, K. D., A. Shatskiy, E. Ohtani, and T. Katsura (2011), Systematic study of hydrogen incorporation into Fe-free wadsleyite, *Physics and Chemistry of Minerals*, *38*(1), 75–84.

Liu, K. H. (2003), Effects of inelasticity on the apparent depth and detectability of seismic discontinuities in the mantle, *Geophysical research letters*, *30*(9).

Lodge, A., and G. Helffrich (2009), Grid search inversion of teleseismic receiver functions, *Geophysical Journal International*, *178*(1), 513–523.

Lombardi, D., J. Braunmiller, E. Kissling, and D. Giardini (2009), Alpine mantle transition zone imaged by receiver functions, *Earth and Planetary Science Letters*, *278*(3-4), 163–174.

Lyubetskaya, T., and J. Korenaga (2007), Chemical composition of Earth's primitive mantle and its variance: 1. Method and results, *Journal of Geophysical Research: Solid Earth*, *112*(B3).

Macmillan, S., and N. Olsen (2013), Observatory data and the Swarm mission, *Earth, Planets and Space*, *65*(11), 1355–1362.

Maguire, R., J. Ritsema, and S. Goes (2017), Signals of 660 km topography and harzburgite enrichment in seismic images of whole-mantle upwellings, *Geophysical Research Letters*, *44*(8), 3600–3607.

Maguire, R., J. Ritsema, and S. Goes (2018), Evidence of subduction related thermal and compositional heterogeneity below the United States from transition-zone receiver functions, *Geophysical Research Letters*.

Manoj, C., A. Kuvshinov, S. Maus, and H. Lühr (2006), Ocean circulation generated magnetic signals, *Earth, Planets and Space*, *58*(4), 429–437.

Mao, Z., S. Jacobsen, F. Jiang, J. Smyth, C. Holl, and T. Duffy (2008), Elasticity of hydrous wadsleyite to 12 GPa: implications for Earth's transition zone, *Geophysical Research Letters*, *35*(21).

Mattern, E., J. Matas, Y. Ricard, and J. Bass (2005), Lower mantle composition and temperature from mineral physics and thermodynamic modelling, *Geophysical Journal International*, *160*(3), 973–990.

Matzka, J., N. Olsen, C. F. Maule, L. W. Pedersen, A. Berarducci, and S. Macmillan (2009), Geomagnetic observations on Tristan da Cunha, south Atlantic ocean, *Annal of Geophysics*, *52*(1), 97–105.

Mavko, G., T. Mukerji, and J. Dvorkin (2009), *The rock physics handbook: Tools for seismic analysis of porous media*, Cambridge university press.

McKenzie, D., and M. Bickle (1988), The volume and composition of melt generated by extension of the lithosphere, *Journal of petrology*, *29*(3), 625–679.

Mei, S., and D. L. Kohlstedt (2000), Influence of water on plastic deformation of olivine aggregates: 1. Diffusion creep regime, *Journal of Geophysical Research: Solid Earth*, *105*(B9), 21,457–21,469.

Meqbel, N. M., G. D. Egbert, P. E. Wannamaker, A. Kelbert, and A. Schultz (2014), Deep electrical resistivity structure of the northwestern US derived from 3-D inversion of USArray magnetotelluric data, *Earth and Planetary Science Letters*, *402*, 290–304.

Metropolis, N., A. W. Rosenbluth, M. N. Rosenbluth, A. H. Teller, and E. Teller (1953), Equation of state calculations by fast computing machines, *The journal of chemical physics*, *21*(6), 1087–1092.

Monteiller, V., S. Chevrot, D. Komatitsch, and N. Fuji (2012), A hybrid method to compute short-period synthetic seismograms of teleseismic body waves in a 3-D regional model, *Geophysical Journal International*, *192*(1), 230–247.

Mookherjee, M., and S.-i. Karato (2010), Solubility of water in pyrope-rich garnet at high pressures and temperature, *Geophysical Research Letters*, *37*(3).

Moorkamp, M., A. Jones, and S. Fishwick (2010), Joint inversion of receiver functions, surface wave dispersion, and magnetotelluric data, *Journal of Geophysical Research: Solid Earth*, *115*(B4).

Mosegaard, K., and A. Tarantola (1995), Monte Carlo sampling of solutions to inverse problems, *Journal of Geophysical Research: Solid Earth*, *100*(B7), 12,431–12,447.

Muller, G. (1985), The reflectivity method - A tutorial, *Journal of Geophysics-Zeitschrift Fur Geophysik*, *58*(1-3), 153–174.

Munch, F., A. Grayver, A. Kuvshinov, and A. Khan (2018a), Stochastic inversion of geomagnetic observatory data including rigorous treatment of the ocean induction effect with implications for transition zone water content and thermal structure, *Journal of Geophysical Research: Solid Earth*, *123*(1), 31–51.

Munch, F., A. Khan, B. Tauzin, M. van Driel, and D. Giardini (2019), Seismological evidence for the existence of thermo-chemical heterogeneity in Earth's continental mantle, *manuscript under consideration for publication in Nature Geoscience*.

Munch, F. D., A. Khan, B. Tauzin, A. Zunino, and D. Giardini (2018b), Stochastic inversion of P-to-s converted waves for mantle composition and thermal structure: Methodology and application, *Journal of Geophysical Research: Solid Earth*.

Murakami, M., Y. Ohishi, N. Hirao, and K. Hirose (2012), A perovskitic lower mantle inferred from high-pressure, high-temperature sound velocity data, *Nature*, *485*(7396), 90.

Nakagawa, T., and B. A. Buffett (2005), Mass transport mechanism between the upper and lower mantle in numerical simulations of thermochemical mantle convection with multicomponent phase changes, *Earth and Planetary Science Letters*, *230*(1), 11–27.

Nakagawa, T., P. J. Tackley, F. Deschamps, and J. A. Connolly (2010), The influence of MORB and harzburgite composition on thermo-chemical mantle convection in a 3-D spherical shell with self-consistently calculated mineral physics, *Earth and Planetary Science Letters*, *296*(3-4), 403–412.

Nettles, M., and A. M. Dziewoński (2008), Radially anisotropic shear velocity structure of the upper mantle globally and beneath North America, *Journal of Geophysical Research: Solid Earth*, *113*(B2).

Nissen-Meyer, T., M. van Driel, S. C. Stähler, K. Hosseini, S. Hempel, L. Auer, A. Colombi, and A. Fournier (2014), AxiSEM: broadband 3-D seismic wavefields in axisymmetric media, *Solid Earth*, *5*(1), 425.

Niu, F., and H. Kawakatsu (1996), Complex structure of mantle discontinuities at the tip of the subducting slab beneath northeast China, *Journal of Physics of the Earth*, *44*(6), 701–711.

Noack, L., D. Breuer, and T. Spohn (2012), Coupling the atmosphere with interior dynamics: Implications for the resurfacing of Venus, *Icarus*, *217*(2), 484–498.

Ohira, I., E. Ohtani, T. Sakai, M. Miyahara, N. Hirao, Y. Ohishi, and M. Nishijima (2014), Stability of a hydrous δ-phase, AlOOH–$MgSiO_2(OH)_2$, and a mechanism for water transport into the base of lower mantle, *Earth and Planetary Science Letters*, *401*, 12–17.

Ohtani, E., K. Litasov, T. Hosoya, T. Kubo, and T. Kondo (2004), Water transport into the deep mantle and formation of a hydrous transition zone, *Physics of the Earth and Planetary Interiors*, *143*, 255–269.

Olsen, N. (1998), The electrical conductivity of the mantle beneath Europe derived from C-responses from 3 to 720 hr, *Geophysical Journal International*, *133*(2), 298–308.

Olsen, N., and A. Kuvshinov (2004), Modeling the ocean effect of geomagnetic storms, *Earth, planets and space*, *56*(5), 525–530.

Olsen, N., and C. Stolle (2017), Magnetic signatures of ionospheric and magnetospheric current systems during geomagnetic quiet conditions—an overview, *Space Science Reviews*, *206*(1-4), 5–25.

Olsen, N., S. Vennerstrøm, and E. Friis-Christensen (2003), Monitoring magnetospheric contributions using ground-based and satellite magnetic data, in *First CHAMP Mission Results for Gravity, Magnetic and Atmospheric Studies*, pp. 245–250, Springer.

Olsen, N., H. Lühr, T. J. Sabaka, M. Mandea, M. Rother, L. Tøffner-Clausen, and S. Choi (2006), CHAOS– A model of the Earth's magnetic field derived from CHAMP, ørsted, and SAC-C magnetic satellite data, *Geophysical Journal International*, *166*(1), 67–75.

Oreshin, S., S. Kiselev, L. Vinnik, K. S. Prakasam, S. S. Rai, L. Makeyeva, and Y. Savvin (2008), Crust and mantle beneath western Himalaya, Ladakh and western Tibet from integrated seismic data, *Earth and Planetary Science Letters*, *271*(1-4), 75–87.

Owens, T. J., A. A. Nyblade, H. Gurrola, and C. A. Langston (2000), Mantle transition zone structure beneath Tanzania, East Africa, *Geophysical Research Letters*, *27*(6), 827–830.

Palme, H., and H. S. C. O'Neill (2003), Cosmochemical estimates of mantle composition, *Treatise on geochemistry*, *2*, 568.

Park, S. K., and M. N. Ducea (2003), Can in situ measurements of mantle electrical conductivity be used to infer properties of partial melts?, *Journal of Geophysical Research: Solid Earth*, *108*(B5).

Pearson, D., D. Canil, and S. Shirey (2003), Mantle samples included in volcanic rocks: xenoliths and diamonds, *Treatise on geochemistry*, *2*, 568.

Pearson, D., F. Brenker, F. Nestola, J. McNeill, L. Nasdala, M. Hutchison, S. Matveev, K. Mather, G. Silversmit, S. Schmitz, et al. (2014), Hydrous mantle transition zone indicated by ringwoodite included within diamond, *Nature*, *507*(7491), 221.

Peslier, A. H. (2010), A review of water contents of nominally anhydrous natural minerals in the mantles of Earth, Mars and the Moon, *Journal of Volcanology and Geothermal Research*, *197*(1-4), 239–258.

Peslier, A. H., and M. Bizimis (2015), Water in Hawaiian peridotite minerals: A case for a dry metasomatized oceanic mantle lithosphere, *Geochemistry, Geophysics, Geosystems*, *16*(4), 1211–1232.

Peslier, A. H., A. B. Woodland, D. R. Bell, and M. Lazarov (2010), Olivine water contents in the continental lithosphere and the longevity of cratons, *Nature*, *467*(7311), 78.

Peslier, A. H., M. Schönbächler, H. Busemann, and S.-I. Karato (2017), Water in the Earth's interior: distribution and origin, *Space Science Reviews*, *212*(1-2), 743–810.

Phinney, R. A. (1964), Structure of the Earth's crust from spectral behavior of long-period body waves, *Journal of Geophysical Research*, *69*(14), 2997–3017.

Pommier, A. (2014), Interpretation of magnetotelluric results using laboratory measurements, *Surveys in Geophysics*, *35*(1), 41.

Püthe, C. (2015), Interpretation of global EM induction data from ground, sea and space: New response functions, inversion schemes and conductivity models, Ph.D. thesis, Diss., Eidgenössische Technische Hochschule ETH Zürich, Nr. 22740.

Püthe, C., and A. Kuvshinov (2014), Mapping 3-D mantle electrical conductivity from space: a new 3-D inversion scheme based on analysis of matrix Q-responses, *Geophysical Journal International*, *197*(2), 768–784.

Püthe, C., A. Kuvshinov, A. Khan, and N. Olsen (2015a), A new model of Earth's radial conductivity structure derived from over 10 yr of satellite and observatory magnetic data, *Geophysical Journal International*, *203*(3), 1864–1872.

Püthe, C., A. Kuvshinov, and N. Olsen (2015b), Handling complex source structures in global EM induction studies: from C-responses to new arrays of transfer functions, *Geophysical Journal International*, *201*(1), 318–328.

Revenaugh, J., and S. Sipkinf (1994), Melt atop the 410-km mantle discontinuity, *Nature*, *369*, 9.

Ringwood, A. (1975), *Composition and petrology of the Earth's mantle*.

Ritsema, J., W. Xu, L. Stixrude, and C. Lithgow-Bertelloni (2009a), Estimates of the transition zone temperature in a mechanically mixed upper mantle, *Earth and Planetary Science Letters*, *277*(1), 244–252.

Ritsema, J., P. Cupillard, B. Tauzin, W. Xu, L. Stixrude, and C. Lithgow-Bertelloni (2009b), Joint mineral physics and seismic wave traveltime analysis of upper mantle temperature, *Geology*, *37*(4), 363–366.

Rondenay, S. (2009), Upper mantle imaging with array recordings of converted and scattered teleseismic waves, *Surveys in geophysics*, *30*(4-5), 377–405.

Roy, C., and B. Romanowicz (2017), On the implications of a-priori constraints in transdimensional bayesian inversion for continental lithospheric layering, *Journal of Geophysical Research: Solid Earth*.

Rychert, C. A., and P. M. Shearer (2009), A global view of the lithosphere-asthenosphere boundary, *Science*, *324*(5926), 495–498.

Schaeffer, A., and S. Lebedev (2013), Global shear speed structure of the upper mantle and transition zone, *Geophysical Journal International*, *194*(1), 417–449.

Schaeffer, A., and S. Lebedev (2015), Global heterogeneity of the lithosphere and underlying mantle: A seismological appraisal based on multimode surface-wave dispersion analysis, shear-velocity tomography, and tectonic regionalization, in *The Earth's heterogeneous mantle*, pp. 3–46, Springer.

Schmandt, B. (2012), Mantle transition zone shear velocity gradients beneath US-Array, *Earth and Planetary Science Letters*, *355*, 119–130.

Schmandt, B., K. Dueker, S. Hansen, J. J. Jasbinsek, and Z. Zhang (2011), A sporadic low-velocity layer atop the western US mantle transition zone and short-wavelength variations in transition zone discontinuities, *Geochemistry, Geophysics, Geosystems*, *12*(8).

Schmandt, B., S. D. Jacobsen, T. W. Becker, Z. Liu, and K. G. Dueker (2014), Dehydration melting at the top of the lower mantle, *Science*, *344*(6189), 1265–1268.

Schmidt, M. W., and S. Poli (1998), Experimentally based water budgets for dehydrating slabs and consequences for arc magma generation, *Earth and Planetary Science Letters*, *163*(1), 361–379.

Schulze, K., H. Marquardt, T. Kawazoe, T. B. Ballaran, C. McCammon, M. Koch-Müller, A. Kurnosov, and K. Marquardt (2018), Seismically invisible water in Earth's transition zone?, *Earth and Planetary Science Letters*, *498*, 9–16.

Semenov, A., and A. Kuvshinov (2012), Global 3-D imaging of mantle conductivity based on inversion of observatory C-responses–II. Data analysis and results, *Geophysical Journal International*, *191*(3), 965–992.

Shan, B., J. Afonso, Y. Yang, C. Grose, Y. Zheng, X. Xiong, and L. Zhou (2014), The thermochemical structure of the lithosphere and upper mantle beneath south China: Results from multiobservable probabilistic inversion, *Journal of Geophysical Research: Solid Earth*, *119*(11), 8417–8441.

Shearer, P. M. (2000), Upper mantle seismic discontinuities, *Earth's deep interior: mineral physics and tomography from the atomic to the global scale*, pp. 115–131.

Shen, J., J. M. Lorenzo, C. D. White, and F. Tsai (2015), Soil density, elasticity, and the soil-water characteristic curve inverted from field-based seismic P-and S-wave velocity in shallow nearly saturated layered soils, *Geophysics*, *80*(3), WB11–WB19.

Shen, W., M. H. Ritzwoller, and V. Schulte-Pelkum (2013), A 3-D model of the crust and uppermost mantle beneath the Central and Western US by joint inversion of receiver functions and surface wave dispersion, *Journal of Geophysical Research: Solid Earth*, *118*(1), 262–276.

Shimizu, H., H. Utada, K. Baba, T. Koyama, M. Obayashi, and Y. Fukao (2010), Three-dimensional imaging of electrical conductivity in the mantle transition zone beneath the North Pacific Ocean by a semi-global induction study, *Physics of the Earth and Planetary Interiors*, *183*(1), 252–269.

Shore, R., K. Whaler, S. Macmillan, C. Beggan, J. Velímskỳ, and N. Olsen (2016), Decadal period external magnetic field variations determined via eigenanalysis, *Journal of Geophysical Research: Space Physics*, *121*(6), 5172–5184.

Simmons, N., and H. Gurrola (2000), Multiple seismic discontinuities near the base of the transition zone in the Eearth's mantle, *Nature*, *405*(6786), 559.

Simmons, N. A., A. M. Forte, and S. P. Grand (2009), Joint seismic, geodynamic and mineral physical constraints on three-dimensional mantle heterogeneity: Implications for the relative importance of thermal versus compositional heterogeneity, *Geophysical Journal International*, *177*(3), 1284–1304.

Simpson, F., and K. Bahr (2005), *Practical magnetotellurics*, Cambridge University Press.

Sobolev, A. V., A. W. Hofmann, D. V. Kuzmin, G. M. Yaxley, N. T. Arndt, S.-L. Chung, L. V. Danyushevsky, T. Elliott, F. A. Frey, M. O. Garcia, et al. (2007), The amount of recycled crust in sources of mantle-derived melts, *Science*, *316*(5823), 412–417.

Sodoudi, F., X. Yuan, Q. Liu, R. Kind, and J. Chen (2006), Lithospheric thickness beneath the Dabie Shan, central eastern China from S receiver functions, *Geophysical Journal International*, *166*(3), 1363–1367.

Song, T.-R. A., and D. V. Helmberger (2006), Low velocity zone atop the transition zone in the western US from S waveform triplication, *Earth's Deep Water Cycle*, pp. 195–213.

Song, T.-R. A., D. V. Helmberger, and S. P. Grand (2004), Low-velocity zone atop the 410-km seismic discontinuity in the northwestern United States, *Nature*, *427*(6974), 530–533.

Stixrude, L., and C. Lithgow-Bertelloni (2005a), Mineralogy and elasticity of the oceanic upper mantle: Origin of the low-velocity zone, *Journal of Geophysical Research: Solid Earth*, *110*(B3).

Stixrude, L., and C. Lithgow-Bertelloni (2005b), Thermodynamics of mantle minerals-I. physical properties, *Geophysical Journal International*, *162*(2), 610–632.

Stixrude, L., and C. Lithgow-Bertelloni (2011), Thermodynamics of mantle minerals-II. Phase equilibria, *Geophysical Journal International*, *184*(3), 1180–1213.

Sun, J., A. Kelbert, and G. Egbert (2015), Ionospheric current source modeling and global geomagnetic induction using ground geomagnetic observatory data, *Journal of Geophysical Research: Solid Earth*, *120*(10), 6771–6796.

Tackley, P. J. (2000), Self consistent generation of tectonic plates in time-dependent, three dimensional mantle convection simulations, part 1: Pseudoplastic yielding, *G3*, *1*(2000GC000036).

Tackley, P. J. (2008), Geodynamics: Layer cake or plum pudding?, *Nature Geoscience*, *1*(3), 157.

Tackley, P. J., S. Xie, T. Nakagawa, and J. W. Hernlund (2005), Numerical and laboratory studies of mantle convection: Philosophy, accomplishments, and thermochemical structure and evolution, *Geophysical Monograph-American Geophysical Union*, *160*, 83.

Tape, C., Q. Liu, A. Maggi, and J. Tromp (2009), Adjoint tomography of the southern California crust, *Science*, *325*(5943), 988–992.

Tarantola, A. (2005), *Inverse problem theory and methods for model parameter estimation*, siam.

Tarantola, A., and B. Valette (1982), Generalized nonlinear inverse problems solved using the least squares criterion, *Reviews of Geophysics*, *20*(2), 219–232.

Tarits, P., and M. Mandéa (2010), The heterogeneous electrical conductivity structure of the lower mantle, *Physics of the Earth and Planetary Interiors*, *183*(1), 115–125.

Tarits, P., S. Hautot, and F. Perrier (2004), Water in the mantle: Results from electrical conductivity beneath the french alps, *Geophysical Research Letters*, *31*(6).

Tauzin, B., and Y. Ricard (2014), Seismically deduced thermodynamics phase diagrams for the mantle transition zone, *Earth and Planetary Science Letters*, *401*, 337–346.

Tauzin, B., E. Debayle, and G. Wittlinger (2008), The mantle transition zone as seen by global Pds phases: no clear evidence for a thin transition zone beneath hotspots, *Journal of Geophysical Research: Solid Earth*, *113*(B8).

Tauzin, B., R. D. Van Der Hilst, G. Wittlinger, and Y. Ricard (2013), Multiple transition zone seismic discontinuities and low velocity layers below western United States, *Journal of Geophysical Research: Solid Earth*, *118*(5), 2307–2322.

Tauzin, B., S. Kim, and B. Kennett (2017), Pervasive seismic low-velocity zones within stagnant plates in the mantle transition zone: Thermal or compositional origin?, *Earth and Planetary Science Letters*, *477*, 1–13.

Tauzin, B., S. Kim, and J.-C. Afonso (2018), Multiple phase changes in the mantle transition zone beneath northeast Asia: Constraints from teleseismic reflected and converted body-waves, *Journal of Geophysical Research: Solid Earth*.

Thio, V., L. Cobden, and J. Trampert (2015), Seismic signature of a hydrous mantle transition zone, *Physics of the Earth and Planetary Interiors*, *250*, 46–63.

Thompson, D., J. Hammond, J.-M. Kendall, G. Stuart, G. Helffrich, D. Keir, A. Ayele, and B. Goitom (2015), Hydrous upwelling across the mantle transition zone beneath the Afar Triple Junction, *Geochemistry, Geophysics, Geosystems*, *16*(3), 834–846.

Tirone, M., J. Ganguly, and J. Morgan (2009), Modeling petrological geodynamics in the Earth's mantle, *Geochemistry, Geophysics, Geosystems*, *10*(4).

Toffelmier, D. A., and J. A. Tyburczy (2007), Electromagnetic detection of a 410-km-deep melt layer in the southwestern United States, *Nature*, *447*(7147), 991–994.

Trampert, J. (1998), Global seismic tomography: the inverse problem and beyond, *Inverse Problems*, *14*(3), 371.

Trampert, J., F. Deschamps, J. Resovsky, and D. Yuen (2004), Probabilistic tomography maps chemical heterogeneities throughout the lower mantle, *Science*, *306*(5697), 853–856.

Utada, H., T. Koyama, H. Shimizu, and A. Chave (2003), A semi-global reference model for electrical conductivity in the mid-mantle beneath the north Pacific region, *Geophysical Research Letters*, *30*(4).

Utada, H., T. Koyama, M. Obayashi, and Y. Fukao (2009), A joint interpretation of electromagnetic and seismic tomography models suggests the mantle transition zone below Europe is dry, *Earth and Planetary Science Letters*, *281*(3), 249–257.

Van Driel, M., L. Krischer, S. C. Stähler, K. Hosseini, and T. Nissen-Meyer (2015), Instaseis: Instant global seismograms based on a broadband waveform database, *Solid Earth*, *6*(2), 701.

Velímskỳ, J. (2010), Electrical conductivity in the lower mantle: Constraints from CHAMP satellite data by time-domain EM induction modelling, *Physics of the Earth and Planetary Interiors*, *180*(3), 111–117.

Verhoeven, O., A. Mocquet, P. Vacher, A. Rivoldini, M. Menvielle, P.-A. Arrial, G. Choblet, P. Tarits, V. Dehant, and T. Van Hoolst (2009), Constraints on thermal state and composition of the Earth's lower mantle from electromagnetic impedances and seismic data, *Journal of Geophysical Research: Solid Earth*, *114*(B3).

Vinnik, L., and V. Farra (2007), Low S velocity atop the 410-km discontinuity and mantle plumes, *Earth and Planetary Science Letters*, *262*(3), 398–412.

Vinnik, L., M. Ravi Kumar, R. Kind, and V. Farra (2003), Super-deep low-velocity layer beneath the Arabian plate, *Geophysical Research Letters*, *30*(7).

Vinnik, L., S. Oreshin, G. Kosarev, S. Kiselev, and L. Makeyeva (2009), Mantle anomalies beneath southern Africa: Evidence from seismic S and P receiver functions, *Geophysical Journal International*, *179*(1), 279–298.

Wang, D., M. Mookherjee, Y. Xu, and S.-i. Karato (2006), The effect of water on the electrical conductivity of olivine, *Nature*, *443*(7114), 977.

Watt, J. P., G. F. Davies, and R. J. O'Connell (1976), The elastic properties of composite materials, *Reviews of Geophysics*, *14*(4), 541–563.

Weidelt, P. (1972), The inverse problem of geomagnetic induction, *J. Geophys.*, *38*, 257–289.

Weidner, D. J. (1985), A mineral physics test of a pyrolite mantle, *Geophysical Research Letters*, *12*(7), 417–420.

Williams, Q., and R. J. Hemley (2001), Hydrogen in the deep Earth, *Annual Review of Earth and Planetary Sciences*, *29*(1), 365–418.

Wood, B. J., and J. R. Holloway (1984), A thermodynamic model for subsolidus equilibria in the system CaO–MgO–Al2O3–SiO2, *Geochimica et Cosmochimica Acta*, *48*(1), 159–176.

Wu, W., S. Ni, and J. C. Irving (2019), Inferring Earth's discontinuous chemical layering from the 660–kilometer boundary topography, *Science*, *363*(6428), 736–740.

Xie, S., and P. J. Tackley (2004), Evolution of U-Pb and Sm-Nd systems in numerical models of mantle convection and plate tectonics, *Journal of Geophysical Research: Solid Earth*, *109*(B11).

Xu, W., C. Lithgow-Bertelloni, L. Stixrude, and J. Ritsema (2008), The effect of bulk composition and temperature on mantle seismic structure, *Earth and Planetary Science Letters*, *275*(1), 70–79.

Xu, Y., T. J. Shankland, and B. T. Poe (2000), Laboratory-based electrical conductivity in the Earth's mantle, *Journal of Geophysical Research: Solid Earth*, *105*(B12), 27,865–27,875.

Yamazaki, Y., and A. Maute (2017), Sq and EEJ–A review on the daily variation of the geomagnetic field caused by ionospheric dynamo currents, *Space Science Reviews*, *206*(1-4), 299–405.

Yoshino, T. (2010), Laboratory electrical conductivity measurement of mantle minerals, *Surveys in Geophysics*, *31*(2), 163–206.

Yoshino, T., and T. Katsura (2009), Effect of iron content on electrical conductivity of ringwoodite, with implications for electrical structure in the transition zone, *Physics of the Earth and Planetary Interiors*, *174*(1), 3–9.

Yoshino, T., and T. Katsura (2012), Re-evaluation of electrical conductivity of anhydrous and hydrous wadsleyite, *Earth and Planetary Science Letters*, *337*, 56–67.

Yoshino, T., and T. Katsura (2013), Electrical conductivity of mantle minerals: role of water in conductivity anomalies, *Annual review of earth and planetary sciences*, *41*, 605–628.

Yoshino, T., G. Manthilake, T. Matsuzaki, and T. Katsura (2008a), Dry mantle transition zone inferred from the conductivity of wadsleyite and ringwoodite, *Nature*, *451*(7176), 326–329.

Yoshino, T., M. Nishi, T. Matsuzaki, D. Yamazaki, and T. Katsura (2008b), Electrical conductivity of majorite garnet and its implications for electrical structure in the mantle transition zone, *Physics of the Earth and Planetary Interiors*, *170*(3), 193–200.

Yoshino, T., M. Laumonier, E. McIsaac, and T. Katsura (2010), Electrical conductivity of basaltic and carbonatite melt-bearing peridotites at high pressures:

Implications for melt distribution and melt fraction in the upper mantle, *Earth and Planetary Science Letters*, *295*(3), 593–602.

Yoshino, T., E. Ito, T. Katsura, D. Yamazaki, S. Shan, X. Guo, M. Nishi, Y. Higo, and K.-i. Funakoshi (2011), Effect of iron content on electrical conductivity of ferropericlase with implications for the spin transition pressure, *Journal of Geophysical Research: Solid Earth*, *116*(B4).

Yoshino, T., A. Shimojuku, S. Shan, X. Guo, D. Yamazaki, E. Ito, Y. Higo, and K.-i. Funakoshi (2012), Effect of temperature, pressure and iron content on the electrical conductivity of olivine and its high-pressure polymorphs, *Journal of Geophysical Research: Solid Earth*, *117*(B8).

Yoshino, T., S. Kamada, C. Zhao, E. Ohtani, and N. Hirao (2016), Electrical conductivity model of Al-bearing bridgmanite with implications for the electrical structure of the Earth's lower mantle, *Earth and Planetary Science Letters*, *434*, 208–219.

Yu, C., E. A. Day, V. Maarten, M. Campillo, S. Goes, R. A. Blythe, and R. D. van der Hilst (2018), Compositional heterogeneity near the base of the mantle transition zone beneath Hawaii, *Nature Communications*, *9*(1), 1266.

Yuan, H., B. Romanowicz, K. M. Fischer, and D. Abt (2011), 3-D shear wave radially and azimuthally anisotropic velocity model of the North American upper mantle, *Geophysical Journal International*, *184*(3), 1237–1260.

Yuan, X., R. Kind, X. Li, and R. Wang (2006), The S receiver functions: synthetics and data example, *Geophysical Journal International*, *165*(2), 555–564.

Zhang, B., T. Yoshino, X. Wu, T. Matsuzaki, S. Shan, and T. Katsura (2012), Electrical conductivity of enstatite as a function of water content: implications for the electrical structure in the upper mantle, *Earth and Planetary Science Letters*, *357*, 11–20.

Zhao, C., and T. Yoshino (2016), Electrical conductivity of mantle clinopyroxene as a function of water content and its implication on electrical structure of uppermost mantle, *Earth and Planetary Science Letters*, *447*, 1–9.

Zhu, H., E. Bozdağ, and J. Tromp (2015), Seismic structure of the European upper mantle based on adjoint tomography, *Geophysical Journal International*, *201*(1), 18–52.

Zunino, A., J. Connolly, and A. Khan (2011), Precalculated phase equilibrium models for geophysical properties of the crust and mantle as a function of composition, *Geochemistry, Geophysics, Geosystems*, *12*(4).

Zunino, A., A. Khan, P. Cupillard, and K. Mosegaard (2016), Constitution and Structure of Earth's Mantle: Insights from Mineral Physics and Seismology, *Integrated Imaging of the Earth: Theory and Applications*, *218*, 219.

List of Tables

List of Figures

Acknowledgements

Working on this project has been an amazing experience for me, both academic and personal. This work would not have been possible without the help and support of a number of people.

First of all, I am deeply grateful to Amir Khan for giving me the chance to work on this project and for his thoughtful supervision over the past four years. He always had time for a discussion when I needed advice and his critical feedback truly shaped my problem-solving skills. I would also like to thank Alexey Kuvshinov, Alexander Grayver, and Benoit Tauzin for their support and advice not only on technical aspects but also on career-related issues.

Furthermore, I would like to thank Martin van Driel for introducing me into the world of *Python* and James Connolly for his help and patience every time I dropped by his office with a naive question on mineral physics. I am also grateful to Domenico Gardini for the opportunity to work in Seismology and Geodynamics group and, in particular, his support during the final stage of my PhD.

Many thanks to Jeroen Ritsema and Jakub Velimský for being part of my committee and be willing to give me feedback on my research. In addition, I would like to thank Paul Tackly for officiating as chairperson.

The four years of my PhD will remain as a very positive memory, thanks to the great environment I found at the Department of Earth Science. In particular, I would like to thank Sebastian Cionoiu, Katharina Schmidt, Barbara Lesniak, Antonio Manjon Cabeza Cordoba, Johannes Käufl, Nicolo Lardelli, Fabian Burnmann, and Charitra Jain for many unforgettable conversations and shared experiences at various conferences. I want to thank the "big office" crew specially for tolerating my "finishing-PhD" mood and I am very grateful to Fabian Burnmann for his help writing the "Zusammenfassung" for this work.

For financial support, I thank the Swiss National Science Foundation (SNF project 200021_159907). For their help in all administrative issues, I thank Elisabeth Läderach, André, Monika Bolliger, and Sigrid Trindler. I would also like to also the men and women who are in charge of keeping the office and building clean.

I would like to acknowledge my friends in La Plata, who, even from Argentina, were always present during these fours years. And last but not least, I thank my parents – Norma and Ricardo – and my sister Beatriz for their constant love and support.